



**HAL**  
open science

# Development of MR fingerprinting for brain oxygenation mapping

Aurélien Delphin

► **To cite this version:**

Aurélien Delphin. Development of MR fingerprinting for brain oxygenation mapping. Physics [physics]. Université Grenoble Alpes [2020-..], 2022. English. NNT : 2022GRALY069 . tel-04003704

**HAL Id: tel-04003704**

**<https://theses.hal.science/tel-04003704>**

Submitted on 24 Feb 2023

**HAL** is a multi-disciplinary open access archive for the deposit and dissemination of scientific research documents, whether they are published or not. The documents may come from teaching and research institutions in France or abroad, or from public or private research centers.

L'archive ouverte pluridisciplinaire **HAL**, est destinée au dépôt et à la diffusion de documents scientifiques de niveau recherche, publiés ou non, émanant des établissements d'enseignement et de recherche français ou étrangers, des laboratoires publics ou privés.

THÈSE

Pour obtenir le grade de

## DOCTEUR DE L'UNIVERSITÉ GRENOBLE ALPES

École doctorale: PHYS - Physique

Spécialité : Physique pour les Sciences du Vivant

Unité de recherche: Grenoble Institut des Neurosciences

### Développements IRM Fingerprint pour la mesure de l'oxygénation cérébrale

### Development of MR Fingerprinting for brain oxygenation mapping

Présentée par :

**Aurélien DELPHIN**

Direction de thèse :

**Emmanuel BARBIER**  
Université Grenoble Alpes

Directeur de thèse

**Thomas CHRISTEN**  
Université Grenoble Alpes

Co-encadrant de thèse

Thèse soutenue publiquement le **28 Novembre 2022**  
devant le jury composé de :

**Olivier DETANTE**  
PUPH, Université Grenoble Alpes

Président du jury

**Jacques FELBLINGER**  
PUPH, CHRU Nancy

Rapporteur

**Matthias J.P. VAN OSCH**  
PROFESSEUR, Leiden University Medical Center

Rapporteur

**Mariya DONEVA**  
DOCTEUR EN SCIENCES, Philips Research Hamburg

Examinatrice

**Benjamin MARTY**  
CHARGE DE RECHERCHE, Institut de Myologie

Examineur

**Angélique STEPHANOU**  
CHARGE DE RECHERCHE, Université Grenoble Alpes

Examinatrice







*Impossible que j'me fâche quand j'entends sonner les cloches des vaches.*

DJ Matafan



## ACKNOWLEDGEMENTS

---

A few words will probably not be enough to express my gratitude to Emmanuel and Thomas for entrusting me with this project, for their patience and kindness, and for their incredible capacity to communicate their dedication and commitment to keep exploring and questioning. You have been a constant source of motivation and this thesis is as much your work as it is mine.

A kind thank you to the rapporteurs and jury members who agreed to review this manuscript and came to the GIN for the defense. It was an honor to defend my work in front of you and I hope we will have more opportunities to meet and collaborate in the future.

I want to thank my friends and colleagues from the team who made the everyday life at the lab an amazing experience. Whether on the break room couch with a coffee or on the skis with génépi, you brought what is needed to go through those days where nothing seems to go as expected.

Nora, tonton Hervé, Vasile, Olivier, Laurent, none of the experiments presented here would have been possible without the experience you shared with me, and the data generation and management would have been so much more painful without Paul and Jan. I would like to give you the gratitude you deserve.

A warm thank you to all those who helped me clear my mind during week-ends and holidays by pulling me out of work for mountain trips and/or food. A special thought to Dr. Yann Alexanian for our daily exchanges during the redaction, for the cheese, and his L<sup>A</sup>T<sub>E</sub>X template.

Finally, nothing would have been possible without the ever supporting and reassuring presence of Charlotte. We managed to do quite a number of things during this thesis, let's see what we can do now that it is done. Thank you for completing me so well and for always being there, especially when it rains!

*I dedicate this thesis to my parents who have been supporting and encouraging me ever since I left home.*



# CONTENTS

---

<b>Contents</b>	<b>i</b>
<b>Ethics statements</b>	<b>v</b>
<b>List of Abbreviations</b>	<b>vii</b>
<b>General Introduction</b>	<b>1</b>
<b>I Brain oxygenation mapping: definitions, rationale and techniques</b>	<b>5</b>
<b>I.1 Brain oxygenation definitions</b>	<b>7</b>
<b>I.2 Rationale for brain oxygenation mapping</b>	<b>8</b>
I.2.1 Hypoxia assessment in tumors . . . . .	9
I.2.2 Penumbra detection in stroke patients . . . . .	10
<b>I.3 Current techniques for brain oxygenation mapping</b>	<b>12</b>
I.3.1 Non-MRI-based techniques . . . . .	12
I.3.2 MRI-based techniques . . . . .	17
<b>I.4 MR Fingerprinting for brain oxygenation mapping</b>	<b>25</b>
I.4.1 Principles and standard applications of MRF . . . . .	26
I.4.2 MR vascular Fingerprinting . . . . .	28
<b>I.5 State-of-the-art summary</b>	<b>31</b>
<b>II Developing tools for MRvF</b>	<b>33</b>
<b>II.1 Development of MRI simulation tools</b>	<b>36</b>
II.1.1 Simulation tools for classical MRF . . . . .	36
II.1.2 Simulation tool for MR vascular Fingerprinting . . . . .	43
II.1.3 Validation of the tools . . . . .	51
II.1.4 Conclusions and perspectives . . . . .	58
<b>II.2 Pre-clinical MRF acquisitions</b>	<b>59</b>
II.2.1 Overview of the existing acquisition tool . . . . .	60
II.2.2 New developments . . . . .	66
II.2.3 First MRF results in vivo . . . . .	69
II.2.4 Conclusions and Perspectives . . . . .	71
<b>II.3 Test of a clinical MRF acquisition module</b>	<b>75</b>

II.3.1	Context: Philips Research collaboration . . . . .	75
II.3.2	Overview . . . . .	75
II.3.3	Evaluation of the MRF module . . . . .	76
II.3.4	Perspectives . . . . .	81
<b>II.4</b>	<b>Development of MRF reconstruction tools</b>	<b>82</b>
II.4.1	Exploratory reconstruction tool . . . . .	82
II.4.2	Developments for MP3 . . . . .	84
II.4.3	Perspectives . . . . .	86
<b>III</b>	<b>Improving MRvF with realistic 3D vascular networks</b>	<b>89</b>
<b>III.1</b>	<b>Using 3D voxels segmented from microscopies for dictionary generation</b>	<b>91</b>
III.1.1	Objectives . . . . .	91
III.1.2	Materials and methods . . . . .	91
III.1.3	Main results on control and 9L rats . . . . .	96
III.1.4	Additional results on C6 tumors and strokes . . . . .	100
III.1.5	Discussion . . . . .	101
<b>III.2</b>	<b>Synthetic vasculature generation: Constructive Constrained Optimization</b>	<b>104</b>
III.2.1	Principles . . . . .	104
III.2.2	Implementations . . . . .	106
III.2.3	Results . . . . .	110
<b>III.3</b>	<b>Conclusion and future perspectives</b>	<b>113</b>
<b>IV</b>	<b>Designing efficient sequences for MRvF</b>	<b>117</b>
<b>IV.1</b>	<b>Methods to evaluate the encoding capacity of a sequence</b>	<b>119</b>
IV.1.1	Point-wise standard deviation of the dictionary . . . . .	119
IV.1.2	Monte-Carlo method . . . . .	121
<b>IV.2</b>	<b>Studies on multi gradient echo sequences</b>	<b>122</b>
IV.2.1	In-silico fingerprint evaluation . . . . .	122
IV.2.2	Evaluation on retrospective pre-clinical data . . . . .	126
IV.2.3	Limitation of GESFIDSE based sequences . . . . .	127
<b>IV.3</b>	<b>Studies on balanced SSFP-based sequences</b>	<b>127</b>
IV.3.1	Review on bSSFP BOLD sensitivity . . . . .	127
IV.3.2	In-silico fingerprint design . . . . .	137
IV.3.3	Preliminary in vivo results . . . . .	143
	<b>General Conclusion</b>	<b>145</b>
	<b>Bibliography</b>	<b>147</b>

**List of Figures**

**I**

**Published work**

**V**

**Résumé français - French summary**

**VII**





## ETHICS STATEMENTS

---

### **Animal experiments**

All animal procedures conformed to French government guidelines and were performed under permits 380820 and A3851610008 (for experimental and animal care facilities) from the French Ministry of Agriculture (Articles R214–117 to R214–127 published on 7 February 2013), and in compliance with the ARRIVE guidelines (Animal Research: Reporting in Vivo Experiments).

All animal preparations were performed by an expert animal technician.

Efforts were made to use animals from other experiments and retrospective data when possible to limit as much as possible this thesis' impact.

### **Human experiments**

All human procedures were performed under the MAP-IRMaGe protocol guidelines (NCT05036629), validated by the CHU Grenoble Alpes, and coordinated by Dr. Arnaud Attyé.



## LIST OF ABBREVIATIONS

---

<b>ADC</b>	Apparent Diffusion Coefficient
<b>BVf</b>	Blood Volume-fraction
<b>CMRO<sub>2</sub></b>	Cerebral Metabolic Rate of O <sub>2</sub>
<b>CA</b>	Contrast agent
<b>EPR</b>	Electron Paramagnetic Resonance
<b>ESRF</b>	European Synchrotron Radiation Facility
<b>FA</b>	Flip Angle
<b>FID</b>	Free Induction Decay
<b>FOV</b>	Field Of View
<b>GRE</b>	Gradient echo
<b>GUI</b>	Graphical User Interface
<b>MC</b>	Monte-Carlo
<b>MGEFIDSE</b>	Multi Gradient Echo of the Free Induction Decay and Spin Echo
<b>NIRS</b>	Near Infrared Spectroscopy
<b>pO<sub>2</sub></b>	Partial oxygen pressure
<b>PV</b>	ParaVision
<b>R</b>	Mean vessel radius
<b>RF</b>	Radio Frequency
<b>SE</b>	Spin echo
<b>SO<sub>2</sub></b>	Oxygen saturation
<b>SSFP</b>	Steady-State Free Precession
<b>TE</b>	Echo time
<b>TR</b>	Repetition time
<b>USPIO</b>	Ultra Small Paramagnetic Iron Oxide

---



## GENERAL INTRODUCTION

---

The role of oxygen in life is central. Two billion years ago, the “great oxygenation event” saw the rise of O<sub>2</sub> concentration in the oceans and atmosphere. This period is often considered as the beginning of the rise of eukaryote organisms, of which complex life forms as we know them, humans included, are members. Eukaryotes cells rely on oxygen-based reactions to produce the energy necessary for their functioning. Not all cells, tissue, and organs have the same demands though. The human brain heavily consumes oxygen: it represents 20% of the entire human body O<sub>2</sub> consumption while only accounting for 2% of its mass. It is, however, as the rest of the body, unable to store oxygen and is thus at risk when the blood flow that ensures its supply is impaired. Such events are often linked with cell injury or death, which for the brain has dire repercussions on cognitive functions.

Several brain pathologies can be linked with oxygenation perturbations. Stroke, which results from local disruptions of blood flow, cut off the oxygen supply of brain cells. Long term stroke effects are directly dependent on how much time these tissues are deprived of their energy source.

In tumors, the unregulated cell growth creates under-perfused areas which are deprived of oxygen supply. In reaction, chaotic angiogenesis is often observed in the lesions, with the creation of new abnormal vessel networks. This process is generally not sufficient and leads to intermittent blood flow and transient hypoxic episodes. In consequence, the hypoxic pressure leads to the selection of aggressive tumor cells, and increases their radio and chemoresistance. Fortunately, stroke and tumor care have been improved in the last years. The therapeutic window for acute stroke is being extended with the rise endovascular therapies and solutions to prevent tumor hypoxia and increase treatment efficiency are under development. The literature on this matter often points to the potential benefits of proper cerebral oxygenation mapping techniques for patient care. Better emergency patient triage, patient-specific therapy, accurate outcome predictions, and a better understanding of pathologies could be foreseen.

Currently, clinically available methods for oxygenation measurements include intracranial probes and positron emission tomography (PET). The first one has been used for decades and is still the preferred oxygenation monitoring technique at the bedside, but only provides local measurement and is particularly invasive. The second one is used to provide maps of the concentration of a hypoxia marker, but gives little information in the rest of the brain. It also requires the injection of a radioactive tracer which is not always possible in an acute care context. Research and development of better oxygenation mapping is thus a topic of interest. Several new techniques have been proposed over the years, and rely on a number of different physical principles. Electron paramagnetism resonance and opto-acoustic techniques have demonstrated promising in vivo results but are only available in a few research laboratories. MRI is known to be sensitive to a large variety of contrasts and physical properties including deoxyhemoglobin paramagnetism. The Blood Oxygenation Level Dependent (or BOLD) effect has revolutionized the field of neurosciences and the study of brain functions. In the context of acute care, MRI yet suffers from its low acquisition speed, and does not provide

robust, quantitative measurements.

In 2013, a new MRI paradigm called MR Fingerprinting (MRF) has been proposed to dramatically reduce the duration of MRI exams and provide multiple quantitative measurements at the same time. The basic principle of MRF relies on the comparison of complex time evolution of in vivo MR signals with advanced numerical simulations of the same experiment. In 2014, our team demonstrated that the technique could be adapted to be able to quantitatively map cerebral oxygenation and several other vascular parameters of interest ([Christen et al. 2014b](#)). However, this proof of concept of the “MR vascular Fingerprinting (MRvF)” approach presented certain limitations. Injection of a contrast agent was required, and the sensitivity of the method was not ideal.

This Ph.D. project took place at the Grenoble Institut des Neurosciences in the “Functional Neuroimaging and Brain Perfusion” team. It is part of a larger project that aims to solve MRvF’s current limitations and include oxygenation measurements in a unique MRF acute stroke imaging protocol. The lab relies on its preclinical and clinical MRI platform IRMaGe and on the combined expertise of neurologists and MR researchers. The scope of this thesis was to develop a flexible MRF pipeline encompassing numerical simulations, preclinical and clinical acquisitions, and image reconstruction, to allow for efficient conception of MRF protocols. It was then used to improve the MRvF measurements. The thesis was funded by the Grenoble Alpes University’s TRACE project which focuses on brain oxygenation and acute care for traumatic brain injury.

The present dissertation is organized into 4 chapters.

Chapter [I](#) briefly introduces definitions of tissue oxygenation and their associated concepts, and provides a rationale for cerebral oxygenation mapping. Existing in vivo oxygenation measurement techniques are then introduced, with a particular focus on MRI-based approaches and the theoretical bases of MRI’s sensitivity to tissue oxygenation. Eventually, an in-depth presentation of Magnetic Resonance Fingerprinting is proposed, as well as a literature review of its application for cerebral oxygenation mapping.

Chapter [II](#) introduces the methods and tools developed during our project using codes available in the lab, tools provided by the community or through collaborations, and new implementations of state-of-the-art literature. We worked on MR simulation tools, acquisition modules for preclinical and clinical scanners, and parametric map reconstruction algorithms to obtain a flexible and robust MRF pipeline.

Chapter [III](#) presents the improvements made on MRvF’s sensitivity to tissue oxygen saturation using new 3D simulations based on vessel networks segmented from microscopy data shared by the scientific community. We compared our estimates to previous MRvF results obtained on animal retrospective data. On tumor-bearing animals, only our proposed method correlated with intracranial oxygenation measurements. Further improvements using generation of realistic vascular networks from scratch have also been evaluated with the help of a master’s student, and are discussed.

Chapter IV present our works towards identifying new MRvF acquisition sequences that do not require contrast-agent injection but still exhibit an increased oxygenation sensitivity. Methods to evaluate the potential of a sequence in silico are presented and tested on previously acquired data. Modification on the initial MRvF sequence already improved the microvascular estimates. Because the MR Fingerprinting framework allows the use of unconventional MR sequences, a literature review was then proposed to identify new sequence types that could exhibit sensitivity to oxygenation. In collaboration with another PH.D. student, we used numerical simulations to propose promising new acquisition schemes that eliminate the need for contrast agent injection. Preliminary results on animal data are eventually discussed.





# CHAPTER I

---

## BRAIN OXYGENATION MAPPING: DEFINITIONS, RATIONALE AND TECHNIQUES

---

This first chapter briefly introduces elements of oxygen transport in the body and different quantities that have been defined to express the presence and consumption of  $O_2$  in the tissues. We discuss the need for brain oxygenation mapping for medical research and patient care. Existing methods for in vivo oxygen quantification and brain oxygenation mapping are introduced, with a particular focus on MRI-based techniques and the theoretical bases of MRI's sensitivity to tissue oxygenation. Finally, an in-depth presentation of Magnetic Resonance Fingerprinting is proposed, including its derived version for cerebral oxygenation mapping.

---

**CONTENTS**


---

<b>I.1</b>	<b>Brain oxygenation definitions</b>	<b>7</b>
<b>I.2</b>	<b>Rationale for brain oxygenation mapping</b>	<b>8</b>
I.2.1	Hypoxia assessment in tumors . . . . .	9
I.2.2	Penumbra detection in stroke patients . . . . .	10
<b>I.3</b>	<b>Current techniques for brain oxygenation mapping</b>	<b>12</b>
I.3.1	Non-MRI-based techniques . . . . .	12
I.3.1.1	pO <sub>2</sub> measurements using Intracranial probes . . . . .	12
I.3.1.2	pO <sub>2</sub> measurements using Electron Paramagnetic Resonance . . . . .	13
I.3.1.3	OEF measurements using Photon Emission Tomography . . . . .	14
I.3.1.4	SO <sub>2</sub> measurements using Near-Infrared Spectroscopy . . . . .	14
I.3.1.5	SO <sub>2</sub> measurements using Photoacoustic Imaging . . . . .	15
I.3.2	MRI-based techniques . . . . .	17
I.3.2.1	SO <sub>2</sub> measurements based on blood relaxometry . . . . .	17
I.3.2.2	SO <sub>2</sub> measurements based on quantitative Susceptibility Mapping . . . . .	18
	Quantitative susceptibility mapping . . . . .	19
I.3.2.3	SO <sub>2</sub> measurements based on Quantitative BOLD imaging . . . . .	20
	Origin of BOLD effect . . . . .	20
	Quantifying the BOLD effect . . . . .	22
	Combining QSM and qBOLD . . . . .	24
<b>I.4</b>	<b>MR Fingerprinting for brain oxygenation mapping</b>	<b>25</b>
I.4.1	Principles and standard applications of MRF . . . . .	26
I.4.2	MR vascular Fingerprinting . . . . .	28
<b>I.5</b>	<b>State-of-the-art summary</b>	<b>31</b>

---

## I.1 Brain oxygenation definitions

“Oxygène” by Jean-Michel Jarre, released in 1976, is one of the best-selling electronic music albums ever. However, this thesis is about another kind of oxygen. Two centuries earlier, in 1774 in England, the english chemist Joseph Priestly discovered a gas that was implied in combustion reactions and had an effect on living organisms when breathed. This gas was found to be one of the constituent of air and named “oxygène” by the french chemist Antoine Lavoisier in 1777.

It is now well known that dioxygen ( $O_2$ ) is necessary for almost all eukaryote organisms. It is the main oxidizing agent used in respiration reactions inside the mitochondria and produces the energy necessary for a cell to function.

Despite its critical role in the human body, oxygen can not be stored for later use. Its supply to the whole body is ensured by constant air ventilation in the lungs and blood circulation. The partial pressure of oxygen ( $pO_2$ ) in the lungs’ alveoli is higher than in the blood capillaries. Following the  $pO_2$  gradient,  $O_2$  passes the capillaries walls and dissolves into the blood. Part of the  $O_2$  molecules simply stays in this state, increasing the  $pO_2$  of the blood. But most of it is captured by hemoglobin (Hb), a protein contained in erythrocytes (red blood cells). Each molecule of hemoglobin can bind to up to 4  $O_2$  molecules and is usually bound to either 4 or none. These two states are called deoxyhemoglobin (dHb) and oxyhemoglobin, ( $HbO_2$ ).

The blood oxygen saturation  $SO_2$  is defined as:

$$SO_2 = \frac{HbO_2}{HbO_2 + dHb} \quad (I.1.1)$$

and is highly dependent on the local  $pO_2$ , as illustrated in fig. I.1.1. Two behaviors can be observed:

- $pO_2 < 60\text{mmHg}$ : small changes in  $pO_2$  bring large variations of  $SO_2$ , meaning that the exchange of  $O_2$  is facilitated. That behavior roughly corresponds to venous blood.
- $pO_2 > 60\text{mmHg}$ : large variations of  $pO_2$  bring little change to  $SO_2$ , corresponding to arterial blood.

The hemoglobin dissociation curve can change locally depending on the temperature, pH, or in pathological environments. In normal conditions, the  $pO_2$  gradient in the alveoli is usually strong enough to keep the blood  $pO_2$  high enough and reach  $SO_2 \approx 1$ . The blood is then pumped by the heart and distributed throughout the body.  $pO_2$  in healthy cells is low due to constant  $O_2$  consumption and the biological membranes that hinder  $O_2$  diffusion. There is thus always a strong  $pO_2$  gradient between blood and healthy tissues. Dissolved  $O_2$  diffuses along the gradient towards the tissues, diminishing  $pO_2$  in the blood. This causes oxygen dissociation from hemoglobin, diminishing the  $SO_2$  in the venous blood. That venous blood is continuously pumped back to the lungs to restore its  $SO_2$ , ensuring the proper oxygenation of the whole body.

In the brain, one defines the cerebral metabolic rate of  $O_2$  ( $CMRO_2$ ) as:

$$CMRO_2 = 4 \times CBF \times [Hb] \times (SaO_2 - SvO_2) \quad (I.1.2)$$

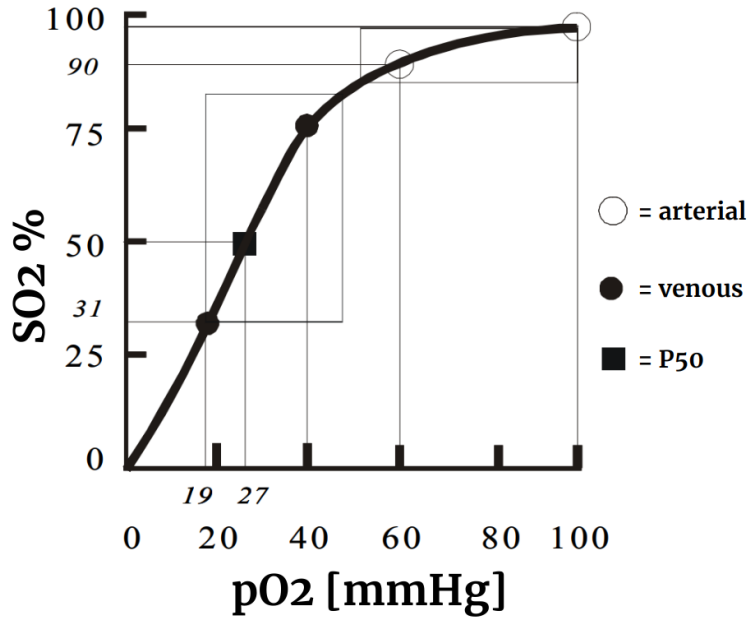


**Figure I.1.1:** Hemoglobin dissociation curve in human physiological conditions, from [Baele et al. 2002](#)

where CBF is the cerebral blood flow, and  $SaO_2$  and  $SvO_2$  are the arterial and venous  $SO_2$ . It is also common to refer to oxygen extraction function (OEF), defined as:

$$OEF = \frac{SaO_2 - SvO_2}{SaO_2} \quad (I.1.3)$$

In healthy subjects,  $SaO_2 \approx 1$  and equation I.1.3 reduces to

$$OEF = 1 - SvO_2 \quad (I.1.4)$$

In this thesis, we will use the term brain oxygenation to refer to either  $pO_2$ ,  $SO_2$ , OEF, or  $CMRO_2$  estimates. As it will be shown in the next sections, accurate measurements of brain oxygenation are not easy to obtain but it is generally admitted that healthy brain tissues present a local  $pO_2$  of 20-50mmHg, local  $StO_2$  (i.e.  $SO_2$  averaged over the venous and arterial compartments) of 60-70%, local OEF of 30-50% and local  $CMRO_2$  of 2-5 mL/100g/min. When the local  $pO_2$  drops below  $\approx 10$ mmHg, the corresponding tissue is said to be hypoxic. It usually corresponds to  $StO_2 < 40\%$ . Hyperoxic tissues have an oxygenation state higher than normal. Hypoxia and hyperoxia are sometimes induced by gas challenge experiments, where patients breath different mixtures of  $N_2$  and  $O_2$  with lower or higher concentrations than air.

## I.2 Rationale for brain oxygenation mapping

The brain represents 20% of the entire human body  $O_2$  consumption while only accounting for 2% of its mass ([Rolfe et al. 1997](#)). Interestingly, cerebral oxygen consumption varies in

time and space. This particularity allows for the identification of brain regions involved in specific cognitive task. It was studied using PET scan, and more recently with MRI, using the famous blood oxygen level dependant (BOLD) contrast (Greve 2011; Drew 2019). BOLD functional MRI (fMRI) is one of the bases of the whole cognitive exploration research field. However, quantifying the oxygen level of the tissue is of little interest for fMRI, albeit for a few applications for calibrated fMRI (Chiarelli et al. 2007; Hoge 2012; Englund et al. 2020). In opposite, a number of pathologies are known to impair cerebral oxygenation, which is directly linked with functional loss and high mortality rates. Brain oxygenation mapping would thus be of interest to improve patient care and pathology outcome. The next section presents possible (non-exhaustive) usages of brain oxygenation measurements in the pathological brain.

### I.2.1 Hypoxia assessment in tumors

Brain tumor incidence has increased in the last 20 years, exceeding 10 cases per 100,000 persons in northern Europe (Farmanfarma et al. 2019). Brain tumor mortality rate is also dramatically high. It is the second cause of death by cancer in children and the third cause in adults (15-54 years old). One of the most frequent types of primary cancers affecting the central nervous system is glioblastoma, with an average life expectancy of about one year (Barnholtz-Sloan et al. 2018; Gould 2018; McFaline-Figueroa et al. 2018). This tumor is known to exhibit highly hypoxic areas.

Hypoxia is considered as an important factor in tumour biology and in treatment response (Brown et al. 2004; Tatum et al. 2006; Graham et al. 2018; Sørensen et al. 2020). Correlations exist between hypoxia and angiogenesis, tumour aggressiveness, patient survival, and local recurrence and metastasis (Semenza 2007; Vaupel et al. 2007; Spence et al. 2008; Vaupel et al. 2014). Tumors are indeed known to cause chaotic angiogenesis resulting in tortuous vessel network and chronic or acute hypoxia (see fig. I.2.1). Such hypoxic regions are known to be more resistant to radiation therapies and chemotherapies, and to show degraded natural anti-cancer immune response (Gray et al. 1953; Graham et al. 2018; Sørensen et al. 2020). It is thus of great interest to be able to accurately and non-invasively measure brain oxygenation to assess tissue hypoxia. With such information, treatment plans could be adapted to the patient and be more efficient. Strategies involving hyperbaric-oxygen breathing could also be used to transiently restore a normoxic environment for the treatment period.

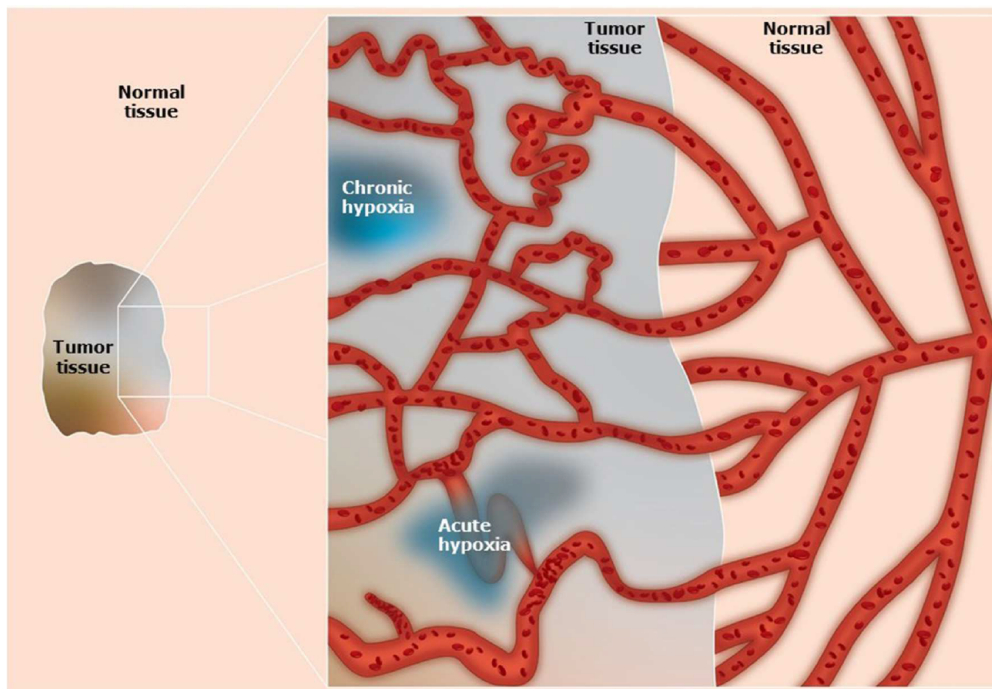


**Figure I.2.1:** Illustration of tumoral angiogenesis from [Sørensen et al. 2020](#)

## I.2.2 Penumbra detection in stroke patients

Strokes are defined as cerebral blood flow impairment. They can be caused by an obstruction of the vascular network (ischemic stroke) or by the rupture of a vessel (hemorrhagic stroke). [Feigin et al. 2021](#) estimate there were 12.2 million strokes and 6.55 million death-related strokes in the world in 2019. [Strliciu et al. 2021](#) report an overall stroke-related economic burden of €40.3 billion (Europe) and \$103.5 billion (United-States) in 2017, mainly due to the high costs of long-term special care and rehabilitation. This burden is expected to increase due to population aging and the sharp rise in hypertension, diabetes, and obesity. Fortunately, acute stroke care is in the midst of a renaissance. In 2015, six clinical trials have changed the evaluation and treatment of stroke lesions by demonstrating the efficacy of new endovascular therapies ([Warach et al. 2016](#)). One of the key findings of these studies was the important role played by brain imaging techniques that select patients who are likely to benefit from treatment and exclude patients who may be unaffected or adversely affected by treatment.

Yet, this major improvement of care was mitigated by the low number of patients ( $\approx 10.5\%$ ) who could actually receive the treatment. The low rate was largely due to patients arriving at the hospital outside the eligibility period recommended by the guidelines for receiving the treatment (i.e. within 6h from symptoms onset). This started to change in 2018 when several clinical trials showed that endovascular thrombectomy and intravenous thrombolysis could also be successful within 24 hours of stroke onset if advanced imaging protocols were used for patients' triage ([Albers et al. 2018](#)).

These successful results support the rationale that cerebral physiology may be a better prognostic indicator of outcome rather than time alone. In particular, a need for a more reliable characterization of salvageable tissue, called the ischemic penumbra, was identified.

The ischemic penumbra is defined as the area of hypoperfused cerebral tissue whose function is in danger but that can be restored if blood flow resumes. OEF mapping with PET imaging (see below) allows for the penumbra delineation but is hardly compatible with the acute stroke clinical environment. In absence of a reliable and fast OEF mapping technique, a surrogate MRI-based method has been proposed to detect the ischemic penumbra. The “mismatch” technique relies on the differences between:

- Diffusion-weighted imaging which allows the delineation of the ischemic core (where function is lost).
- Perfusion-weighted imaging which measures the blood flow, or the delay of perfusion of an exogenous contrast agent (CA), and thus identifies the hypoperfused tissue.

Although encouraging, the mismatch model is known to be limited and does not necessarily agree with PET-measured OEF maps, as shown in fig. I.2.2.

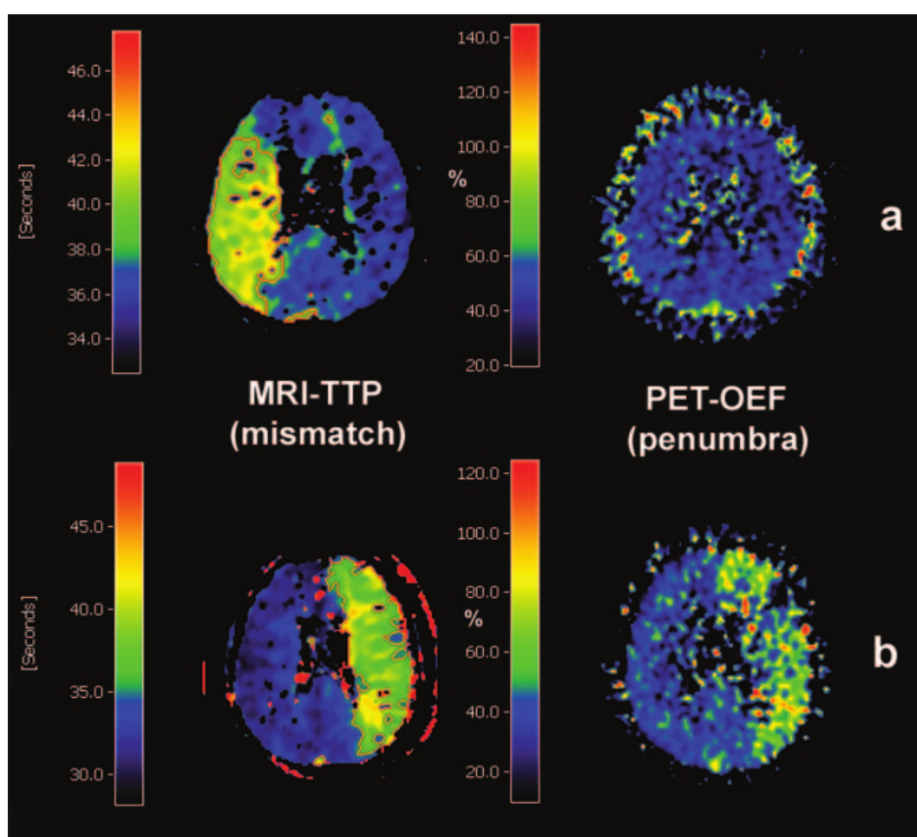


**Figure I.2.2:** Comparison of MRI perfusion/diffusion mismatch and PET-measured OEF maps, from Sobesky et al. 2005. Two chronic stroke patients (a and b) were imaged. The left column shows MRI perfusion images. The mismatch with diffusion imaging is contoured in red. Both patients present a volume mismatch. The right column shows PET-obtained OEF maps. Only patient a presents an ischemic penumbra, characterized by the increased OEF that compensates a default of blood oxygen supply.

A cerebral oxygenation mapping method suitable for the acute stroke clinical context would



thus be a must-have for better patient triage and offer hope for a significant increase in the number of treated patients ( $\approx 30\%$  of patients with unknown symptom onset time), better selection of therapies and better prediction of stroke outcomes.

## I.3 Current techniques for brain oxygenation mapping

Requirements for a reliable brain oxygenation measurement technique are high. It should have minimal invasiveness, spatial and temporal resolution suiting its application (emergency patient triage, repeated frequent measurements for trend monitoring...), and good clinical availability. Thankfully, a large variety of physical principles (optic, magnetism, etc) can be used to detect the amount of oxygen in the tissues. We present here several existing brain oxygenation measurement techniques, already used in the clinic or still at the research and development stage. Without going into the details of the methods, we show some of their latest results and discuss their pros and cons. Given our thesis goal, we artificially separated the non-MRI and MRI techniques. Note that only in vivo measurements are considered, although ex vivo hypoxia markers can be used for validation (pimonidazole, hypoxia-induced factor (HIF), etc).

### I.3.1 Non-MRI-based techniques

#### I.3.1.1 $pO_2$ measurements using Intracranial probes

The earliest oxygen measurements have been achieved in situ with intracranial probes. Two main probe types exist, as detailed below.

Polarographic electrodes have been clinically used since the 1980s and have been the gold standard for bedside  $pO_2$  monitoring (Kirkman et al. 2016; Hosford et al. 2019). They are composed of an anode and a cathode between which an electrical tension is applied. Exposed to this tension, oxygen atoms are ionized, giving rise to an electrical current between the electrodes. This current is directly proportional to the amount of dissolved oxygen in the tissues, that is to  $pO_2$ .

This measurement technique is simple and effective but is limited by its high invasiveness. The measurements performed are localized and are known to be highly sensitive to probe position. The probes need to be frequently calibrated in solutions of known  $pO_2$  to give accurate measurements and are poorly reliable at lower  $pO_2$ . In addition, the working principle of the probe consumes  $O_2$  in the tissues, forbidding rapidly repeated measurements.

The second category of oxygen probes relies on the measurement of an optical phenomenon in the tissue. The most common type uses  $O_2$  fluorescence quenching. Such probes are composed of an optic fiber and a fluorescent material (photophore). The fiber is used to convey photons with the right wavelength to trigger the photophore's fluorescence. The photons flux emitted by the photophore can be measured with the optic fiber. It is known that this flux is dependent on the amount of oxygen in the tissue, which allows for quantitative measurements of  $pO_2$  (Yoshihara et al. 2017). A common commercially available solution is the Oxylite<sup>TM</sup> system from Oxford Optronics, which we used in chapter III.

This type of probe does not consume  $O_2$  which allows for easier experiment repetition. It still provides localized and position-sensitive measurements. However, it remains highly invasive.

### I.3.1.2 $pO_2$ measurements using Electron Paramagnetic Resonance

Electron paramagnetic resonance (EPR) relies on principles similar to nuclear magnetic

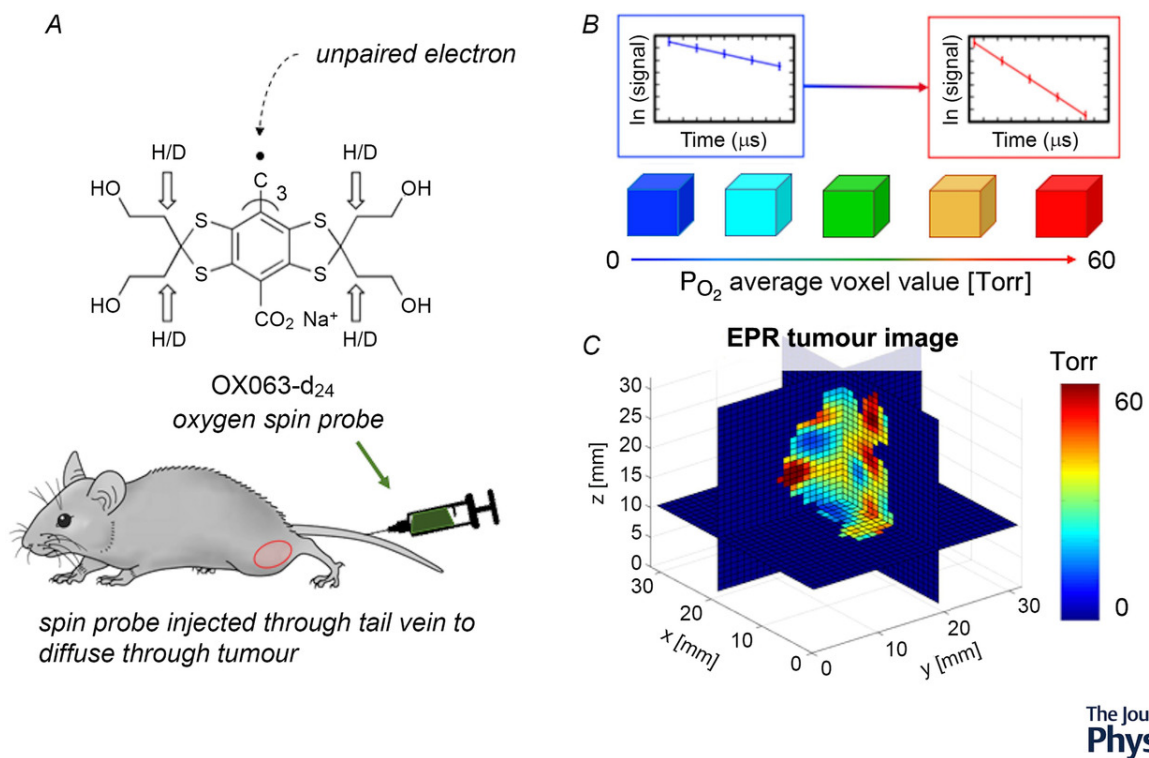


**Figure I.3.1:** EPR imaging principle from [Gertsenshteyn et al. 2021](#). A mouse bearing a leg tumor is injected with an oxygen-sensitive EPR probe. The relaxation rate of the probe is linearly linked with tissue  $pO_2$  as shown in B. Repeating measurements in several voxels in three planes allows  $pO_2$  mapping.

resonance but applied to atoms bearing unpaired electrons. Each oxygen atom in  $O_2$  has an unpaired electron (in opposition to the usual double liaison model) explaining the paramagnetism of the molecule. It is thus possible to perform EPR on  $O_2$ , but usually not in physiological conditions, due to the resonance peak broadening in liquids at body temperature. It is more common to use an exogenous material that can either be an injected solution or a solid probe (generally derivative of lithium phthalocyanine). Carbon blacks (such as India Ink) can also be used as a long term probe. These materials have a relatively narrow resonance peak in hypoxic conditions that broadens when their surrounding medium's  $pO_2$  increases ([Swartz et al. 2014a](#); [Swartz et al. 2014b](#)).

EPR can be used for spectrometry, giving a local measurement of  $pO_2$ . Carbon inks are relatively safe for measurements on surface tissue. In this case, the EPR sensor needs to be placed within 10mm of the measurement point, which does not allow the investigation of deeper organs. Solid probes solve this limitation, offering a better SNR in deeper tissue, but

require surgery for implantation (Swartz et al. 2016; Flood et al. 2020).

EPR can also be used for imaging tissue, as demonstrated in fig. I.3.1.

EPR is interesting for its capacity to repeat localized measurements with a rather simple set-up, to monitor tissue response to hyperoxic treatment for example. The maximal imaging depth is however relatively limited up to about between 1 to 8 cm depending on the frequency used, and its increase comes with SNR loss (Gertsenshteyn et al. 2021). It also remains invasive and at a development stage, and hence rarely available.

### I.3.1.3 OEF measurements using Photon Emission Tomography

Photon Emission Tomography (PET) is a well-known and widely used medical imaging technique. It relies on the introduction (by injection or breathing) of a radiotracer in the body, which will be involved in a metabolic or physiological process. Several radiotracers have been developed, each targeting a specific process. A radiotracer contains a radioactive element that undergoes a  $\beta+$  decay, emitting a positron (anti-electron). This positron will travel a short path in the matter before annihilating with an electron, which emits two photons of specific energy (511 keV) in approximately opposite directions. These are detected by a circular array of detectors around the patient. The specific energy, the direction of emission of the photons, and the timing of their detection allow for discriminating photons from an annihilation event and computing its position in the body.

$^{15}\text{O}$  is an oxygen isotope that is known for its  $\beta+$  decay. It can thus be injected into the body and its spatial distribution can be measured with PET. Several radiotracers can be built with  $^{15}\text{O}$ . Using  $\text{H}_2^{15}\text{O}$ ,  $\text{C}^{15}\text{O}$ ,  $\text{C}^{15}\text{O-O}$ , and  $^{15}\text{O-O}$  scans, it is possible to map the OEF, the Blood Volume fraction (BVf), and cerebral blood flow (Wang et al. 2020b; Fan et al. 2020). Figure I.3.2 shows an example of PET-measured OEF maps. PET measurements are versatile and usually considered a gold standard for research on cerebral physiology. Yet, the inherent spatial resolution of PET is limited to a few millimeters. This is mostly due to the short migration of the positron before the emission of the photons and to their propagation directions, which are not perfectly opposed. The temporal resolution of the detectors is also a source of inaccuracy, and technical improvements are not clinically available. In addition,  $^{15}\text{O}$  has a very short half-life (2 minutes), meaning that it has to be produced very close to the PET scanner, which is usually impracticable in clinical settings. PET is however clinically used to detect hypoxia, using fluoromisonidazole ( $^{18}\text{F-FMISO}$ ) which is specifically captured by hypoxic cells.

### I.3.1.4 $\text{SO}_2$ measurements using Near-Infrared Spectroscopy

Near-Infrared Spectroscopy (NIRS) measures the change in the absorption coefficient of a chromophore in different physiological conditions. An emitter (LED or laser) is placed on the skin. The light travels inwards the body and is either reflected, absorbed, or scattered. A receptor measures the amount of light that reflects back through the skin. Interestingly, the absorption coefficient of hemoglobin varies with its oxygenation state for wavelengths comprised between approximately 650 and 950nm, as illustrated in fig. I.3.3.

Tissues are relatively transparent to this wavelength range, which allows for penetration of the emitted light. The concentration of dHb can be quantitatively estimated in tissue with NIRS but the measurement does not discriminate between the arterial, venous, and capillary compartments. Usually, several wavelengths are used to improve the accuracy of

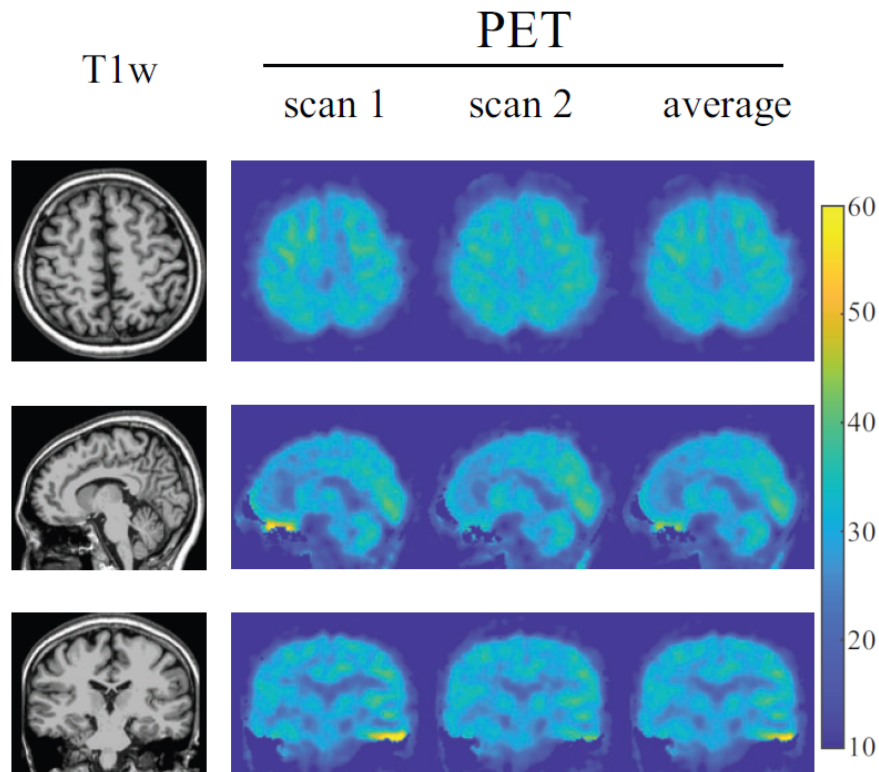


**Figure I.3.2:** MRI anatomical scan and PET-measured OEF maps on a healthy volunteer, adapted from [Cho et al. 2021](#). Two maps were acquired and averaged. Scale in %.

the estimates. NIRS systems are easily available and provide continuous and non-invasive measurements. NIRS is thus attractive for both patient screening in an emergency context and bedside monitoring of longer-term  $\text{SO}_2$  evolution ([Kirkman et al. 2016](#)). Unfortunately, NIRS suffers from a number of limitations. Hemoglobin is not the only chromophore that absorbs light at the used wavelengths, and a number of factors such as skin pigmentation or even room lighting further disturb the quantification of the reflected light. The light scattering in the tissues diminishes the spatial resolution of the measurement, allowing for regional measurements only. The maximal imaging depth is about 10cm in soft tissue (typically breast imaging), and around 3cm in the brain. In addition, skin blood vessels and skull contribute to both absorbing and reflecting a part of the transmitted light, diminishing the attractiveness of NIRS for cerebral studies ([Barud et al. 2021](#); [Roldán et al. 2021](#); [Kovacsova et al. 2021](#)).

### I.3.1.5 $\text{SO}_2$ measurements using Photoacoustic Imaging

Photoacoustic (or optoacoustic) imaging (PAI) consists in sending light into the tissue while detecting ultrasound generated by photon absorption and thermoelastic expansion. In usual optical imaging such as NIRS, multiple scattering randomizes photon direction and deteriorates the resolution and contrast. PAI detects energy as ultrasound waves, which are much less scattered in tissue. Better contrast and greater depth can be achieved. Since light is used to trigger the measured signal, it is possible to use specific wavelengths to select the imaged tissue. In particular, it is possible to image tissue containing hemoglobin, similar to what is done with NIRS ([Manohar et al. 2016](#); [Steinberg et al. 2019](#)). Using such a technique,



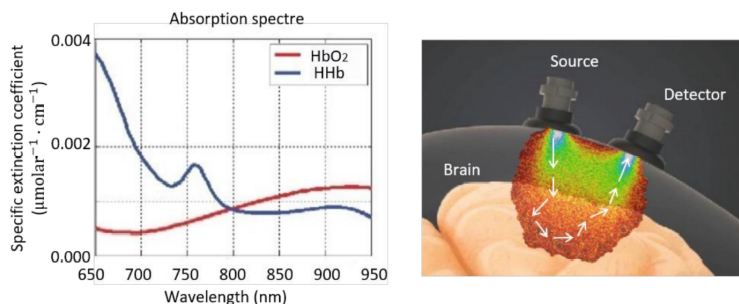


**Figure I.3.3:** Illustration of NIRS working principle from [Roldán et al. 2021](#). The left panel shows the difference in absorbance (extinction) of oxyhemoglobin ( $\text{HbO}_2$ ) and deoxyhemoglobin (HHb) at different wavelengths. The right panel proposes a schematic view of a NIRS experiment, with the probabilistic trajectory of photons emitted from the source and measured by the receptor.

[Zhu et al. 2022](#) present a real-time mapping of mouse cortex in a normoxia-hypoxia-normoxia challenge, shown in fig. [I.3.4](#). To obtain such high resolution and contrast, the mouse skull

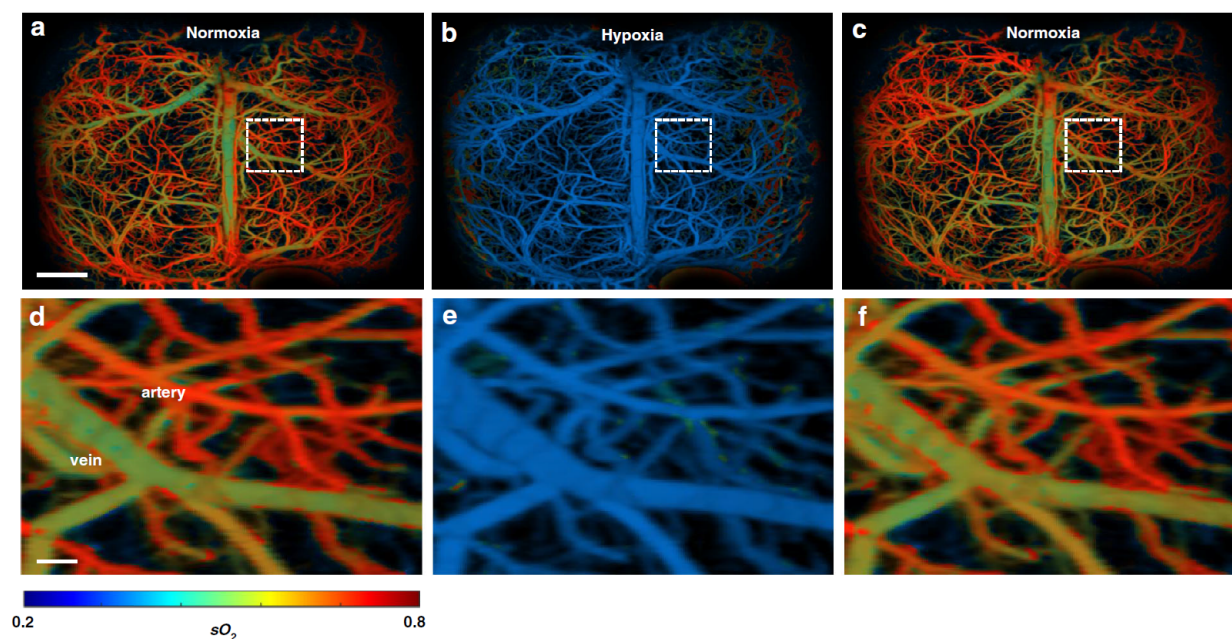


**Figure I.3.4:** PAI imaging of an entire mouse cortex under a cycle of normoxia-hypoxia-normoxia challenges, from [Zhu et al. 2022](#). The scale bar measures 1mm in the upper row, 100µm in the lower row.  $\text{SO}_2$  is color-coded from 0.2 (blue) to 0.8 (red).

was removed and replaced by an optically and acoustically transparent window, specifically built for the experiment. Indeed, PAI imaging does not penetrate through bone structures and is difficultly suited for imaging in vivo tissue deeper than about 3cm ([Steinberg et al. 2019](#)). Human brain imaging is thus hardly achievable with PAI, except in young children where immature skull joints offer an interesting gateway. High resolution tissue-selective imaging such as presented in fig. [I.3.4](#) is still of great interest for in vivo lesion exploration on small animals, potentially providing new cross-validation to other methods.

### I.3.2 MRI-based techniques

MRI is an attractive tool for brain oxygenation measurements due to its large field of view and imaging depth, its high spatial resolution, and its non-invasiveness. Several MR methods have been proposed to measure  $\text{SO}_2$  over the years and are reviewed in [Christen et al. 2013](#) and [Jiang et al. 2022](#). The following section proposes an overview of the current state of these MR-based  $\text{SO}_2$  measurements and discusses the pros and cons of the techniques. The reader can refer to section [II.1.1](#) for elements on MR theory. Note also that we only cover  $^1\text{H}$  MRI techniques that have been used in clinical research. Oxygenation measurements including local  $\text{pO}_2$  estimates can also be performed using  $^{17}\text{O}$  MRI or  $^{19}\text{F}$  MRI and are reviewed in [Zhu et al. 2017](#), and in [Janasik et al. 2022](#), respectively.

#### I.3.2.1 $\text{SO}_2$ measurements based on blood relaxometry

$\text{SO}_2$  changes in blood vessels are known to induce local changes in the longitudinal and transverse relaxation rates  $R_1$  and  $R_2$ .

The relationship between  $\text{SO}_2$  and blood  $T_2$  has been studied for more than thirty years (see [Wright et al. 1991](#)). The model has been refined over the years and it is thus theoretically possible to extract  $\text{SO}_2$  values from a  $T_2$  measurement from voxels containing only blood. Variations of  $T_2$  with  $\text{SO}_2$  and hematocrit predicted by the model from [Lu et al. 2012](#) are shown in [fig. I.3.5](#). During the reconstruction process, the dependence on hematocrit is

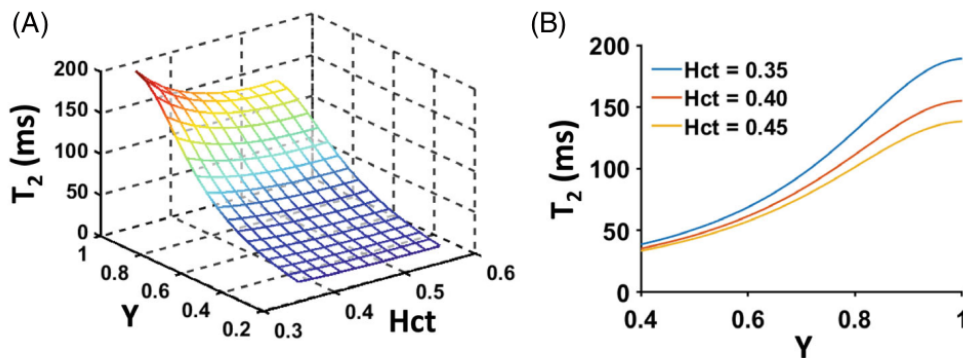


**Figure I.3.5:**  $T_2$  variations with  $\text{SO}_2$  ( $Y$ ) for different hematocrit predicted by the model from [Lu et al. 2012](#). Figure [Jiang et al. 2022](#).

usually fixed by measuring its value in a blood sample assuming that it does not change locally. A problem of the method is the partial volume contamination: any contribution from non-blood tissue to the measured  $T_2$  will induce an error on the computed  $\text{SO}_2$ . Methods have been proposed to solve this limitation by suppressing the signal from non-blood compartments. The  $T_2$ -relaxation-under-spin-tagging (TRUST) approach ([Lu et al. 2008](#); [Jiang et al. 2021](#)) measures  $T_2$  in the brain with and without spin tagging preparation. The difference between the two scans allows isolating the signal from venous blood. This approach has been extensively tested against other measurements with hypo and hyperoxia challenges in multi-site experiments. TRUST has shown to provide reliable estimates and to be robust to imaging conditions ([Jiang et al. 2022](#)). It is however limited to large brain vessels, such as the

superior sagittal sinus, and doesn't allow for local tissue  $\text{SO}_2$  measurements. Trying to solve this spatial limitation, several methods proposed to use velocity-selective spin tagging such as QUantitative Imaging of eXtraction of Oxygen and Tissue Consumption (QUIXOTIC) from [Bolar et al. 2011](#), and Velocity-Selective Excitation with Arterial Nulling (VSEAN) from [Guo et al. 2012](#). Briefly, these methods allow the separation of smaller veins from static tissue and spatially resolved measurements. More recently, using another velocity selective spin tagging scheme, [Li et al. 2022](#) improved the method and largely increased the SNR of the  $T_2$  estimates, allowing for  $\text{SO}_2$  maps with a spatial resolution similar to PET imaging in one slice:  $7.9 \times 7.9 \times 10.0\text{mm}^3$ . Maps obtained are shown in fig. I.3.6. While the results are

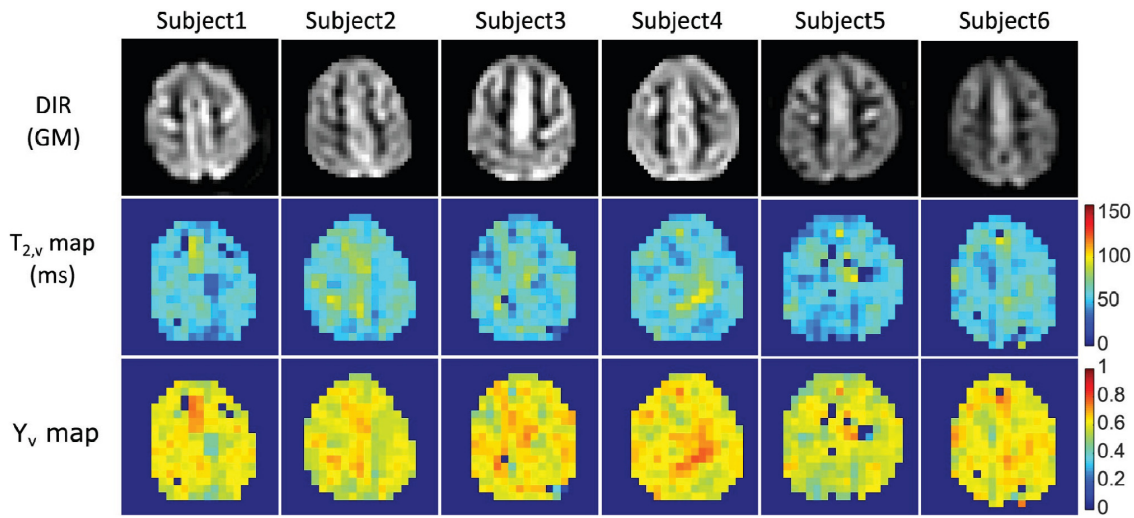


**Figure I.3.6:** Anatomical (double inversion recovery), venous  $T_2$  and associated oxygenation maps in 6 volunteers, from [Li et al. 2022](#)

encouraging, the authors still note the contamination of their  $T_2$  measurements with CSF and propose solutions to further improve the accuracy of their  $\text{SO}_2$  estimates.

The  $R_1$  and  $\text{SO}_2$  relationship has also been studied in the literature. [Hales et al. 2016](#) proposed a model expressing blood  $R_1$  as a function of  $\text{SO}_2$ , hematocrit, and main magnetic field strength. More recently, [Bluemke et al. 2022](#) refined the model by adding parameters. The new model was fitted on measurements from the literature and proved to perform better than that from [Hales et al. 2016](#) on a wider  $\text{SO}_2$  range. Fig. I.3.7 shows variations of  $T_1$  with  $\text{SO}_2$  for different hematocrit, simulated from their proposed model. Although the authors note the difficulties to measure  $T_1$  in blood and how it can affect the model, it should however be possible to also perform  $T_1$  measurements to measure blood  $\text{SO}_2$ .

### I.3.2.2 $\text{SO}_2$ measurements based on quantitative Susceptibility Mapping

The phase difference  $\Delta\varphi$  between two voxels in a gradient echo experiment is directly linked to their difference in the local magnetic field  $\Delta B$ :

$$\Delta\varphi(\text{TE}) = \gamma \times \Delta B \times \text{TE} \quad (\text{I.3.1})$$

When considering the phase difference between a blood vessel and its surrounding tissue, one

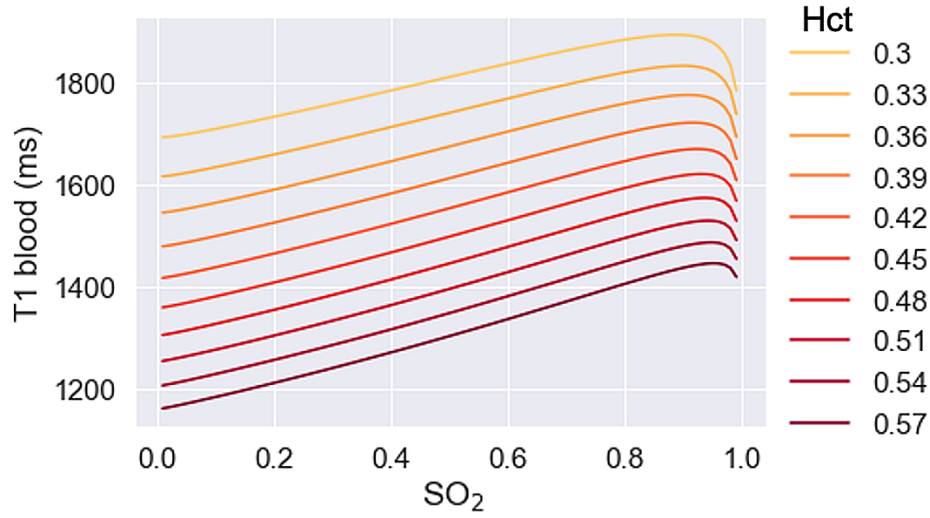


**Figure I.3.7:**  $T_1$  variations with  $SO_2$  for different hematocrit predicted by the model from [Bluemke et al. 2022](#).

can link  $\Delta B$  to  $SO_2$  through the relation

$$\Delta B = \frac{1}{6} \times \Delta\chi_{do} \times \text{Hct} \times (1 - SO_2) \times B_0 \times (3 \cos^2(\theta) - 1) \quad (\text{I.3.2})$$

where  $\Delta\chi_{do}$  is the susceptibility difference between fully oxygenated and deoxygenated erythrocytes, Hct is the local hematocrit and  $\theta$  is the angle of the vessel (considered straight) with the main magnetic field  $B_0$ . Assuming or measuring the global hematocrit, gradient echo phase measurements can be easily used for  $SO_2$  estimates.

The main challenge of this technique is however the minimum size of the vessels than can be imaged, which needs to be bigger than the actual voxel size. It also requires knowledge of the blood vessel orientation and thus, is mostly used to measure the  $SO_2$  in large veins, typically the superior sagittal sinus ([Cao et al. 2018](#)).

### Quantitative susceptibility mapping

The QSM technique has been proposed 15 years ago to derive magnetic susceptibility ( $\chi$ ) maps from MR phase maps ([Rochefort et al. 2010](#)). It relies on the following relationship:

$$\mathfrak{F}(\varphi) = \gamma \times B_0 \times \text{TE} \times \mathfrak{F}(\chi) \times \left( \frac{1}{3} - \frac{k_z^2}{k^2} \right) \quad (\text{I.3.3})$$

where  $\mathfrak{F}$  denotes a spatial Fourier transform,  $k$  is the norm of the k-space vector, and  $k_z$  is its component aligned with the main magnetic field. Inverting this relation gives access to susceptibility maps provided a normalization step is performed, because the problem is ill-posed. Note that the same principles can be used to compute magnetic field inhomogeneities from susceptibility distribution, and are used in our simulations in section II.1.2.1. QSM can be used to study iron content in the brain and can be linked to blood oxygenation in large vessels using the same principle as presented above for single blood vessels but without the need to know the vessel's orientations. It has also been used recently by [Zhang et al. 2015](#) to



derive local microvascular  $SO_2$  by using the following model:

$$\chi = BVf_v \times \Psi_{Hb}(X_{dHb} - X_{HbO_2}) \times \frac{[dHb_v]}{[Hb]} + \chi_0 \quad (I.3.4)$$

where a  $v$  is the venous part of a quantity,  $\Psi_{Hb}$  is the volume fraction of hemoglobin in the blood,  $X_{dHb}$  and  $X_{HbO_2}$  denote the volume susceptibilities of deoxy- and oxyhemoglobin,  $[ ]$  are concentrations, and  $\chi_0$  account for all susceptibility contributions from non-blood tissue. Using a caffeine challenge, the authors were able to obtain  $CMRO_2$  maps from quantitative susceptibility imaging on healthy volunteers. Cerebral blood flow estimation was performed with an arterial spin labeling sequence. These maps were compared to  $R_2^*$ -based  $CMRO_2$  maps (see section below) with a good agreement, as shown in fig. I.3.8. Estimating the

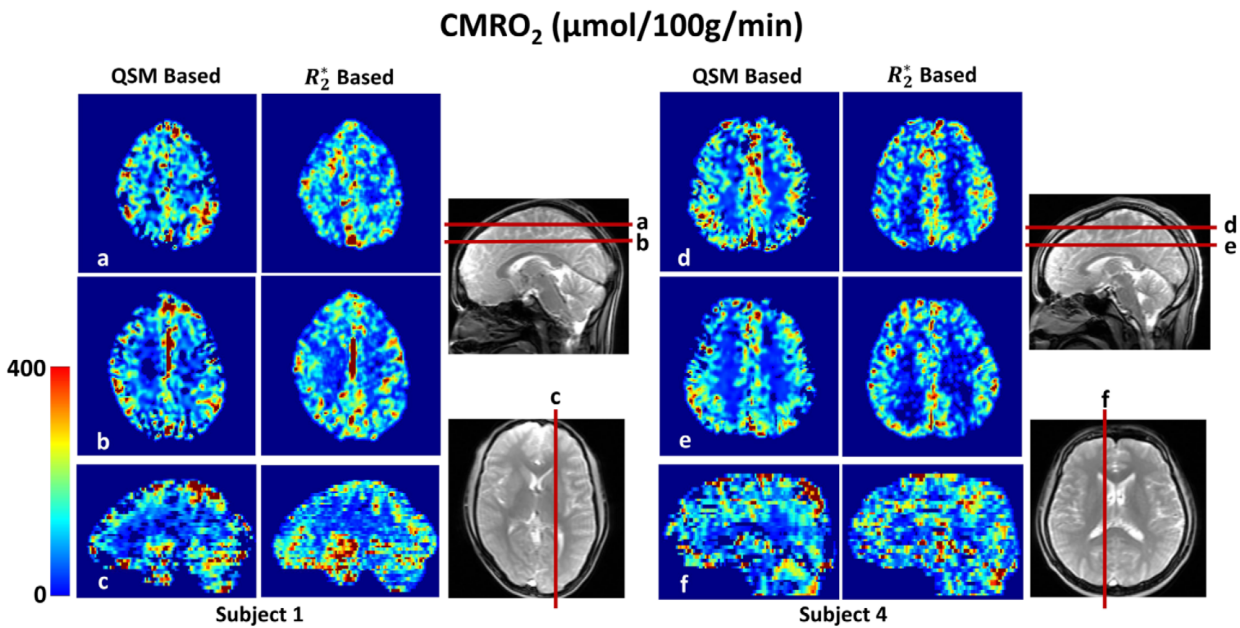


**Figure I.3.8:** Comparison of  $CMRO_2$  maps from QSM and qBOLD ( $R_2^*$ -based) in healthy volunteers from [Zhang et al. 2015](#)

venous fraction of BVf is however challenging, and is currently based on an empirical linear model, which does not suit all tissue types, in particular in pathological cases.

### I.3.2.3 $SO_2$ measurements based on Quantitative BOLD imaging

#### Origin of BOLD effect

The well-known Blood Oxygenation-Level Dependent (BOLD) effect has been extensively used as a contrast mechanism to study brain function at rest and during mental tasks. Its principle is rather simple: oxyhemoglobin is weakly diamagnetic and its presence in the blood vessels does not affect the MR signal. On the opposite, deoxyhemoglobin is strongly paramagnetic and induces magnetic perturbation around blood vessels. The spatial scale of these perturbations can extend up to five times farther than the vessel radii, as illustrated in fig. II.1.5. In presence of dHb,  $^1H$  nuclei inside (but also outside) the blood vessels will thus experience different main magnetic fields depending on their position. Thus, they precess

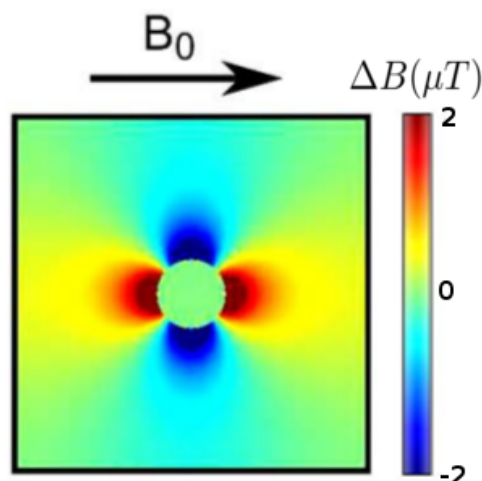


**Figure I.3.9:** Magnetic field perturbation around a blood vessel, adapted from [Pannetier et al. 2013](#)

at different frequencies, rapidly losing phase coherence and resulting in a faster-decaying signal. The BOLD effect corresponds to that signal change: the higher the  $SO_2$  the lower the perturbations and the slower the signal decays.

The BOLD effect is classically observed as  $T_2^*$  changes in gradient echo experiments, but the diffusion of water molecules around vessels means that they also acquire a phase history that can not be compensated by a spin echo:  $T_2$  weighted spin echo images are also affected. [Boxerman et al. 1995](#) showed that the BOLD effect on  $T_2$  weighted acquisitions is largely dependent on the vessel size, which is not as much the case for  $T_2^*$  weighted sequences. In addition, gradient echo sequences provide stronger contrast than spin echo, hence the preference for gradient echo sequences for BOLD fMRI experiments. Note that the BOLD effect can also be explored with other types of sequences, as discussed in section [IV.3](#).

Due to its nature, the BOLD effect should give access to  $SO_2$  estimates, and indirectly to  $pO_2$  through the Hb dissociation curve. However, most of the BOLD acquisitions don't try to measure these parameters at baseline. Usual experiments look at contrasts variations between different brain states and even in this case, quantification of these variations are usually not performed. The reasons come from the complex dependence of the BOLD MR signal on blood oxygenation as well as several other parameters that affect the signal evolution. For example, the magnitude of the BOLD effect is affected by the total quantity of dHb in the imaged voxel, i.e. by the  $SO_2$ , but also by the Blood Volume fraction and hematocrit (the fraction of the blood volume actually occupied by erythrocytes, which contain hemoglobin). Vessel orientation in the magnetic field is also of importance. Furthermore, the signal is affected by:

- any magnetic field inhomogeneity that does not originate from the presence of dHb: uncorrected main magnetic field spatial variations, susceptibility interfaces, metallic implants, calcifications, microbleeding, myelin...
- the continuous renewal of blood in vessels that induces flow effect in the magnitude

images.

- the presence of tissue with high transverse relaxation  $T_2$ , e.g. areas containing liquid:  $T_2$  is linked to  $T_2^*$  through  $\frac{1}{T_2^*} = \frac{1}{T_2} + \frac{1}{T_2'}$ . An increase of  $T_2$  will thus increase  $T_2^*$  independently of  $SO_2$  changes

### Quantifying the BOLD effect

Extracting the oxygenation information from BOLD experiments and disentangling the contribution of the different parameters has been the focus of MR techniques called quantitative BOLD or qBOLD approaches. These techniques rely on mathematical models describing the MR signal evolution of GRE and SE sequences in presence of inhomogeneous tissues including multiple blood vessels. A commonly used model was described in [Yablonskiy et al. 1994](#) and considered a two compartments model where vessels are described as infinite straight cylinders without preferential orientation. Neglecting water diffusion (static-dephasing regime) and considering enough blood vessels in the voxel to make statistical assumptions, the mathematical expression of the field perturbations were derived as well as the temporal evolution of the MR signal. The model was later refined by [He et al. 2007](#) by including different tissue (white and gray matter, cerebrospinal fluid, and pure blood) contributions. Other groups have also slightly refined the models over the years. The qBOLD methods use of GRE and SE signals sampled at multiple TE and have in common to fit a complex model to these signals in order to extract  $SO_2$  estimates.

An example of minimization problem for a qBOLD experiment from [Cho et al. 2018](#) is presented below:

$$\sum_{TE} \||S(TE)| - F_{qBOLD}(SO_2, BVf_v, S^0, R_2, TE)\|_2^2 \quad (I.3.5)$$

with

$$F_{qBOLD}(SO_2, BVf_v, S^0, R_2, TE) = S^0 \cdot e^{-R_2 \cdot TE} \cdot F_{BOLD}(SO_2, BVf_v, TE) \cdot G(TE) \quad (I.3.6)$$

$S^0$ , the initial amplitude of the signal, is an unknown. Here, the signal decay is attributed to three components: the transverse relaxation of rate  $R_2$ , the macroscopic field inhomogeneities (accounted for through  $G$ ), and the inhomogeneities due to deoxygenated blood in the vessel network:

$$F_{BOLD}(SO_2, BVf_v, TE) = 1 - \frac{BVf_v}{1 - BVf_v} \cdot f_s(\delta\omega \cdot TE) + \frac{1}{1 - BVf_v} \cdot f_s(BVf_v \cdot \delta\omega \cdot TE) \quad (I.3.7)$$

with  $f_s$  the decay due to the blood vessel network and  $\delta\omega$  the characteristic frequency shift between fully deoxygenated blood and the surrounding tissue:

$$\delta\omega(SO_2) = \frac{1}{3} \cdot \gamma \cdot B_0 \cdot (\text{Hct} \cdot \Delta\chi_0 \cdot (1 - SO_2)) \quad (I.3.8)$$

Hct is the hematocrit and  $\Delta\chi_0$  the susceptibility difference between fully oxygenated and deoxygenated red blood cells. The surrounding tissue susceptibility is assimilated here to that of fully oxygenated blood. Note the use of the venous part of BVf here, where some other methods use the total BVf.

The model has an asymptotic quadratic exponential behavior in the first milliseconds ( $TE \ll 1/\delta\omega$ ) before following an exponential ( $TE \gg 1/\delta\omega$ ) decay, which theoretically allows separating contributions from  $SO_2$  and BVf. In practice, this effect is only visible at a high signal-to-noise ratio (SNR), and it is difficult to obtain accurate  $SO_2$  maps in vivo by adjusting all the model's parameters at once. Christen et al. 2011 proposed to independently measure the confounding parameters of the qBOLD model with dedicated MR scans to simplify the problem and leave  $SO_2$  as the sole unknown parameter in the fitting step. Fig. I.3.10 from Christen et al. 2014a shows examples of maps obtained on a rat under different breathing conditions. Panel I.3.10a shows an anatomical scan and a  $T_2^*$  map acquired from a

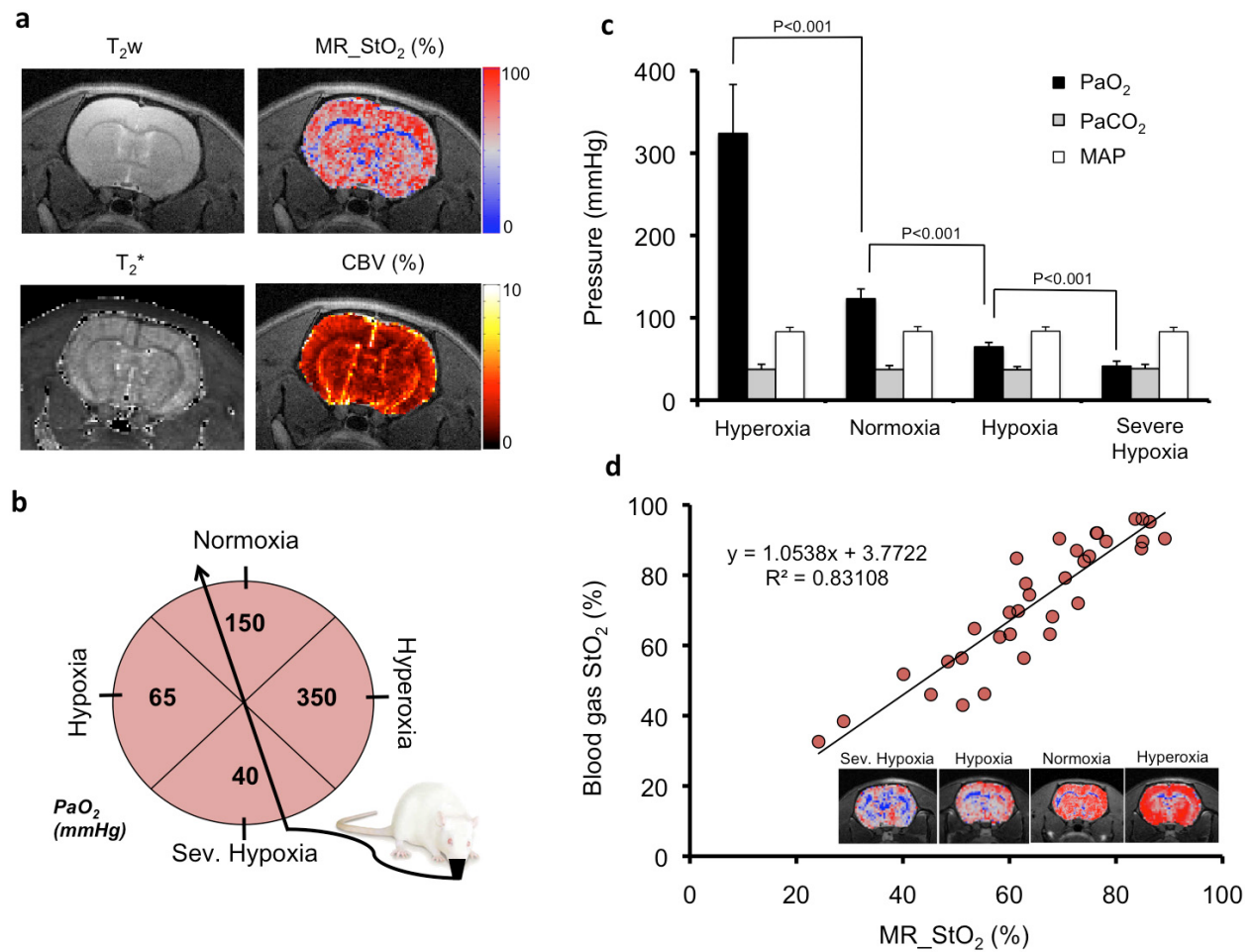


**Figure I.3.10:**  $SO_2$  measurements during a gas challenge, from Christen et al. 2014a. 17 animals were imaged to measure  $T_2^*$  and BVf (CBV in the figure), the latter requiring the injection of a steady-state contrast agent (see Christen et al. 2011). a shows an anatomical scan as well as measured  $T_2^*$ , BVf, and  $SO_2$  on one animal under normoxic conditions. b and c show the arterial  $pO_2$  measured from blood sample analysis when varying the amount fraction of inspired  $O_2$  ( $FiO_2$ ). The influence of  $FiO_2$  on the arterial  $pO_2$  during the MR acquisition is clear in c. d shows the correlation between the  $SO_2$  measured on blood samples and with the proposed qBOLD method in a cortical ROI on 17 animals.

multi-gradient echo sequence. The BVf (CBV in the figure) map shown is obtained from images acquired before and after injection of a contrast agent. The top right image is the

SO<sub>2</sub> map resulting from the processing described in [Christen et al. 2011](#). Panel [I.3.10b](#) and [c](#) describe arterial pO<sub>2</sub> measured from blood sample analysis when varying the amount fraction of inspired O<sub>2</sub> (FiO<sub>2</sub>). Measurements in [b](#) were obtained prior to the MR exam, and those in [c](#) were obtained during the challenge in the MR magnet. The impact of FiO<sub>2</sub> on the arterial pO<sub>2</sub> is clear. Finally, panel [I.3.10d](#) shows the correlation between the SO<sub>2</sub> measured on blood samples and with the proposed qBOLD method in a cortical ROI on 17 animals. The agreement is good with R<sup>2</sup>= 0.83. Obtained SO<sub>2</sub> maps are shown for different FiO<sub>2</sub>.

### Combining QSM and qBOLD

It is important to note that the qBOLD models generally do not account for non-blood tissue susceptibility. In particular, considering SaO<sub>2</sub> = 1 means that only capillaries and veins contribute to the BOLD effect. This effect has been noted in multiple qBOLD studies in humans (see [Christen et al. 2012](#)) where the apparent SO<sub>2</sub> estimates appear lower in the white matter regions where myelin fibers are present. One can however notice that qBOLD can be used to estimate BVf<sub>v</sub> at the expense of neglecting tissue susceptibility variations, whereas the QSM method presented above neglects BVf<sub>v</sub> variations to estimate blood and tissue susceptibilities. In consequence, [Cho et al. 2018](#) recently proposed a combined approach, coined QQ (QSM + qBOLD), to improve both SO<sub>2</sub> and CMRO<sub>2</sub> estimates. The proposed model has 5 unknown parameters: BVf<sub>v</sub>, SO<sub>2,v</sub>, non-blood  $\chi$ , transverse relaxation rate R<sub>2</sub> and S<sup>0</sup>, the initial amplitude of the GRE signal. This model is fitted to both the magnitude and phase data of the acquired GRE data. A comparison of results from the proposed QQ method against pure QSM and qBOLD is given in [fig. I.3.11](#). The proposed QQ method better agrees with CMRO<sub>2</sub> and OEF values found in PET studies in the literature than the pure QSM and qBOLD approaches. The OEF maps obtained are flatter and the contrasts are generally in better agreement with expectations. In the same line of study, [Lee et al. 2022](#) proposed a 3D sequence whose magnitude and phase can be used to estimate the R<sub>2</sub> and R<sub>2</sub>' decay rates as well as the tissue susceptibility. During qBOLD analysis, BVf<sub>v</sub> is estimated through a dedicated arterial spin labeling sequence and initial SvO<sub>2</sub> estimates are obtained using large vessel phase oximetry.

Although these new qBOLD developments have led to encouraging results in human volunteers, a number of issues still remain. First, many parameters need to be adjusted during reconstruction and given the dimensions of the minimization problem, it is extremely sensitive to initial conditions as well as local minima. Second, the techniques are bound to the multi-gradient-echo sequences, for which there likely exists better alternatives. More importantly, the results are limited by the initial assumptions of the mathematical model of spin dephasing around infinite straight cylinders. Voxels containing tortuous large blood vessels, preferential orientation of the microvascular network, and low or large capillary bed densities will not fall under this assumption. Finally, the effect of water diffusion on the MR signal is always neglected in the qBOLD analysis. Although refinement of the equations can be considered, it seems unlikely that it will fit all tissue types and pathological conditions. A more adapted MR paradigm that allows flexible acquisitions, vascular modeling, and image reconstruction has been proposed in 2014 and its potential for SO<sub>2</sub> mapping will be discussed in the next section.



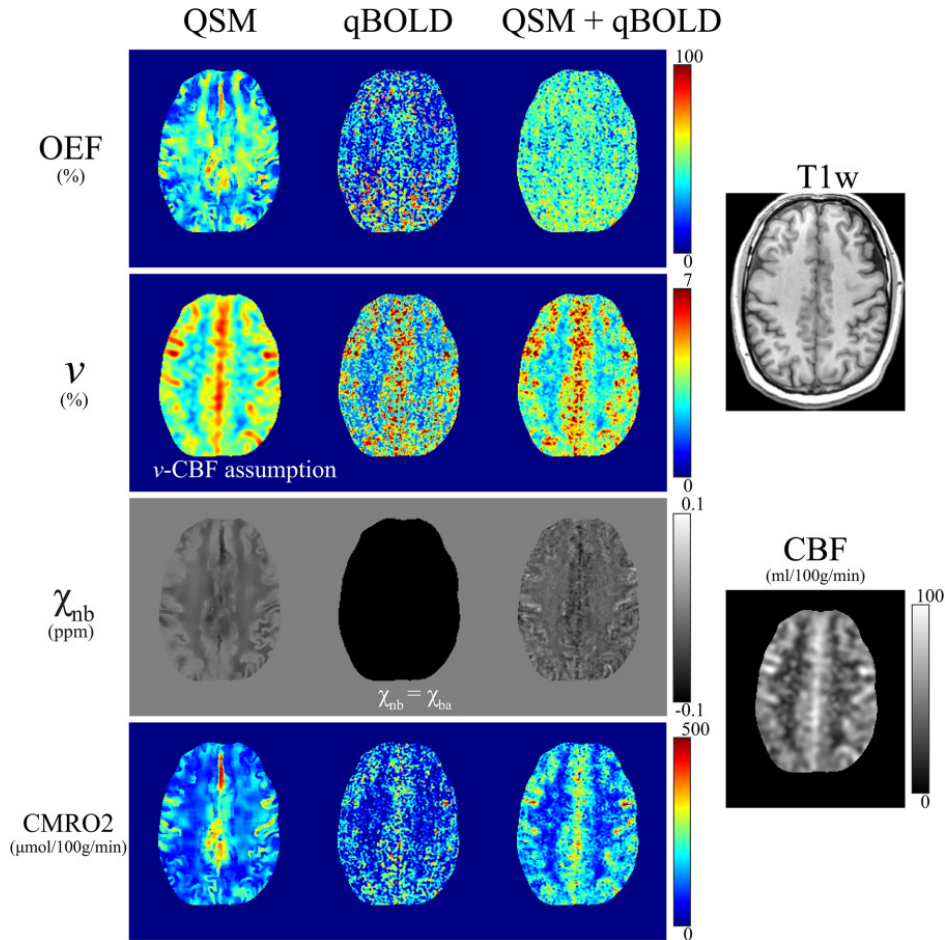


**Figure I.3.11:** Parametric maps from QSM, qBOLD, and the proposed QSM+qBOLD from [Cho et al. 2018](#).  $v$  corresponds to  $BVf_v$  and  $\chi_{nb}$  is the non-blood susceptibility.

## I.4 MR Fingerprinting for brain oxygenation mapping

Magnetic Resonance Fingerprinting (MRF) was first introduced in [Ma et al. 2013](#). It proposed a complete paradigm shift in quantitative MRI by using a dictionary approach instead of a model-fitting one. Indeed, all the quantitative MRI methods presented above rely on performing a rather simple MR sequence acquisition to produce images and signals that can be compared to a mathematical model derived from theoretical simplifications. These approximations are necessary to obtain a model simple enough to suit a fitting procedure. However, they tend to introduce systematic errors in the measurements. In addition, these models are generally derived from observations in healthy tissue and are not guaranteed to be valid in pathological cases. For example, the signal decay in the qBOLD model assumes straight vessels of infinite lengths, which is a poor representation of the tortuous networks resulting from chaotic angiogenesis in a tumor.

MRF proposes to reverse the quantification process with a dictionary of signals produced with numerical simulations. Doing so eliminates the need for the signal to evolve with simple temporal variations such as exponential decay. It also allows for the incorporation of many special cases (such as those found in pathological environments) that otherwise would be lost

under model generalization. All the parameters used as inputs of the numerical simulation model can be retrieved at the same time after comparison (or matching) of in vivo and in silico signals, provided that the atoms of the dictionary can be separated. MRF also allows for the measurement of physical effects ( $B_0$ ,  $B_1$  inhomogeneities, slice profile, etc.) that are usually considered as artifacts in standard quantitative MRI protocol. In MRF, in order to avoid too many model assumptions, the simulation model usually starts with the well-known Bloch equations (presented in section II.1.1) that predict the motion of nuclear magnetization and are sufficient to describe a large majority of quantitative MRI experiments routinely performed.

The following section presents the principles of MRF acquisitions and reconstructions and the strategy for applying MRF to cerebral oxygenation measurements.

### I.4.1 Principles and standard applications of MRF

The working principle of MRF is illustrated in fig. I.4.1.

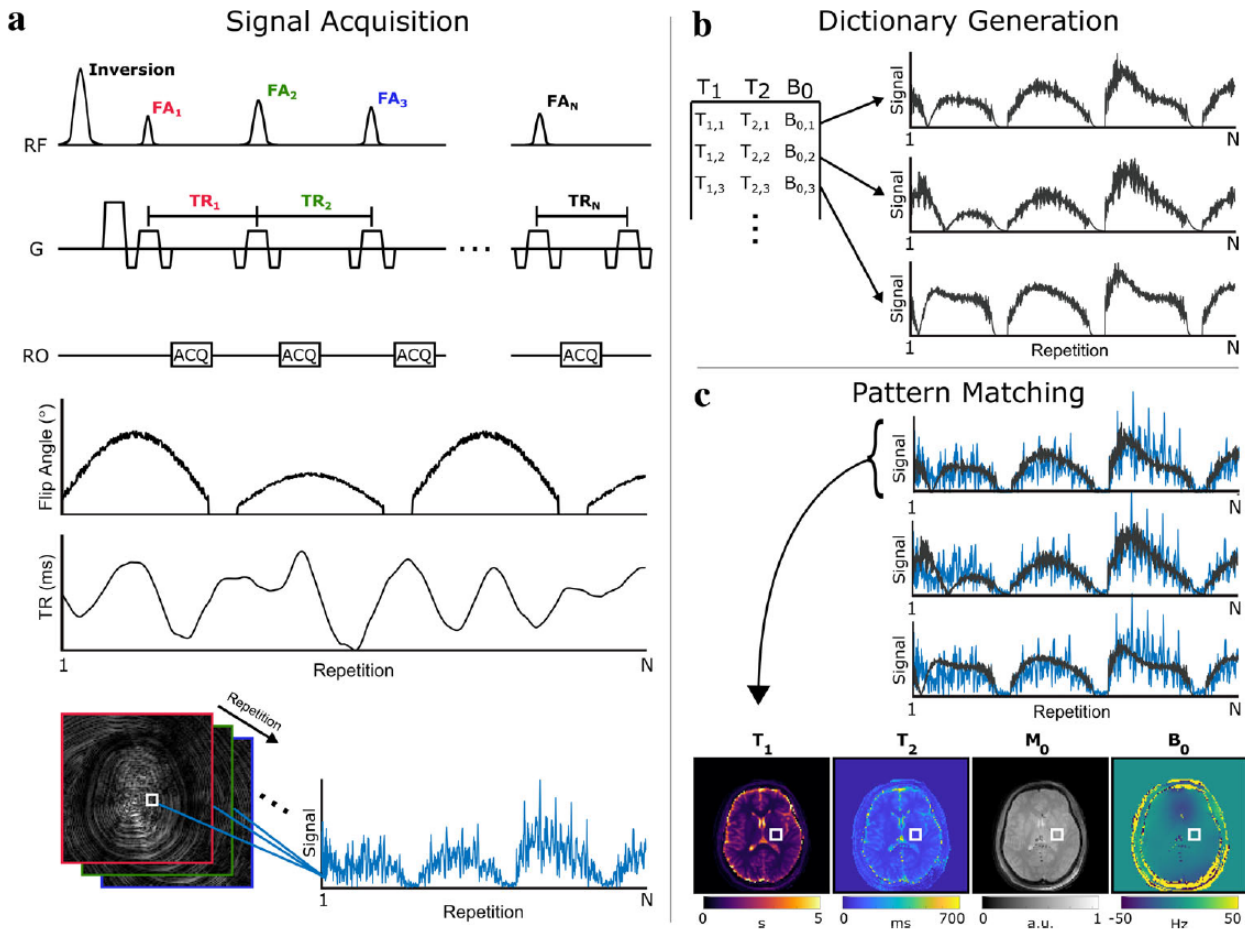


**Figure I.4.1:** MR Fingerprinting basic principles, from [Poorman et al. 2020](#)

Three main elements are required to produce quantitative maps:

- An MR sequence (train of RF pulses separated by controlled duration, magnetic field

gradients, and Fourier-space acquisition scheme, fig. I.4.1a). In standard quantitative MRI acquisitions, a small number of RF pulses is usually applied to produce a corresponding small number of images ( $<20$  for relaxometry experiments). Except for magnetization preparation, the timing of the sequence and the amplitude of RF pulses are usually constant. In MRF, all the parameters of the sequence can vary with time (see flip angle (FA) and TR evolutions in fig. I.4.1a)) and many images ( $>1000$ ) can be produced with a single acquisition scheme. Although there are no theoretical limitations to the design of an MRF sequence, the resulting acquired signal (called the “fingerprint”) must vary with the voxel properties (e.g.  $T_1$ ,  $T_2$ , off-resonance frequency...) to obtain accurate quantitative maps. The sequence design must also comply with the MRI scanner’s physical limitations, meaning that timings and amplitudes must be chosen within realistic boundaries. Strategies for designing efficient MRF sequences are discussed in chapter IV.

The large number of pulses used in the MRF sequences would create overly long acquisition times if k-space sampling schemes respecting the Nyquist criterion were used. But in MRF, fast undersampling schemes such as variable density multi shots spirals are usually used to produce low-quality images with large artifacts. By rotating the spiral sampling between the different images, incoherent noises are created and the initial shapes of the signals can be retrieved after dictionary matching.

- A simulation tool able to compute the fingerprint resulting from the application of the chosen sequence on a voxel of known properties. Repeating simulations for different property combinations yields a so-called dictionary of fingerprints and associated property combinations (fig. I.4.1b). This tool must be complex enough to properly account for the effect of the voxel properties. Classical Bloch equations are sufficient when considering only relaxation properties ( $T_1$ ,  $T_2$ ). Exploring vascular properties however requires a more complex simulation, considering sub-voxel scale structures and biophysical effects. It is worth noting that dictionaries usually contain several hundred thousand fingerprints or more. The simulation tools must be able to generate such large datasets in a tractable time. Chapter II focuses on several tools, either available from the community or developed during this project.
- An algorithm able to compare simulated and acquired fingerprints and attribute property combinations to the latter. The first implementations of MRF used pattern matching, as shown in fig. I.4.1c. The method consists in finding for each acquired fingerprint its best match in the dictionary. The property combination of the best match is eventually attributed to the acquired fingerprint’s voxel. Over the years, many groups have proposed advanced MRF reconstruction tools using machine learning strategies, fingerprint space decomposition, regressions, and deep learning algorithms. This reconstruction step was not the focus of this Ph.D thesis, but is discussed in McGivney et al. 2020, Assländer 2020 and Tipparedy et al. 2021.

MRF was first designed to map relaxometric properties, such as classical  $T_1$ ,  $T_2$  and later  $T_2^*$  (Ma et al. 2013; Jiang et al. 2015; Wang et al. 2019; Boyacioglu et al. 2021). Carefully optimizing the sequence, acquisition scheme, and reconstruction step, Schuman et al. 2022 now report a 1-minute acquisition and 5 minutes reconstruction MRF protocol for 1mm isotropic, 3D whole-brain imaging. The proposed method outputs parametric maps of  $T_1$ ,  $T_2$ , and proton density, and in addition, synthesizes 5 conventional contrast volumes such



as  $T_1w$  or FLAIR images. These state-of-the-art results illustrate the potential of MRF in terms of acquisition duration and clinical value. For comparison, the authors report a 28 minutes exam to obtain the same 5 contrasts using state-of-the-art non-MRF methods.

Given the flexibility of the MRF concept, it has been extended to the measurements of a large variety of properties, among which:

- Water diffusion coefficients [Kobayashi et al. 2019](#); [Fan et al. 2022](#)
- Cerebral blood flow with MRF ASL [Su et al. 2017](#); [Flassbeck et al. 2019](#); [Portnoy, Sharon et al. 2019](#); [Fan et al. 2022](#)
- Musculoskeletal properties [Cencini et al. 2018](#); [Marty et al. 2021](#)
- MR spectrum [Wang et al. 2017](#); [Kulpanovich et al. 2018](#)
- Chemical exchange saturation transfer (CEST) and Magnetization transfer (MT) [Cohen et al. 2018](#); [Perlman et al. 2020](#); [Perlman et al. 2022](#)

It is in fact theoretically possible to quantify any tissue property, as long as it can be included in the simulations and that the shape of the fingerprints varies when the values of the properties change. This approach, where all properties of interest can be precisely put into a simulation model that eventually sums up their contributions in a low-dimensional signal, can be preferable to a more classic fit of a mathematical model. Indeed, establishing such a model generally requires a number of assumptions and approximations that can restrict the scope of the method. This is especially true in pathological tissues, where models established on ideal healthy cases tend to lose accuracy. Using a dictionary approach such as MRF allows for setting tissue property ranges and combinations that suit any situation, yielding accurate estimates in more situations.

In our case, the effect of the paramagnetic nature of the blood on nuclear magnetization time evolution is well established and numerical simulations of the BOLD effect have been proposed for many years. It should thus be possible to quantify vascular properties in the brain using MRF. Our team has recently proposed a technique called MR vascular Fingerprinting (MRvF) for blood oxygenation measurements which is described below.

## I.4.2 MR vascular Fingerprinting

MR vascular Fingerprinting was introduced in [Christen et al. 2014b](#) in human subjects, and in [Lemasson et al. 2016](#) in pathological animal models. The MRvF workflow is described in [fig. I.4.2](#). Contrary to classical MRF for relaxometry, the simulated voxels don't merely consist of a list of properties such as global  $T_1$  or  $T_2$  values. A sub-voxel structure is generated to represent the microvascular network. Such a structure can be generated by randomly placing straight vessels of a certain radius  $R$  until a desired blood volume fraction (BVf) is reached. In the first implementations of MRvF, a 2D representation was chosen, with straight vessels perpendicular to the plane being discs. The blood inside the vessels is given an  $SO_2$  value, giving rise to a difference in susceptibility between the blood and extravascular compartments. The simulations including magnetic field distributions, magnetization evolution, and water diffusion effects were performed using the tool proposed in [Pannetier et al. 2013](#) that will be described later in the manuscript. The MRF sequence used in the first papers was the

“gradient echo sampling of the free-induction decay and spin echo”, or GESFIDSE (Ma et al. 1996) sequence. Acquisitions were performed before and after the injection of a contrast agent, and the ratio of the two signals obtained was used as a fingerprint. The MR sequence was simulated on the whole voxel, to obtain a signal whose shape varies according to BVf, R,  $SO_2$  and to produce the corresponding parametric maps after matching.

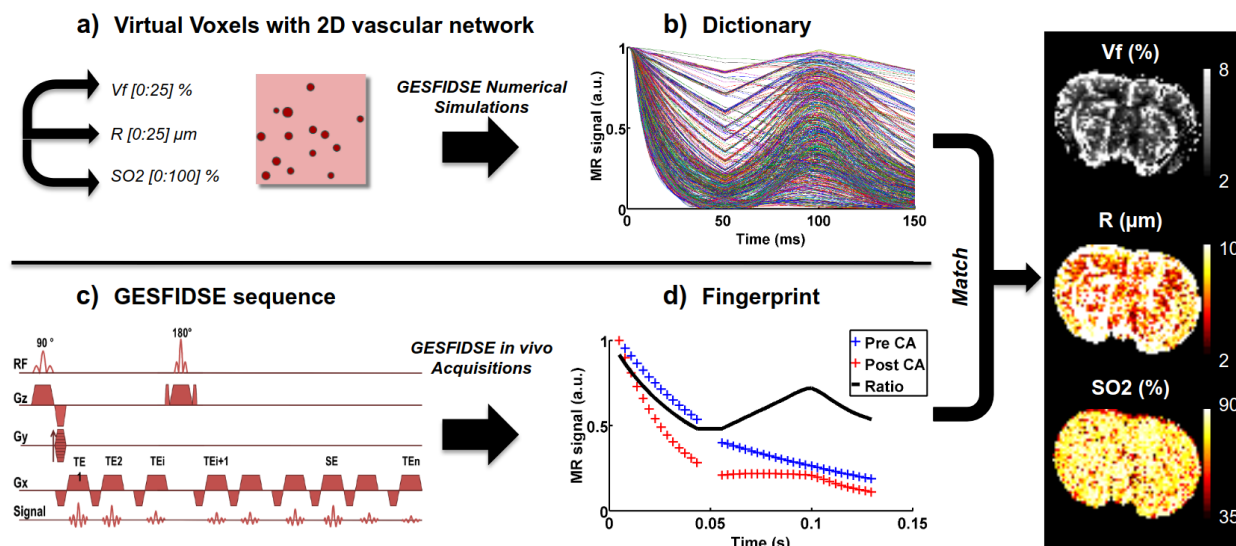


**Figure I.4.2:** MR vascular Fingerprinting basic principles

In Christen et al. 2014b, 5 healthy human volunteers were imaged at 3T. A dictionary of 52,920 signals was generated with three varying parameters, BVf, R, and  $SO_2$ . Diffusion effects were also accounted for. The BVf and R maps obtained with MRvF were in good agreement with the literature and correlated with steady-state perfusion measurements acquired in the same volunteers.

In the gray matter, the MRvF-obtained  $SO_2$  values were in agreement with both the literature from other imaging methods and from an MR-based phase measurement of  $SO_2$  in the sagittal sinus. The values obtained in the white matter were however lower than expected, and the interface between gray and white matter was systematically estimated as highly deoxygenated. The authors identified a lack of uniqueness in the used fingerprint in the parameter space and a probable lack of diversity in the generated dictionary. The simplicity of the 2D voxel representation was also pointed out as a limitation. It was also suggested that additional parameters should be considered in the simulations before being able to apply MRvF to pathological cases.

The study nevertheless produced maps of vascular properties at the sub-voxel level and demonstrated the feasibility of MR vascular fingerprinting. Fig. I.4.3 shows slices from the subject with the highest matching score between the acquisitions and the dictionary. 5 slices are shown for an anatomical scan and three vascular parameters: BVf (Cerebral blood volume, BVf (CBV, on the figure), R, and  $SO_2$ . Note the presence of many completely deoxygenated regions in the  $SO_2$  maps.

The second study (Lemasson et al. 2016) proved the feasibility of MRvF in rats, both in healthy and pathological conditions. 115 rats were imaged at 4.7T, divided into three groups:

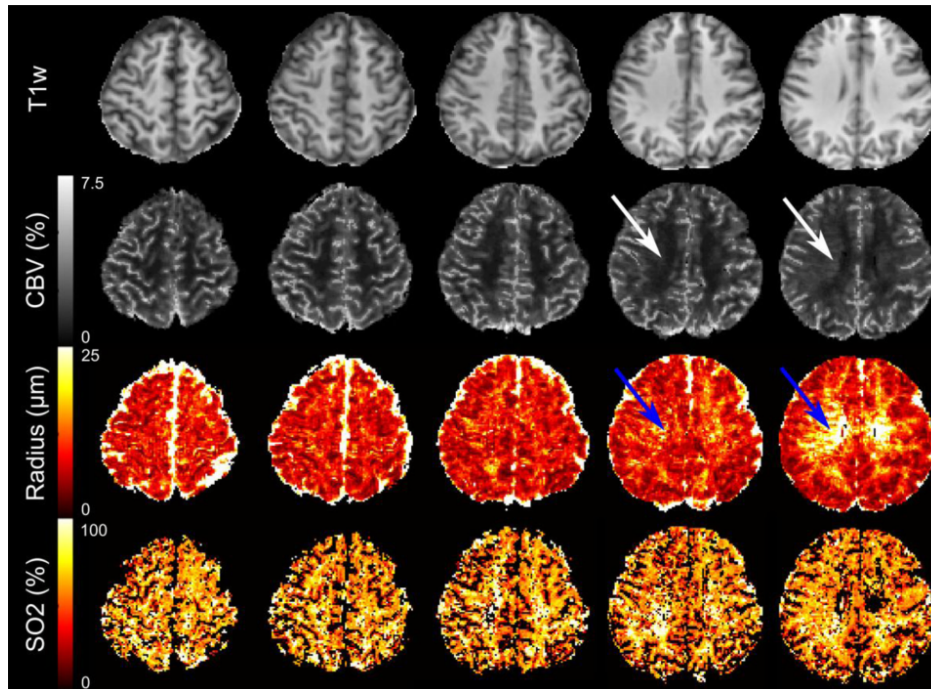


**Figure I.4.3:** Parametric maps obtained on a healthy subject with MRvF at 3T, from Christen et al. 2014b. Arrows indicate relatively small medullary veins in the white matter, that the method is sensitive enough to detect.

brain tumors (9L, C6, and F98), permanent stroke, and healthy control. Three dictionaries were generated:

- A: varying BVf, R, and  $SO_2$  with a fixed apparent water diffusion coefficient (ADC), similar to what was done in the previous study, containing 38,976 fingerprints
- B: dictionary A enriched with 27 ADC values, bringing the total number of fingerprints to 1,052,352
- C: dictionary B enriched with 97,440 fingerprints corresponding to voxels containing two large blood vessels with a specific orientation w.r.t the plane.

After imaging, some animal brains were sampled and frozen. They were later sliced, immunostained, and imaged with a microscope to be used as references for geometrical metrics. Steady-state perfusion measurements were also made.

The study showed that MRvF benefits from the addition of new dimensions in the dictionary, as dictionary C provided better results than dictionary A. The authors also showed that the ratio of the GESFIDSE pattern is sensitive enough to vascular parameters to allow the delineation of pathological regions and to distinguish tumor models from one another. For BVf and R, only MRvF followed the trends observed in histologies.  $SO_2$  maps from MRvF differed from those obtained with the qBOLD measurements, in absolute values and in trends between healthy and pathological tissues. Fig. I.4.4 compares vascular parameter maps obtained with steady-state approaches and MRvF for the F98 and 9L glioma models.

For BVf, both methods show similar variations between the tumor and healthy tissue, which

are not the same for the two gliomas. The same can be observed for R measurement, even if the agreement between MRvF and steady-state is not as good. This is explained by the fundamental difference between VSI (vessel size index, weighted mean) and mean R measurements. The agreement between  $\text{SO}_2$  maps from both methods is however degraded. For the F98 model, a decrease of  $\text{SO}_2$  is observed in the tumor in both cases, but it is more pronounced with steady-state than with MRvF. For the 9L model, steady-state analysis shows a normoxic tumor whereas MRvF shows hypoxia. The authors identified the lack of ground truth for  $\text{SO}_2$  measurement as a major limitation for MRvF validation.

It is worth noting that [Pouliot et al. 2017](#) reproduced an MRvF experiment using a dictionary generated using geometries observed from microscopies, which will be discussed in chapter [III](#).

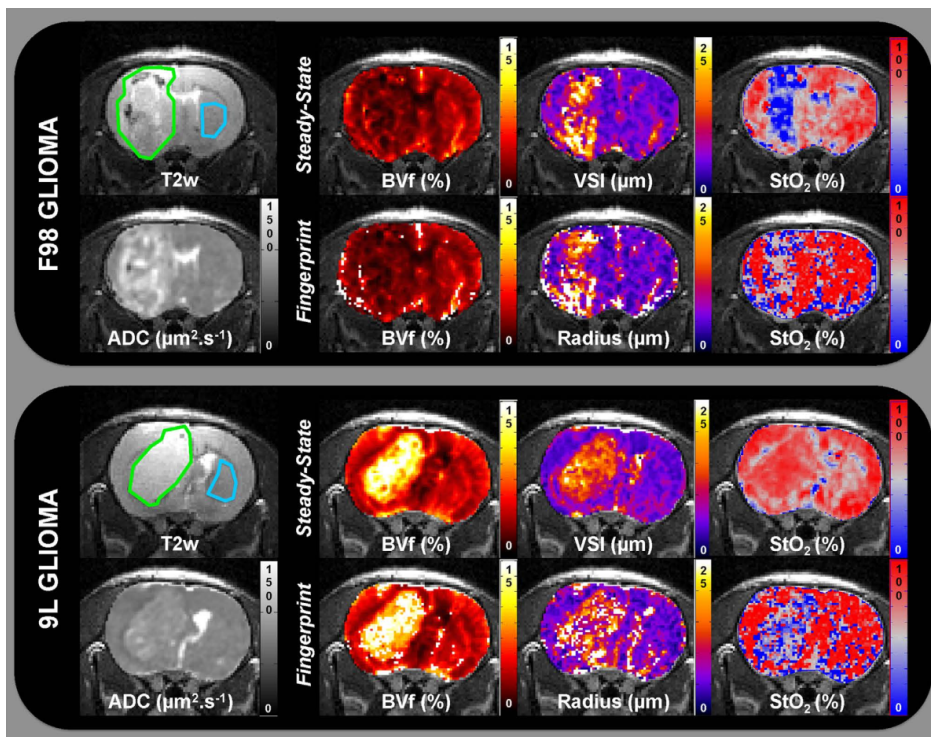


**Figure I.4.4:** Parametric maps obtained with MRvF and steady-state analysis at 4.7T, from [Lemasson et al. 2016](#).

## I.5 State-of-the-art summary

In conclusion, there is a strong need for a cerebral oxygenation mapping technique compatible with the acute care context. A large variety of physical principles have been used to develop imaging techniques for cerebral oxygenation mapping. As detailed above, MRI seems to be a promising candidate due to its high spatial resolution and sensitivity to soft tissue contrasts. In addition, the MRF technique allows now for circumventing the prohibitive long acquisition time of an MRI exam and the lack of quantitative estimates. MRvF, its application to vascular properties measurement, already demonstrated that oxygenation

mapping is achievable but with some limitations.

In MRvF, a sub-voxel scale vascular network representation is mandatory. For the moment, a 2D representation where vessels are straight parallel cylinders, has been used. This is a poor approximation of the complexity of a real vascular network and better results are expected with more realistic simulations.

In addition, the MRvF sequence used so far is a combination of GRE and SE inherited from qBOLD experiments. It was designed to have a temporal evolution simple enough to be used in conjunction with analytical models. Yet, the MRF framework offers the possibility to use new types of sequences with much more complex signal evolutions, and are likely to provide an increased sensitivity to tissue oxygenation.

Maybe due to the two constraints above, the current MRvF implementation requires data acquisition before and after the injection of a contrast agent. Such a procedure poses several problems. Injections are not possible in every clinical context and can be harmful to some patients. The exam duration is also doubled, reducing its interest for emergency patient triage. Finally, the contrast agents have a non-negligible cost, further preventing the use of MRvF as a routine imaging technique.

In the following, developments will be made to try to overcome the current MRvF implementation's limitations, encompassing new numerical simulations, preclinical and clinical acquisitions, and image reconstruction.



## CHAPTER II

---

# DEVELOPING TOOLS FOR MRvF

---

As exposed in [I.4](#), MR Fingerprinting consists of several steps. Each one of them requires careful thought, development, and validation. This chapter presents the work done on MR simulation tools, acquisitions at the preclinical and clinical level, and reconstruction solutions to obtain a flexible but robust MR Fingerprinting pipeline. Developments were driven by the need to overcome the current MRvF's limitations exposed in the precedent chapter.

We worked from previous codes already developed in the lab, tools provided by the community or through collaborations, and on implementing state-of-the-art literature. Validations of the tools were made in conditions related to the MRvF context.

---

**CONTENTS**


---

<b>II.1</b>	<b>Development of MRI simulation tools</b>	<b>36</b>
II.1.1	Simulation tools for classical MRF . . . . .	36
II.1.1.1	Bloch equations . . . . .	36
	Theory . . . . .	36
	Matrix formulation for MRI simulations . . . . .	37
II.1.1.2	Extended Phase Graph . . . . .	38
	Phase configuration states . . . . .	38
	RF pulses . . . . .	40
	Application: Extended Phase Graph . . . . .	41
II.1.1.3	Implementations . . . . .	41
II.1.2	Simulation tool for MR vascular Fingerprinting . . . . .	43
II.1.2.1	MRVox2D . . . . .	43
	Dictionary generation . . . . .	44
	2D vessel network generation . . . . .	46
II.1.2.2	MRVox3D . . . . .	47
	2D to 3D . . . . .	47
	External geometry importation . . . . .	50
II.1.3	Validation of the tools . . . . .	51
II.1.3.1	Cross-validation on relaxometry experiments . . . . .	51
	Balanced steady-state . . . . .	51
	Gradient Spoiling . . . . .	52
	RF spoiling . . . . .	54
	Bloch isochromats . . . . .	56
II.1.3.2	Validation of MRVox against theoretical models . . . . .	56
	MRVox2D . . . . .	57
	MRVox3D . . . . .	58
II.1.4	Conclusions and perspectives . . . . .	58
II.1.4.1	Classical MRF simulation tools . . . . .	58
II.1.4.2	MRVox . . . . .	59
<b>II.2</b>	<b>Pre-clinical MRF acquisitions</b>	<b>59</b>
II.2.1	Overview of the existing acquisition tool . . . . .	60
II.2.1.1	Tests and validations . . . . .	60
	First images . . . . .	60
	Spoiling gradients . . . . .	61

---

	Timing flexibility . . . . .	63
	Comparing acquisitions and simulations . . . . .	64
II.2.2	New developments . . . . .	66
II.2.2.1	Improving inversion pulses . . . . .	66
II.2.2.2	B <sub>1</sub> phase . . . . .	67
II.2.3	First MRF results in vivo . . . . .	69
	Gómez et al. 2019 . . . . .	69
	Jiang et al. 2015 . . . . .	70
II.2.4	Conclusions and Perspectives . . . . .	71
II.2.4.1	Limitations . . . . .	72
	Need for compilation when the sequence changes . . . . .	72
	Pulse number limitation . . . . .	72
	Slice number limitation . . . . .	72
	Spiral shape and sampling rate . . . . .	72
	Phase offset vs. distance to magnet . . . . .	73
II.2.4.2	Perspectives . . . . .	73
<b>II.3</b>	<b>Test of a clinical MRF acquisition module</b> . . . . .	<b>75</b>
II.3.1	Context: Philips Research collaboration . . . . .	75
II.3.2	Overview . . . . .	75
II.3.3	Evaluation of the MRF module . . . . .	76
II.3.3.1	Tests on acquisition parameters . . . . .	77
	Spiral and cartesian acquisition schemes . . . . .	77
	RF phase cycling . . . . .	78
	MRF sequences from the literature . . . . .	79
II.3.4	Perspectives . . . . .	81
<b>II.4</b>	<b>Development of MRF reconstruction tools</b> . . . . .	<b>82</b>
II.4.1	Exploratory reconstruction tool . . . . .	82
II.4.1.1	Data processing software: MP3 . . . . .	83
II.4.2	Developments for MP3 . . . . .	84
II.4.2.1	Pattern options . . . . .	84
II.4.2.2	Parametric maps screening tool . . . . .	85
II.4.3	Perspectives . . . . .	86

---



## II.1 Development of MRI simulation tools

The following section presents the MR signal simulation tools developed through this project.

MRI simulations mostly rely on the mathematical model presented in [Bloch 1946](#) and getting a good grasp on basic MR modeling is required before trying to account for more complex effects that can be needed for MRvF. Additionally, most standard MRF simulations are based on numerical implementations of these equations. It was thus decided to work on two independent simulation tools:

- a standard simulation tool, based on Bloch Matrix formulation and the “Extended Phase Graph” framework, that would be able to generate MRF dictionaries for relaxometry experiments. This fast tool was used for comparison and validation of both MR simulations and acquisition results.
- a simulation tool dedicated to vascular simulations with the possibility to integrate realistic vascular networks as well as biophysical interactions.

The two methods were cross-validated as well as compared to theoretical expectations in multiple experiments involving RF phase variations, gradient spoiling, water diffusion, and local changes of magnetic susceptibility.

### II.1.1 Simulation tools for classical MRF

This section introduces the Bloch equations and presents their implementation as matrix formulation and Extended Phase Graph framework.

#### II.1.1.1 Bloch equations

##### Theory

Nuclei with a non-zero nuclear spin have a magnetic moment. These magnetic moments precess around the direction of a strong, constant, external magnetic field  $\mathbf{B}$ . This precession occurs at the Larmor frequency  $\omega = \gamma\|\mathbf{B}\|$ , where  $\gamma$  is the gyromagnetic ratio, specific to the considered nucleus (42.58MHz/T for  $^1\text{H}$ , the most common element considered in MRI). In a volume element, the magnetic moments interact and partly align themselves along the external field. In addition, the nuclei distribute on different spin states ( $-\frac{1}{2}$  and  $\frac{1}{2}$  for  $^1\text{H}$ ). These phenomena give rise to a polarization vector called the net magnetization  $\mathbf{M}$ .  $\mathbf{M}$  is aligned with  $\mathbf{B}$  at equilibrium, but can be tipped out of this state by a transverse magnetic field rotating at the Larmor frequency.  $\mathbf{M}$  then precesses back to equilibrium, its transverse component decaying with a characteristic time  $T_2$ , and its longitudinal component recovering with a time  $T_1$ . The precession of  $\mathbf{M}$  around  $\mathbf{B}$  can induce a signal in an appropriate coil, which is the origin of the MR signal. A description of the temporal evolution of  $\mathbf{M}$  was first given in [Bloch 1946](#):

$$\frac{d\mathbf{M}}{dt} = \gamma(\mathbf{M} \times \mathbf{B}) - \frac{M_x}{T_2}\mathbf{x} - \frac{M_y}{T_2}\mathbf{y} + \frac{(M_0 - M_z)}{T_1}\mathbf{z} \quad (\text{II.1.1})$$

where  $\mathbf{M} = (M_x, M_y, M_z)$  and  $\mathbf{B} = (B_x, B_y, B_z)$ , in an orthonormal frame  $(\mathbf{x}, \mathbf{y}, \mathbf{z})$ .  $T_1$  and  $T_2$  are the longitudinal and transverse relaxation times, respectively.  $M_0$  is the net

magnetization at equilibrium.

When the main magnetic field is along  $z$ , one can separate the longitudinal ( $M_{\parallel}$ ) and transverse ( $M_{\perp}$ ) components of  $\mathbf{M}$  with respect to  $\mathbf{z}$ :

$$\begin{aligned} M_{\parallel}(t + \delta t) &= M_{\parallel}(t) \cdot \exp\left(\frac{-\delta t}{T_1(t)}\right) + M_0 \left(1 - \exp\left(\frac{-\delta t}{T_1(t)}\right)\right) \\ M_{\perp}(t + \delta t) &= M_{\perp}(t) \cdot \exp\left(-i\gamma B_z(t)\delta t - \frac{\delta t}{T_2(t)}\right) \end{aligned} \quad (\text{II.1.2})$$

Diffusion effects are neglected here.

Note the temporal dependence of  $B_z$ , which can be decomposed as

$$B_z(t) = B_0 + \Delta B_z(t) + G(t) \quad (\text{II.1.3})$$

Where  $B_0$  is the applied field.  $\Delta B_z$  represents the local off-resonance effect, which can be due, among other reasons, to inhomogeneities of  $B_0$  and local tissue susceptibility.  $G(t)$  is the amplitude of an additional weak magnetic field that can be applied for imaging purposes. Only temporal considerations are presented here for sake of simplicity, but there is of course a spatial dependence as well: the amplitude of the gradients, the field inhomogeneities, and the relaxation times may vary spatially in the imaged sample.

It is common to consider the evolution of  $\mathbf{M}$  in a so-called ‘‘laboratory’’ frame that rotates at the Larmor frequency, to eliminate the rotation term  $\exp(-i\gamma B_0 \delta t)$ .

There is of course no magnetization evolution without any initial perturbation. In practice, an RF pulse applied in the  $(\mathbf{x}, \mathbf{y})$  plane tips  $\mathbf{M}$  away from  $\mathbf{z}$ . A pulse can be seen as an instantaneous rotation in the so-called ‘‘hard pulse’’ approximation. For a pulse of flip-angle  $\alpha$  and phase  $\Phi$  with respect to  $\mathbf{x}$  one multiplies  $\mathbf{M}$  with:

$$R_{\Phi}(\alpha) = \begin{pmatrix} \cos^2 \frac{\alpha}{2} & e^{2i\Phi} \sin^2 \frac{\alpha}{2} & -ie^{i\Phi} \sin \alpha \\ e^{-2i\Phi} \sin^2 \frac{\alpha}{2} & \cos^2 \frac{\alpha}{2} & ie^{-i\Phi} \sin \alpha \\ -\frac{i}{2}e^{-i\Phi} \sin \alpha & \frac{i}{2}e^{i\Phi} \sin \alpha & \cos \alpha \end{pmatrix} \quad (\text{II.1.4})$$

which is the result of  $R_z(\Phi) \cdot R_x(\alpha) \cdot R_z(-\Phi)$ , where  $R_u$  denotes a rotation about any  $u$  axis (Weigel 2015).

### Matrix formulation for MRI simulations

The previous equations are easy to implement as matrix formulation to perform numerical simulations of the MR signal evolution. Relaxation and precession effects are computed as follows. Over a time period  $\tau$ :

- Any off-resonance effect, either local ( $\Delta B$ ) or due to constant amplitude gradients ( $G$ ), will rotate  $\mathbf{M}$  around  $\mathbf{z}$  by an angle

$$\varphi = 2\pi \cdot \gamma \cdot (\Delta B + G) \cdot \tau \quad (\text{II.1.5})$$

- The relaxations are written as

$$\mathbf{A} = \begin{pmatrix} E2 & 0 & 0 \\ 0 & E2 & 0 \\ 0 & 0 & E1 \end{pmatrix} \cdot R_z(\varphi) \quad \text{and} \quad \mathbf{B} = \begin{pmatrix} 0 \\ 0 \\ 1 - E1 \end{pmatrix} \quad (\text{II.1.6})$$

where

$$\begin{aligned} E1 &= \exp(-\tau/T_1) \\ E2 &= \exp(-\tau/T_2) \end{aligned} \quad (\text{II.1.7})$$

to eventually obtain  $\mathbf{M}$  after a free precession over duration  $\tau$ :

$$\mathbf{M}(t + \tau) = \mathbf{A} \cdot \mathbf{M}(t) + \mathbf{B} \cdot M_0 \quad (\text{II.1.8})$$

Computing the evolution of a single magnetization vector is usually not enough to accurately model a whole tissue voxel. Simulations have to be repeated for multiple isochromats, i.e. ensembles of spins processing at the same frequency. Choosing the number of isochromats is then a trade-off between computation cost and required precision.

### II.1.1.2 Extended Phase Graph

An efficient tool for Bloch equations simulations is the Extended Phase Graph (EPG) framework. The major advantage of EPG is that it takes into account multiple isochromats simultaneously and thus reduces the simulation cost. New technical developments are still under consideration and EPG now allows multiple physical effects in the simulations (Hennig 1988; Hennig 1991; Scheffler 1999; Weigel 2015; Guentner et al. 2021).

EPG relies on two key concepts described below. Following the formalism from Weigel 2015, one can write:

#### Phase configuration states

For a single isochromat of magnitude  $M$  in the reference frame, in a position  $\mathbf{r}$  where a gradient  $\mathbf{G}$  is non-null, the temporal evolution of  $M$ , neglecting relaxations, is:

$$\begin{aligned} M_x(\mathbf{r}) &= M \cos \left( \gamma \mathbf{r} \int_0^\tau \mathbf{G}(\tau) d\tau \right) \\ M_y(\mathbf{r}) &= M \sin \left( \gamma \mathbf{r} \int_0^\tau \mathbf{G}(\tau) d\tau \right) \end{aligned} \quad (\text{II.1.9})$$

Considering the angular wave vector  $\mathbf{k}$ :

$$\mathbf{k} = \gamma \int_0^\tau \mathbf{G}(\tau) d\tau \quad (\text{II.1.10})$$

that describes the helix corresponding to the dephasing of isochromats along the gradient axis, illustrated in fig. II.1.1, one obtains

$$\begin{aligned} M_x(\mathbf{r}) &= M \cos(\mathbf{k}\mathbf{r}) \\ M_y(\mathbf{r}) &= M \sin(\mathbf{k}\mathbf{r}) \end{aligned} \quad (\text{II.1.11})$$

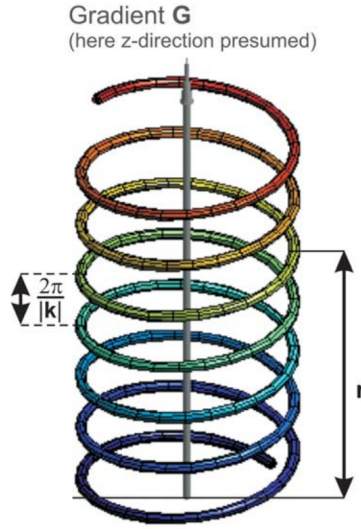


**Figure II.1.1:** Dephasing helix of a number of isochromats after applying a gradient along the z-axis, from Weigel 2015. The lowest isochromat is on-resonance. Upper isochromats experienced a gradient amplitude variable with their position  $G(\mathbf{r})$ . Their dephasing w.r.t. the on-resonance isochromat increases with  $r$ , as illustrated by the color scale. The vector  $\mathbf{k}$  represents the pitch of the helix described by the isochromats.

These two components can be seen in a complex plane:

$$\begin{aligned} M_+(\mathbf{r}) &= M_x(\mathbf{r}) + iM_y(\mathbf{r}) = Me^{i\mathbf{k}\mathbf{r}} \\ M_-(\mathbf{r}) &= M_x(\mathbf{r}) - iM_y(\mathbf{r}) = Me^{-i\mathbf{k}\mathbf{r}} \end{aligned} \quad (\text{II.1.12})$$

Note that  $(M_+)^* = M_-$ . Considering only  $M_+$ , computing the net magnetization over a volume  $V$  sufficiently large to contain several dephasing orders  $\mathbf{k}$  gives:

$$\begin{aligned} \tilde{F}_+(\mathbf{k}) &= \int_V Me^{i\mathbf{k}\mathbf{r}} d^3r \\ \tilde{F}_+(\mathbf{k}) &= \int_V M_+(\mathbf{r})e^{-i\mathbf{k}\mathbf{r}} d^3r \end{aligned} \quad (\text{II.1.13})$$

which is the Fourier transform of  $M_+$ , and also yields

$$M_+(\mathbf{r}) = \int_V \tilde{F}_+(\mathbf{k})e^{i\mathbf{k}\mathbf{r}} d^3k \quad (\text{II.1.14})$$

For all  $\mathbf{k}$ ,  $\tilde{F}_+(\mathbf{k})$ , depicts the radius and phase (in the rotating frame) of the dephasing helix, as illustrated in fig. II.1.2.  $M$  can thus be described as a sum of  $\tilde{F}_+(\mathbf{k})$  configuration states. This is particularly interesting as one does not need to keep track of individual isochromats to compute the net magnetization at any time. It is enough to keep track of the configuration states.

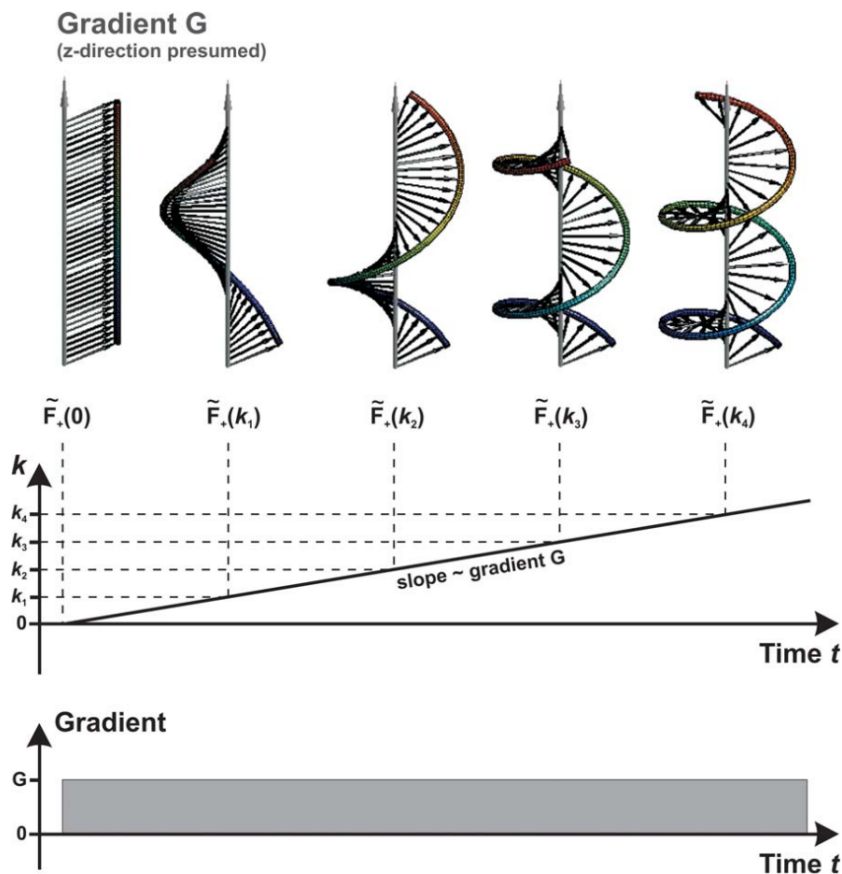


**Figure II.1.2:** EPG representation of dephasing states of the magnetization in a voxel, from Weigel 2015. The gradient applied in the z direction causes the dephasing.

### RF pulses

Fig. II.1.3 from Scheffler 1999 gives a graphical description of the effect of a RF pulse. Any RF pulse rotates the whole isochromats ensemble around a given axis. Each isochromat noted  $M^-$  before a pulse will be transformed into three parts after the pulse:

- Two transverse components, which are either dephasing ( $M_+^+$ ) or rephasing ( $M_-^+$ )
- A longitudinal component  $M_z^+$

The  $M_+^+$  part will keep dephasing if a gradient is applied, which will result in a new dephasing configuration  $\tilde{F}_+(\mathbf{k})$  of higher order. The  $M_-^+$  part will refocus until the fundamental state  $\tilde{F}(0)$  is reached, creating an echo.

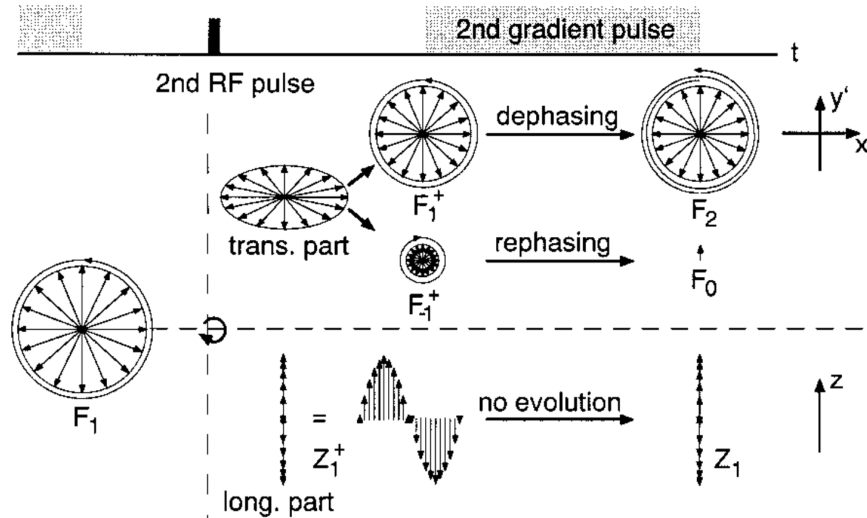


**Figure II.1.3:** Graphical depiction of the effect of an RF pulse on the magnetization; from Scheffler 1999. After a first pulse and a dephasing period, the magnetization is in a dephasing state  $\tilde{F}_+(1)$ . An arbitrary pulse rotates that magnetization, which results in a transverse and longitudinal part. The transverse part can be decomposed into a dephasing and rephasing part, which will evolve towards  $\tilde{F}_+(2)$  and  $\tilde{F}_+(0)$ , respectively. The  $\tilde{Z}$  part will not dephase anymore until a new pulse converts a partition of it into transverse magnetization.

### Application: Extended Phase Graph

One can use the two concepts above to describe the evolution of magnetization.

For any isochromat  $M$ , the influence of any RF pulse can be computed, as well as states  $\tilde{F}_+(\mathbf{k})$ ,  $\tilde{F}_-(\mathbf{k})$  and  $\tilde{Z}(\mathbf{k})$  corresponding to the three components of  $M$  (see Weigel 2015 for full mathematical details). The two first ones are states with reversed phase history, corresponding to the dephasing and rephasing parts of the magnetization.  $\tilde{Z}(\mathbf{k})$  is the configuration state of transverse components that were converted to longitudinal magnetization by a pulse. The isochromats dephasing state is frozen, or stored, as they will not experience further dephasing unless a new pulse rotates them back to the transverse plane.

The EPG framework is computationally efficient as there is no dependence on a number of isochromats to keep track of, as long as the dephasing states have the right amplitudes, which is obtained through a simple rotation operator. It also allows a graphical representation of a multi-pulse experiment that very clearly explains the origin of echoes and their timings. Fig. II.1.4 shows two multi-pulse experiments represented with EPG, where the echoes are easily identifiable.

#### II.1.1.3 Implementations

We used Pr. Brian Hargreaves' (Stanford University) straightforward Matlab EPG implementation (Hargreaves 2015) and a Matlab-interfaced C implementation of Bloch's equations (Hargreaves 2005) as starting points for our simulation tools. A unified framework for dictionary generation was then built based on both these two implementations. The goal

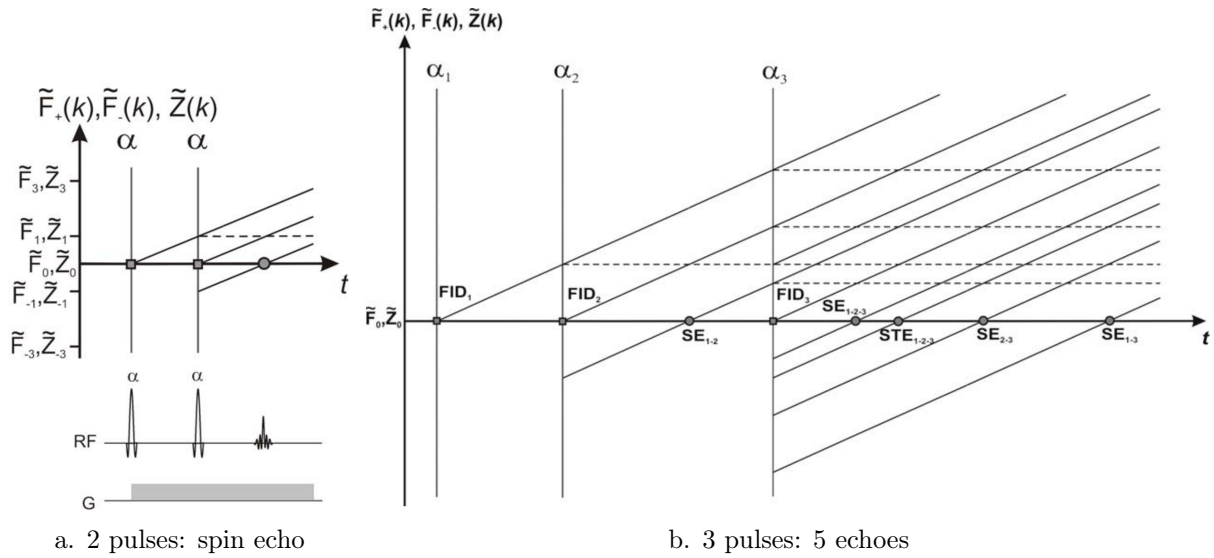


**Figure II.1.4:** Visual representation of the evolution of dephasing states with EPG, from Weigel 2015. a. Spin echo. The first pulse places a part of the magnetization, initially at equilibrium, into the transverse plane. There, it dephases due to the applied gradient (solid lines) and reaches the state  $\tilde{F}(1)$ . A second pulse places a part of the magnetization along the longitudinal axis, in state  $\tilde{Z}(1)$  where it is stored (dashed horizontal line). Part of the magnetization is placed in the state  $\tilde{F}_+(1)$  where it will keep dephasing towards configurations of higher order. Another part is placed in the state  $\tilde{F}_-(1)$  where it refocuses towards  $\tilde{F}(0)$ , where the isochromats are in phase coherence again, generating an echo. b. Typical 3 pulses experiment, generating 5 echoes, which can be predicted and understood from EPG representation.

was to simulate any dictionary based on relaxation parameters with two different and well-documented simulation methods. As such, it could serve as a basis for further validations of acquisition tools, or more advanced simulation codes. Our MRF simulation tool accepts parameters through a structured text file. Part of the file describes the sequence: number of pulses, spoiling, flip angles (FA), TR and TE. Classical evolutions of FA, TR, and TE can be used, such as ramps, triangles, or Perlin noise. The complete sequence is generated at run time. For more complex or non-trivial parameter evolutions, the sequence can be loaded from a pre-existing `.mat` file.

The parameters of the dictionary are given as lists. The user can consider  $T_1$ ,  $T_2$ , off-resonance, and  $B_1$ . A mesh is created to obtain all the combinations of the parameters given, excluding cases where  $T_2 > T_1$ . All the cases are then treated in parallel using a Matlab `parfor`.

All simulation parameters are saved along with the dictionary generated, allowing for a robust tracking of the simulation parameters and easy reproducibility.

The tool allows fast simulation of dictionaries from basic MR sequences or more complex ones from the literature. It has been used during our work to test our acquisition tools (see sections II.2 and II.3) on classical MRF experiments with  $T_1$ ,  $T_2$ ,  $B_1$  and off-resonance parameters. It was also used to cross-validate the simulation tool suited for MR vascular Fingerprinting described below.



## II.1.2 Simulation tool for MR vascular Fingerprinting

The Bloch implementations presented in the precedent section are powerful simulation tools, but in their current state they only consider homogeneous voxels. The aim of MRvF is to explore the vascular structure at a sub-voxel level, which implies having non-homogeneous, structured voxels. We present here the tool developed in the lab for such simulations.

### II.1.2.1 MRVox2D

MRVox is a Matlab MR simulation software initially developed in the team to simulate dynamic contrast enhanced experiments, where a contrast agent bolus is injected in the vascular network. The core simulation steps are introduced in [Pannetier et al. 2013](#). Its main particularity consists in its ability to simulate the MR response of a heterogeneous, 2D voxel, to any MR sequence. A three compartments model is used to independently set the physical and physiological properties of the extravascular space, the blood vessels, and the cells. In particular, each compartment is given a magnetic susceptibility, which is directly linked to oxygen saturation in the blood compartment. These spatial variations of the susceptibility will locally interact with the main magnetic field, adding positive or negative contributions, as shown in fig. [II.1.5](#). Such local perturbations are computed using a Fourier approach

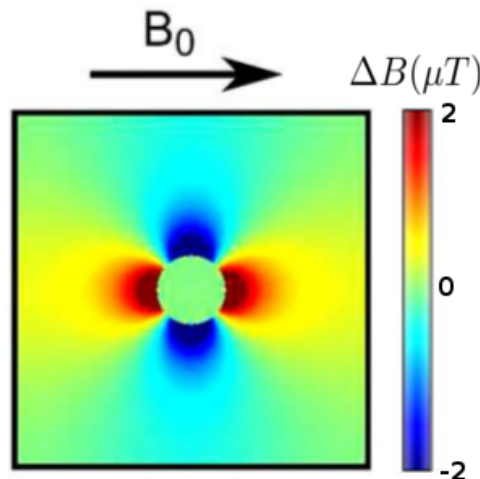


**Figure II.1.5:** Magnetic field perturbation around a blood vessel, adapted from [Pannetier et al. 2013](#)

([Salomir et al. 2003](#); [Marques et al. 2005](#)). A Fourier approach is also used to account for the water molecules diffusion in the voxel ([Bandettini et al. 1995](#); [Klassen et al. 2007](#)), inside a compartment and/or between them.

The state of the magnetic field and magnetization in the voxel can be visualized during the simulation, as shown in fig. [II.1.6](#). The MR sequence, the simulated signal, as well as 2D and 3D representations of the isochromats in the rotating frame are also displayed in real-time, see fig. [II.1.7](#).

To mitigate the lack of reality of a 2D network with parallel vessels, the magnetic field perturbations can be averaged in the three directions with respect to the plane.



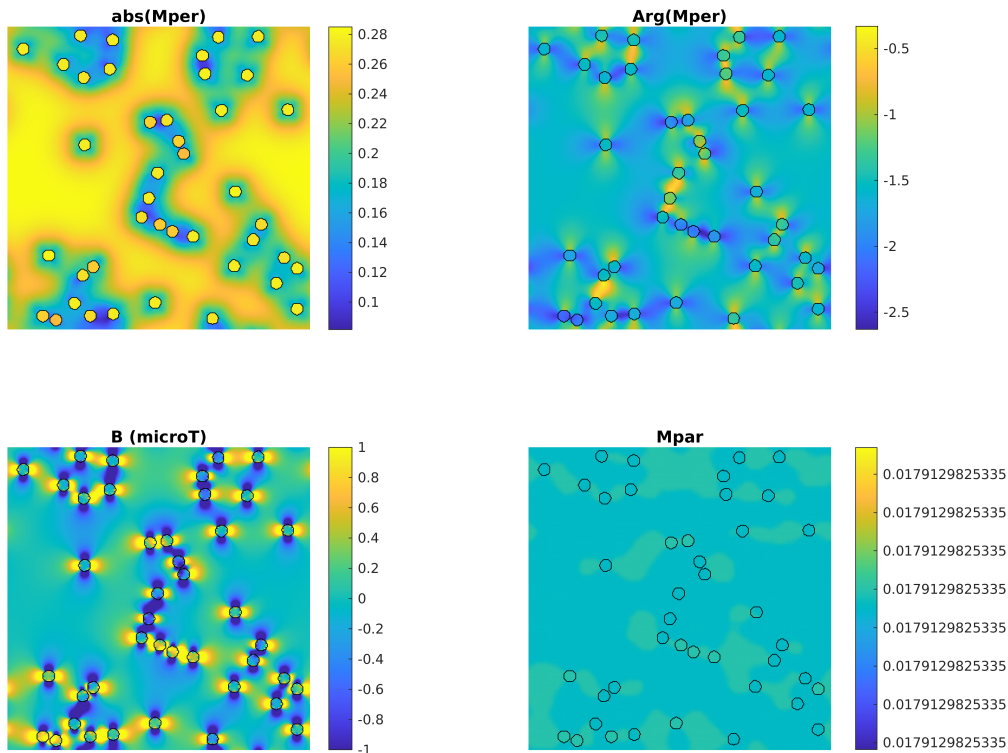


**Figure II.1.6:** Representation of the magnetic field and magnetization inside a voxel in MRVox. The two top panels show the module and argument of transverse magnetization. The magnetic field perturbations are shown on the bottom-left panel. Note that they are cropped between  $-1$  and  $1 \mu\text{T}$  but expand further than this range. The bottom-right panel shows the module of the longitudinal magnetization.

### Dictionary generation

MRVox was not initially developed to generate dictionaries of many signals, but rather to follow contrast agent diffusion and related MR signal changes on longer acquisitions. The different computation steps are demanding, and obviously strongly correlated to spatial and temporal resolution. Degrading either up to a certain point necessarily degrades the quality of the simulations. Solutions hence had to be developed for our project to generate dictionaries with hundreds of thousands of signals or more. Taking advantage of modern multi-core CPUs, a parallel computing approach was used to try and make dictionary generation tractable. Matlab proposes a toolbox for parallel computing. Two options to execute  $N$  times the MRVox main function were considered:

- **parfor**: parallel execution of a classical **for** loop. Several iterations are done at the same time instead of one. If a pool of  $n$  workers is available on the machine, each one is attributed  $N/n$  jobs to perform. All the workers then process their jobs in parallel.
- **parfeval**: asynchronous evaluation of a function.  $N$  “futures” are created and stored in a pile. When a worker is free, it takes the top-most future in the pile and executes it. When several workers are available, they run in parallel.

**parfor** is easier to implement but suffers from the fact that the jobs are pre-allocated to the

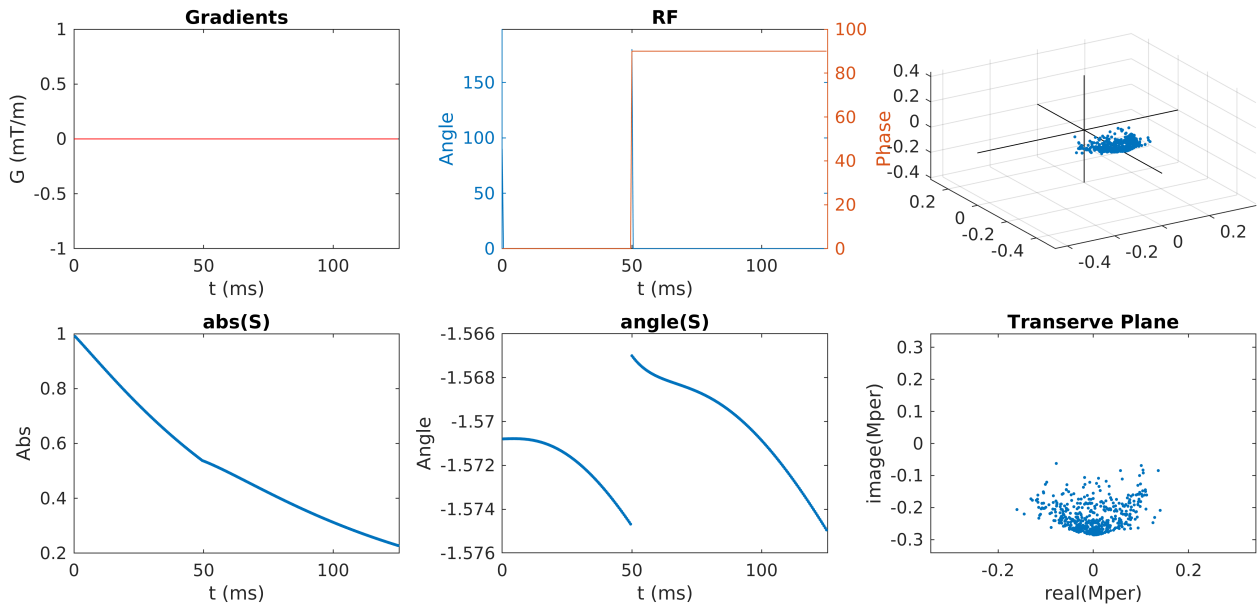


**Figure II.1.7:** Sequence, signal, and isochromats in real-time, from MRVox. The right-hand side column shows the state of the isochromats in the rotating frame, in 3D and 2D. On the two left-hand side columns, the top line represents a chronogram of the sequence; the bottom line the module and argument of the signal simulated.

workers, which do not communicate. The geometry generation step in MRVox (described below) takes a variable amount of time. It often happens that some workers finish all their jobs before others, and are thus idle for a long period of time. This is sub-optimal as the machine is not used at its maximum. It was frequently observed that all workers but one were idle.

The final choice was therefore to use `parfeval`. The workers all have access to the jobs pile. As long as there are more futures left than workers in the pool, all the available resources are used. This solution shortens the computation time and increases computer time efficiency. However, on large simulation tasks, e.g. more than a million jobs, the code started to lose performance. This slowdown was attributed to the cost of managing such a large pile of futures, keeping track of which are already completed or yet to be processed. The issue was discussed with the MathWorks support who confirmed the hypothesis. A simple solution could be to break down a one million simulation task into 10 batches of one hundred thousand simulations, which is easy to implement. A more robust solution could be to re-write the parallel part of MRVox to change the futures pile management, as suggested by MathWorks. However, this new implementation would require deep changes in the code and seem unnecessary compared to the little cost represented by running several smaller tasks one after the other.

It is up to the user to define a suitable parallel pool. It is possible to set the number of workers and the number of CPU cores per worker. Matlab being able to use multi-processing to perform matrix operations, it is more pertinent to set fewer workers with more cores each. Trials should be done on every machine to find optimal settings.

## 2D vessel network generation

As described in the original article (Pannetier et al. 2013), the user had to specify a blood volume fraction (BVf), mean radius (R), and a number of vessels to place N. The field of view (FOV) was then adapted to obtain

$$\text{FOV} = \sqrt{\frac{N\pi R^2}{\text{BVf}}} \quad (\text{II.1.15})$$

The BVf value was thus always precisely reached, and the FOV was variable. However, this method was quite impractical for our applications. Setting N by hand does not ensure realism. In addition, while the FOV was variable, the number of elements considered to discretize the 2D voxel was fixed. Two successive simulations with two different N were thus performed with different resolutions, which was not robust for accurate dictionary generation.

It was decided to consider equation II.1.15 with a fixed FOV, and to adapt N automatically (rounded to the closest integer):

$$N = \frac{\text{BVf} \cdot \text{FOV}^2}{\pi R^2} \quad (\text{II.1.16})$$

Doing so fixed the problems mentioned above but introduced a degree of freedom that can only take integer values. It is thus likely that some combinations of BVf and R can not be achieved for a certain FOV. Vessel geometries were generated in a  $250 \times 250 \mu\text{m}^2$  FOV for all the combinations of  $0 \leq \text{BVf} \leq 30\%$  and  $0 \leq R \leq 30 \mu\text{m}$  and checked for passed or failed cases. The result is presented in fig. II.1.8a. It can be seen that two failure modes exist, and

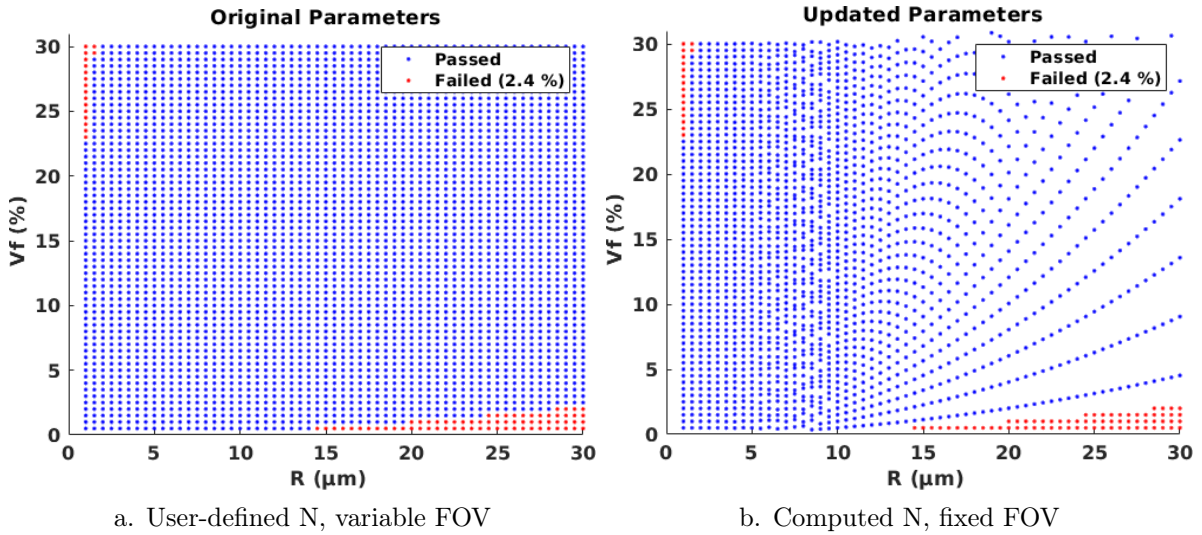


**Figure II.1.8:** Assessing the possible geometries with a fix FOV. a. Passed or failed geometry generation for user-input BVf and R combinations. b. Same results represented with their BVf value updated with eq. II.1.17

are purely based on geometrical constraints:

- In the top left corner, a large BVf with a small R means an extremely high number of vessels, which can not all be placed without overlapping.

- In the bottom right corner, the radius becomes too large and equation II.1.16 is rounded to 0, which is considered as a failed case.

However, this representation shows the user-input BVf and R, not what is actually achieved after computing the number of vessels and placing them. Fig. II.1.8b shows the exact same results after recomputing the BVf value actually reached. As expected, the rounding of N creates cases that can not be achieved, and curves of possible values appear. This means that the generated dictionary does not exactly correspond to the user input. The parameter table must be updated after dictionary generation to account for this BVf modification.

To have the most accurate value when computing the new BVf, it was preferred to use the discrete representation of vessels used by MRVox rather than equation II.1.16. It consists of a square matrix  $\mathbf{P}$  of  $M \times M$  elements. Intravascular space is represented with ones, extravascular space with zeros. The BVf is thus obtained through

$$\text{BVf}_{\text{updated}} = \frac{\sum \mathbf{P}}{M^2} \quad (\text{II.1.17})$$

### II.1.2.2 MRVox3D

#### 2D to 3D

The 2D version of MRVox is inherently limited by the fact that it can only consider vessels in a single plane. No magnetic field perturbation from vessels outside of the plane can be considered. This lack of realism could be a limitation to the precision of MRvF. A 3D version of MRVox was therefore developed.

In MRVox3D, the simulated voxel is now a 3D matrix, whose dimensions can be controlled on the 3 axis. The resolution of the sub-elements inside the voxel is isotropic, and the number of elements needs to be even in the three dimensions. The  $B_0$  field can be given arbitrary orientations with respect to the voxel.

Vessels are generated as straight cylinders, iteratively placed in the voxel to avoid collisions. They can be isotropically oriented, or have a preferential orientation, either perfectly parallel or not. Their radii can be distributed on a uniform or gaussian distribution. The  $\text{SO}_2$  values can be distinct from one to the other to emulate arterial and venous blood. Fig. II.1.9 shows examples of 3D voxels with different vessel configurations and  $\text{SO}_2$  distributions. The BVf is recomputed after geometry generation, as for the 2D version. The mean radius is computed based on what was generated. The  $\text{SO}_2$  is computed as an average weighted by the volume of the vessels.

The display interface was also renewed for more clarity, see fig. II.1.10. A first panel shows the 3D geometry of the voxel and its oxygenation. A second panel shows 2D maps of the central slice. The geometry in that slice is shown, as well as the magnetic field perturbations and contrast agent concentration. As before, the three components of the magnetization are shown. The lower left panel displays the sequence while it is simulated, showing successive pulses' amplitudes and phases, gradient lobes, and CA injection. The last panel shows the magnitude and the phase of the signal being simulated, with a 3D view of isochromats in the reference frame.

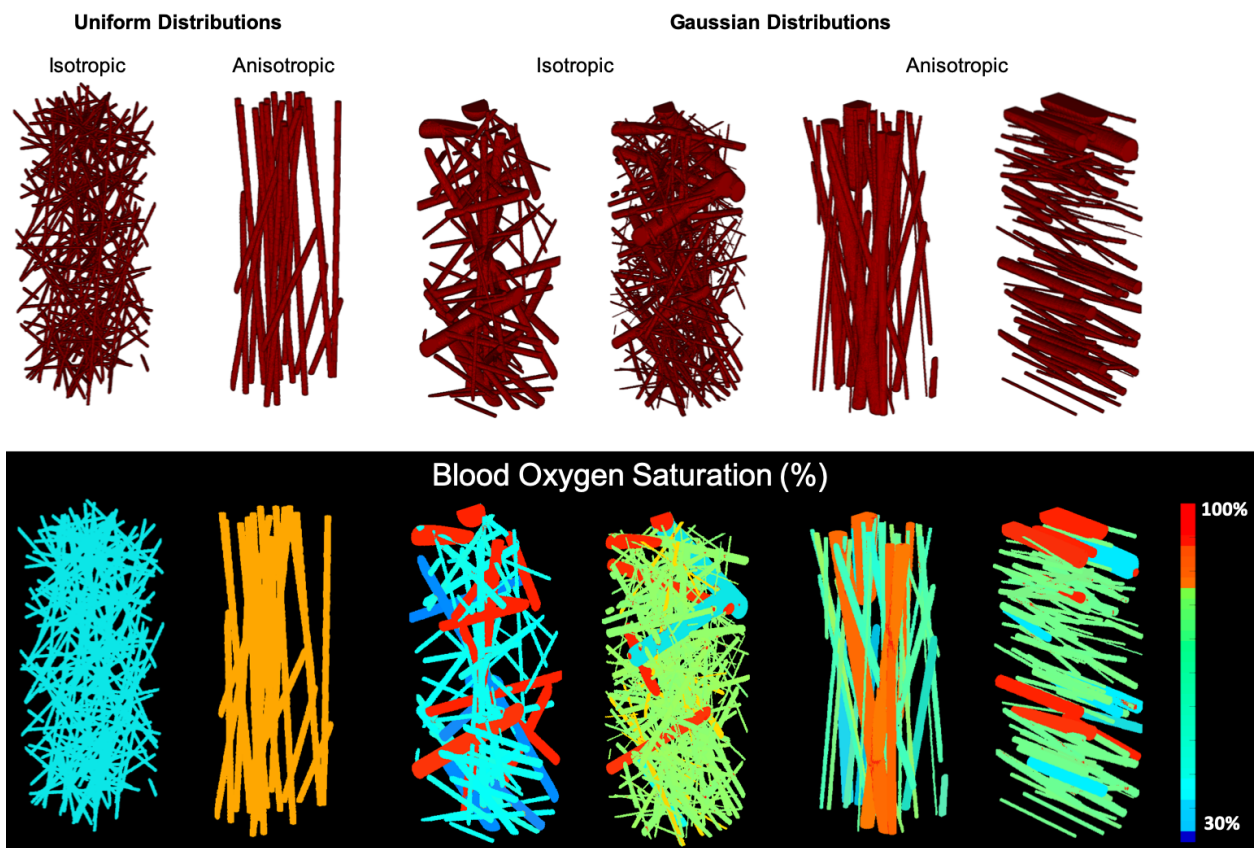


**Figure II.1.9:** 3D vascular geometries generated by MRVox3D. Vessels can have isotropic or preferential orientations. Their radii can have a gaussian distribution, and the  $SO_2$  can vary from one to another.



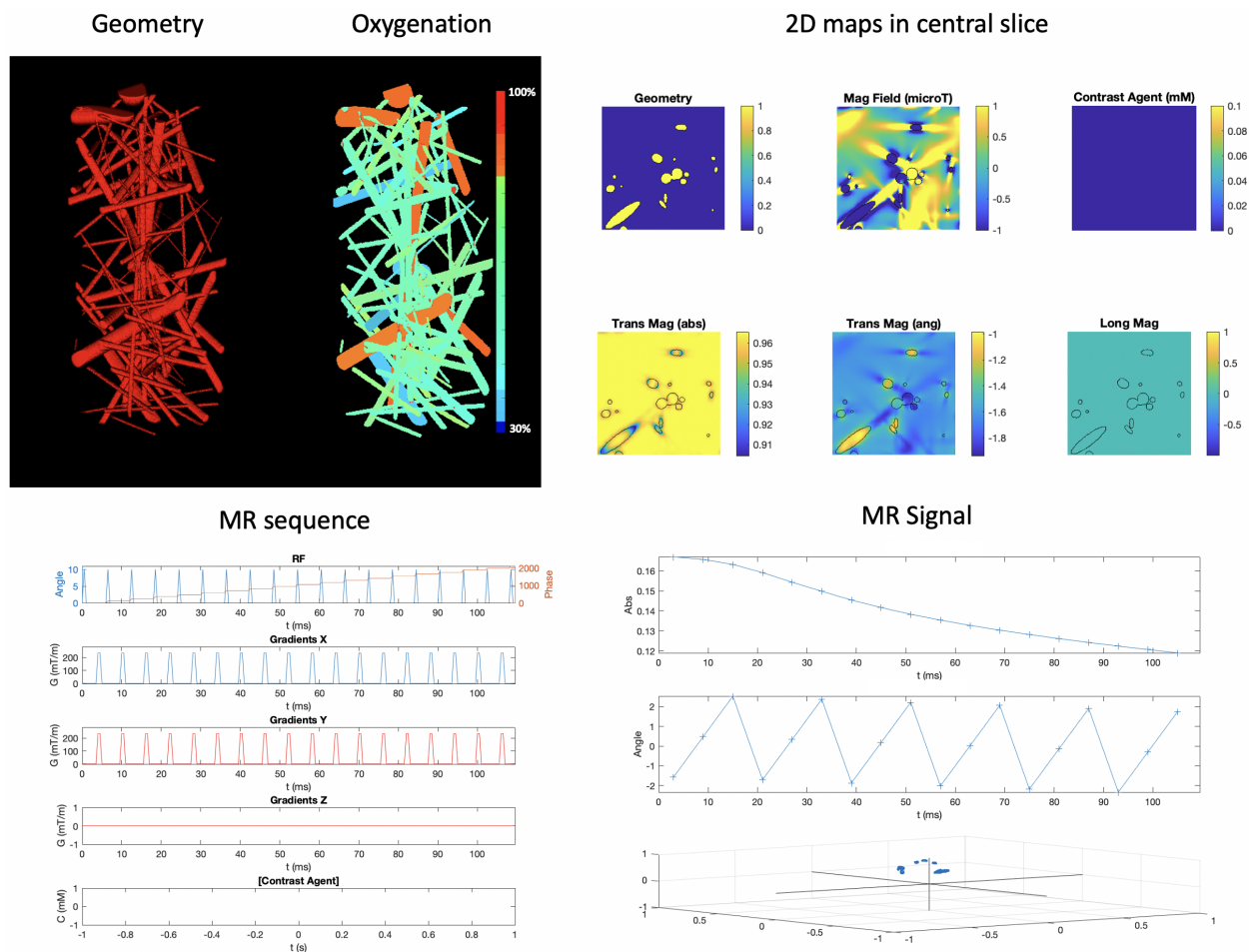
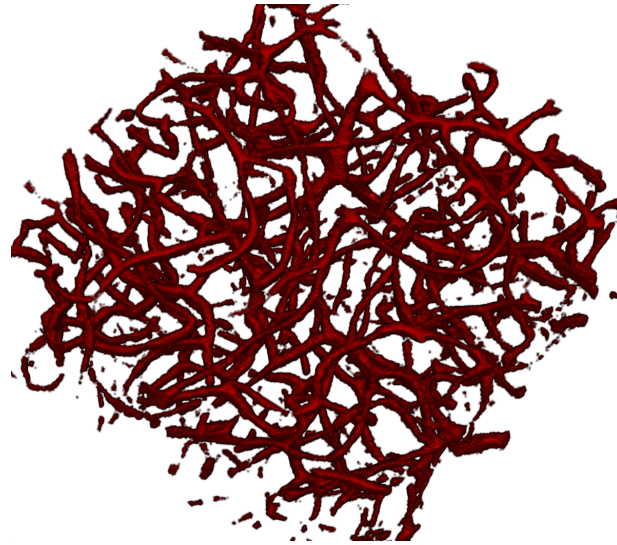


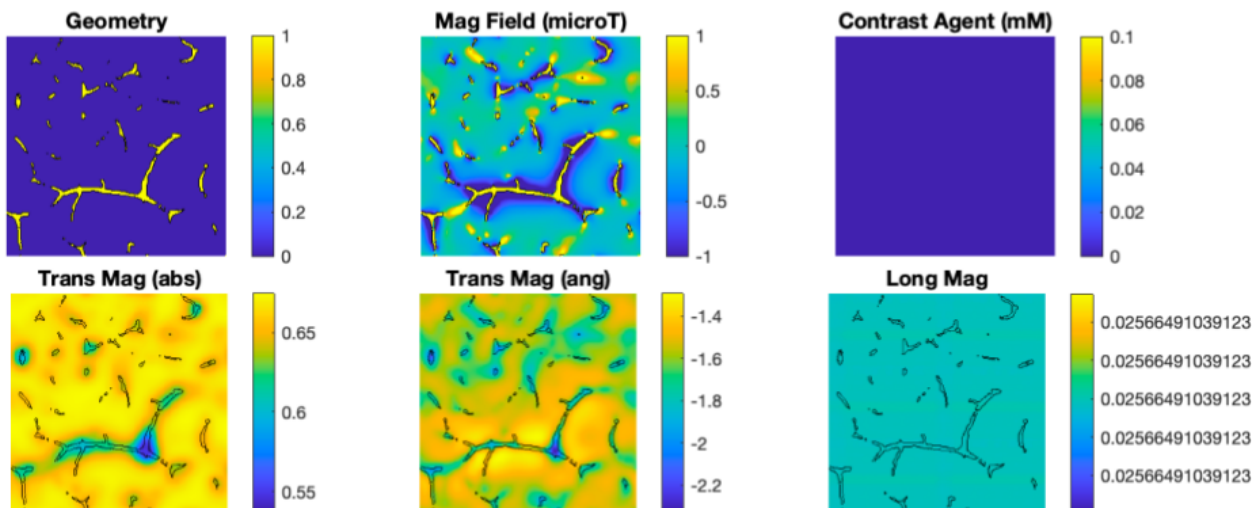
**Figure II.1.10:** Graphical outputs from MRVox3D. Upper left shows the geometry generated and its oxygenation. Upper right shows maps on the central slice of the voxel. Lower left is the sequence pulses, gradients, and CA injection. Lower right shows the simulated signal's amplitude and phase, as well as isochromats in the reference frame.

### External geometry importation

External geometries can be loaded into MRVox3D instead of generating one from scratch. A 3D volume, representing the vascular network as a binary matrix, is loaded and dimensions are given by the user. It is thus important to carefully prepare the volume and indicate the dimensions in order to reach a proper resolution. Examples of such geometries are given in fig. II.1.11 and III.1.2. The loaded geometry must be characterized to measure  $R$ . The BVf value is computed as before and only one global  $SO_2$  value can be given to the vascular network. Such geometry import is at the core of section III.1.



a. 3D geometry from 2-photon microscopy



b. Magnetization components and field perturbation computed in the central slice

**Figure II.1.11:** Example of geometry imported in MRVox3D. a. shows an example of 3D voxel segmented from 2-photon microscopy loaded by MRVox3D. b. shows the computed maps for the central slice of the voxel. The field perturbations are correctly computed, as well as the magnetization components. No contrast agent was used here.

### II.1.3 Validation of the tools

The following section presents the experiments run to validate all our simulation tools. The Bloch, EPG, and MRVox tools were validated against each other by comparing the results from the same experiments. Theoretical models were also used to validate some of the simulated effects.

#### II.1.3.1 Cross-validation on relaxometry experiments

In order to validate the methods against each other, we generated dictionaries based on relaxometry effects using either the direct Bloch or EPG simulations, or with MRVox with plain voxels. When not specified, the Bloch method was used with 1000 spins and the 2D version of MRVox with a voxel resolution of 256x256.

#### Balanced steady-state

The easiest sequence type to simulate is a balanced steady-state free-precession or bSSFP. It consists in a regular succession of RF pulses of constant FA separated by a constant repetition time. The signal is acquired at a constant time TE after the pulse. An illustration of such a sequence is proposed in fig. II.1.12. The sequence is called “balanced” as the integral of the

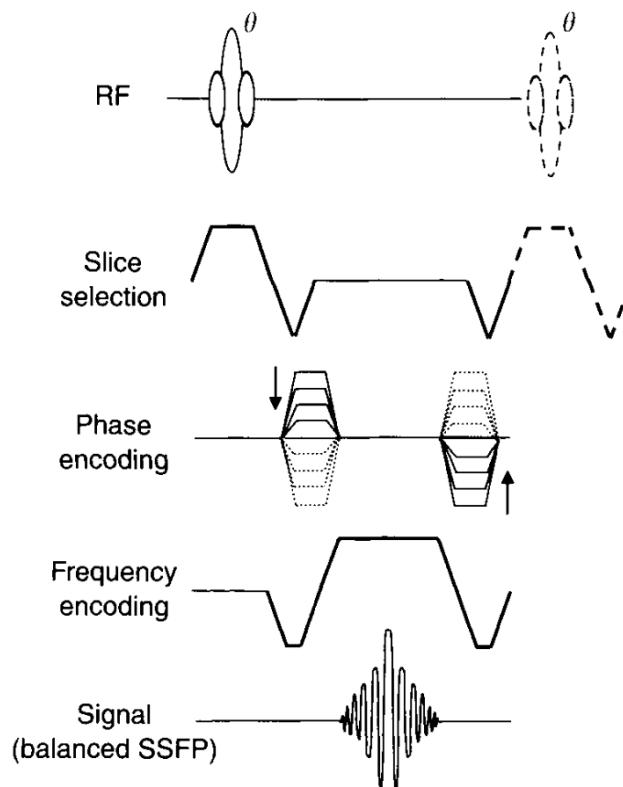


**Figure II.1.12:** Chronogram of a bSSFP sequence, from [Bernstein et al. 2004](#).  $\Theta$  is the flip-angle.

gradients applied in each direction is null and the sequence induces no dephasing. Fixing FA, TE, and TR, a bSSFP sequence can be simulated on a voxel with parameters  $T_1$  and  $T_2$ , with the three methods. An example of the generated signals is given in fig. II.1.13. The



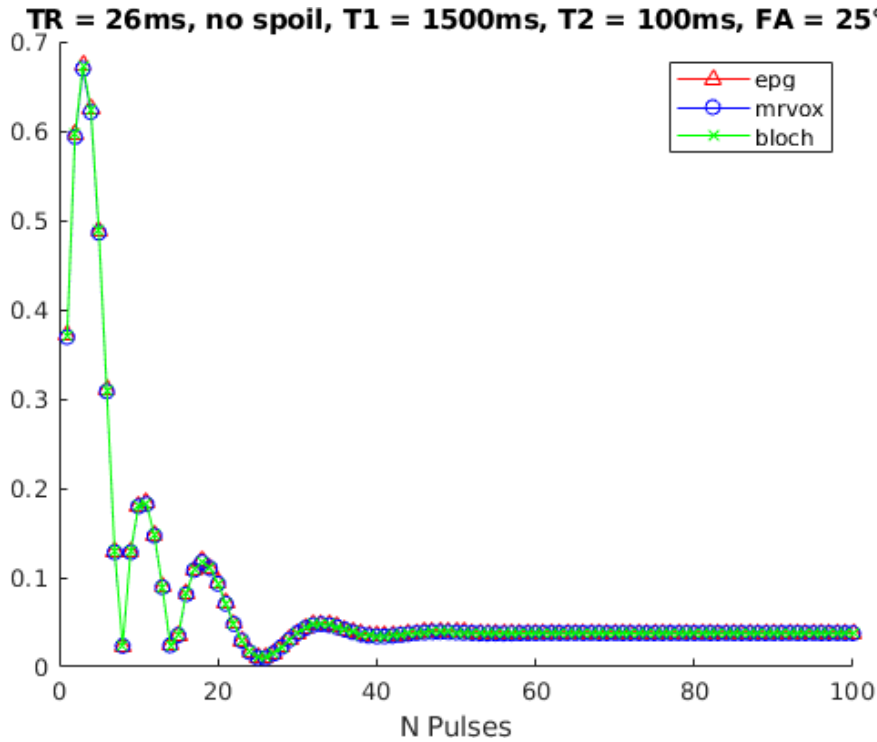


**Figure II.1.13:** Comparison of the 3 simulation methods for a bSSFP sequence.  $T_1 = 1500\text{ms}$ ,  $T_2 = 100\text{ms}$ ,  $\text{FA} = 25^\circ$ ,  $\text{TR} = 26\text{ms}$ ,  $\text{TE} = \text{TR}/2$

agreement between the three methods is visually very good. This type of experiment was conducted for several values of FA and TR, and for ranges of  $T_1$  and  $T_2$ . In each case, the relative error was computed for each pair of methods (EPG vs. Bloch, EPG vs. MRVox, MRVox vs. Bloch). Fig. II.1.14 shows the results from these repeated experiments. The relative error between the methods is globally low across the parameter space. Signal by signal investigation shows that cases where the error rises correspond to cancellation of the signal. The relative error gets higher but the amplitude is almost null.

### Gradient Spoiling

The same experiments were also done for spoiled steady-state sequences. They were similar to the bSSFP with the addition of a spoiling gradient, either before or after the acquisition. These sequences are usually called an FID- or Echo- spoiling type, as shown in fig. II.1.15. These spoiling gradients are used to intently remove all coherence in the transverse magnetization before or after a pulse. They can be used to avoid unwanted echoes or banding artifacts. In EPG, the presence of gradients changes the order of the  $\tilde{F}$  states. For Bloch and MRVox, a gradient amplitude  $G$  and duration  $\tau$  have to be computed to correspond to a  $2\pi$  dephasing across a voxel of size FOV:

$$G = \frac{2\pi}{\gamma\tau \cdot \text{FOV}} \quad (\text{II.1.18})$$

Fig. II.1.16 shows the agreement between the three methods for the FID and Echo types of spoiling. The presence of gradients does not seem to change the error between the methods. As for the bSSFP case, fig. II.1.17 shows the maximum relative errors computed for several sequences on a range of  $T_1$  and  $T_2$ , for the FID spoiling. The error is low for this case as well,

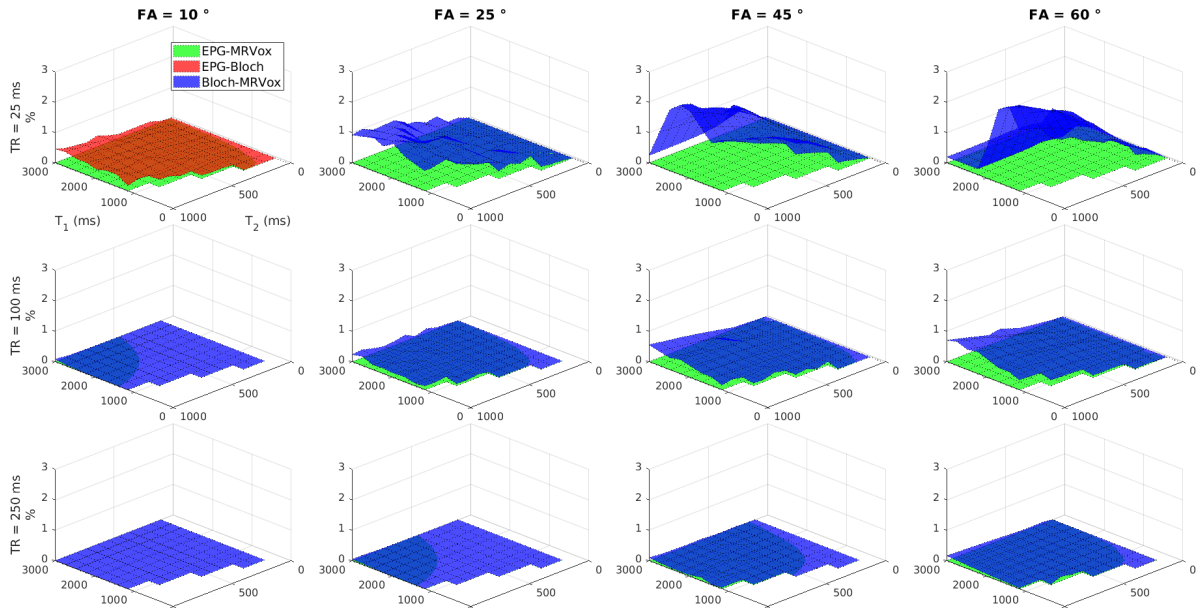


**Figure II.1.14:** Maximum relative error between the different simulation methods for bSSFP acquisitions, for different TR and FA combinations and large ranges of  $T_1$  and  $T_2$

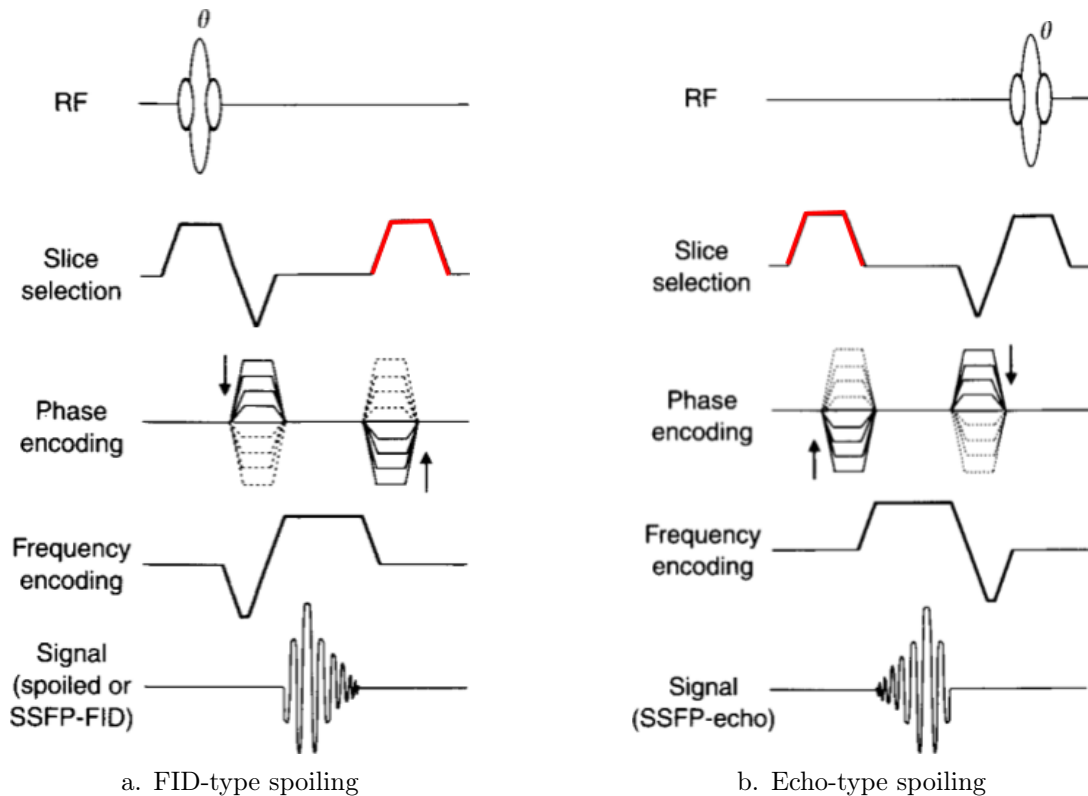


**Figure II.1.15:** Chronograms of the FID- and Echo-type of gradient spoiling strategies. Note the different positions of the spoiler on the slice selection gradient (in red), with respect to the signal. Adapted from [Bernstein et al. 2004](#).

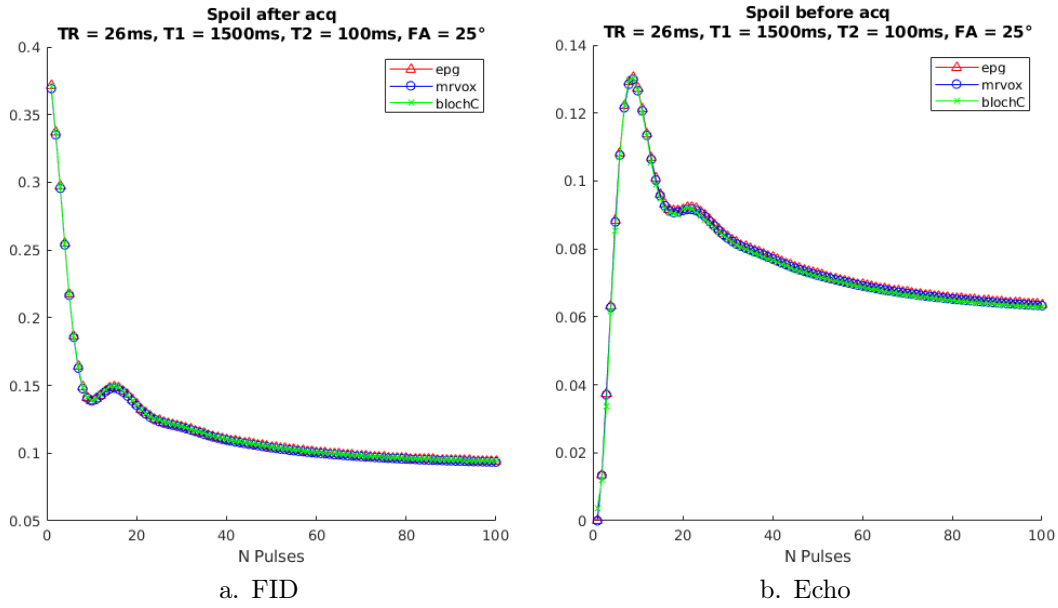


**Figure II.1.16:** Comparison of the 3 simulation methods for different types of gradient spoiling.  $T_1 = 1500\text{ms}$ ,  $T_2 = 100\text{ms}$ ,  $FA = 25^\circ$ ,  $TR = 26\text{ms}$ ,  $TE = TR/2$

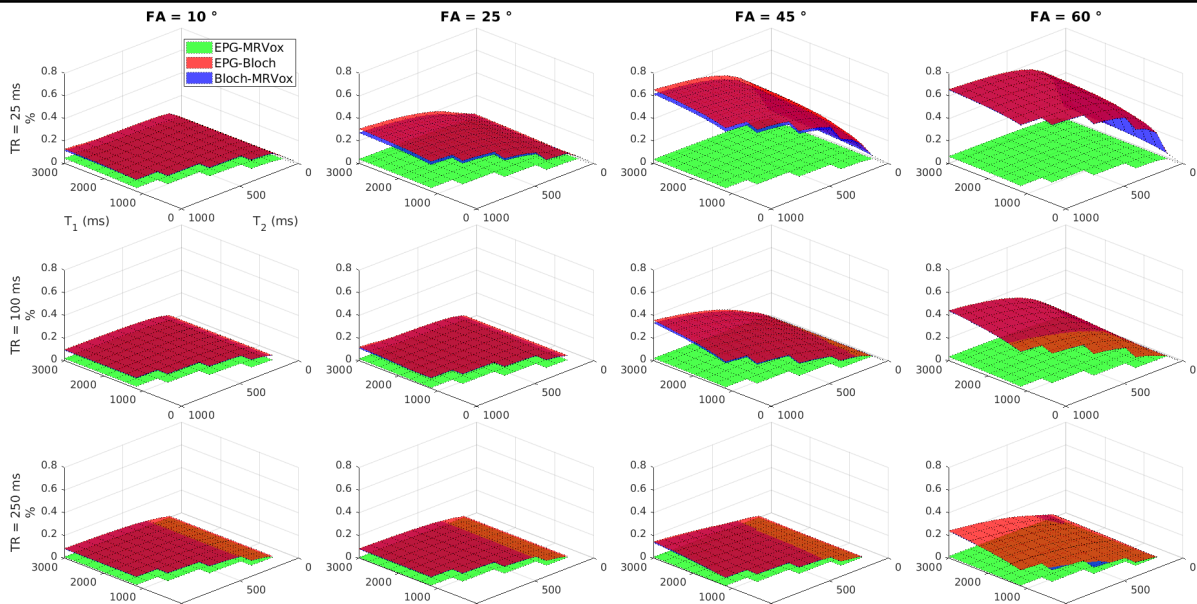


**Figure II.1.17:** Maximum relative error between the different simulation methods for FID acquisitions, for different TR and FA combinations and large ranges of  $T_1$  and  $T_2$

and higher errors are also associated with signal cancellation. Similar results were obtained for the Echo-type spoiling, and are not shown here.

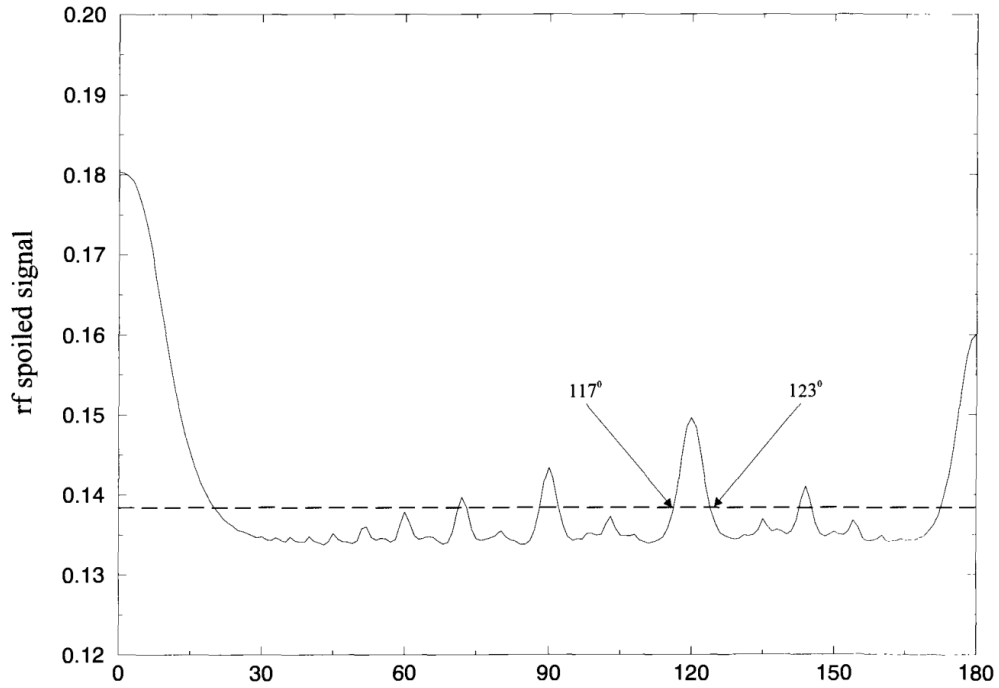
### RF spoiling

The bSSFP experiment validated that the pulses were correctly applied, yet it was conducted without changing their phase. To assess the accuracy of the pulse phase simulations, RF spoiling was performed with our tools. The phase of the pulse was varied according to a

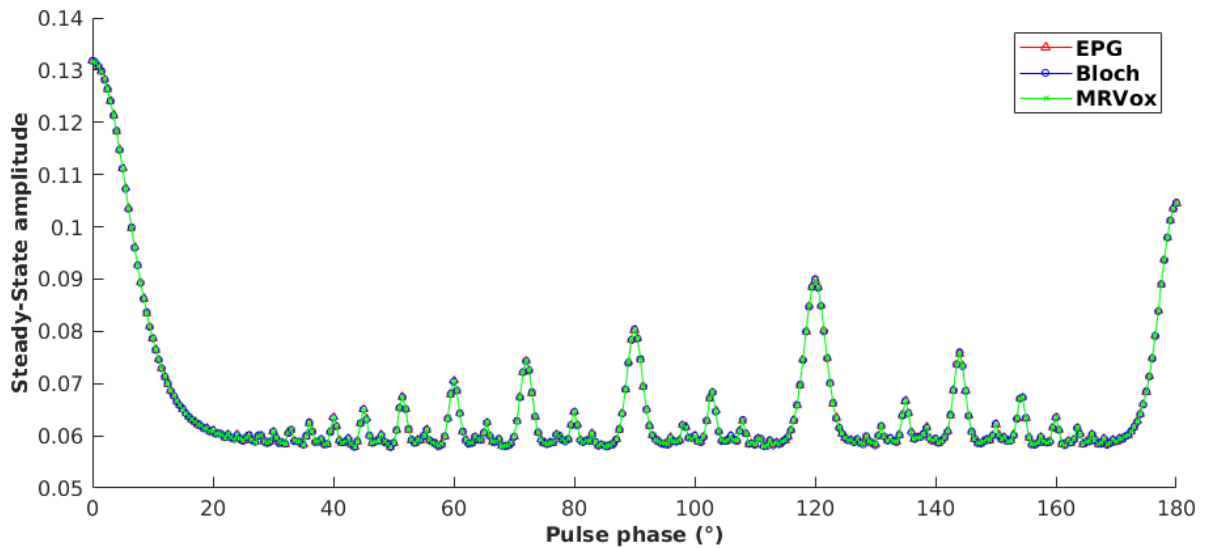
classical quadratic scheme (Zur et al. 1991; Bernstein et al. 2004):

$$\Phi_j = \frac{1}{2}\Phi_0(j^2 + j + 2) \tag{II.1.19}$$

where  $\Phi_j$  is the phase of pulse number  $j = 0, 1, 2\dots$  and  $\Phi_0$  the phase increment. A classical figure shows the level of the steady state reached for this phase cycling as a function of  $\Phi_0$ . This figure was reproduced with our tools, in fig. II.1.18. The agreement between the three



a. From Haacke et al. 1999



b. Simulated with our tools

**Figure II.1.18:** RF spoiled signal vs. quadratic phase increment

curves is good and the curve shape corresponds to the theoretical expectations.

### Bloch isochromats

The previous experiment was also used to assess the influence of the number of isochromats when running Bloch simulations. Fig. II.1.19 shows the relative error on the steady-state level between the methods for different numbers of isochromats in the simulation. Note the excellent agreement of EPG and MRVox. The dependence of the error on the number of isochromats is clear, and further exhibits the interest in the EPG framework. For further work, when using Bloch simulations, 1000 isochromats were used to minimize potential errors at the expense of increased simulation cost.

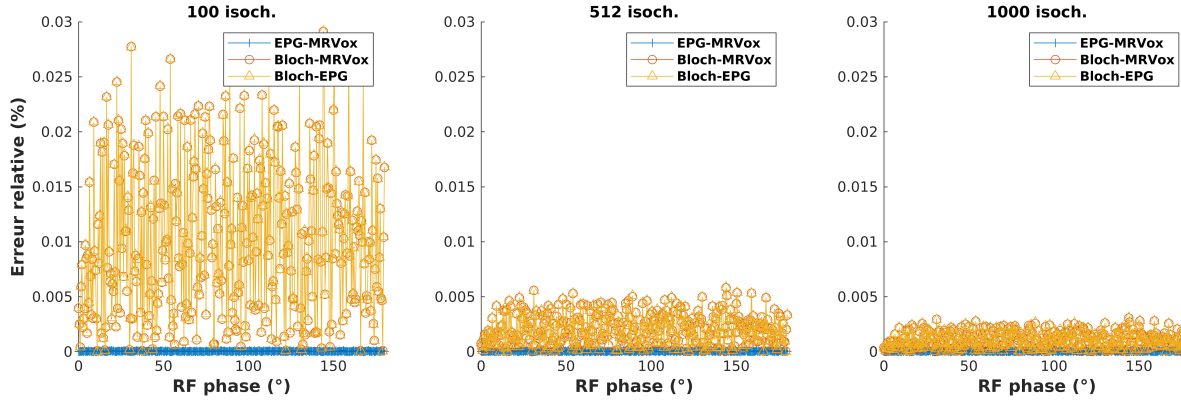


**Figure II.1.19:** Relative error between methods for 100, 512, and 1024 isochromats considered in Bloch simulation

These experiments validated the three tools against each other on rather simple cases of plain, homogeneous voxels. We concluded that the EPG and Bloch methods could be used to generate dictionaries suited for relaxometry-based MRF experiments.

#### II.1.3.2 Validation of MRVox against theoretical models

MRVox needs to be tested for cases where voxel inhomogeneity is expected to contribute to the signal. In order to validate our tools, we conducted experiments on BOLD effects similar to the ones originally presented in [Boxerman et al. 1995](#). Blood vessels with various radii and homogeneous magnetic susceptibility are randomly positioned in the voxel and the signal is computed at a particular echo time in both Gradient echo and Spin echo sequences. The presence of deoxyhemoglobin inside the vascular compartment of a voxel is expected to create magnetic field inhomogeneities. Subsequent changes in the transverse relaxation rates  $T_2$  and  $T_2^*$  are expected to depend on the vessel size. However, for a given blood oxygenation, the variations of  $T_2$  and  $T_2^*$  with R are expected to differ due to the effect of water diffusion. Simply put, the gradient echo behavior is expected to first increase during a “diffusion narrowing” regime and plateau when the radii are large enough (static dephasing regime). The spin echo behavior is more complex with an increase followed by a decrease. The external magnetic field amplitude, vascular magnetic susceptibility, and diffusion coefficient will tend to shift the curves but the global behavior generally follows these trends.

Following the work done by [Dickson et al. 2011](#), we also compared our simulation results to those obtained from several independent mathematical models of the BOLD effect. All these

models make assumptions about the imaged voxels and are usually valid only in specific regimes of the curves.

### MRVox2D

Simulations of a voxel with a given BVf and a  $\Delta\chi$  corresponding to the presence of deoxyhaemoglobin inside the vessels were performed. The relaxation rates are interpreted as

$$\Delta R = \frac{-\log S(TE)}{TE} \quad (\text{II.1.20})$$

for both gradient and spin echo sequences. The simulations were repeated 10 times each, with a varying vessel radius  $R$ . Fig. II.1.20 shows the relaxation rates as a function of  $R$ , compared to models listed in Dickson et al. 2011.

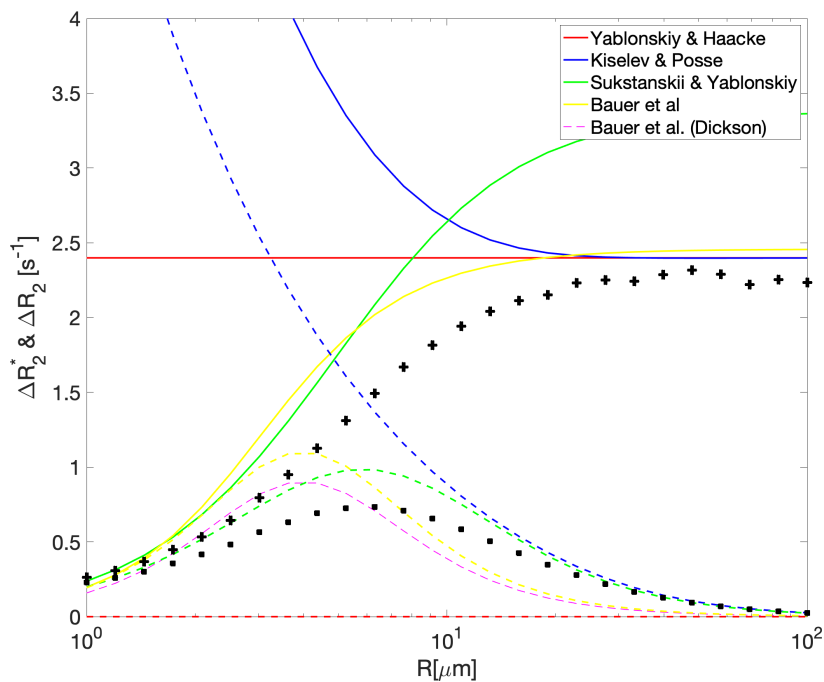


**Figure II.1.20:**  $\Delta R_2$  and  $\Delta R_2^*$  changes observed with  $R$  variation for a given  $\Delta\chi$ . Comparison of MRVox2D and models listed in Dickson et al. 2011. Dashed lines correspond to the spin echo and solid lines to the gradient echo. Black crosses correspond to the MRVox-simulated gradient echo, squares to the spin echo. Experiments were repeated 10 times and averaged. Vertical bars representing standard deviation across the repetitions are too small to be seen.

It can be seen that MRVox2D follows the general expected trends for both relaxation rates. Almost no deviation is observed on the 10 repetitions of the experiment and the values seem to agree with the different models in the static dephasing regime (large vessel radii). However, it does not precisely match any of the models in the diffusion narrowing regime. A possible explanation for this discrepancy might be that the combination of the 3 axes in our 2D experiments (see section II.1.2.1) does not match the assumptions made to derive the mathematical models.

## MRVox3D

The same comparison was conducted for the 3D version of the code. Fig. II.1.21 shows the results. This time, MRVox3D agrees with several of the mathematical models, especially for

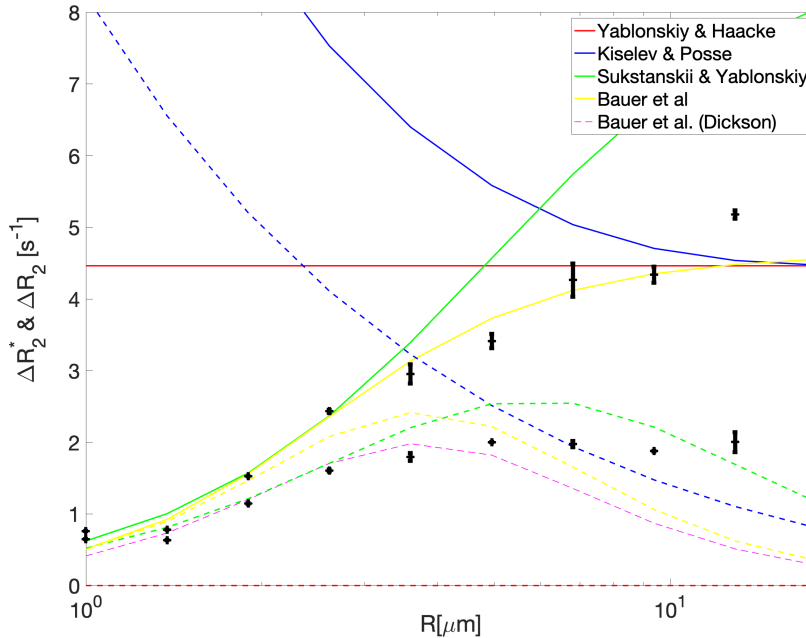


**Figure II.1.21:**  $\Delta R_2$  and  $\Delta R_2^*$  changes observed with  $R$  variation for a given  $\Delta\chi$ . Comparison of MRVox3D and models listed in Dickson et al. 2011. Dashed lines correspond to the spin echo and solid lines to the gradient echo. Results from MRVox are displayed as black crosses with vertical bars for standard deviation across 10 repetitions. Due to the long simulation time, the number of  $R$  values tested was reduced compared to the 2D experiment.

$R < 5\mu\text{m}$  in the spin echo case. This improved agreement between our results and theoretical models confirms that the development cost and increased computation time of the 3D version were worth it, as they seem to bring precision and realism. Note that the large error obtained for large vessels might be due to a low spatial resolution of the simulation for such large voxels.

## II.1.4 Conclusions and perspectives

### II.1.4.1 Classical MRF simulation tools

As presented above, a tool was developed to easily generate dictionaries based on classical MRF parameters. The tool is based on two different well-known simulation methods and has been extensively used for validation purposes. At this time, it has also been shared with the team of Pr. Nedergaard at Copenhagen University for MRF relaxometry experiments for the study of perivascular space. Future developments could involve finer effects implementation, such as slice profiles. It would also be interesting to only perform EPG simulations in a first time, and to account for other effects in a second time. Off-resonance frequency distributions could be modelled with weighted sums of signals, each simulated at a single off-resonance



frequency (as done in [Guo et al. 2020](#) and [Wang et al. 2019](#)). The possibility to model the effect of diffusion in the voxel through machine learning should be investigated.

#### II.1.4.2 MRVox

MRVox developments were done on both 2D and 3D versions and promising results have been obtained. In particular, the tool now allows for studying complex 3D vascular geometries and generating dictionaries for a large range of MR sequences.

The strength of MRVox is its ability to simulate MR signals coming from inhomogeneous 2D or 3D voxels. Yet, it implies sub-voxel scale resolution for all the computations which sometimes brings some limitations. For example, the use of a convolution of a kernel in a Fourier space requires isotropic sub-voxel resolution and an even number of elements in each dimension. It is thus important to carefully set up the voxel size. This is particularly true when loading an external geometry matrix, as its resolution is already set. The spatial and temporal resolutions also have notable impacts on the precision of the computations, especially when the vessel diameter reaches the simulation resolution.

MRVox certainly suffers from long computation times and might benefit from an implementation in a more efficient language than Matlab. However, it is the only tool of this kind and it has already been successfully used in the team for a number of published works ([Pannetier et al. 2013](#); [Christen et al. 2014b](#); [Lemasson et al. 2016](#); [Boux et al. 2021](#)). It has also been shared during this Ph.D. work with two partner laboratories. At UC Davis (CA, USA), Dr. Audrey Fan and her team intend to use the tool for MRvF studies aiming at measuring vessel wall stiffness to detect the onset of neurological disorders. In Leiden University Medical Center, Pr. Matthias Van Osch and his team use MRVox to follow contrast agent injection and tumor perfusion with MRvF.

## II.2 Pre-clinical MRF acquisitions

Our MR facility, IRMaGe ([irmage.univ-grenoble-alpes.fr](http://irmage.univ-grenoble-alpes.fr)), is equipped with 2 preclinical MRI scanners:

- a Bruker (Bruker Biospin, Ettlingen, Germany) 4.7T scanner, that uses Paravision (PV) 7.0.9, 660mT/m gradients, and multiple coils for rat and mouse imaging
- a Bruker 9.4T, that uses Paravision 7.0.0, 660mT/m gradients, multiple surface coils for multi-nuclear experiments, and a 1H cryoprobe for mouse head

At the beginning of our project, Bruker did not propose any MRF sequence for his scanners (it is still the case today). However, between 2015 and 2017, our lab had already started to implement an MRF module for Paravision 6 as part of a Ph.D. project, based on the Bruker spiral module. The next section introduces some of the work done on this existing pre-clinical acquisition tool.



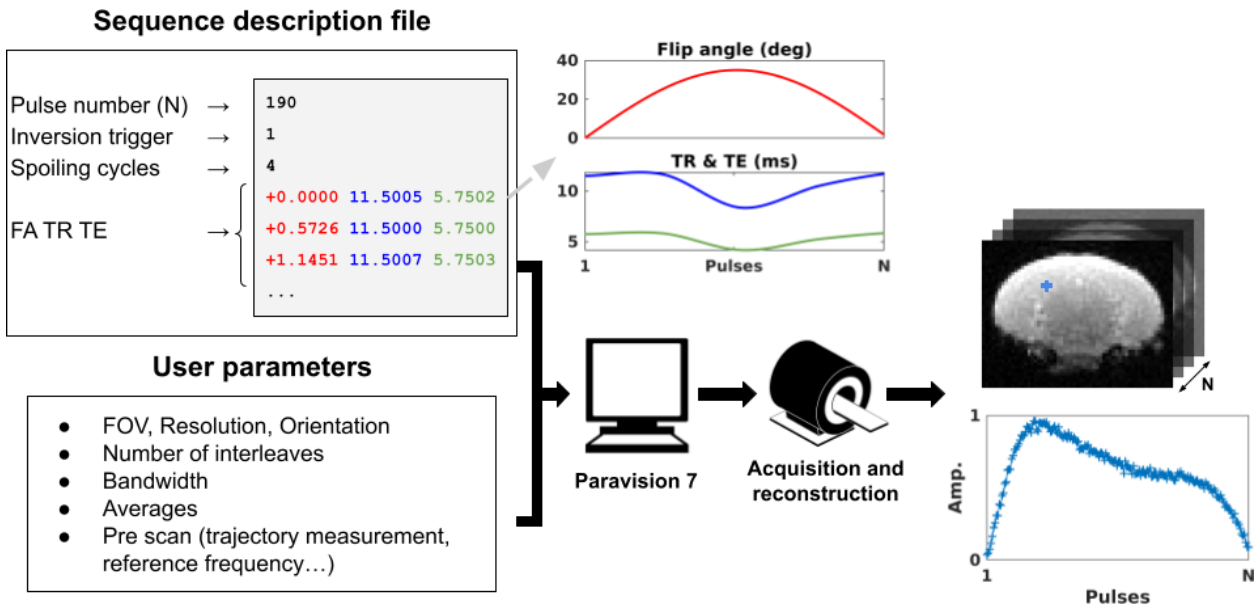


**Figure II.2.1:** Overview of the Bruker MRF Modules

## II.2.1 Overview of the existing acquisition tool

The working principle of the Bruker implementation is presented in fig. II.2.1.

The previous developments were made on PV6. The lab upgraded to PV7 at the beginning of the Ph.D. project. Very few changes were needed to transfer existing modules to PV7.

Using the existing MRF module, one can perform 2D acquisitions with variable FA, TE and TR. An inversion pulse before the sequence can be added. The spoiling intensity is given as a number of dephasing cycles across the FOV. Phase cycling is implemented by  $90^\circ$  steps. The desired sequence parameters are given as a text file as presented in fig. II.2.1.

At compilation time, the module calls a function that reads the path to the text file. The module can then be added to the scan protocol to tune the acquisition parameters. As for any sequence, the user has control over the FOV, the resolution and other usual parameters. A spiral k-space sampling is performed. When the TE and TR are not suited for a full sampling in a single spiral, the module requires to sample the k-space with several spiral interleaves. In that case, the sequence is acquired as many times as there are interleaves.

The module combines the interleaves to produce a single image per pulse in the sequence. Data are then stored under the proprietary Bruker format, but can also be obtained as Dicom files. In that cases, one Dicom file is produced per shot, e.g. a 1000 pulses sequence will produce 1000 Dicom files.

Two fingerprinting modules are coded, corresponding to the FID- and Echo-type SSFP illustrated in figure II.1.15.

### II.2.1.1 Tests and validations

**First images** For first validation tests, the modules were simply used with sequences consisting of repetitions of constant FA, TR and TE blocks. Spiral measurements on several interleaves were performed to assess the quality of the trajectories and validate the variation

of the number of interleaves. Fig. II.2.2 shows an example of a 4 interleaved trajectories. The trajectories were in line with expectations and the successive images were correctly

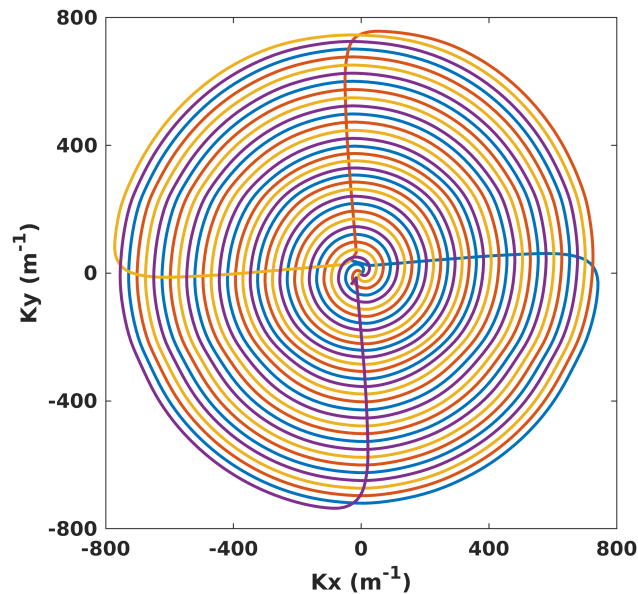
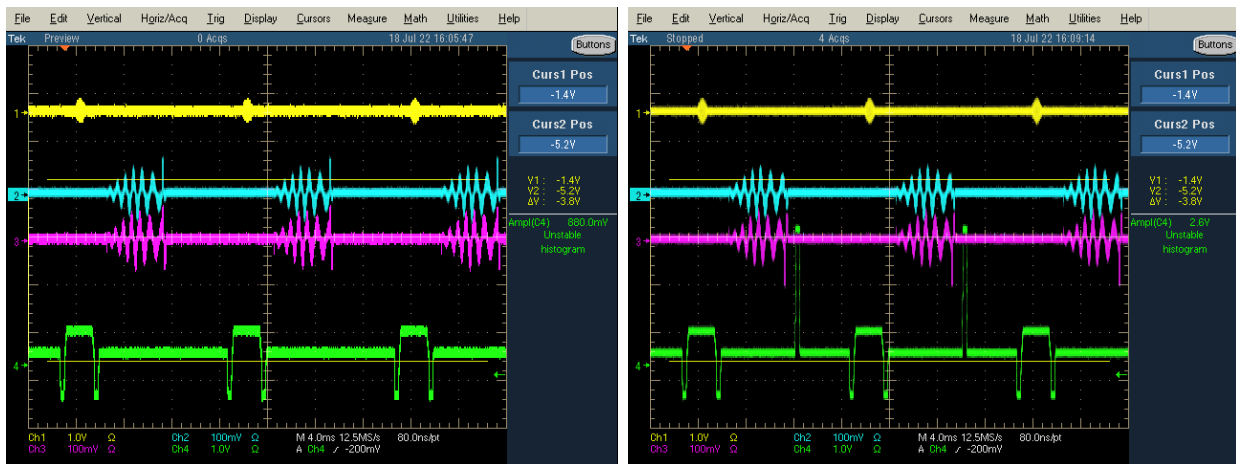


**Figure II.2.2:** Examples of 4 interleaved spiral trajectories measured on a 4.7T Bruker scanner. The interleaves expand from the center of the k-space, before being balanced, hence returning towards the center.

reconstructed as illustrated below.

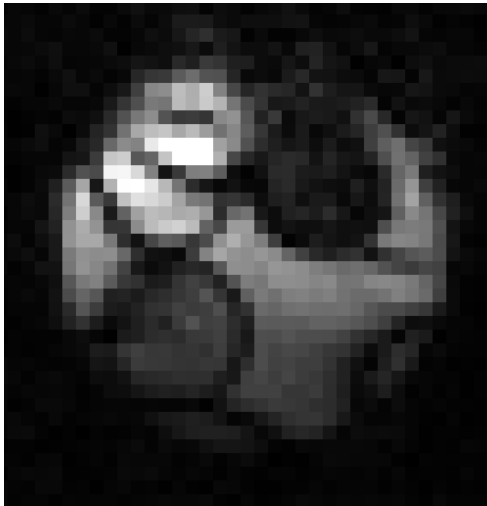
### Spoiling gradients

The gradient behaviour between spoiled and unspoiled acquisitions was then assessed. Fig. II.2.3 displays measured chronograms of a 12 dephasing cycles spoiled sequence and a 0 dephasing cycles balanced sequence. The images shown in fig. II.2.3c and II.2.3d correspond to acquisitions made with 0 and 4 spoiling cycles, respectively. Both of these acquisitions have a FOV of  $58 \times 58 \text{ mm}^2$ ,  $64 \times 64$  matrix,  $\text{FA} = 45^\circ$ ,  $\text{TR} = 25 \text{ ms}$ ,  $\text{TE} = \text{TR}/2$ . The object used is a 50ml plastic tube filled with water, containing 3 smaller tubes filled with different gadolinium concentrations to vary their relaxation times. It can be seen that a spoiling gradient is added when needed in the FID-type sequence (fig. II.2.3b) and that the acquisition is effectively unspoiled when set so (absence of spoiling gradient in fig. II.2.3a). Considering that the Bruker spiral trajectories accurately come back to the center of the k-space, the sequence would effectively be balanced. Furthermore, fig. II.2.3c displays expected banding artifacts from a balanced acquisition, which are not present in fig. II.2.3d. The integral of the spoiler gradient was not measured but several spoiling values were tested and no difference after 4 cycles were found (data not shown). It was thus decided to always use at least 4 cycles or more when possible.

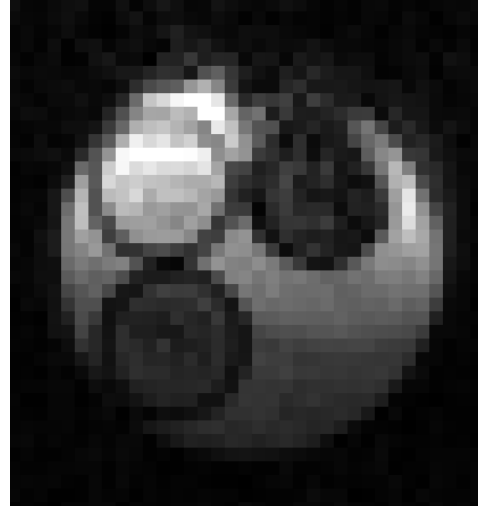


a. Chronogram for unspoiled acquisition

b. Chronogram for spoiled acquisition



c. Second echo from unspoiled acquisition (0 dephasing cycles)



d. Second echo from spoiled acquisition (4 dephasing cycles)

**Figure II.2.3:** Chronograms of acquisitions without and with spoiling, measured with a Tektronix (Tektronix, Beaverton (OR), USA) TDS 5054 oscilloscope. The spoiler can be seen in b. compared to a. on the slice selection gradient (green channel). c. shows the typical banding artifacts expected in a balanced acquisition, which are not present in d. Note that the chronograms do not correspond to that specific acquisition.

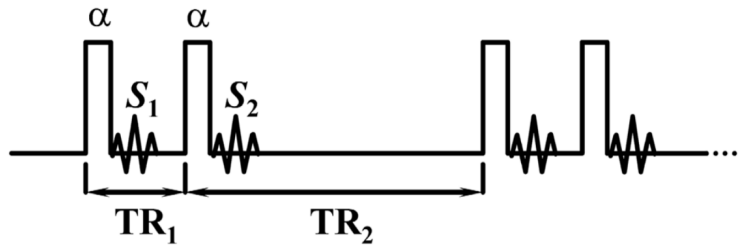
### Timing flexibility

The flexibility of the timing was tested with the FID module by implementing a 2D version of the Actual Flip angle Imaging (AFI) method from [Yarnykh 2007](#) to map  $B_1$ . This approach was chosen for its variable TR and because  $B_1$  is a parameter of interest in MRF. Acquisitions were performed on a stabilized rat brain obtained through the following protocol:

- Anesthesia with intra-peritoneal injection of pentobarbital, 200mg/kg for a rat
- Assess the animal's reflexes by pinching one of its paws
- Open its chest cavity
- Pierce left ventricle with the needle of a peristaltic pump
- Start pumping PBS in the animal's blood system
- Open right atrium to allow the blood and PBS to wash out
- Stop when the liver is decolorated

The animal is then decapitated and its whole skull is collected to preserve the shape of the brain. After removal of skin and muscles, it is placed in a syringe filled with Fomblin (FenS chemicals, Goes, Netherlands), an oil with a susceptibility close to that of tissues but that does not generate MR signal. The syringe set-up allows for easy removal of bubbles that can appear with gas release.

A sequence description file with 100 repetitions of an AFI acquisition scheme was written, i.e.  $TR_1/TR_2 = 15/75\text{ms}$ ,  $TE = 2\text{ms}$ , see chronogram in fig. [II.2.4a](#). Acquisition of a FOV  $35 \times 35\text{mm}^2$ ,  $64 \times 64$  matrix, 1.16mm slice thickness. The AFI scheme establishes a steady-state after a few pulses. One can then use the signals coming from a single  $TR_1/TR_2$  couple or on a mean of several of them. Doing so allows obtaining the  $B_1$  map shown in fig. [II.2.4b](#). A second  $B_1$  measurement was performed through a classical Variable Flip Angle ([Murphy-boesch et al. 1987](#); [Barker et al. 1998](#)) scheme. Results from both experiments and their relative error are presented in fig. [II.2.4](#). The  $B_1$  map obtained through the MRF-like measurement, although not perfect, is close enough to the one obtained through the VFA method. This confirms a correct application of variable timings inside a single sequence.



a. Chronogram of the AFI scheme, from Yarnykh 2007

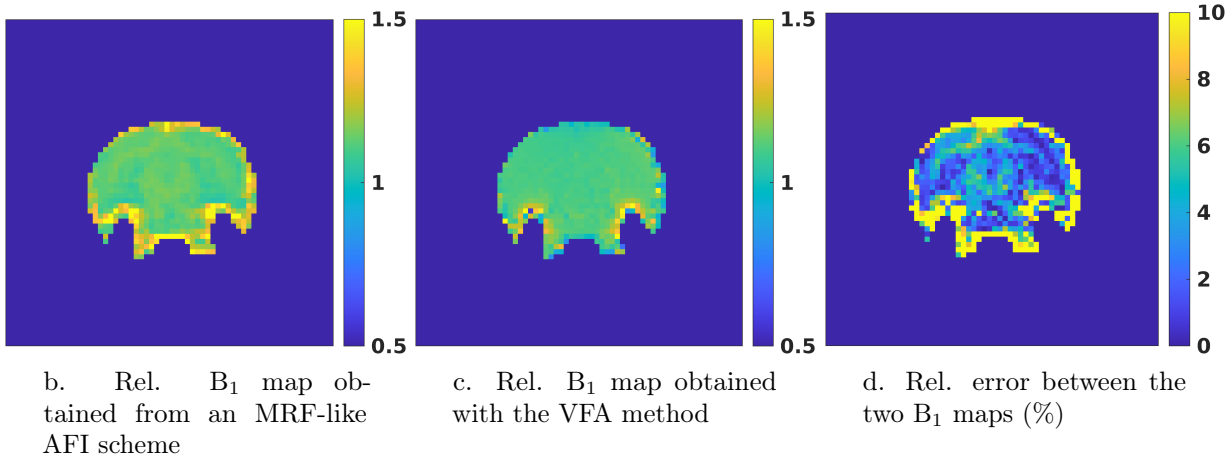
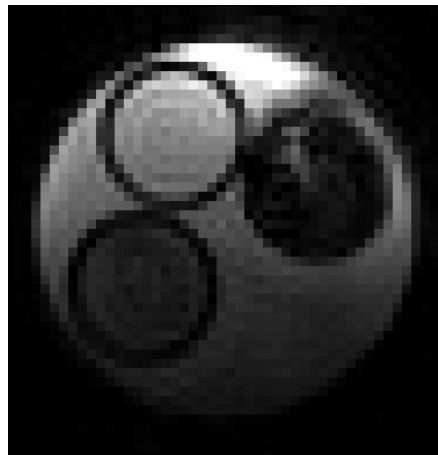


**Figure II.2.4:** Relative (measured/desired)  $B_1$  maps produced with different methods on a stabilized rat brain. a. presents the chronogram of an AFI scheme. The FID module was used to acquire such a sequence and the signals obtained were treated to produce the  $B_1$  map on panel b. Another  $B_1$  measurement method was used to produce the map on c., without using MRF modules. d. presents the relative difference between b. and c.

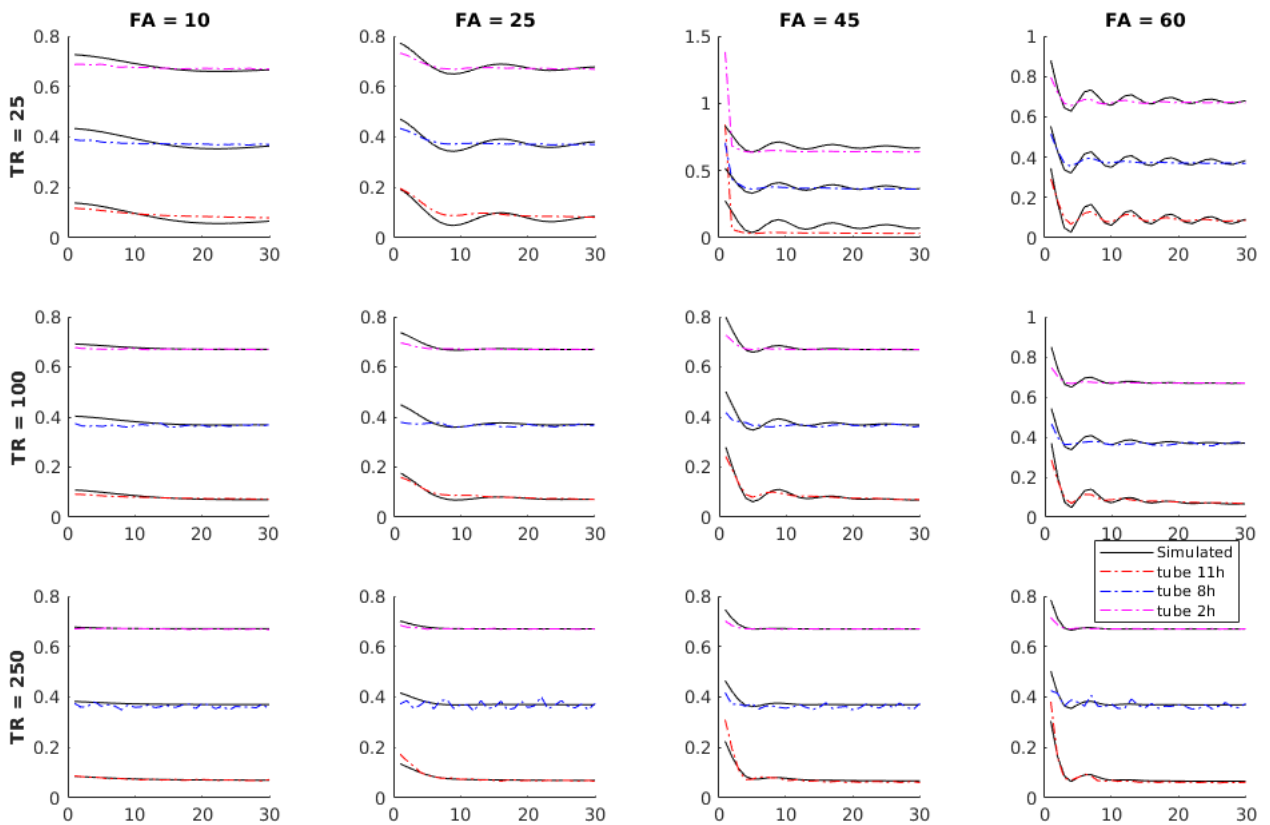
### Comparing acquisitions and simulations

Using the tube phantom described above, it is possible to see different signal evolutions from a single sequence due to the different gadolinium concentrations. MRF acquisitions with different TR ( $TE = TR/2$ ) and FA were performed on the phantom with the FID- and Echo-type modules. Image parameters are  $FOV = 62.5 \times 62.5$  mm, 1 mm slice thickness,  $64 \times 64$  matrix.  $T_1$  and  $T_2$  measurements were performed with reference methods (multi-inversion time and MSME, respectively). Using these relaxation values, simulations were made with the Bloch tool for all the sequences used. Fig. II.2.5 and II.2.6 show the mean signal in each small tube and the corresponding simulation for the FID and Echo module, respectively. The tubes are called by their clockwise position. The averaged signals are computed in each tube with a square  $8 \times 8$  ROI. Signals and simulations are L2-normalized for comparison purposes.

The agreement between the acquired signals and the simulations is overall not great. Low-frequency oscillations are generally well simulated but their amplitude does not match that of the acquisitions. We observed a capital sensitivity to the relaxation times (particularly  $T_1$ ) used in the simulation tool. Achieving a proper shim in such a phantom is also challenging. Air bubbles in the tubes were observed, and the phantom was placed to try and keep them as far from the imaging plane as possible. It is likely that  $B_1$  imperfections should also be



a. First echo for an FID-type sequence with  $TR = 25\text{ms}$ ,  $TE = 12.5\text{ms}$ ,  $FA = 25^\circ$



b. Agreement between simulations and mean in ROIs inside the smaller tubes of the phantom

**Figure II.2.5:** Examples of agreement between FID-type acquisitions and simulations. Signals are presented with an offset on the y-axis for sake of readability. FA in degrees and TR in ms.

accounted for, which was not the case in these simulations. The agreement is still correct in many cases, and mismatches can be attributed to inaccuracies in the simulations parameters. These experiments were thus encouraging and indicated that our modules are functioning

properly.

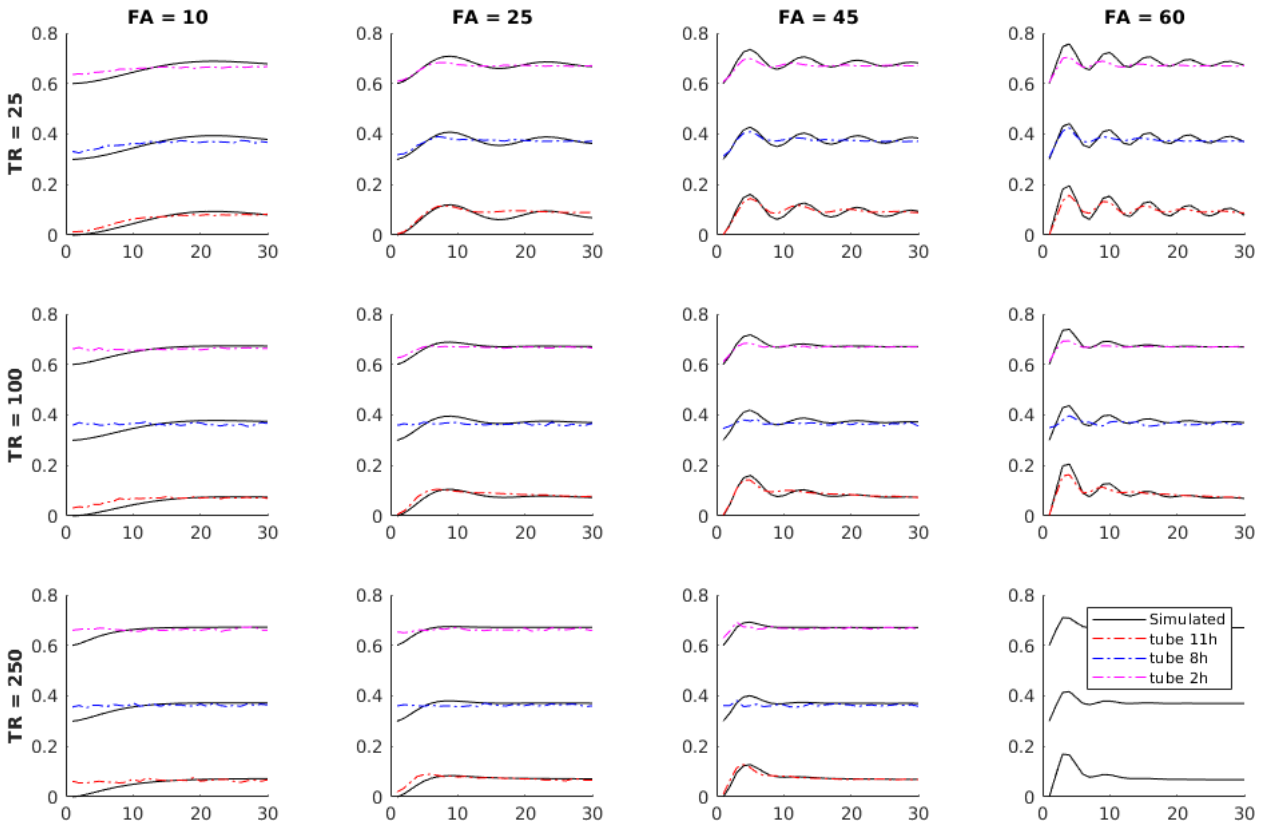


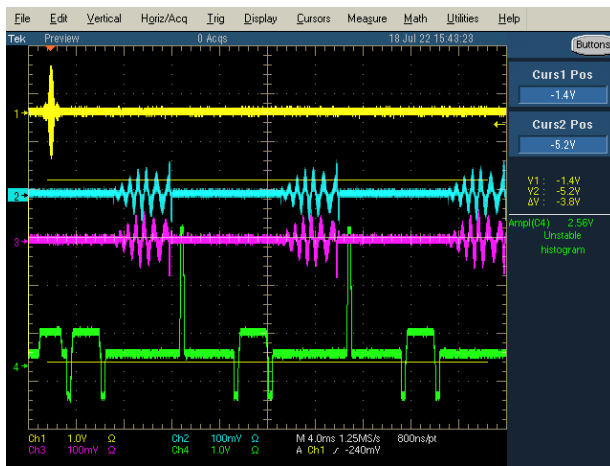
**Figure II.2.6:** Examples of agreement between Echo-type acquisitions and simulations. Signals are presented with an offset on the y-axis for sake of readability. FA in degrees and TR in ms.

## II.2.2 New developments

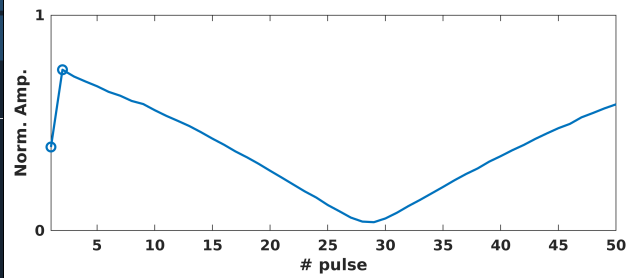
Our first tests suggested that our preclinical module was able to perform standard MRF acquisition with a good level of flexibility. In order to be able to perform MRvF experiments and more generally  $T_2^*$ -based MRF acquisitions, we improved the inversion pulse behavior and added new RF phase options.

### II.2.2.1 Improving inversion pulses

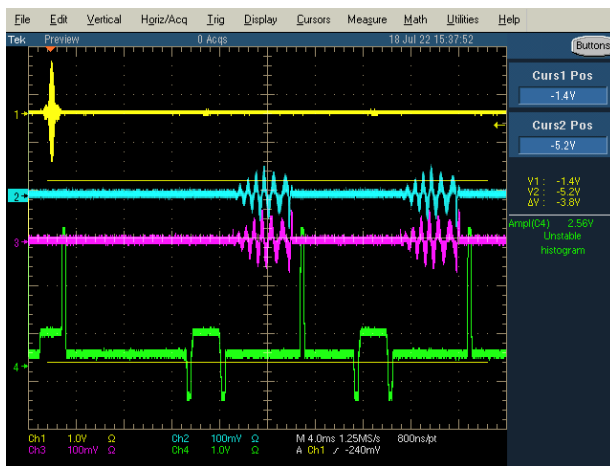
When testing an MRF sequence described in [Gómez et al. 2019](#) with an inversion pulse, it was observed that the first acquired point was systematically lower than the first one, which was not expected, see fig. [II.2.7b](#). Investigation revealed that the inversion time was always as short as possible in the module's pulse program, and that the inversion pulse was not spoiled, as displayed in the measured chronogram [II.2.7a](#). In consequence, we set up the inversion time to a longer value, corresponding to the sequence TR, and added a spoiler after the pulse (see fig. [II.2.7d](#)). The effect of these modifications is clearly visible in the signal in fig. [II.2.7c](#): the two first points follow the decreasing trend of that part of the curve. Experiments were conducted at 9.4T with a Bruker mouse cryoprobe, FOV  $22 \times 22 \text{mm}^2$ , 1.16mm slice thickness,  $96 \times 96$  matrix.



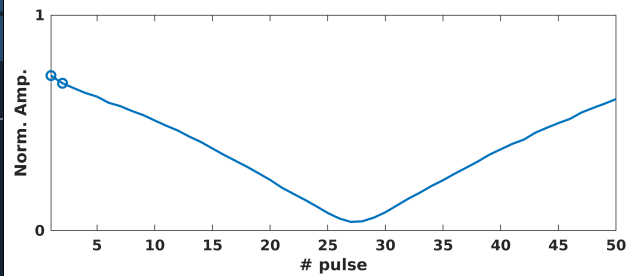
a. Chronogram with a short inversion time and no spoiling



b. Resulting signal from a stabilized mouse brain



c. Longer TI, with spoiler



d. Longer inversion time, spoiler

**Figure II.2.7:** Effects of the inversion time change and spoiling. The chronograms a. and c. show the RF pulses in yellow. Blue and pink are the spiral readouts and green is the slice selection gradient. In a., the inversion pulse and the first sequence pulse are about 3 ms apart, as indicated by the proximity of the two slice selection lobes. The resulting signal is shown in b. exhibits an unexpected signal trend for the first two points. c. shows that the inversion time was effectively increased to correspond to the sequence TR, and a spoiling gradient is visible on the slice selection channel. The resulting signal in d. has a monotonous trend on its first points as a result. A temporal shift of the signal cancellation can also be observed.

### II.2.2.2 $B_1$ phase

Several recent studies have proposed to use complex RF phase cycling to produce quantitative  $T_2^*$  maps with MRF sequences or to use for fMRI experiments (Wang et al. 2019; Guo et al. 2020; Boyacioglu et al. 2021). Because of the relationship between BOLD effect,  $T_2^*$ , and oxygenation, we decided to test these acquisitions for MRvF. To be able to reproduce the MRF patterns, the function reading the sequence description text file was modified to accept



the phase as an input for each pulse.

A first simple experiment was conducted to verify that phases were accounted for. A stabilized mouse brain was used at 9.4T. Two balanced acquisitions were performed, the first one without phase variation, the second one with a  $180^\circ$  increment in the phase for each pulse, starting at  $0^\circ$ . In both cases, the FOV was  $22 \times 22 \text{mm}^2$ ,  $96 \times 96$  matrix, and 1.16mm slice thickness. Fig. II.2.8 shows typical banding artifacts from a balanced sequence. It can be seen that the artifacts are reversed when incrementing each RF pulse phase by  $180^\circ$ .

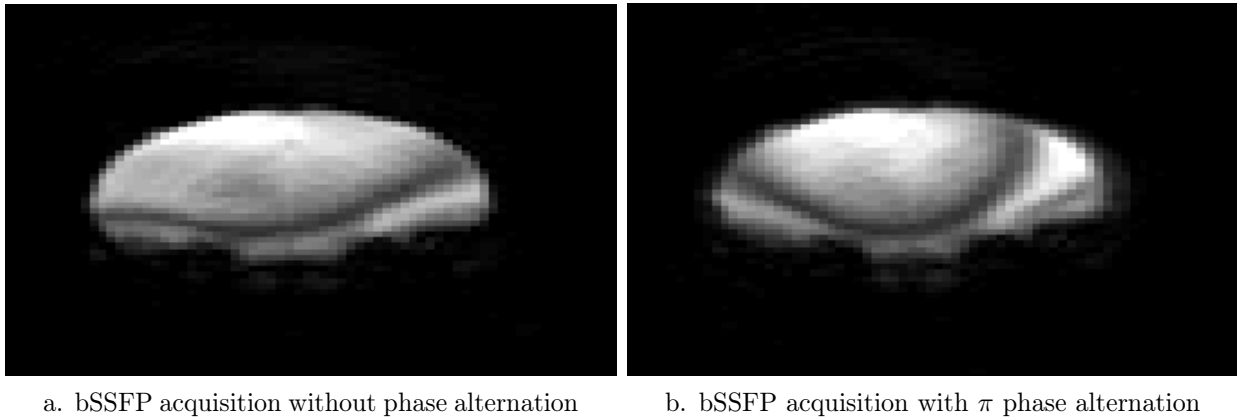


**Figure II.2.8:** Second echoes of two balanced SSFP acquisitions on a stabilized mouse brain at 9.4T,  $TR = 15\text{ms}$ ,  $FA = 15^\circ$ . The spatial variation of the banding artifacts between the two images indicates a phase variation.

A sequence with a more complex phase pattern was designed based on [Guo et al. 2020](#). It consists of 4 identical blocks separated by 1 second for magnetization recovery, each generating a transient state followed by a pseudo-steady state, which is achieved with RF phase cycling. Only the phase is varied: FA, TR, and TE are the same for all the pulses. The acquisition was performed at 4.7T on a healthy rat brain, FOV  $32 \times 32 \text{mm}^2$ ,  $64 \times 64$  matrix, 1.5mm slice thickness. The phase pattern is presented in fig. II.2.9a. The corresponding signal, averaged over the brain, is presented in fig. II.2.9b. It can be seen that the signal regularly oscillates when the phase is varied, which suggests the correct application of the phases specified in the sequence description file.

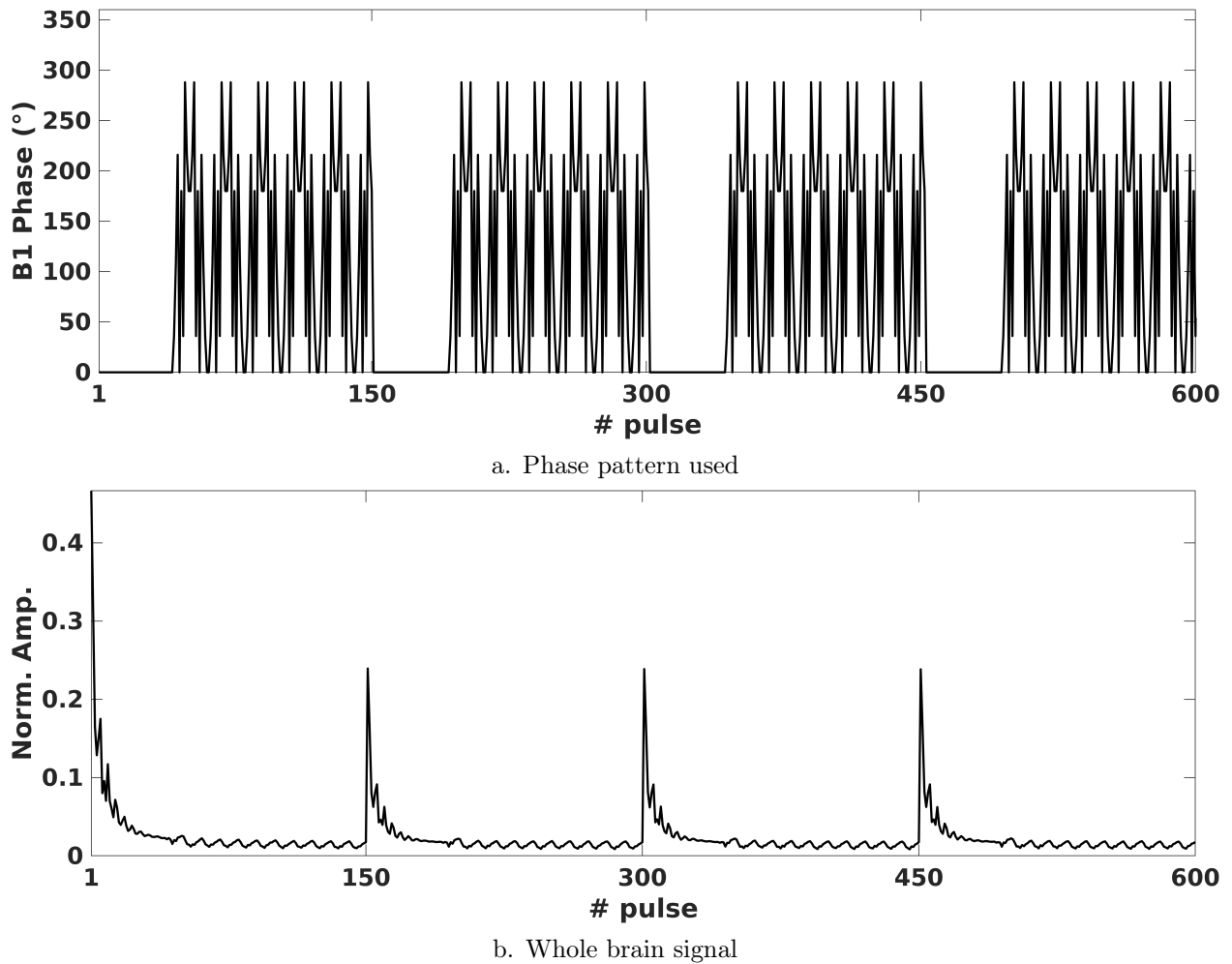


**Figure II.2.9:** Acquisition with a complex phase pattern inspired from [Guo et al. 2020](#). a. presents the phase of the pulses. All other parameters are constant for all pulses. The signal-averaged on the whole brain is shown in b. shows regular oscillations when the phase varies, which conforms to expectations.

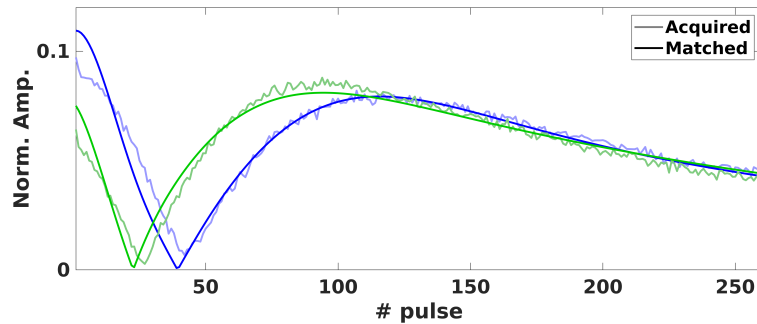
### II.2.3 First MRF results in vivo

The validations and developments presented above showed that the modules were able to work with complex sequences. Patterns from the literature were thus reproduced to perform actual MRF experiments. Dictionaries were generated accordingly using the EPG tool presented above.

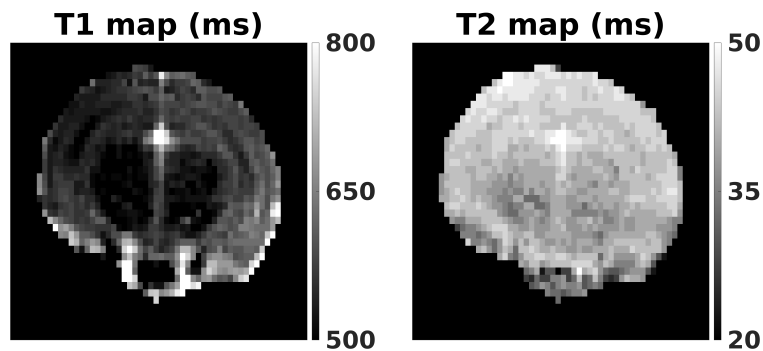
#### Gómez et al. 2019

The sequence proposed in [Gómez et al. 2019](#) was used to perform  $T_1$  and  $T_2$  measurements on a stabilized mouse brain. At 9.4T, 8 interleave were used, for a FOV of  $22 \times 22 \text{mm}^2$  and a  $96 \times 96$  resolution. Standard relaxometry was also acquired, namely an MTI for  $T_1$  and an MSME for  $T_2$ . Fig. [II.2.10a](#) presents 2 couples of acquired and matched signals. A low level of noise in the acquisitions can be observed and the general trends of the signals seem to agree with the simulations. However, the match is not good at the beginning of the sequence.

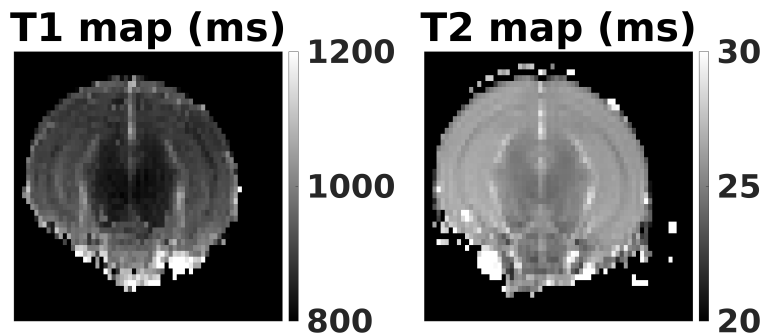
The corresponding parametric maps are shown in fig. II.2.10b. The maps exhibit expected contrasts, but the values don't agree with the reference maps shown in fig. II.2.10c.



a. Signals and matches from two voxels



b.  $T_1$  and  $T_2$  maps reconstructed from the MRF acquisition



c.  $T_1$  and  $T_2$  maps obtained with classical measurement methods

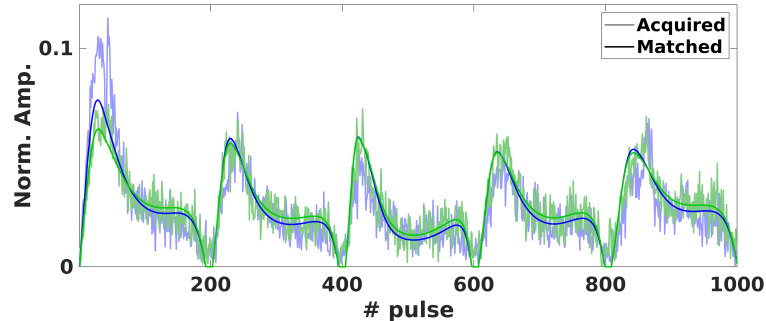
**Figure II.2.10:** Sequence from Gómez et al. 2019 on a stabilized mouse brain. a. shows the agreement between signals and matches in two voxels. b. presents the parametric maps reconstructed with the MRF method. c. presents the corresponding parametric maps obtained with classical relaxometry sequences.

### Jiang et al. 2015

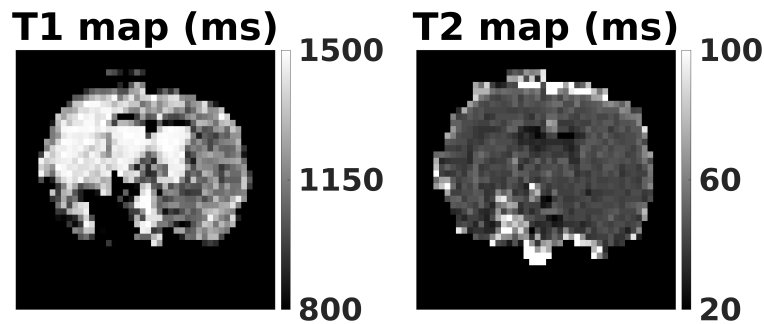
The same effect can be observed in vivo in rats at 4.7T. Stroke-bearing rats were imaged with a sequence inspired from Jiang et al. 2015 and using classical quantitative methods. Fig. II.2.11a shows acquired signals and their best match in a dictionary. Discrepancies can be observed in this case as well. Maps obtained from the MRF acquisition are shown in fig. II.2.11b. Here, they compare poorly to those obtained from classical sequences presented in fig. II.2.11c. In particular, the lesion shape varies largely between the  $T_1$  maps, and the

MRF-acquired  $T_2$  map shows no lesion at all.

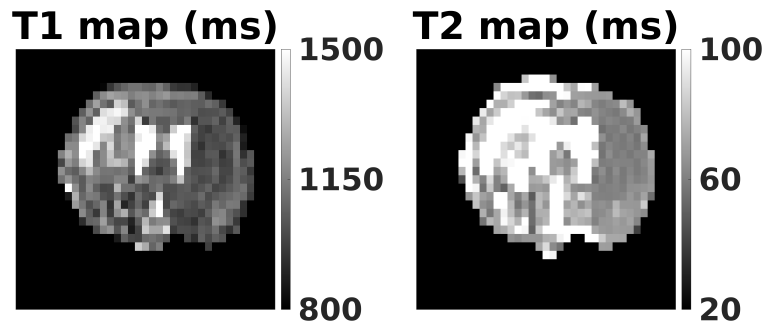
Possible explanations for these results are discussed in the next section.



a. Signals and matches from two voxels



b.  $T_1$  and  $T_2$  maps reconstructed from the MRF acquisition



c.  $T_1$  and  $T_2$  maps obtained with classical measurement methods

**Figure II.2.11:** Sequence from [Jiang et al. 2015](#) on a stroke-bearing live rat. a. shows the agreement between signals and matches in two voxels. b. presents the parametric maps reconstructed with the MRF method. c. presents the corresponding parametric maps obtained with classical relaxometry sequences. Note the difference in the shape of the lesion. In particular, the  $T_2$  map from the MRF experiment does not present any hyper-intensities, while the map from an MSME acquisition does.

## II.2.4 Conclusions and Perspectives

The preclinical MRF module was extensively used on two different scanners at the IRMaGe facility. The following section proposes a comprehensive overview of the limitations identified

and ideas to overcome them.

#### II.2.4.1 Limitations

##### Need for compilation when the sequence changes

The sequence description is contained in a text file and changing the sequence parameters requires recompiling the module after changing the path to the text file. This can be inconvenient when working with several successive sequences as one needs to wait for an acquisition to be completed before recompiling the module with another sequence. A solution is to duplicate the module, but their multiplication is error-prone.

A more suitable option would be to ask the user for the number of pulses and slices at runtime, which would allow for dynamic allocation of the matrices required. The description file could then be read and changed without recompiling, as long as the user enters by hand the right pulse number for the right file.

##### Pulse number limitation

The current method can not use more than 1024 pulses in total. This comes from the *movie* loop used to create time frames. For each movie repetition, the *spiral* subroutine is called to perform the spiral trajectory in the k-space. The problem is that the *movie* makes copies of the spiral trajectories used by *spiral* and that the maximum number of reproductions of the spirals is set to 1024.

##### Slice number limitation

The number of acquired slices is also limited by the *movie* loop. One can acquire up to 1024 pulses on a single slice, but only 512 on two slices, and so on. In the current state of the module, we also faced another reconstruction problem when acquiring 2 slices with a sequence containing less than 500 pulses. For unidentified reasons, the slices are mixed together in a non-trivial way. The temporal reconstructed signal contains an alternation of both slices and the alternation changes at the median pulse number. We tried exporting the raw data and reconstructing the images ourselves, but the problem still persisted.

Bruker support suggested removing the *movie* loop and taking advantage of other lower-level loops. These changes have been investigated but they imply a complete reprogramming of the module.

##### Spiral shape and sampling rate

In the current state of the module, the acquisition needs to be fully sampled. The sampling rate is computed based on the number of interleaves planned by the operator, the field of view, the available time for the acquisition, and the capabilities of the gradient amplifiers. When the parameters specified are not suitable for a full k-space sampling, the module increases the repetition time to be able to perform a long spiral and eventually obtain a complete sampling. This is problematic as the sequence played is not the one expected. One needs to increase the number of interleaves to solve this problem.

The spiral interleaves have a constant sampling density in the k-space. This is not ideal as one would prefer to spend more time acquiring the center of the k-space. In addition, due to

the full sampling constraint, the spiral shape is fixed during the execution of a sequence. If a 1000 pulses sequence is acquired, the same interleave is repeated 1000 times without rotation. A second interleave is then performed, again on 1000 pulses, and so on. One needs to wait for the magnetization to come back to the equilibrium state between each interleave, as it is the currently considered initial state of our simulations. This pause typically lasts around 10 seconds, which is long compared to the sequences we try to play. It would be much more interesting to proceed as done in state-of-the-art methods: using a variable density spiral arm that rotates from one pulse to the other. This would allow us to play the sequence only once, instead of repeating it as many times as we have interleaves.

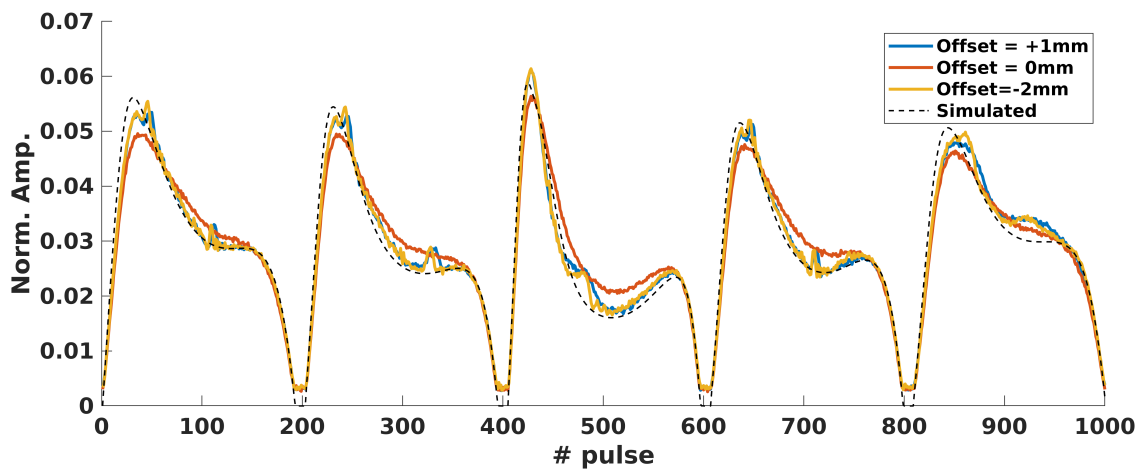
### Phase offset vs. distance to magnet

A more critical problem arises when repeating an acquisition on several slices of a sample. Fig. II.2.12a shows the difference between a magnet-centered and two off-centered acquisitions, using the sequence from Jiang et al. 2017. The expected signal shown is simulated with  $T_1$  and  $T_2$  values measured from a multi-inversion time and an MSME sequence, respectively. The general shape of the centered signal is different from the other two, which also exhibit unexpected rapid variations. Fig. II.2.12b and II.2.12c investigate the SNR and noise level of these acquisitions and find no significant noise variation between them. Especially, the noise does not seem responsible for the observed rapid variations. To see if the problem could come from the use of a numerical 0 in a centered acquisition, a test with an offset of 0.001mm was performed (not shown here). The signals acquired with offset 0 and 0.001mm were similar, excluding the possibility of a numerical error. This phenomenon was observed on both our 4.7 and 9.4T systems, as well as on the system from Copenhagen University.

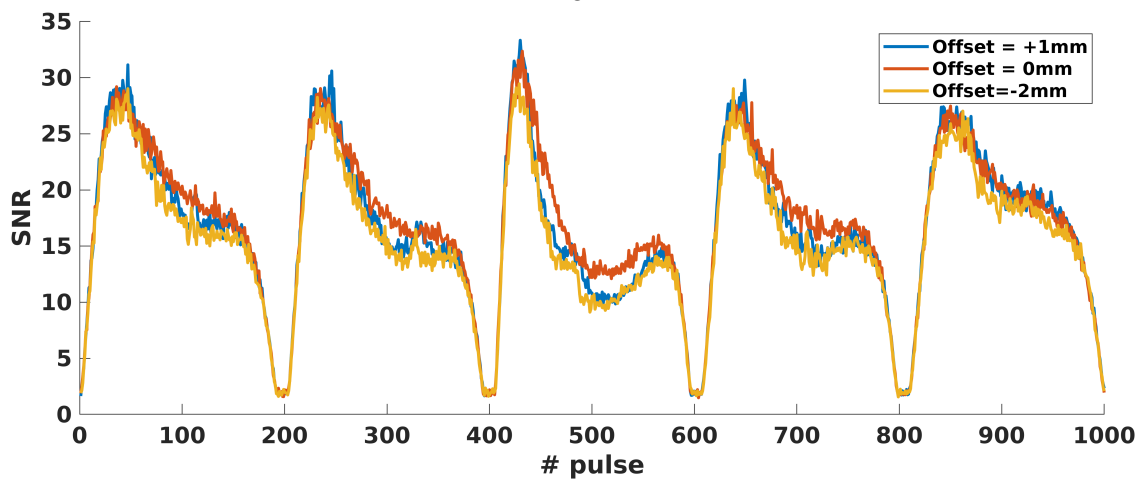
No satisfying solution to this problem was found yet, and the matter will be discussed with the Bruker development team.

#### II.2.4.2 Perspectives

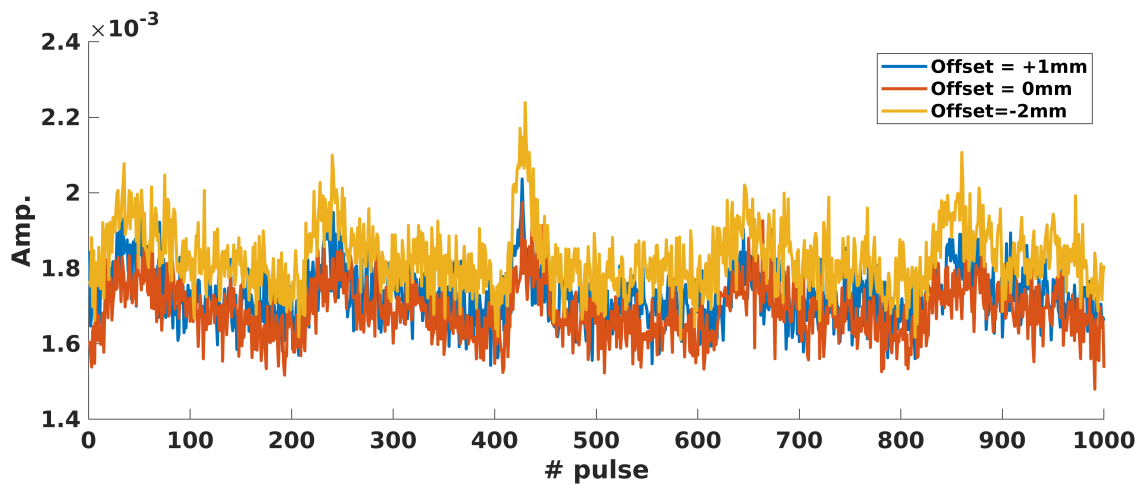
In conclusion, the module has clear room for improvement. Nevertheless, it still allows for sequence testing on phantom and small animals with the limitations listed above. Using short sequences such as the one proposed in Gómez et al. 2019 counterbalances the long acquisition time brought by the full sampling constraint. With this knowledge, the team of Pr. Nedergaard at Copenhagen University has started using the module to follow changes in relaxation rates in mice brains after injection of contrast agent in the extravascular space. Repeating acquisitions on the 3 orientations or on several central slices will allow for tracking of relaxation changes, even though the actual values are yet to be validated.



a. Signals



b. SNR



c. Noise level

**Figure II.2.12:** Demonstration of the difference in signal shape vs offset to magnet center. The same sequence with the same parameters was used for the 3 acquisitions. Note the similarity between the off-center acquisitions, and their dissimilarity with the magnet-centered acquisition.

## II.3 Test of a clinical MRF acquisition module

### II.3.1 Context: Philips Research collaboration

Our MR research facility is equipped with one 3T scanner dedicated to clinical research: Achieva 3.0T dStream Philips (Best, The Netherlands), quasar dual gradient,  $\leq 40$  mT/m amplitude, and multiple head coils up to 32 channels. As for our preclinical scanners, Philips does not offer a commercial MRF solution at the time being, but a research module is under development. We were granted access to this module through a research agreement with Philips Research (Philips GmbH, Innovative Technologies, Research Laboratories Hamburg) and the following section introduces the work done with this module.

### II.3.2 Overview

The MRF patch is under development and can not be used under the certified software patch. Any acquisition performed with this patch is not intended for medical use. The images shown here were acquired on healthy volunteers and are printed with their agreement. All acquisitions were performed in agreement with the MAP-IRMaGe protocol (see ethics statement).

The workflow of the module is very similar to what was developed on our preclinical scanner: parameters are passed through a structured CSV (comma-separated values) file, shown in fig. II.3.1. Lines starting with # are part of the file header. Philips uses these files both

```
# MRF sequence pattern
# created: 2020-10-27T15:35:27.829177
# revision: 336
# type: generic
# class: BlochGeneric
# length: 390
# repetition_delay (ms): 5000
# n_dummies: 0
# fixed_te: 0.0
# rf_pulse: inv=inversion_nsls
# rf_pulse: exc=am_sg_300_100_0
# rf_pulse: t2prep=t2_prep_4
# mDIXON: no
# fa, tr, phase, te, aq, slice_profile_corr, spoil, rf_pulse
180.0,20,0.0,4,False,False,1.0,inv
5.0,15,0.0,4,True,False,1.0,exc
5.21809693683,15,0.0,4,True,False,1.0,exc
5.43577871374,15,0.0,4,True,False,1.0,exc
...
```

**Figure II.3.1:** CSV sequence description file for Philips scanners

for dictionary simulation and acquisition. Part of the header lines are instructions for the



simulator, which we do not have access to. Those of particular interest at acquisition time will be discussed below.

The last line of the header indicates the order in which the acquisition parameters are to be read. Most of their names are self-explanatory. Each line below corresponds to a so-called “block”, lasting TR, with a pulse of flip angle FA that can be an excitation (`rf_pulse=exc`) or an inversion (`rf_pulse=exc`), an optional acquisition at TE (triggered by the `aq` boolean), and an optional spoiler of `spoil`  $\times \pi$  across the voxel. The `slice_profile_corr` parameter is a flag for the simulator. These parameters are read at scan time. The module dynamically reads parameters from any CSV file stored in the proper directory, which allows for easy testing and session planning.

A large number of acquisition parameters can be set, taking advantage of many of the commercially available Philips tools. Acquisitions can be performed with a cartesian, spiral, or radial scheme. In the first case, a SENSE acceleration algorithm is available to speed up the acquisition. For the radial and spiral schemes, the number of spirals or spokes per image can be set to more than 1. It is worth noting that a  $B_0$  pre-scan is performed before a spiral acquisition for deblurring.

When more than 5 slices are imaged, their acquisition is performed in an interleaved way, allowing for continuous acquisitions without pause to return to thermal equilibrium. When fewer slices are acquired, one must pay attention to let an appropriate amount of time between each repetition of the sequence, e.g. between each line of a cartesian acquisition. This is easily done with the `repetition_delay` option of the header.

The module is proposed with a custom 500-pulses sequence dedicated to  $T_1$  and  $T_2$  measurements. The acquisitions are temporally compressed before applying the FFT from the k-space to the image space. This step diminishes the computational cost of reconstruction, as the compressed signals contain only 24 temporal points. The corresponding compressed dictionary is included with the module, allowing for  $T_1$ ,  $T_2$ , and proton density maps directly reconstructed at the console. A  $B_1$  correction step is applied at the reconstruction step. A  $B_1$  map must then be acquired before the reconstruction.

The module can output the images from the uncompressed sequence (such as magnitude or phase), the compressed images, or directly the parametric maps. When acquiring other sequences, the compression must be deactivated to output raw images.

Data can be exported in a number of formats, among which the Philips proprietary format Par/Rec and the classical Dicom. Our image converter (see section II.4.1.1) can deal with both formats, but dimensions are better managed when using the Philips format. In particular, when using Dicoms, 4D scans (3D spatial + temporal evolution) with only one slice are read as 3D scans in the current state of our tools. The Philips format is thus preferred.

### II.3.3 Evaluation of the MRF module

This section presents some of the tests and experiments that were done with the Philips module.

### II.3.3.1 Tests on acquisition parameters

The different acquisition parameters that can be tuned in the module should be understood before trying to acquire complex sequences. We tested some of these parameters as independently as possible.

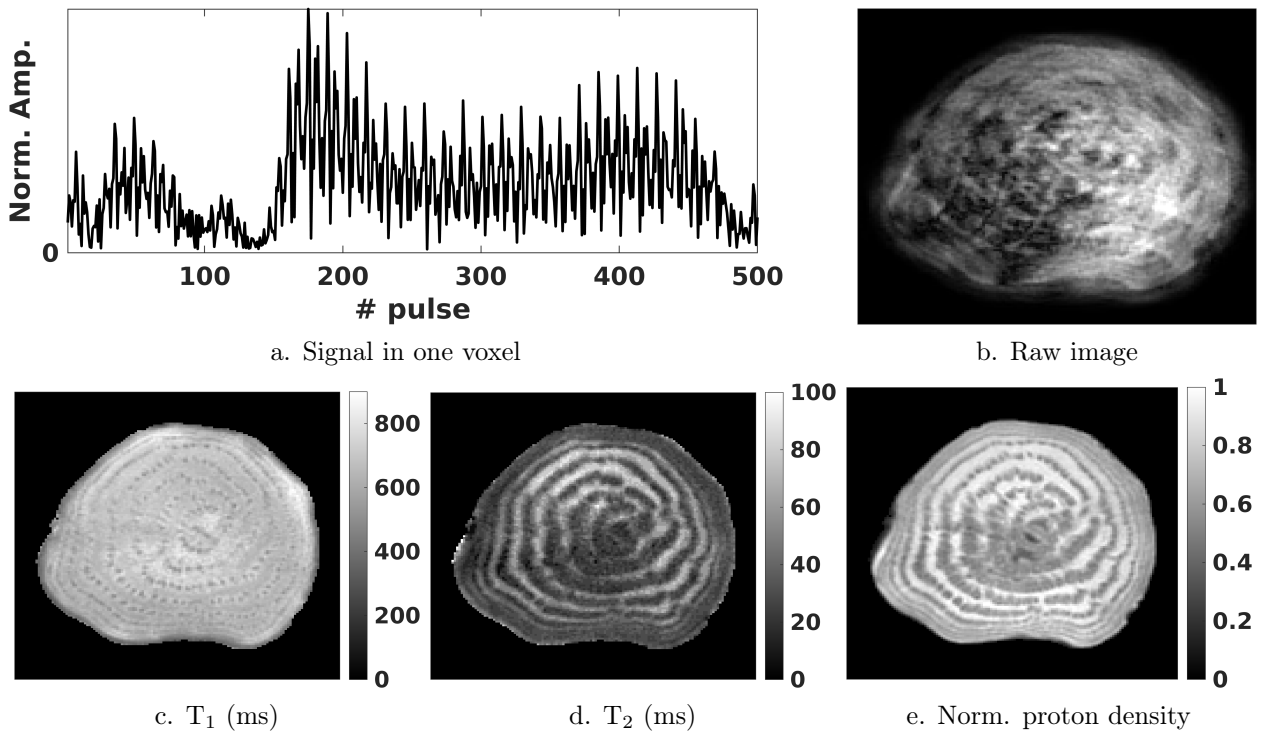


**Figure II.3.2:** Parametric maps (zoomed in) acquired on a beetroot with the MRF-brain sequence.  $240 \times 240$  spiral acquisition on a  $240 \times 240 \text{mm}^2$  FOV, 4mm slice thickness. Constant density spiral, 14 interleaves for full sampling. 10 seconds acquisition.

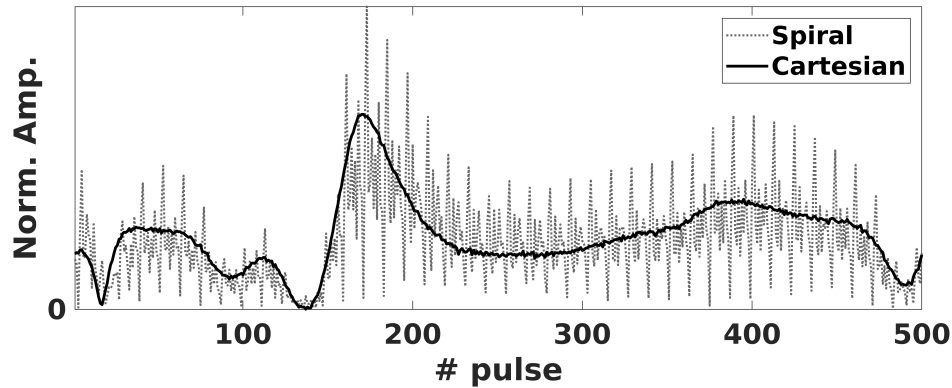
#### Spiral and cartesian acquisition schemes

The module offers several acquisition schemes, among which are the commonly used spiral, and the traditional cartesian one. Acquisitions were performed with the MRF-brain sequence to validate the proper functioning of the module. Parametric maps were obtained on a beetroot with the following parameters:

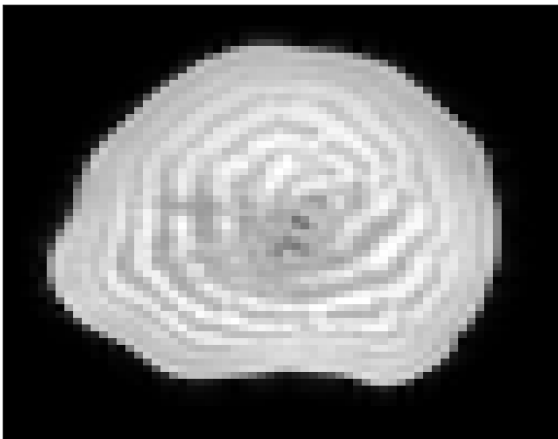
- Constant density spiral, requiring 14 interleaves for full sampling (one interleave per image is used here)
- $240 \times 240 \text{mm}^2$  FOV and a  $240 \times 240$  matrix
- 4mm slice thickness, one slice

for a scan time of 10 seconds for one slice. Fig. II.3.2 shows an example of a signal obtained and a raw image. Undersampling aliases are well visible in both the temporal and spatial domains. They are in line with what is classically seen in the MRF literature. Parametric maps reconstructed by the software are also shown. The image quality of these reconstructions is high and no particular artifacts are visible.

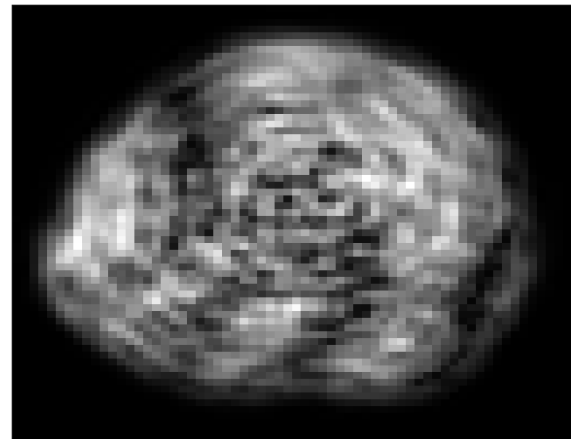
To test the cartesian acquisition scheme, two additional acquisitions were made. The first one used a fully sampled cartesian scheme, and the second one the spiral scheme. To shorten the acquisition, we reduced the matrix size to  $64 \times 64$ , keeping other parameters as they were. The acquisition window of the cartesian scheme in such conditions is 3ms, a value we reported on the spiral scheme. Keeping the constant spiral density, each interleave samples  $1/12$  of the k-space. The cartesian acquisition took 10:41 minutes, repeating the sequence for each of the 64 lines of the acquisition matrix, and the spiral one 10 seconds. Raw images and signals are shown in fig. II.3.3. The image quality is good in the cartesian-acquired image, as expected.



a. Comparison of signals from a single voxel, L2-normalized



b. Cartesian (64 segments)



c. Spiral (1 segment)

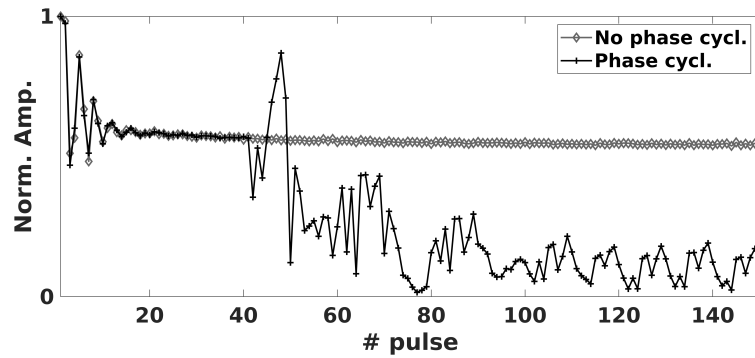
**Figure II.3.3:** Comparison of image quality for a cartesian and spiral acquisition.  $64 \times 64$  matrix,  $240 \times 240 \text{mm}^2$  FOV, 3ms acquisition window.

The circular patterns inside the object are visible, despite the reduced matrix size. The borders of the objects are sharp and no pronounced artifact is visible. The spiral-acquired image contains artifacts, as expected, similarly to the acquisition on the  $240 \times 240$  matrix. The L2-normalized signals from both acquisitions are comparable in their evolution. The noise artifacts are clearly visible but are not coherent with the shape of the signal, as is expected.

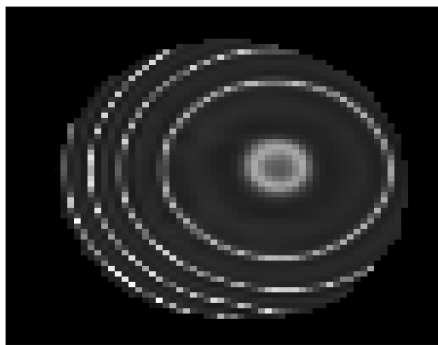
### RF phase cycling

Using cartesian acquisitions and taking advantage of the compressed-sensing options, two 150-pulses-long bSSFP acquisitions were performed on a plastic phantom provided by Philips.

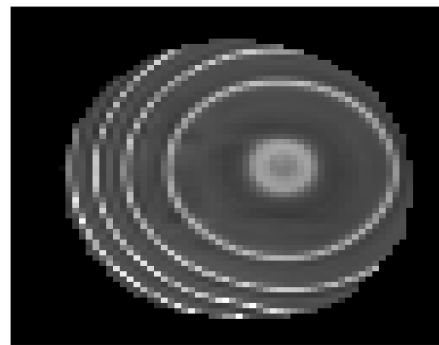
One of the MRF sequences has an RF phase cycling inspired by [Guo et al. 2020](#) starting at pulse 40, similar to what was done in [fig. II.2.9](#). The SENSE factor is set to 2. The first echoes of both acquisitions are shown in [figs. II.3.4b](#) and [II.3.4c](#). The banding artifacts are characteristic of bSSFP acquisitions. Images from the 48<sup>th</sup> echoes shown in [figs. II.3.4d](#) and [II.3.4e](#), as well as the signal comparison from the same voxel of the two acquisitions ([fig. II.3.4a](#)), confirm the presence of the phase cycling.



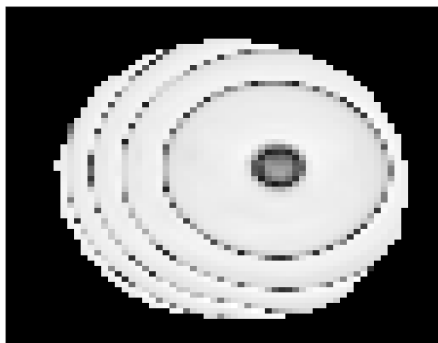
a. Comparison of signals from a single voxel in acquisitions with and without RF phase cycling



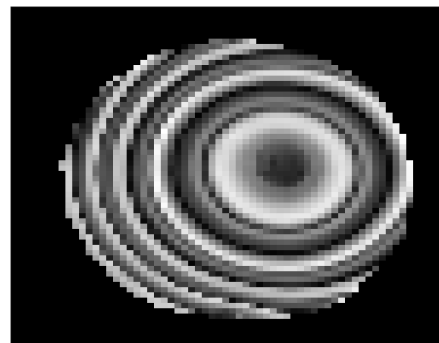
b. No Phase cycling, first echo



c. Phase cycling, first echo



d. No Phase cycling, echo 48



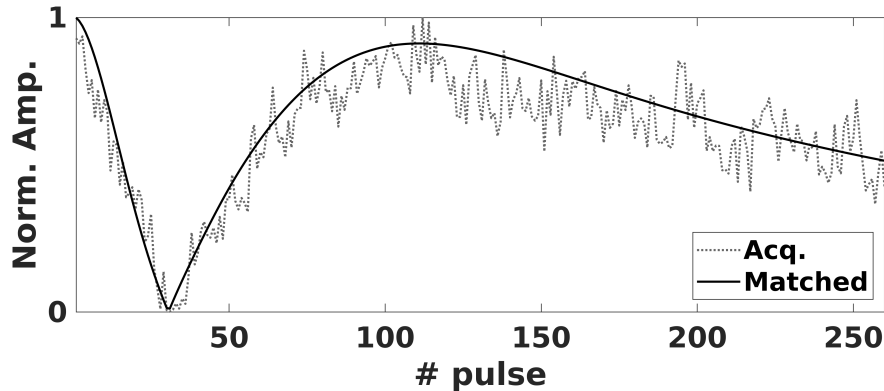
e. Phase cycling, echo 48

**Figure II.3.4:** Echoes from bSSFP acquisitions with and without RF phase cycling.  $64 \times 64$  matrix,  $240 \times 240 \text{mm}^2$  FOV

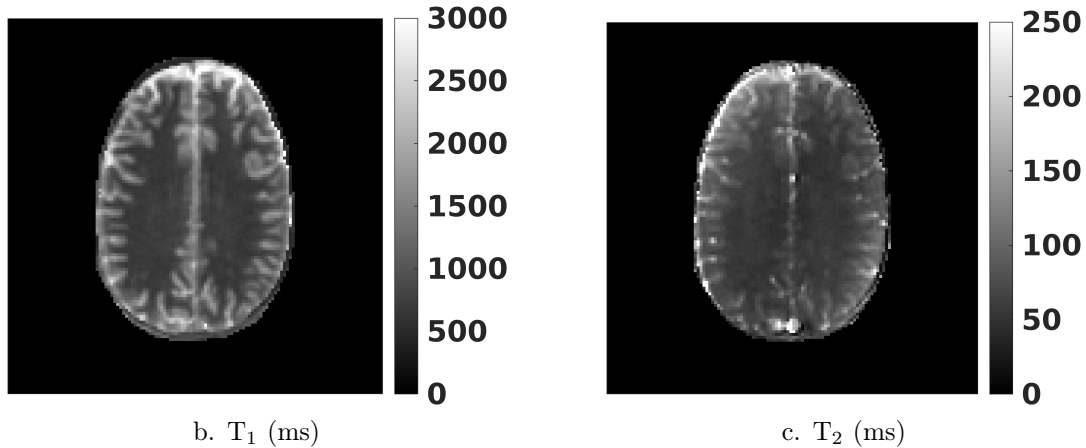
### MRF sequences from the literature

On healthy volunteers, we were able to reproduce sequences from the literature. [Fig. II.3.5](#) shows the results from an experiment using the sequence from [Gómez et al. 2019](#), acquired

with a cartesian scheme,  $112 \times 112$  matrix,  $240 \times 240 \text{mm}^2$  FOV, SENSE factor = 3. The sequence was chosen for it demonstrated robust  $T_1$  and  $T_2$  estimations with only 260 pulses,  $TE/TR = 2/14$  ms, keeping the acquisition time short.



a. Comparison of acquisition and match from a single voxel in a healthy volunteer using the [Gómez et al. 2019](#) sequence.



b.  $T_1$  (ms)

c.  $T_2$  (ms)

**Figure II.3.5:** Acquisitions on a healthy volunteer with the [Gómez et al. 2019](#) sequence.  $112 \times 112$  cartesian acquisition on a  $240 \times 240 \text{mm}^2$  FOV, 4mm slice thickness. SENSE factor = 3, 8:25 minutes acquisition.

The same sequence was used again, along with that from [Jiang et al. 2015](#), with a spiral scheme. The acquisitions are performed on a  $64 \times 64$  matrix,  $240 \times 240 \text{mm}^2$  FOV. The Jiang acquisition takes 13.7 seconds, with a quadratically variable spiral density, and 6 interleaves for full sampling. The Gómez acquisition takes only 3.7 seconds with the same spiral acquisition and 4 interleaves.

Reconstructed  $T_1$  and  $T_2$  maps are shown in fig. [II.3.6](#). The  $T_1$  maps are rather similar and correspond to that from the higher resolution acquisition (fig. [II.3.5b](#)). The  $T_2$  map from Jiang shows artifacts around the superior sagittal sinus. Signals shown in fig. [II.3.6](#) present noise levels that fit the two different sampling rates. In particular, the Jiang signal exhibits a noise comparable to what is presented in the original article.

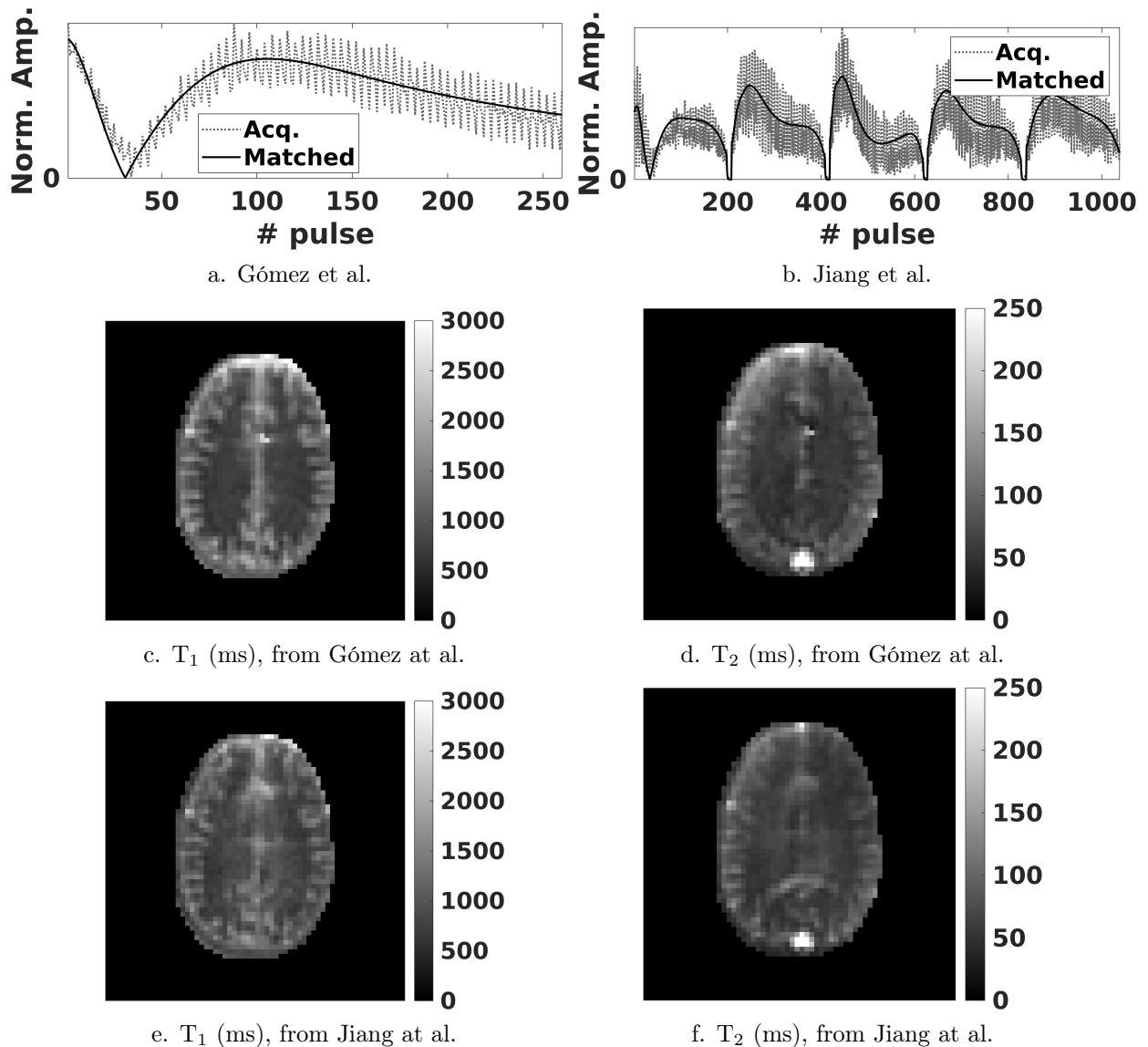


**Figure II.3.6:** Parametric maps obtained on a healthy volunteer with sequences from [Gómez et al. 2019](#) and [Jiang et al. 2015](#).  $64 \times 64$  matrix,  $240 \times 240 \text{mm}^2$  FOV, 4mm slice thickness. A quadratic spiral sampling was used in both cases: 4 interleaves for the Gómez sequence, 4 for the Jiang one.

### II.3.4 Perspectives

Most of the functionalities of the module have been tested. Fine-tuning the spiral parameters, and the different types of variable density, for example, will be the object of further experiments. It is however already possible to test sequences designed for MRvF and chapter IV describes sequence developments made for vascular exploration.

## II.4 Development of MRF reconstruction tools

After acquiring data on either a pre-clinical or clinical scanner and having suitable dictionaries generated, the remaining MRF step is to perform the reconstruction of the parametric maps. This section presents the tools developed for this purpose.

### II.4.1 Exploratory reconstruction tool

The final results of an MRvF experiment are usually multiple parametric maps. After reconstruction, it is thus important to be able to easily navigate the several 3D images obtained. Yet, at an exploratory and developmental stage of the process, the quality of these maps can not be considered without assessing the agreement of the matched and acquired signals. A tool able to show several parametric maps at the same time and dynamically display both the acquired and matched signals by clicking on a voxel was thus developed. A graphical interface has been developed as well, using the Matlab GUI tools. It is displayed in fig. II.4.1.

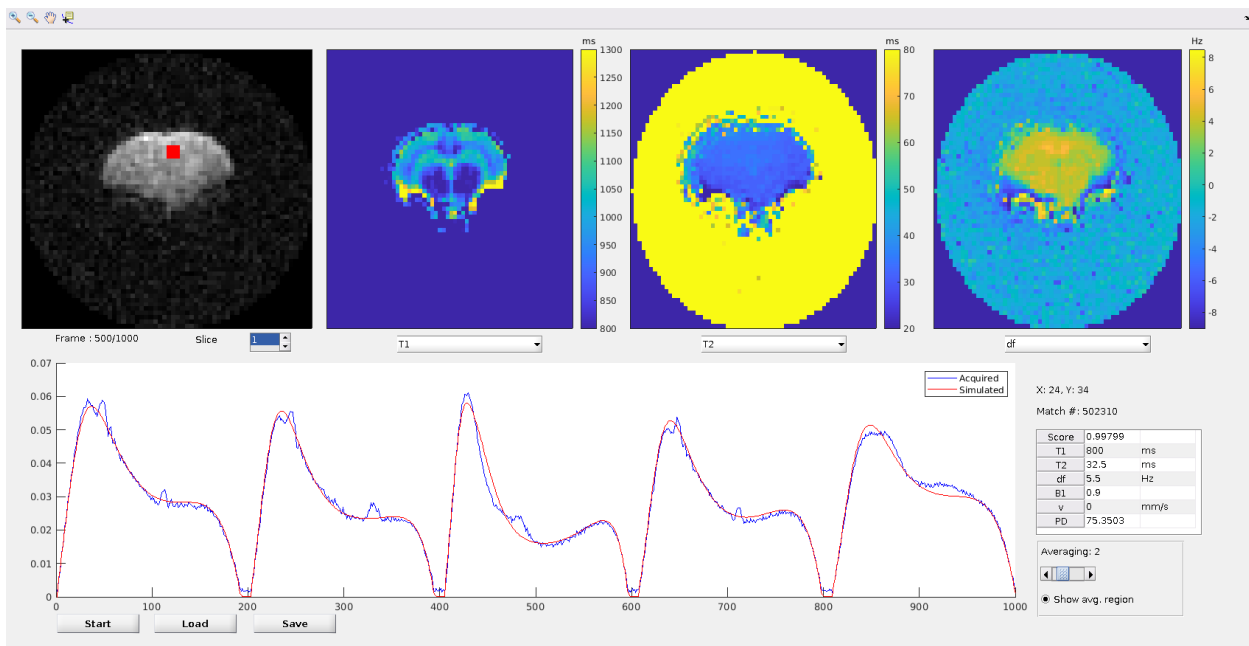


**Figure II.4.1:** Tool for reconstruction exploration. The upper row displays a raw acquired image and different parametric maps. Clicking on a map will display in the lower panel the acquired and matched signals in the corresponding voxel. The different values in the clicked voxel or ROI are listed in the right-side table.

The tool can work with 4D scans and with several slices. The top row displays the image corresponding to the median echo. The 3 other boxes show user-selected parametric maps and the associated color bars with their unit. Clicking on a map will display the acquired and matched signals in the corresponding voxel. It is also possible to show a mean of the acquisitions and matches in a square ROI, whose size can be modified. The different values in the selected voxel or ROI are listed in the right-side table. Clicking on the displayed signals



will update the upper-left display to show the acquired image corresponding to the clicked echo.

The tool is either called at runtime by a function performing the matching step or can be used as a stand-alone tool by loading the previously saved output.

#### II.4.1.1 Data processing software: MP3

Most data processing was done on MP3, an open-source, cross-platform, Matlab-based software developed by the team and IRMaGe and fully described in [Brossard et al. 2020](#). Its core concept is to create a structured database of subjects, with potentially several time points per subject, and several scans per time point.

Data processing pipelines are created from pre-coded blocks, called modules, in which the user simply inputs parameters. The database structure makes it possible to save and reuse any pipeline on other data, provided the same naming convention was used. In particular, all patients of a study can be processed through the same pipeline, making group studies easier to process.

The data is stored as a NIfTi/Json files pair, the first one containing the image volume, the second one the metadata, structured following the France Life Imaging guidelines ([Kain et al. 2020](#)). This Json file also contains the history of which modules were used from the raw data to the current files.

A strength of the software is its data converter developed and maintained by O. Montigon from the IRMaGe facility, which can deal with the following data formats:

- Bruker proprietary
- Philips PAR/REC
- Dicom
- NIfTi

The converter generates the Json file with the appropriate metadata, with possible addition from the user, if required. This converter is freely available on GitHub: [Montigon 2020](#). MP3 and a number of modules are publicly available as well, see [Brossard et al. 2020](#).

The main graphical interface of MP3 is well suited for 3D and 4D data visualization, as demonstrated in [fig. II.4.2](#). ROIs can be drawn for masking and statistical purposes, which makes quantitative analysis convenient. MP3 is able to automatically interpolate any volume in the resolution and orientation of another. ROIs can thus be drawn on high-resolution anatomical scans and used on any scan from the same patient, even of lower resolution.

A first MRF module was developed for MP3, corresponding to the initial MRvF implementation (ratio of GESFIDSE pre- and post-contrast agent injection, [Christen et al. 2014b](#)). The module is able to perform two types of reconstruction:

- **DBM**: Dictionary-based Matching, which is the classical matching described in [Ma et al. 2013](#). The dot-product between the acquisitions and the simulated dictionary is computed. Each acquired signal is matched with the simulated entry yielding the

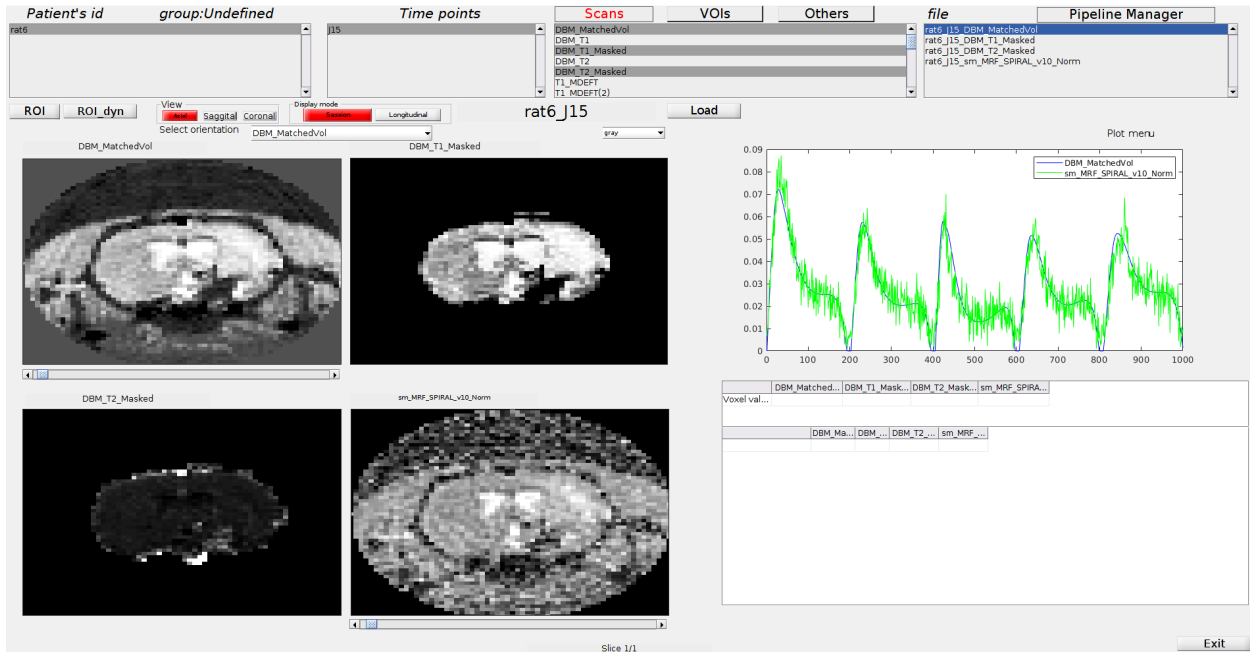


**Figure II.4.2:** Graphical interface of the MP3 software. Up to 4 imaged volumes, 2, 3, or 4D can be displayed at the same time. In the 4D case, the signals in a clicked voxel can be displayed. This example presents a  $T_1$  and  $T_2$  map from an MRF experiment, and the corresponding acquisition and matched signals.

highest product.

- **DBL:** Dictionary-based Learning, a Bayesian-based regression, developed in the lab by [Boux et al. 2021](#). It implements the Gaussian locally linear mapping (GLLiM) approach ([Deleforge et al. 2015](#)), which models non-linear relationships between the parameters and signal spaces in a piece-wise linear fashion.

The module is fed a 4D volume containing acquisitions of length  $T_{acq}$ , and a dictionary of  $N$  signals  $\times$   $T$  time points. When the signals are simulated with a time step that does not necessarily match the acquisition times of the sequence, the module interpolates the dictionary to correspond to the acquired signals. Along with simulated signals, the dictionary contains a matrix of  $N$  vector parameters. When using the DBL method, some GLLiM parameters can be tuned.

The user simply indicates the data and dictionary to use and the parameters for which maps have to be reconstructed. This module serves as a basis for the developments described below.

## II.4.2 Developments for MP3

### II.4.2.1 Pattern options

The existing MP3 MRF module was initially designed to use the ratio of a pre- and post-injection of contrast agent. In practice, the module receives the “Pre” and “Post” scans, and a dictionary containing the simulations in both conditions. The dictionary is interpolated

and the ratio of the acquisitions and simulations is computed. Although perfectly functional, such a module is rather limited and lacks flexibility.

Building on the existing code, two additional modules were developed.

- A first module was designed for acquisitions with CA, typically Pre and Post GESFIDSE sequences for MRvF. The difference with the existing one is the pattern used: we implemented the possibility to choose the pattern at runtime, keeping the ratio and adding the concatenation of the Pre and Post, or any “hybrid” pattern.
- A second module was designed for general MRF use, as the provided data is used without any particular pattern or echo reordering.

Working with the new patterns, one must care about the application of proper normalization steps. Indeed, the amplitudes of the acquired and simulated signals largely differ. The final fingerprint used must be normalized or the dot-product would always be the highest for the dictionary entry with the highest amplitude. Yet, creating the final fingerprint requires taking care of properly normalizing or not each of the acquisitions used.

We also added the possibility to produce the map of the matching product score, showing in each voxel the value of the highest product. The matched signal can also be produced for each voxel, generating a 4D volume that can be compared voxel by voxel with the acquisition.

#### II.4.2.2 Parametric maps screening tool

The nature of MP3 makes it useful for group studies, processing several subjects at the same time. In addition, it is not uncommon to repeat an experiment under different conditions, changing the dictionary or the reconstruction method. To be able to rapidly assess the results of several reconstructions on a large number of subjects, a visualization module was developed and is presented in fig. II.4.3. The user can select different scans per subject and time point and display them all in a “table” with an appropriate color bar. The contrasts are adapted to be the same for all the images. Several tables can be produced to be visualized one after the other.

This module creates .png images for all the user-selected scans and writes an HTML table where each cell refers to an image. A main HTML file calls the different tables generated at each run of the module. A small Python script allowing a web browser to reach locally stored files is generated with the main HTML table.

After launching the Python server in a console (one command line), any web browser can be used to open the main HTML file, which calls the different tables through JavaScript interactions. It is then easy to scroll through a large number of subjects, change from one table to another to see different metrics, and zoom in on images.

This tool proved useful in many cases to compare dictionaries and reconstruction methods or simply to screen databases. Typical use is to load a large number of anatomical scans acquired after a lesion-inducing task or a CA injection, to rapidly spot any subject on which the operation failed. It was also suited to quickly visualize the different metrics produced by MRvF and see their variations in lesions, as shown in fig. II.4.4 on 40 animals, 4 metrics and 2 reconstruction methods. Such visualization gives information on the relative performances of two methods before having to draw ROIs and perform statistical analysis.

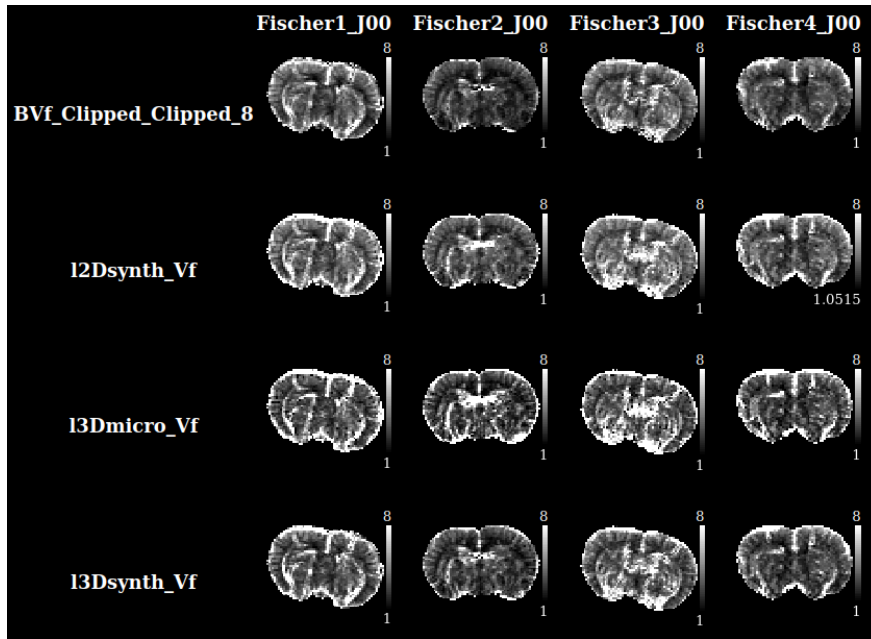


**Figure II.4.3:** MP3-based screening tool. Several subjects and several patients can be displayed at the same time on an internet explorer page, allowing for easy scrolling and zoom.

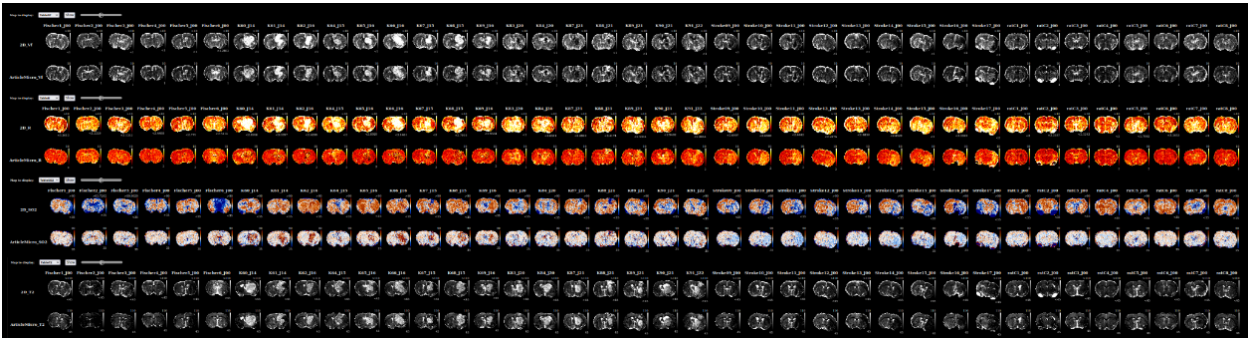


**Figure II.4.4:** Example of use of the MP3 screening tool. 4 MRvF-obtained metrics are displayed on about 40 subjects and for 2 reconstruction methods. Variations of the different metrics in the different animals are easy to assess.

The module was tested on Linux and Windows for several browsers and is used by other members of the team.

### II.4.3 Perspectives

The reconstruction tools presented here have been extensively used and proved to be convenient and efficient. As for all training-based methods, the DBL takes a longer time as the dictionary size increases, but the following inferences are almost instantaneous. The DBM method is reliable, although its use with larger dictionaries requires more time and RAM. These methods are satisfying and allow for reliable reconstructions. It could be interesting to implement dictionary compression methods able to better process dictionaries with many

dimensions ([Assländer et al. 2018](#); [Zhao et al. 2018](#)).



## CHAPTER III

---

# IMPROVING MRvF WITH REALISTIC 3D VASCULAR NETWORKS

---

Chapter II presented the tools available for MRF and MRvF and the proposed developments. Efforts were made both on the acquisition and simulation aspects, which are the two main leverages to improve the accuracy of MRF estimates.

In particular, it was shown that we were now able to simulate dictionaries based on 3D vascular models, with geometries more complex than the simple 2D models used so far. An easy step to obtain signal evolution that better suit reality could be to produce 3D vascular networks containing straight cylinders with isotropic orientations. However, such a model is still far from the actual complexity of microvascular structures, whether in healthy or pathological tissue. In several recent studies, state-of-the-art microscopy techniques have been used to reconstruct whole-brain vasculature structures on mice. Furthermore, several authors have proposed methods to generate fully connected vascular networks from scratch, ensuring realism through constraints from physiological observations and fluid mechanics principle. These data or codes are available and could be used in our simulations.

Simulating 3D volumes comes of course with an increased simulation time that makes the generation of large dictionaries prohibitively long. In this case, state-of-the-art reconstruction methods, such as the Bayesian-based approach from [Boux et al. 2021](#) recently developed in the lab, could come handy to reconstruct high quality parametric maps from smaller dictionaries.

This chapter proposes an in vivo study on retrospective rodent data using 3D vascular networks segmented from microscopies for MRvF dictionary generation. We used our regression algorithm to generalize the results and show positive impact on the MRvF estimates. A generative method building realistic vascular networks from scratch was also implemented and preliminary results are discussed in a second section.



---

**CONTENTS**


---

<b>III.1 Using 3D voxels segmented from microscopies for dictionary generation</b>	<b>91</b>
III.1.1 Objectives . . . . .	91
III.1.2 Materials and methods . . . . .	91
III.1.2.1 Generation of synthetic 3D voxels with realistic microvascular networks	91
III.1.2.2 Generation of MRvF dictionaries . . . . .	93
III.1.2.3 MR Data acquisition . . . . .	93
III.1.2.4 MR Data processing . . . . .	95
III.1.2.5 In vivo pO <sub>2</sub> measurements . . . . .	95
III.1.2.6 Numerical and statistical analysis . . . . .	96
III.1.3 Main results on control and 9L rats . . . . .	96
III.1.3.1 3D micro DBL vs DBM . . . . .	96
III.1.3.2 3D-micro vs synthetic dictionaries . . . . .	97
III.1.3.3 Oxylite pO <sub>2</sub> measurements . . . . .	100
III.1.4 Additional results on C6 tumors and strokes . . . . .	100
III.1.5 Discussion . . . . .	101
<b>III.2 Synthetic vasculature generation: Constructive Constrained Optimization</b>	<b>104</b>
III.2.1 Principles . . . . .	104
III.2.2 Implementations . . . . .	106
III.2.2.1 VascuSynth . . . . .	106
III.2.2.2 Matlab implementation . . . . .	106
Initialisation . . . . .	107
Adding a new terminal node . . . . .	107
Constrain the tree . . . . .	107
Optimizing the tree: choosing the right branching point . . . . .	108
III.2.3 Results . . . . .	110
<b>III.3 Conclusion and future perspectives</b>	<b>113</b>

---

## III.1 Using 3D voxels segmented from microscopies for dictionary generation

### III.1.1 Objectives

In recent years, several groups used state of the art microscopes and complex data processing tools to obtain whole brain vascular networks at high spatial resolution (about  $1\mu\text{m}$  isotropic). Thanks to the development of open data, some of these datasets are now accessible online (Di Giovanna et al. 2018; Todorov et al. 2020; Kirst et al. 2020). In addition, the computing power and the developments of optimized codes for MR simulations (Pannetier et al. 2013; Genois et al. 2021) allow handling such large and complex datasets. A first attempt to use realistic structures in the MRvF framework was made by Pouliot et al. 2017 using 6 voxels from mouse cortex acquired at  $1\mu\text{m}$  isotropic resolution. Different geometrical transformations were used as data augmentation to compensate for the small number of animals and the lack of brain structure diversity. However, the maps and quantitative results at the group level were not as promising as expected, probably due to a lack of generalization of the dictionary.

We propose in this study to use multiple open access datasets to create about 28,000 3D voxels segmented from whole-brain, healthy mice vascular networks. After MR simulations and dictionary creation, we use a Bayesian-based machine learning algorithm from Boux et al. 2021 in order to extend the dictionary coverage to larger parameter ranges, including the ones expected in several pathological conditions. Our MRvF approach is tested in rat brains bearing tumors, and the results are compared to those obtained using dictionaries with simulations based on 2D or 3D cylinders. MR estimates are also compared to existing histological analyses and in vivo  $\text{pO}_2$  measurements made with optic fiber probes.

### III.1.2 Materials and methods

#### III.1.2.1 Generation of synthetic 3D voxels with realistic microvascular networks

Two open access datasets of whole-brain mice vasculature are used:

- Dataset 1 (Di Giovanna et al. 2018) contains images from a single adult male C57BL/6 mouse brain acquired with a spatial resolution of  $0.65 \times 0.65 \times 2\mu\text{m}^3$ . The available dataset is not segmented and thus needs to be processed.
- Dataset 2 (Todorov et al. 2020) contains already segmented blood vessels imaged from 9 male, 3 months old, mice brains (C57BL/6J, CD1, and BALB/c) acquired at  $3\mu\text{m}$  isotropic resolution and is already segmented. Due to the large volume of data represented, only two brains from the C57 mice are used.

All images are acquired post-mortem with a light-sheet microscope after blood vessel fluorescent staining and tissue clearing.

Both datasets are processed using ImageJ (Rasband, W.S., NIH, Maryland, USA), with the purpose of obtaining a set of MRI-sized voxels (i.e.  $248 \times 248 \times 744 \mu\text{m}^3$ ) containing binary masks representing the vascular network. Dataset 1 is chopped into MRI-sized voxels rescaled to  $2 \times 2 \times 2 \mu\text{m}^3$  resolution, denoised, segmented and characterized in terms of

total BVf and R. In a sample of 24 voxels, we compared the simulated MR signals obtained with the rescaled and the original spatial resolution. Results were not significantly different between the two approaches and the coarser resolution was chosen because simulations were less computationally demanding. Dataset 2 is chopped to MRI-sized voxels, rescaled to a  $2 \times 2 \times 2 \mu\text{m}^3$  resolution, and BVf and R are derived voxel-wise.

The combination of the two datasets led to about 11,000 voxels. However, the histograms of BVf and R showed two distinct distributions of parameters, corresponding to the two different datasets. To obtain a more continuous global distribution of the vascular parameters, new MRI-sized voxels were obtained by numerical erosion of the rescaled dataset 2. A total of 28,005 MRI-sized voxels with continuous BVf and R distributions is finally obtained. Examples of voxels from dataset 1 and final histograms across the 28,005 voxels are shown in fig. III.1.1.

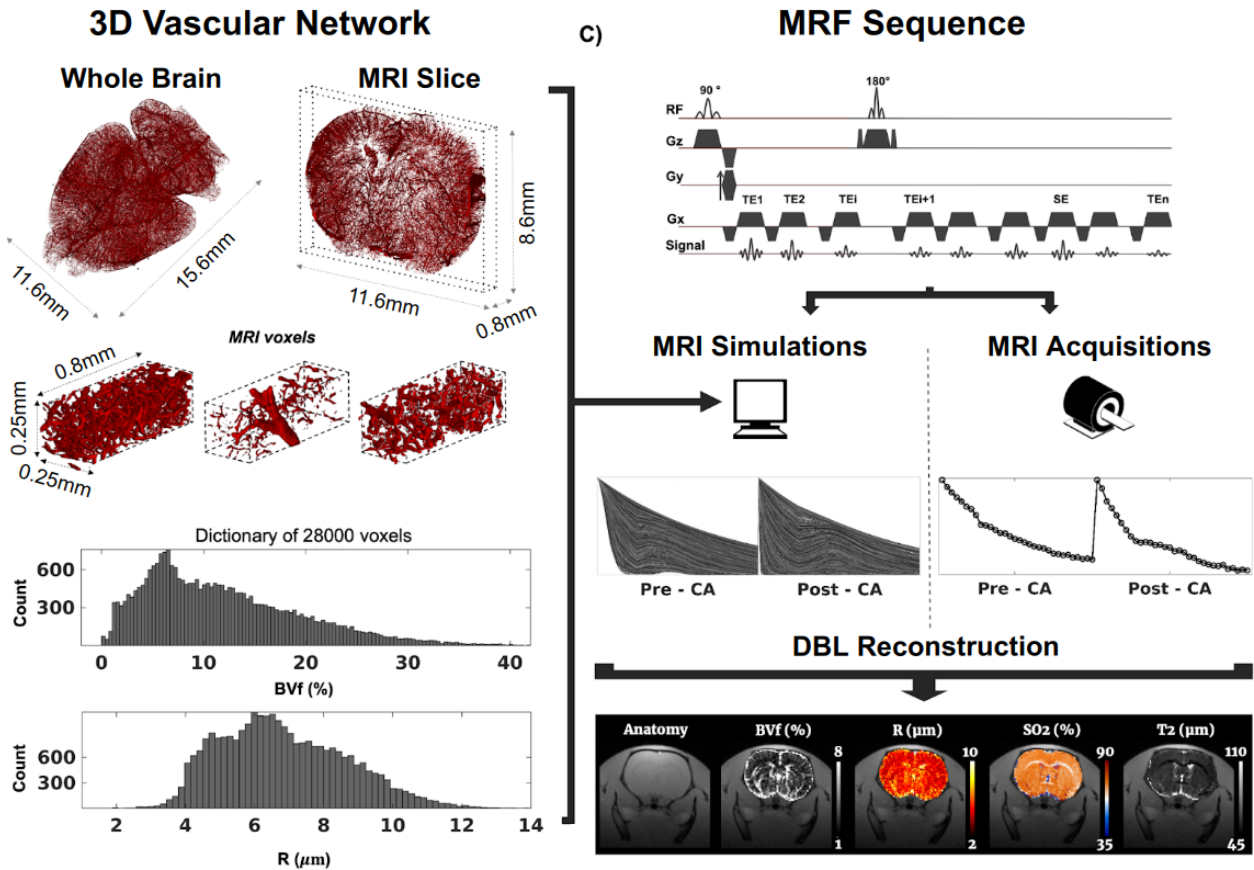


**Figure III.1.1:** Overview of the use of realistic voxels for MRvF. Whole-brain acquisitions are chopped into MRI-sized voxels, in which the vascular network is segmented. These voxels are characterized to extract their Blood Volume fraction (BVf) and mean radius (R). They are used as a simulation basis with a GESFIDSE sequence in the MRVox software. Both simulations and MR acquisitions are performed twice: before and after Contrast Agent (CA) injection. The obtained dictionary is compared against acquired data using a bayesian Dictionary Based Learning (DBL) approach to produce parametric maps.

### III.1.2.2 Generation of MRvF dictionaries

MR signal simulations are performed using MRVox, described in section II.1.2.1. For each voxel, the vascular network is represented as a binary matrix. A single  $SO_2$  value is attributed to the vessels in the voxel, resulting in a different magnetic susceptibility inside and outside the blood vessels. The  $SO_2$  values are distributed between voxels according to a scrambled Sobol series and cover the value range of [35, 90] % (Boux et al. 2021). 3D magnetic field perturbations are computed using a Fourier approach (Salomir et al. 2003). Each voxel is attributed a single  $T_2$  value, again using a Sobol series, in the range of [45, 110] ms to account for transverse relaxation. Water diffusion effects are taken into account using a diffusion kernel convoluted with the magnetization matrix (Bandettini et al. 1995; Klassen et al. 2007). In our study, all voxels have the same water diffusion coefficient ( $1,000 \mu\text{m}^2/\text{s}$ ). Simulations are performed using a main magnetic field of 4.7T.

3 dictionaries are eventually generated:

- The “3D-micro” dictionary is based on the 3D realistic voxels obtained using the microvascular data described above. The vascular network resolution is that of the segmented voxels, i.e.  $2\mu\text{m}$  isotropic.
- The “2D-synth” dictionary is based on 2D voxels, as described in the initial MRvF implementation (Christen et al. 2014b; Lemasson et al. 2016), vessels are represented as disks in the 2D voxel, with a fixed radius.
- The “3D-synth” dictionary is based on 3D voxels containing straight cylinders with variable radii. The cylinders are isotropically oriented in the volume.

Both 2D-synth and 3D-synth dictionaries were generated with BVf, R,  $SO_2$  and  $T_2$  combinations similar to those obtained in the 3D-micro dictionary. Each dictionary thus contains between 28,002 and 28,005 entries, the number varying slightly as the geometrical constraints of the cylinder generation can not always accommodate all (BVf, R) combinations. Both synthetic dictionaries use voxel networks with a  $1.94 \mu\text{m}$  isotropic resolution, also due to the constraint of the simulation tool. Examples of the three types of voxels are given in fig. III.1.2. The coverage of the vascular parameter space by each of the 3 dictionaries is similar and is shown in fig. III.1.3.

### III.1.2.3 MR Data acquisition

Animal data used in this chapter were acquired under permits 380820 and B3851610008 (for experimental and animal care facilities) from the French Ministry of Agriculture, and with the approval of the “Grenoble Institut des Neurosciences” ethical committee (National agreement n°004).

MRI data acquisition is conducted on a horizontal 4.7T Bruker (Bruker Biospin, Ettlingen, Germany; IRMaGe facility) system. Two groups of animals (n=17 total) are scanned:

- 8 healthy Wistar rats (7 weeks old,  $268\pm 23\text{g}$ , Charles River, France) are used as controls
- 9 Fischer 344 rats (7 weeks old,  $235\pm 13\text{g}$ , Charles River, France) implanted with 9L (9LGS, ATCC, American Type Culture Collection) tumors are imaged 14 to 16 days after induction

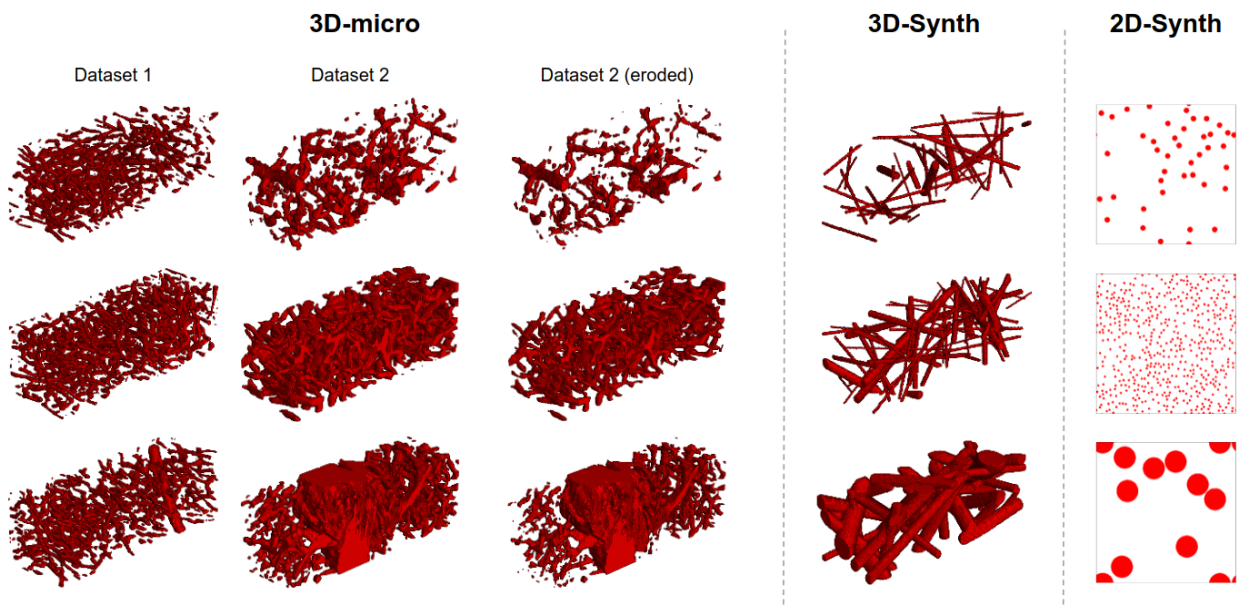


**Figure III.1.2:** Example of voxels used in the 3 dictionaries. In the 3D-micro dictionary, tried to show voxels representative of the diversity of the network. Voxels with comparable geometrical properties are shown for the two other dictionaries.

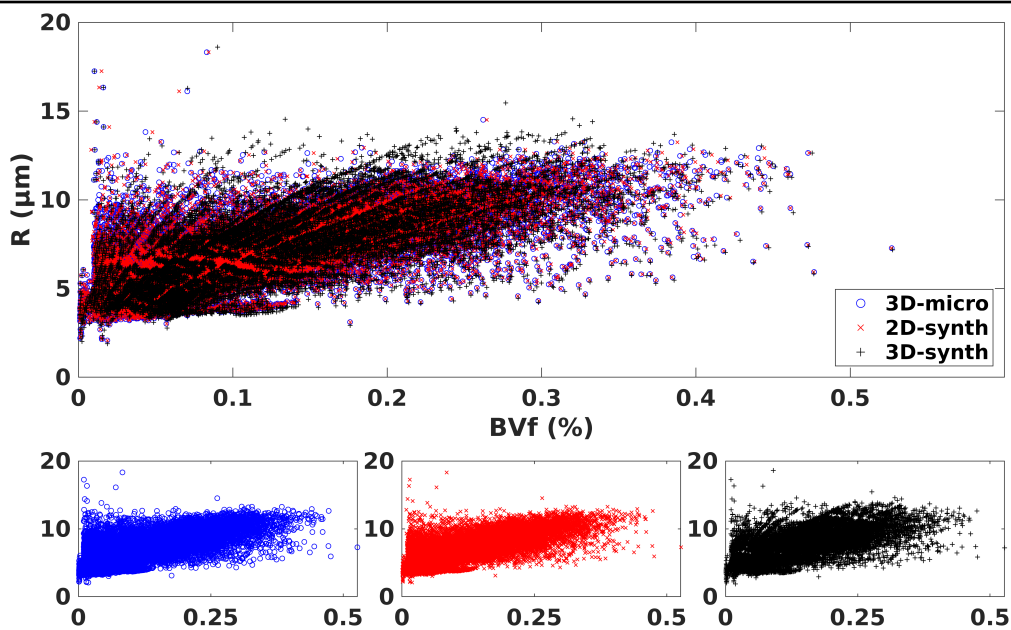


**Figure III.1.3:** Coverage of the geometrical parameter space in the three dictionaries. The top panel is a superposition of the 3 lower panels, which each show the (BVf, R) space coverage.

Anesthesia is induced by the inhalation of 5% isoflurane (Abbott Scandinavia AB, Solna, Sweden) in air, and maintained throughout the measurements with 2-2.5% isoflurane through a facial mask. The imaging protocol includes relaxometry ( $T_2$  - using a multi-echo sequence - and  $T_2^*$  - using a multi-gradient-echo sequence), ADC (3 orthogonal directions), and perfusion acquisitions, as described in [Lemasson et al. 2016](#). Vascular fingerprints are acquired using a



2D Gradient Echo Sampling of the Free Induction Decay and Spin Echo (GESFIDSE) (Ma et al. 1996) sequence, TR = 4000ms, 32 echoes,  $\Delta TE = 3.3\text{ms}$ , SE = 60ms, NEX 1, 5 slices,  $128 \times 128 \times 32$  matrix,  $234 \times 234 \times 800\mu\text{m}^3$  resolution. One GESFIDSE acquisition is performed before and one after injection of Ultrasmall superparamagnetic iron oxide (USPIO) (P904, Guerbet, France,  $200\mu\text{mol Fe/kg}$ ) and the two acquisitions are concatenated in order to produce a single fingerprint per voxel.

#### III.1.2.4 MR Data processing

All processing is performed on MP3 (Brossard et al. 2020), described in II.4.1.1. Three processing approaches are considered: two MRvF reconstructions and the original analytical approach.

For MRvF processing, two reconstruction methods are used:

- In the Dictionary-based matching (DBM) approach, the dot product of each acquired fingerprint (signal time evolution in one voxel) with the whole dictionary is computed. The dictionary entry yielding the highest value is kept as the best match and the corresponding parameters (BVf, R,  $\text{SO}_2$ ,  $T_2$ ) are used to create the parametric maps.
- In the Dictionary-based learning (DBL) approach, a Bayesian-based method (Boux et al. 2021) is used to learn the relationship between the signals and the parameters space. Once trained, the algorithm produces BVf, R,  $\text{SO}_2$  and  $T_2$  values in response to the acquired fingerprints. Estimates from the DBL method can fall outside of physiological ranges. In that case, BVf and  $\text{SO}_2$  values are clipped between 0 and 100%, and R values are clipped between 0 and  $250\mu\text{m}$ .  $T_2$  values are only clipped to 0 ms on the lower end. When visualizing maps, displayed values have different clips for better visual comparison between the different methods.

An overview of the whole process in one animal is presented in fig. III.1.1.

Microvascular properties are also calculated according to previously published methods based on analytical models (see section I.4.2).  $T_2$  and  $T_2^*$  maps obtained pre- and post- contrast agent (CA) injection (Christen et al. 2014b) are combined with the ADC map to compute the local BVf,  $\text{SO}_2$ , and Vessel Size Index (VSI, an average weighted by higher values of the vessel radius). Note that the analytically obtained parameter maps, therefore, require additional information, such as the ADC map, than is required for MRvF.

#### III.1.2.5 In vivo $\text{pO}_2$ measurements

In order to obtain reference oxygenation values in our animals,  $\text{pO}_2$  measurements are made in the tumor group after the imaging protocol using optic fiber probes (Oxylite, Oxford Optronix, Oxford, UK) and under the same anesthesia as the one described above. Using guidance from MR anatomical images, two catheters are implanted to guide the optical fibers in both the tumoral and contralateral hemispheres. Measurements are repeated between 5 and 10 times, and at two different depths (1.5 mm apart). In total,  $\text{pO}_2$  estimates are available in 6 animals, as the measurements failed in one rat and two others died before this step.

### III.1.2.6 Numerical and statistical analysis

Regions of interest (ROI) are manually drawn using MP3.

- For the control group, an ROI called “Healthy” is drawn in the striatum of the left hemisphere. The whole brain is not used to avoid the presence of the ventricles.
- For the tumoral group, lesions are manually delineated from anatomical and ADC scans (“Tumor” ROI), and contralateral ROIs (“Contra”) are drawn in the other hemisphere, trying to match both tumor location and volume.

We carefully avoid including signals from the ventricles in these ROIs. For the 4 parameters, voxel values are averaged inside each ROI, for each animal. Statistical significance between methods is evaluated through a 2-sample t-test with a 0.05 p-value threshold.

### III.1.3 Main results on control and 9L rats

#### III.1.3.1 3D micro DBL vs DBM

We present in fig. III.1.4 (top row) the results obtained in one representative animal of each group (control and tumor) using the 3D-micro dictionary and the DBL reconstruction. It can be observed that without the need of any prior information on the tissue composition, the MRvF method produces high quality BVf maps exhibiting fine details of the vasculature while flatter contrasts are obtained for R or SO<sub>2</sub> maps. Averaged values of BVf=3.1%, R=5.0 $\mu$ m and SO<sub>2</sub>=74.0% in healthy tissues are in line with previous literature reports and will be discussed below. In the tumor bearing animal, the lesion is clearly visible in all parametric maps with a global increase of BVf, heterogeneous R variations and a global increase of SO<sub>2</sub> indicating hyperoxic areas. T<sub>2</sub> maps show healthy gray matter values around 57.5ms as well as high T<sub>2</sub> in the CSF and in the tumor.

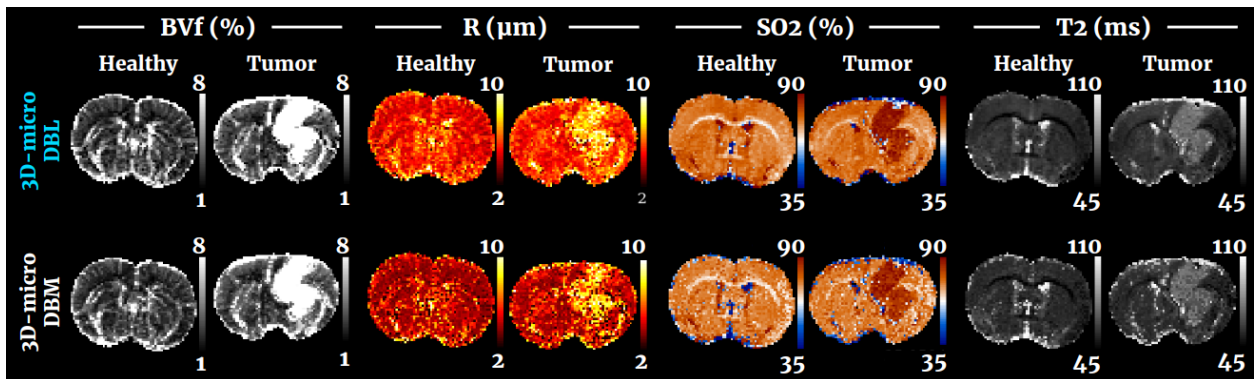


**Figure III.1.4:** Maps obtained with the DBM and DBL reconstruction methods on a healthy and tumoral animal.

The same maps obtained in the same animals, using the same 3D-micro dictionary, but analyzed using the DBM are shown in fig. III.1.4 (bottom row). The BVf maps obtained through DBL tend to exhibit a better contrast for large blood vessels. The mean R values estimated with DBL (5.0 $\mu$ m) are higher than those obtained with DBM (4.7 $\mu$ m), and the maps are less noisy. For both methods the tumor is visible. The SO<sub>2</sub> maps obtained with



DBL in healthy tissues present slightly lower values than with DBM and although the tumor is visible in both cases, the contrast is higher with DBL. Finally, the  $T_2$  maps obtained with DBL are smoother with comparable values in both healthy tissue and lesion.

### III.1.3.2 3D-micro vs synthetic dictionaries

We illustrate in fig. III.1.5 the results obtained in two other animals from both groups. Here,

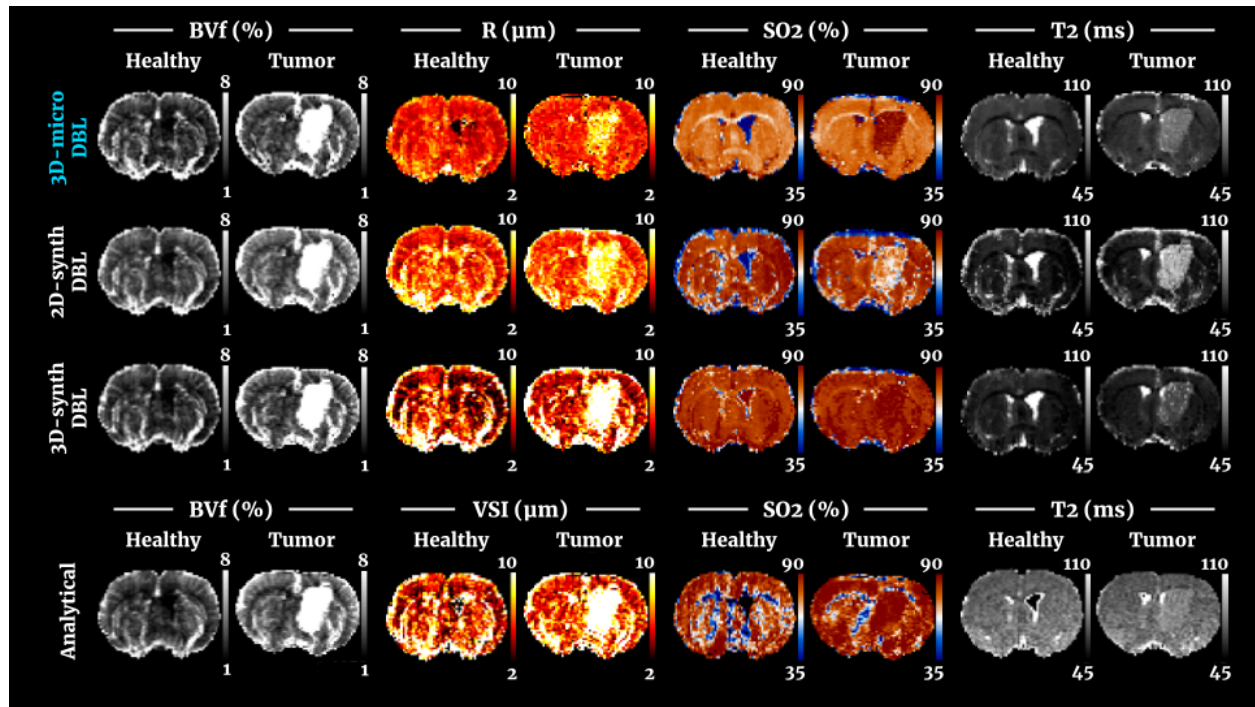


**Figure III.1.5:** Maps obtained with the different dictionaries using the DBL method on a healthy and tumoral animal.

the maps obtained with the 3D realistic model and DBL reconstruction are compared to those obtained with the cylindrical model (2D/3D simulations and analytical models) in order to assess the benefits of realistic vascular geometries. Quantitative results obtained for all groups are presented in fig. III.1.6 using boxplot representations. Crossed statistical analyses between all methods and all ROIs for the  $SO_2$  maps obtained through DBL are summarized in fig. III.1.7. The data analysis performed for DBL in fig. III.1.6 was also performed for DBM and can be found in fig. III.1.8.

For BVf estimates (fig. III.1.5 and fig. III.1.6 top left panel), all methods produce maps with visible vascular structures. No significant differences are found between the approaches in the healthy tissues (BVf about 3-4%). All maps show visible tumors, with a statistically significant increase of BVf values in the lesion for all methods (from 6% to 10% increase). The values found in the tumor with 3D-micro are, however, statistically higher than that with the cylinder approaches.

For R estimates (fig. III.1.5 and fig. III.1.6 top right panel), the 3D-micro dictionary yields maps that differ from the ones obtained with the 2D-synth dictionary. The normal-appearing

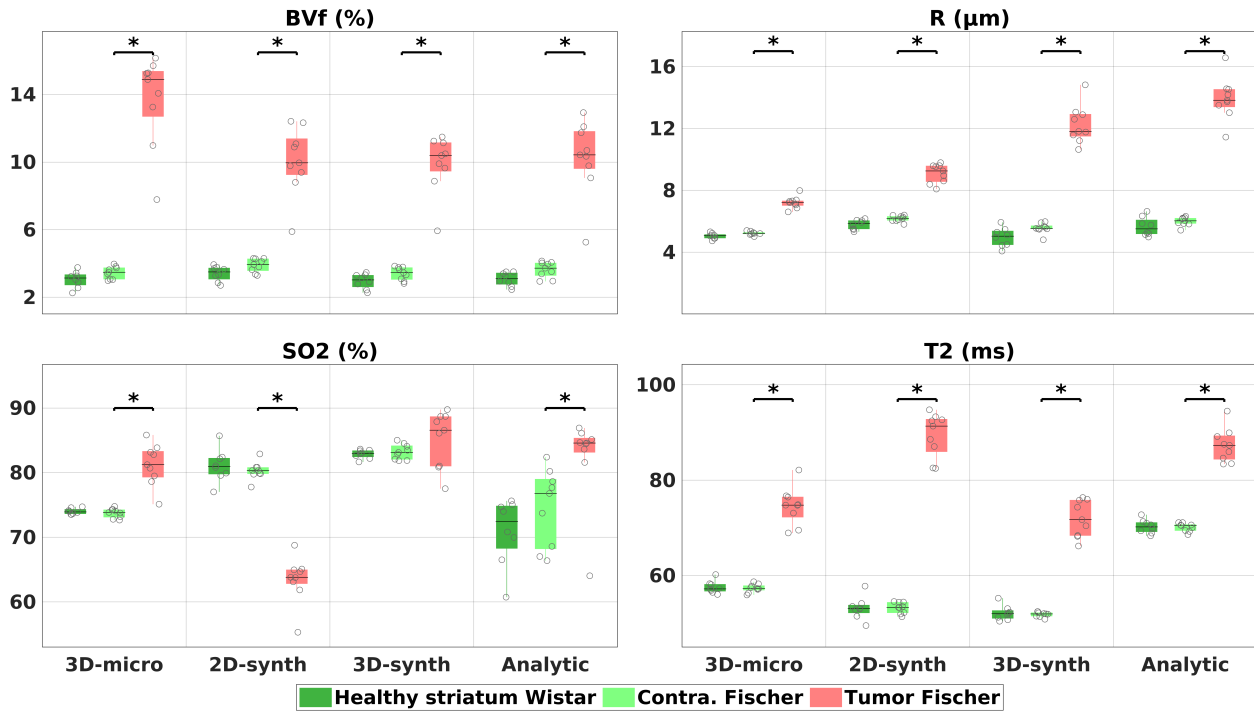


**Figure III.1.6:** Boxplot representation of parameters values in the three ROIs, obtained with the DBL reconstruction method using the three dictionaries, as well as the analytical method. Circles represent the mean value measured in each animal in the corresponding ROI.

SO2		3D-micro			2D-Synth			3D-synth			Analytic		
		Control	Healthy	Tumor	Control	Healthy	Tumor	Control	Healthy	Tumor	Control	Healthy	Tumor
3D-micro	Control		0.392	<0.001	<0.001	<0.001	<0.001	<0.001	<0.001	<0.001	0.116	0.781	0.004
	Healthy			<0.001	<0.001	<0.001	<0.001	<0.001	<0.001	<0.001	0.126	0.673	0.002
	Tumor				0.935	0.438	<0.001	0.168	0.094	0.039	<0.001	0.010	0.661
2D-Synth	Control					0.418	<0.001	0.073	0.037	0.031	<0.001	0.012	0.637
	Healthy						<0.001	<0.001	<0.001	0.005	<0.001	0.013	0.399
	Tumor							<0.001	<0.001	<0.001	0.003	<0.001	<0.001
3D-synth	Control							0.478	0.149	<0.001	0.001	0.837	
	Healthy								0.195	<0.001	0.001	0.720	
	Tumor									<0.001	0.001	0.309	
Analytic	Control										0.198	0.002	
	Healthy											0.023	
	Tumor												

**Figure III.1.7:** Table of p-values for crossed 2-sample t-test in all ROIs and for all dictionaries, for DBL SO<sub>2</sub> results. Color change at p=0.05.

tissues are also less contrasted, which is confirmed in the lower dispersion of mean values in fig. III.1.6. Mean values obtained with the 2D-micro approach are 5.0 and 5.2 $\mu$ m in ROI Healthy and Contra, respectively. The 2D-synth and analytical maps average between 5.6

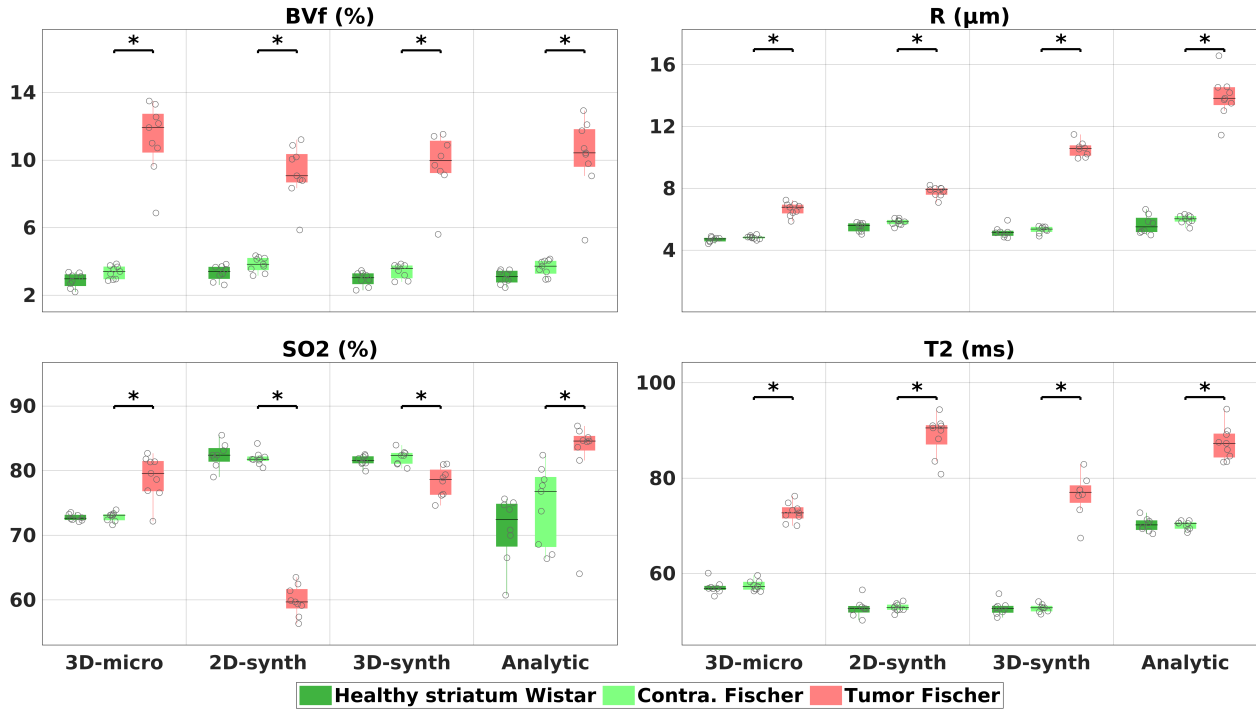


**Figure III.1.8:** Boxplot representation of parameters values in the three ROIs, obtained with the DBM reconstruction method using the three dictionaries, as well as the analytical method. Circles represent the mean value measured in each animal in the corresponding ROI.

and  $6.2\mu\text{m}$ . The tumor is visible with all methods, but the difference between non-lesion and lesion tissues is less pronounced when using the 3D-micro dictionary. In this case, we measured an average significant difference of  $2.0\mu\text{m}$  between the Contra and Tumor ROIs, while we found increases from  $2.9$  to  $7.9\mu\text{m}$  with the other methods. The tumor also appears very inhomogeneous when using the 3D-micro dictionary, where other approaches tend to saturate at the highest value of the dictionaries.

For  $\text{SO}_2$  estimates (fig. III.1.5 and fig. III.1.6 bottom left panel), the 3D-micro dictionary also produces results that differ from the other methods. Normal-appearing tissues present lower average  $\text{SO}_2$  values ( $74.0$  and  $73.7\%$ , Healthy and Contra ROIs, respectively) than those obtained through MRvF with the other dictionaries (between  $80.2$  and  $82.2\%$ ). The analytic method produces maps with a mean value in the healthy tissues comparable to that obtained with the 3D-micro dictionary, but the maps are noisy, which is reflected by the large value dispersion in fig. III.1.6. Conversely, the 3D-micro maps are flatter, which is visible in the remarkably smaller value dispersion in the healthy tissue boxplot in fig. III.1.6. The contrast between normal-appearing tissues and tumors is pronounced in the 3D-micro maps. Fig. III.1.6 and fig. III.1.7 show that only the 3D-micro dictionary and the analytical methods find a significant  $\text{SO}_2$  increase in the lesion. The increase is comparable ( $7.5$  and  $7.4\%$ , respectively) with both methods. On the contrary, the 2D-synth dictionary shows hypoxia in the Tumor ROI, while the 3D-synth dictionary yields no significant difference.

For  $T_2$  estimates (fig. III.1.5 and fig. III.1.6 bottom right panel), the MRvF maps have

comparable contrasts. The  $T_2$  maps obtained from the multi-echo sequence (analytical method) appear noisier and flatter than the  $T_2$  maps obtained with the MRvF approach (only one spin echo). Moreover, the analytical approach failed to provide  $T_2$  estimates in one ventricle, whereas all MRvF approaches yield a  $T_2$  estimate in that same area. The values estimated in the normal-appearing tissues are higher (70.3 and 70.1ms, Healthy and Contra ROIs respectively) than for the MRvF methods. The 3D-micro dictionary yields values of 57.5 and 57.3ms in the Healthy and Contra ROIs, while the 2D- and 3D-synth dictionaries produce values in the range of 51.9 to 53.2ms. In all cases, the tumor is visible and significantly distinct from the contralateral tissue. The variation seen in the lesion, compared to healthy tissues, with the 3D-micro dictionary and the analytical method are comparable, with an increase of 17.2 and 17.2ms, respectively. On the other hand, The 3D-synth and the 2D-synth yields an increase of 20.1 and ms and 36.2ms, respectively.

### III.1.3.3 Oxylite $pO_2$ measurements

Fig. III.1.9 presents the  $pO_2$  measurements. The left panel shows boxplots of the values obtained in the contralateral and tumor tissues in all the animals, combining the results from the two probed depths. The mean value in each of the considered animals is also shown. The right panel shows the values obtained in the tumor animal presented in fig. III.1.5. The single readings at each depth are given, as well as the boxplots corresponding to each hemisphere. These values clearly indicate a  $pO_2$  increase in the tumor in all animals, confirming the findings obtained with the 3D-micro dictionary and the analytical method.

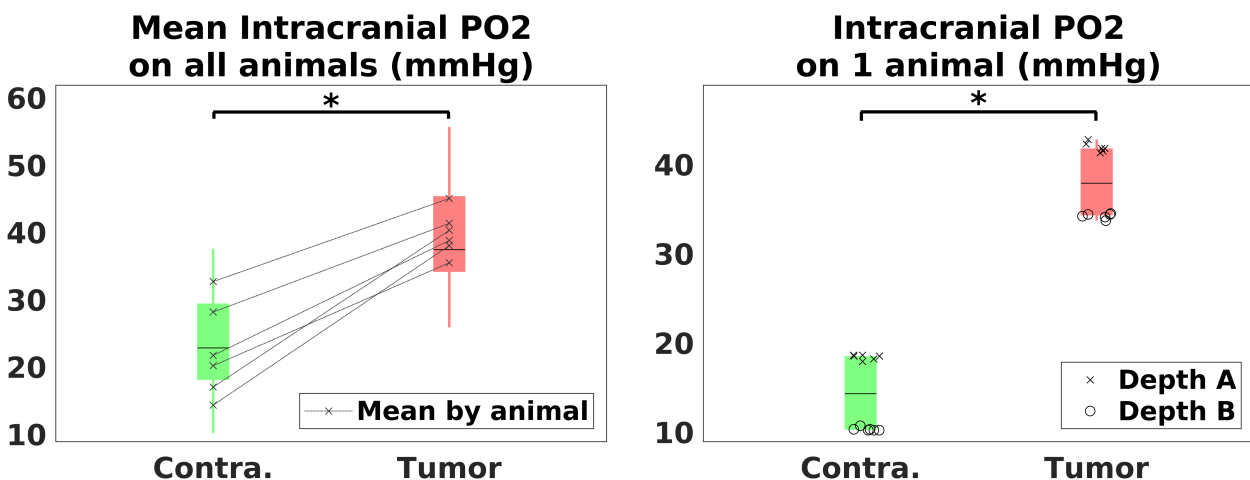


**Figure III.1.9:**  $pO_2$  measurements from the intracranial optic-fiber probe. The left panel shows a significant increase ( $p < 0.05$ ) in the  $pO_2$  measurement between the healthy and tumoral hemispheres of each animal, for all locations. The right panel shows the distribution of the repeated measurement at both depths in both hemispheres for a single animal. The increase found between the two hemispheres is again statistically significant.

### III.1.4 Additional results on C6 tumors and strokes

The same dictionaries were used on two other animal groups. The first group is composed of 7 male Wistar rats bearing C6 tumors. The second group is composed of 9 male Sprague-Dawley

rats undergoing permanent focal brain ischemia. Details on animal preparation can be found in [Broisat et al. 2018](#). The obtained  $\text{SO}_2$  maps for the C6 group are shown in fig. [III.1.10](#).

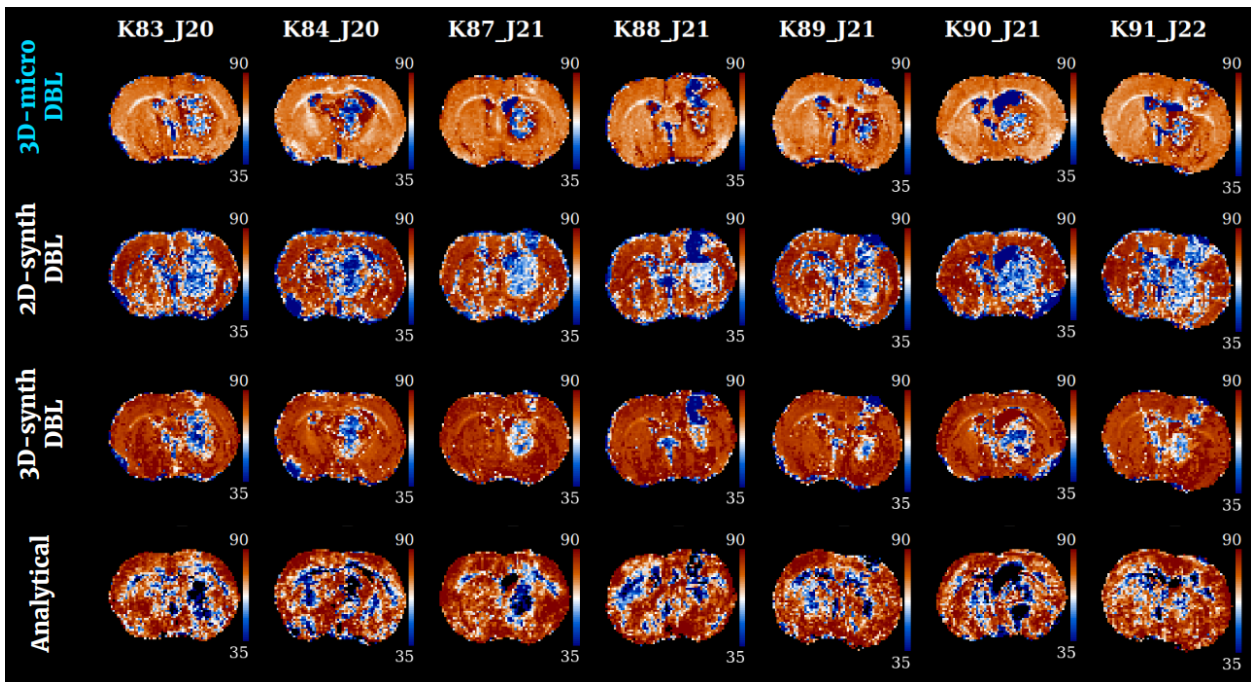


**Figure III.1.10:**  $\text{SO}_2$  maps obtained with the DBL method on C6 tumor-bearing rats. Values are clipped between 35 and 90%

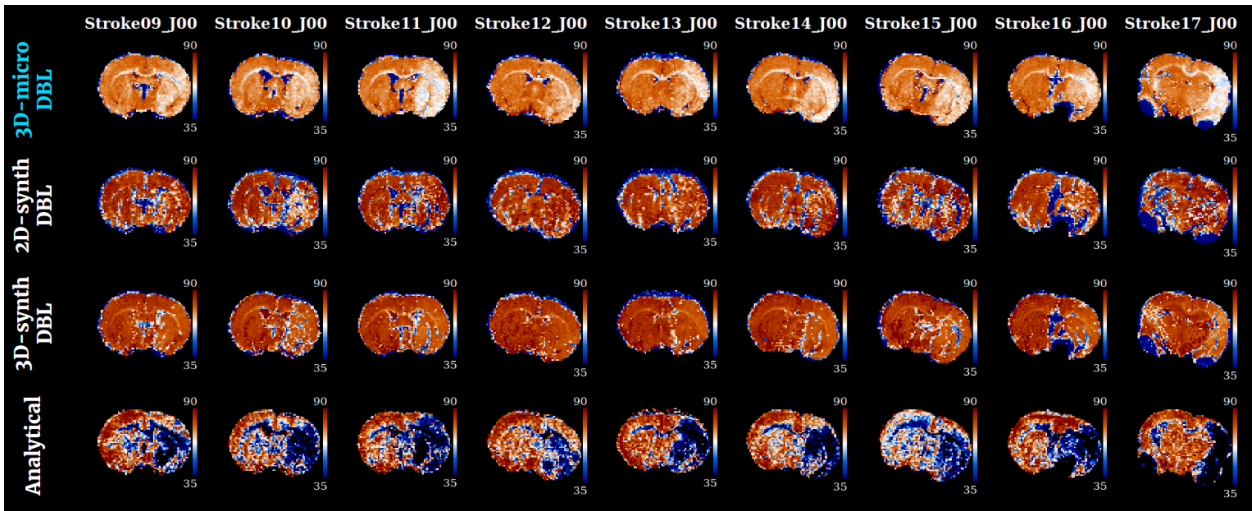
This animal group shows that our proposed method is able to separate hyperoxic and hypoxic tissues in heterogeneous tumors. The hyperoxic values are comparable to that found in the 9L group. The hypoxic values are generally low, which is expected in such an environment where necrosis is frequent. Such heterogeneous tissues require careful ROI delineation to statistically evaluate the findings. Such a task was not undertaken yet.

Fig. [III.1.11](#) shows the  $\text{SO}_2$  maps obtained in the stroke group. The affected hemisphere is clearly visible, with a moderate loss of  $\text{SO}_2$ . The analytical method often fails to provide values in the concerned hemisphere, producing black voxels. The 3D-synth dictionary shows a marginal  $\text{SO}_2$  decrease, but the values are still high. The 2D-synth dictionary shows no visible  $\text{SO}_2$  decrease in most animals.

### III.1.5 Discussion

We show in this study the possibility to include realistic vascular networks extracted from high-resolution whole-brain microscopy acquisitions into the MRvF framework. Using approximately 28,000 synthetic voxels to create the dictionary and a standard matching procedure for reconstruction, we obtain encouraging MRF microvascular maps in rat brains. In particular, the BVf maps exhibit fine details and quantitative values in the range of those previously reported using MRI perfusion techniques. It is worth mentioning that the results obtained using fewer voxels in the dictionary (<12,000) led to poor and unreliable results (data not





**Figure III.1.11:**  $\text{SO}_2$  maps obtained with the DBL method on stroke bearing rats. Values are clipped between 35 and 90%

shown). This is consistent with the difficulties already identified by [Pouliot et al. 2017](#) working with a small number of realistic voxels, and noting that the MRvF signal pattern varies even between voxels with similar vascular parameters. The following discussion considers the control and 9L groups for which statistical analysis is available.

One of the main purposes for using realistic vascular networks in MRvF was to improve the quality and precision of the maps initially obtained using the cylinder models. In particular, it was hoped that realistic simulations that include blood vessels with different shapes, densities or anisotropic orientations could capture the inherent heterogeneity of the microvascular networks. Our comparison of the different simulation approaches seems to validate this hypothesis. In healthy tissues, we find BVf estimates close to 3% with the 3D-micro dictionary. This is consistent with previous histological measurements made in similar animals ([Lemasson et al. 2013](#)), and significantly lower than BVf values found here with the 2D cylinders model (about 3.5%). The R values found with the 3D-micro dictionary (about  $5\mu\text{m}$ ) are also slightly closer to histology (about  $5\mu\text{m}$  in [Lemasson et al. 2013](#)) than the 2D-synth dictionary (about  $6\mu\text{m}$ ). The 3D cylinder models provide BVf and R results closer to the reference values than the 2D models but were often significantly different from the 3D-micro estimates. We also find significant differences between 3D-micro and cylinders approaches for the  $\text{SO}_2$  estimates. Oxygenation measurements using PET technology,  $^{17}\text{O}$  MRI, or near-infrared spectroscopy suggest that  $\text{SO}_2$  should be homogeneous and range from 55% to 75% in rat brains ([Hashem et al. 2020](#); [Horitsugi et al. 2017](#); [Zhu et al. 2013](#)). These observations are in line with the 3D-micro estimates ( $\text{SO}_2$  about 74% vs  $>80\%$  for cylinder approaches). Yet, it is not easy to conclude given the uncertainty of expected values. A better indication that the use of realistic geometries improves  $\text{SO}_2$  measurement is the clear increase in tumor  $\text{pO}_2$  measured with Oxylite, which was only observed when using the 3D-micro dictionary.

The additional results on C6 tumors and strokes show that the method we propose is also able to measure different levels of hypoxia, whether mild as in the stroke case, of more severe and with high spatial variations, as is the case for the C6 group.

For R measurements, the 3D-micro values found in the tumor are statistically different from the ones found in healthy tissues but the difference is less pronounced than with the other methods. A reason for this discrepancy could be the absence of a tumoral network in the realistic dictionary that is not entirely compensated by the learning approach. A study that would include pathological networks in the dictionary, as well as tests in other types of pathologies, could lead to a better understanding of these results. Finally,  $T_2$  values found with the MRvF approach in both healthy tissues and tumoral environment seem to agree with previous reports using standard relaxometry methods (Vonarbourg et al. 2004). However, our multi-spin echo sequence and analytical analysis provide significantly higher values than the MRvF approach. This modest variation could be ascribed to the effects of water diffusion, more pronounced in the GESFIDE sequence used for the MRvF analysis, and to the contribution of stimulated echoes, present in the multi-spin echo sequence but not in the GESFIDE. Further exploration of this difference is certainly of interest as it may carry additional information about the voxel properties.

A second purpose for using realistic networks in MRvF is the possibility to extract more information from the acquired fingerprints. In our study, we focused the analysis on the measurements of BVf, R and  $SO_2$  values. Yet, several other parameters could be extracted from the vascular networks. For example, tortuosity, global anisotropy, fractal dimension (Lorthois et al. 2010; Lorthois et al. 2014; Peyrounette et al. 2018), or distribution of oxygenation (Lininger et al. 2013; Stéphanou et al. 2017) could also impact the MR signal. For the moment, these parameters act as confounding factors in our MRF analysis but could be measured if taken properly into account and added as extra dimensions in the dictionaries. By using more complex geometries, it should also become possible to measure dynamic biomarkers such as blood flow or distribution of transit times using MRvF. Indeed, several studies have shown that combinations of angiographic data with vascular growth algorithms can generate entire synthetic brain microvasculature with closed networks and realistic properties. Such generative methods will be the focus of section III.2.

Increasing the number of dimensions in the dictionaries and the complexity of the simulations automatically impact the simulation and reconstruction times. In order to keep reasonable processing times, we use a combination of a machine-learning algorithm with a Sobol approach to sampling the parameter space. This allows, in future studies, for the addition of new dictionary dimensions such as the diffusion coefficient without increasing the size exponentially. In the current state, working on a computing server with 104 CPU cores divided into 13 groups of 8 cores each, simulating a GESFIDSE sequence on a single 3D voxel requires about 10 seconds. In order to further accelerate the process and be able to create a large variety of realistic MRF voxels, it should be possible to accelerate the simulations with GPU implementations (Wang et al. 2020a) or to create surrogate deep learning simulators (Liu et al. 2021; Yang et al. 2020). These would be trained to learn the relation between sequence parameters, dictionary parameters, and signal shape and generate dictionaries for new sequences in a fraction of the usual simulation time. Finally, it is clear that complex reconstruction will only be useful if they are linked to an efficient MRF sequence design. A number of studies have already shown great improvements in relaxometry measurements when using automatic MRF sequence optimization algorithms (Jordan et al. 2021; McGivney et al. 2020). These tools could be applied here to further improve the results, reduce the acquisition time or even remove the need for exogenous contrast injection.



## III.2 Synthetic vasculature generation: Constructive Constrained Optimization

As briefly discussed above, generating realistic vascular networks would be beneficial to further improve MRvF. Having control over the type of vascular networks used for dictionary generation would allow for more diversity and even better modeling of pathological tissues. Having such control on parameters such as vessel tortuosity or vessel density would allow to quantify them with the MRvF technique, whereas the difficulty we currently have to quantify them in segmented voxels makes them confounding factors. Several groups proposed solutions for vascular growth simulation, among which [Karch et al. 1999](#); [Stéphanou et al. 2006](#); [Hamarnah et al. 2010](#); [Caraguel et al. 2016](#). We directed our work on the so-called Constructive Constrained Optimization (CCO) generation method, described in [Karch et al. 1999](#) and [Hamarnah et al. 2010](#), and more recently in [Linninger et al. 2019](#) and [Hartung et al. 2021](#), as it was well suited with our objective of obtaining realistic vascular geometry with a rather simple implementation. This section will present our implementation of this algorithm.

### III.2.1 Principles

The Constructive Constrained Optimization [Karch et al. 1999](#); [Hamarnah et al. 2010](#); [Linninger et al. 2019](#); [Hartung et al. 2021](#) is a numerical method aiming at iteratively building a vascular tree using a graph representation. Blood vessels are represented as edges while perfusion, terminal, and bifurcation points are nodes. The CCO progressively builds a vascular network by connecting newly added nodes to the existing tree, as shown in [fig. III.2.1a](#) and [III.2.1b](#). The method is constrained by the need for homogeneous perfusion in the modeled volume, which implies constraints on the bifurcation nodes. This ensures a geometrically realistic vascular network ([fig. III.2.1c](#)). The following describes more in-depth the principles of network generation.

Blood is considered a homogeneous and incompressible liquid. The homogeneous perfusion constraint translates into an equal value of flow and pressure for all endings of our microvascular network, a condition that takes the following form for flow:

$$Q_{term} = \frac{Q_{perf}}{N_{term}} \quad (\text{III.2.1})$$

with  $Q_{perf}$  and  $Q_{term}$  the blood flows at the entrance of the tree and at the terminal nodes, and  $N_{term}$  the number of terminations of the tree. The flow is locally conserved at each bifurcation:

$$Q_{parent} = Q_{left} + Q_{right} \quad (\text{III.2.2})$$

Along segment  $i$ , the pressure difference  $P_i$  and the flow  $Q_i$  are related by the hydraulic resistance  $R_i$ :

$$\Delta P_i = Q_i R_i \quad (\text{III.2.3})$$

Each terminal node must be perfused by the same blood flow. According to [III.2.3](#), this results in a fixed resistance for each branch from the initial point of perfusion to a terminal node. Now, blood flow can be described as a Poiseuille flow of viscosity  $\eta$ , and the hydraulic

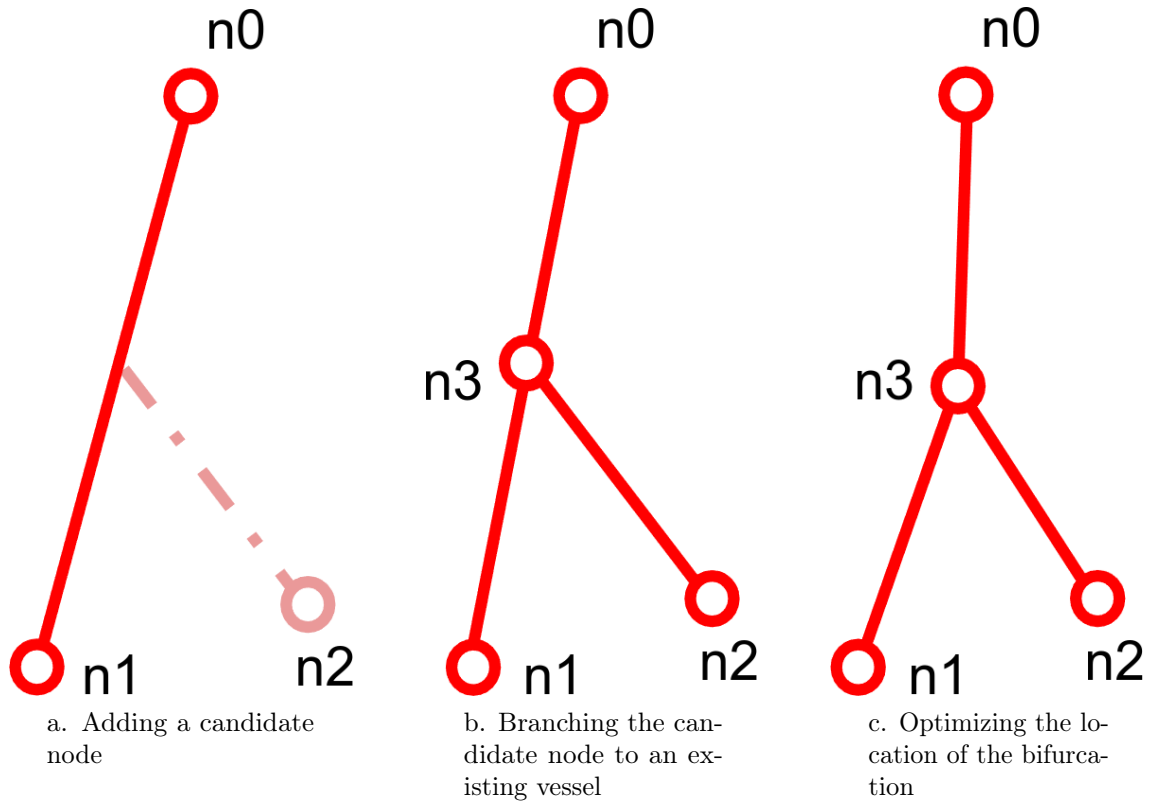


**Figure III.2.1:** Basic working principle of CCO, reproduced from [Linninger et al. 2019](#). From left to right, a new node is added to the graph, connected to an existing edge, and the bifurcation location is optimized.

resistance for a segment of radius  $r_i$  and length  $L_i$  is then written:

$$R_i = \frac{8\eta L_i}{\pi r_i^4} \quad (\text{III.2.4})$$

Substituting  $r = 1$ , one obtains

$$R_i^* = \frac{8\eta L_i}{\pi} \quad (\text{III.2.5})$$

where  $R^*$  is the reduced resistance, whose form facilitates the calculation of the resistance of a subtree, consisting of a main segment  $i$ , and the two segments *left* and *right*:

$$R_{i \text{ subtree}}^* = \frac{8\eta L_i}{\pi} + \left[ \frac{(r_{\text{left}}/r_i)^4}{R_{\text{left}}^*} + \frac{(r_{\text{right}}/r_i)^4}{R_{\text{right}}^*} \right] \quad (\text{III.2.6})$$

Murray's experimental law of radii ([Fung 1997](#)) describes the optimal proportions of a transport network (in this case flow):

$$r_{\text{parent}}^\gamma = r_{\text{left}}^\gamma + r_{\text{right}}^\gamma \quad (\text{III.2.7})$$

This law describes the tendency of the effective cross-section to shrink at a bifurcation of the network. Previous work by [Karch et al. 1999](#) established that  $\gamma \in [2, 3]$  most closely matches the ground truth.

## III.2.2 Implementations

### III.2.2.1 VascuSynth

VascuSynth is an open-source C implementation of the CCO from [Hamarneh et al. 2010](#). Input parameters are defined in a text file which is read at the beginning of a simulation run. We were able to run the code and generate vascular trees shown in fig. [III.2.2](#).

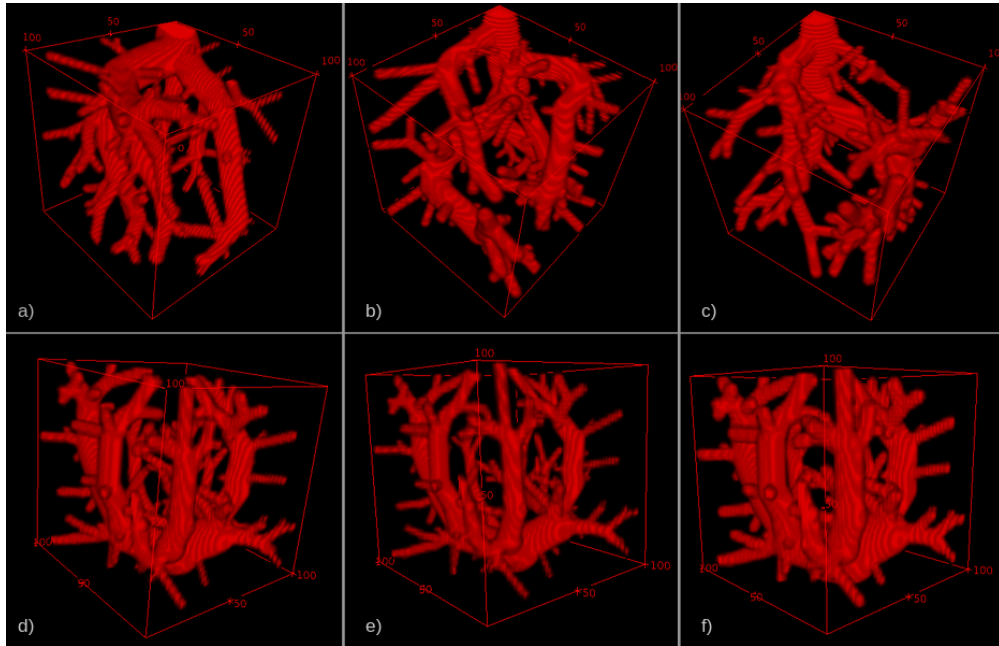


**Figure III.2.2:** Examples of trees obtained using VascuSynth. These volumetric images are generated by the code at the end of the vascular growth process, and visualized with ImageJ.

The code requires specific versions of libraries and compiler, which made its use only possible on a dedicated virtual machine, severely limiting practicality and computational power. The FOV and resolution controls were not suited for our projected use, being dependent one on the other. Furthermore, the code only allows for the growth of a single vascular tree, where state-of-the-art studies show the possibility of growing simultaneously an arterial and venous tree and connecting them ([Hartung et al. 2021](#)). It was thus undertaken to develop our own CCO implementation to better exploit our computation stations and gain flexibility. The following will detail the steps required, as described in [Hamarneh et al. 2010](#).

#### III.2.2.2 Matlab implementation

The data structure used is that of a Matlab directed graph, which ensures a chronological naming of the nodes and edges. The nodes are given the following properties:

- a name (e.g.  $n0$ )
- 3D coordinates ( $x, y, z$ )
- the names of other nodes to which it is linked when it is the case, i.e. a parent and two children nodes

- a boolean indicating if it is a terminal node

and the edges the following:

- the name of the nodes defining them (e.g.  $n0$  and  $n1$ )
- the 3D coordinates of their middle point
- their length
- the radius of the corresponding vessel
- the flow  $Q$  running through them
- the reduced resistance of the tree portion that is below them (cf. eq. III.2.6)

### Initialisation

The generation space is initialized as a bloc of dimensions (FOVx, FOVy, FOVz). A perfusion point is placed, typically in the middle of one of the sides of the volume. The perfusion flow  $Q_{perf}$ , the number of terminal nodes  $N_{term}$  and the perfusion and terminal pressures  $P_{perf}$  and  $P_{term}$  are given.

A first terminal point is randomly selected, an edge is created between these two nodes and attributed the perfusion flow value  $Q_{term} = Q_{perf}/N_{term}$ . Its length  $L$  and resistance  $R^* = 8\eta L/\pi$  are computed, as well as the coordinates of its middle point.

### Adding a new terminal node

A new terminal point is randomly selected. The case corresponds to fig. III.2.1a. We will create a new edge between this node and the middle of an existing edge. Choosing the right branching point will be discussed below. Following the example of fig. III.2.1a, the candidate node is called  $n2$ , the branching node  $n3$  is created in the middle of the edge  $n0$ - $n1$  which is removed. The nodes are then connected by edges  $n0$ - $n3$ ,  $n3$ - $n1$  and  $n3$ - $n2$ . Node  $n3$  is not terminal, contrary to  $n1$  and  $n2$ . The two edges connected to terminal nodes are given a flow  $Q_{term}$ , and their reduced resistance is computed with III.2.4.

### Constrain the tree

We now need to satisfy the flow and resistance constraints presented above. The flow in each edge above the newly added terminal is increased by  $Q_{term}$ , up to the perfusion edge, which thus has a flow of  $Q_{perf} = NQ_{term}$  with  $N$  the number of terminal nodes placed so far. In the same fashion, using equation III.2.6, the reduced resistance of the whole tree above the newly added node is updated up to the perfusion edge. The radius of the perfusion edge can now be computed using

$$r_{perf} = \left( \frac{R_{perf}^*}{R_{perf}} \right)^{1/4} \quad (\text{III.2.8})$$

which, considering the pressure drop along a branch  $i$

$$\Delta P = Q_i R_i \quad (\text{III.2.9})$$

rewrites as

$$r_{perf} = \left( \frac{Q_{perf} R_{perf}^*}{P_{perf} - P_{term}} \right)^{1/4} \quad (\text{III.2.10})$$

where all terms are known. The tree has now been updated for flow and resistance from bottom to top, where the perfusion radius is known. The next step is to go down the tree, computing the radii on the left and right sides of each bifurcation, and obtain a realistic geometry, matching the constraints imposed.

To do so, starting from III.2.7, dividing by  $r_{left}^\gamma$ , one gets

$$f_{left} = \frac{r_{left}}{r_{perf}} = \left(1 + \left(\frac{r_{left}}{r_{right}}\right)^\gamma\right)^{-1/\gamma} \quad (\text{III.2.11})$$

and the same can be done with  $r_{right}$ . Knowing the ratio  $f_{left}$ , a simple multiplication by  $r_{perf}$  would give  $r_{left}$  (same for  $r_{right}$ ). From III.2.8 we derive

$$R = \frac{R^*}{r^4} \quad (\text{III.2.12})$$

and the pressure drop between the perfusion and any terminal nodes being  $P_{perf} - P_{term}$ , from III.2.10 one gets

$$\frac{r_{left}}{r_{right}} = \left(\frac{Q_{left}R_{left}^*}{Q_{right}R_{right}^*}\right)^{1/4} \quad (\text{III.2.13})$$

Starting from the perfusion edge and going down the tree, using this ratio  $r_{left}/r_{right}$ , the radii of every edge can be computed.

These steps were implemented on Matlab in a recursive way, the structure of the tree being well suited for this kind of progression. Going up a branch only stops when reaching the perfusion node, which is the only one without a parent node. From there, the recursive function going down the tree is called on both children trees at each bifurcation and stops when it reaches a node flagged as terminal.

### Optimizing the tree: choosing the right branching point

We are now able to add a branch to an existing tree while respecting the constraints imposed for realistic radius evolution along branches, which allows for iterative growing. Yet, the point of the tree to which add the new branch needs to be carefully chosen to ensure a realistic global shape of the tree. The following will describe the steps to take to optimize the addition of a new node in the tree.

When adding a new terminal node, all the middle points of existing edges are potential branching points. However to avoid too long computation time we will not consider them all. The literature [Karch et al. 1999](#) informs that the length of the edges is generally bounded. That implies that the branching points resulting in the shortest new edges are generally preferred. Yet the edges should not be too short either. The VasculSynth implementation actually uses an oxygen demand map of the same size as the modeled volume. New nodes will more likely be added in regions of high demand. Oxygen perfusion around the vessels is modeled to modify the oxygen demand map each time a new edge is added. We did not implement this solution yet and used the simpler solution of user-specified  $[L_{min}, L_{max}]$  boundaries. The distance between the new terminal node and all the middle points of the edges is computed. Middle points resulting in new edges outside the length boundaries are

removed from the list of the potential branching points.

The remaining edges are tested for collision with the existing tree, and again those not respecting these conditions are removed from the potential new edges. A graphical illustration is given in fig. III.2.3a.

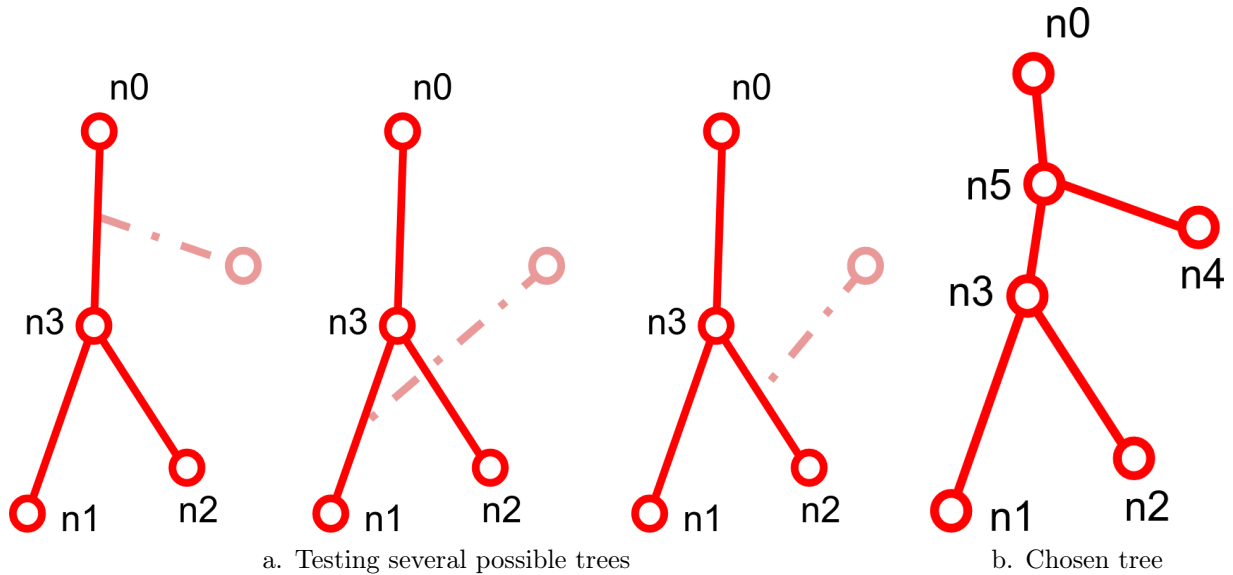


**Figure III.2.3:** Graphical illustration of tree optimization. (a) shows how a new node could be connected to an existing tree. (b) shows the resulting tree, after a solution was selected and the bifurcation position optimized.

Deciding which of the remaining potential branching points to choose will now be an optimization problem. Our aim will be to select the branching that results in a tree minimizing the cost function

$$\sum_{\forall j} L_j^\mu r_j^\lambda \quad (\text{III.2.14})$$

where increasing  $\mu$  will give shorter edges and larger radii edges, and increasing  $\lambda$  will tend to reduce the radii. Using  $\mu = 1$  and  $\lambda = 2$  would minimize the total tree volume, which is the option we chose in this implementation for its intuitiveness. We start by sorting the potential edges by their length, keeping the 5 shorter ones, as they would better minimize the cost function.

For each of the five candidates the position of the bifurcation will be optimized to minimize III.2.14, as done between fig. III.2.1b and III.2.1c. To simplify this operation, the plane of the bifurcation defined by  $[n0, n1, n2]$  is rotated to the plane  $z = 0$ , see fig. III.2.4. A gradient descent method is then applied to move  $n3$  in order to minimize the cost function. For each tested position of  $n3$  the tree updating described above is performed. Once an optimal position is found, the rotation is reversed to replace the bifurcation in its plane. This temporary tree is stored, along with the value of its cost function. This is done in parallel for the 5 candidates, and the one with the lowest cost is kept, the others being discarded.

This optimization of the bifurcation position differs from that of VasuSynth, which only optimizes along the existing edge. We designed ours based on the works of [Linninger et al. 2019](#).

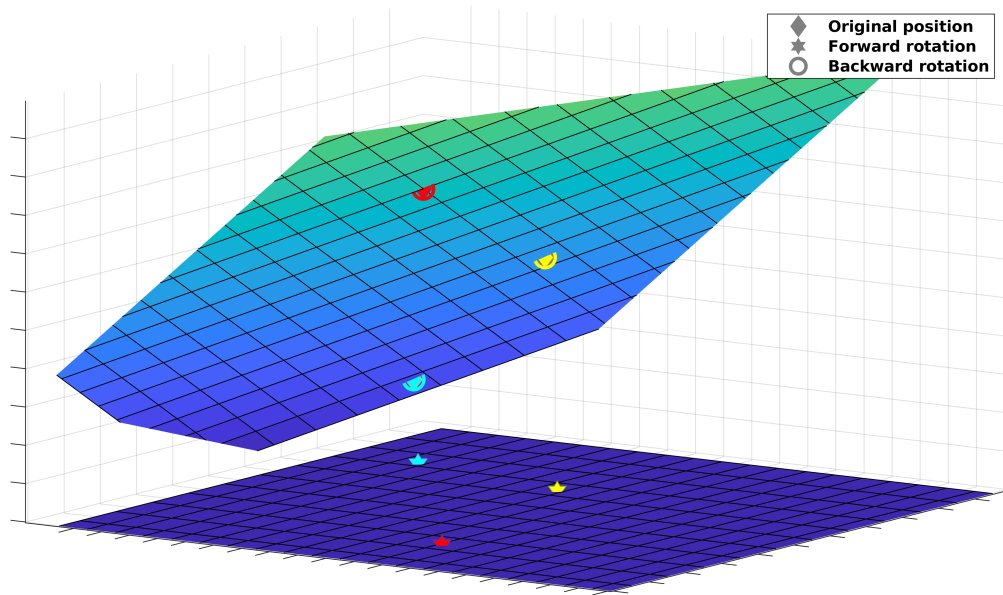


**Figure III.2.4:** Demonstration of the rotation from the bifurcation plane to  $z = 0$ . The rotation is tested back and forth to ensure a correct bifurcation position after optimization.

The tree has been added a node and updated. A new node can be randomly generated and the cycle restarts, up to the point where  $N_{term}$  terminal nodes have been placed. This code is publicly available on GitHub (Delphin 2022).

A work-in-progress version is also available, which develops two trees one after the other. Inspired by Linninger et al. 2019, it should be possible to grow two vascular trees in the same volume corresponding to the arterial and venous networks. Using different values of  $P_{perf}$  and  $P_{term}$  would ensure realistic geometries.

### III.2.3 Results

We validated the bifurcation optimization on simple cases, that behave as expected: the bifurcation moves to a point that corresponds to a decrease of the cost function. Fig. III.2.5 gives an example of a test case. We have been able to generate trees and to represent them as graph objects, with the width of the edges proportional to their radii, or as 3D cylinders with radii drawn to scale, as shown in fig. III.2.6. It is easy to generate bigger networks, at the cost of computation time. Fig. III.2.7 shows a tree with 50 terminal points. We generated even bigger trees, up to 300 terminal nodes, but the amount of edges makes their graphical representation illegible.

We have also been able to build two trees in the same volume, with  $N_{term} = 50$  in both cases, as displayed in fig. III.2.8. This kind of generation is very time consuming, making its fine-tuning quite impracticable for the time being.

Overall, this tool is flexible, easy to modify and maintain, and produces vascular trees that meet our expectations. Fig. III.2.9 compares the distribution of vessel diameters  $D$  in a graph generates with 300 terminal nodes to the distribution measured in non-terminal vessels



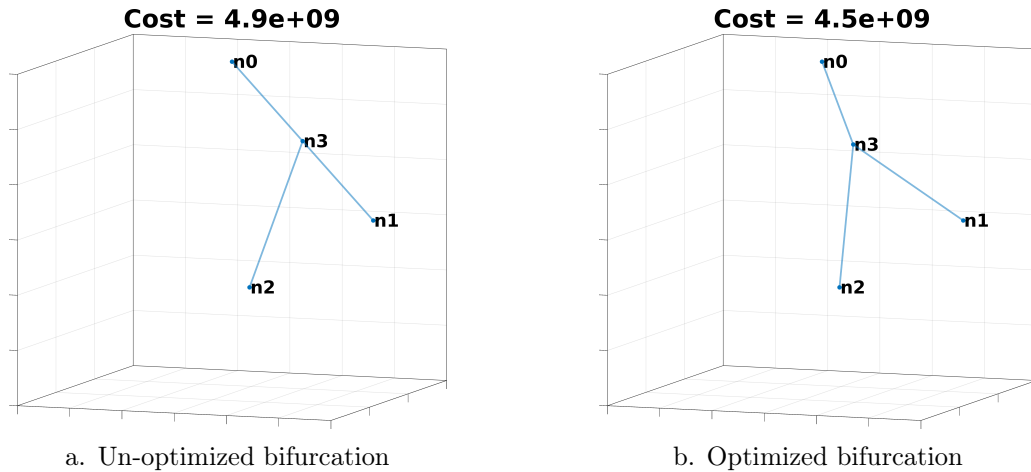


**Figure III.2.5:** Example of an optimization of the bifurcation position. The objective cost correctly decreases after the optimization.

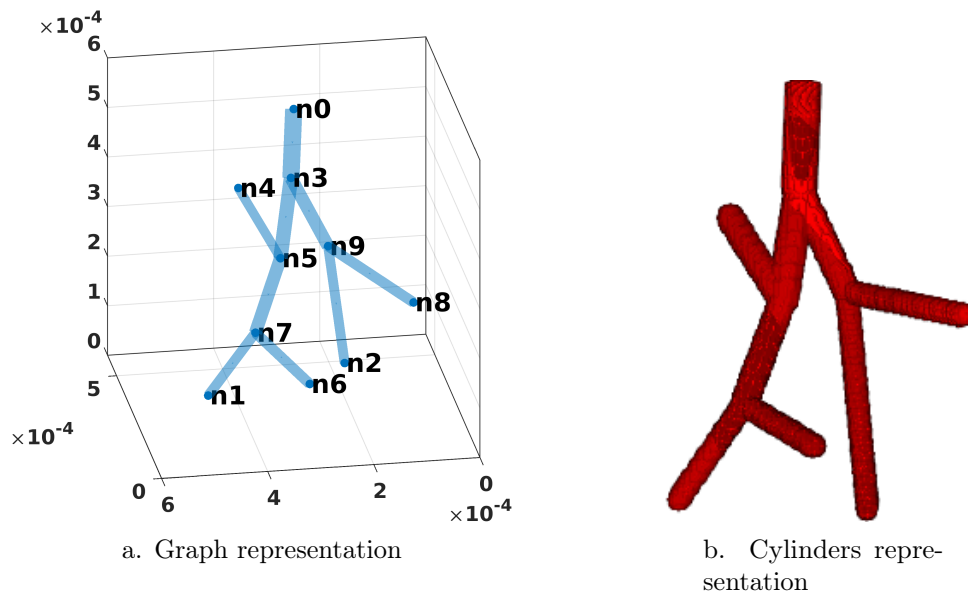


**Figure III.2.6:** Example of a small graph, with 5 terminal nodes,  $Q_{perf} = 1.10^{-4}m^3.min^{-1}.kg$ ,  $P_{perf} = 130mmHg$ ,  $P_{term} = 80mmHg$ ,  $N_{term} = 5$ ,  $FOV = 0.21mm^3$ ,  $L_{min} = 150\mu m$ ,  $\gamma = 3$ , generated in 13 seconds

in the human brain, published in [Lauwers et al. 2008](#). We considered our whole graph, as our ultimate goal is to fully connect two trees similar to the one used here. Our CCO implementation produces a  $D$  radii distribution similar to that found in the literature, although the values found differ. This discrepancy comes from input parameters used to generate the studied graph. Such values are not measured in [Lauwers et al. 2008](#), but they likely differ from the ones we used.

The authors found that the  $1/\sqrt{D}$  distribution should fit a skewed gaussian, which is not our case. This result is nevertheless encouraging, due to the many improvements that can be done to our code.

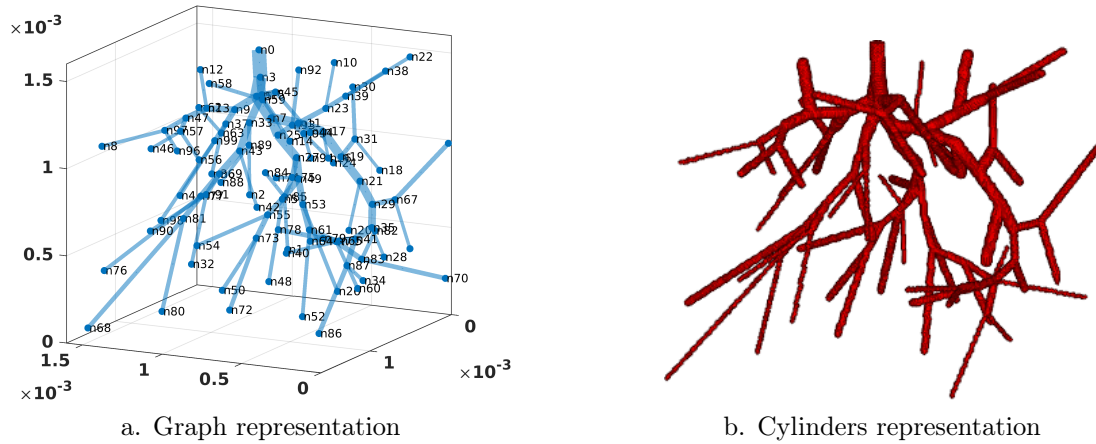


**Figure III.2.7:** Example of a small graph, with 5 terminal nodes,  $Q_{perf} = 1.10^{-4} m^3 \cdot min^{-1} \cdot kg$ ,  $P_{perf} = 130 mmHg$ ,  $P_{term} = 80 mmHg$ ,  $N_{term} = 50$ ,  $FOV = 4.1 mm^3$ ,  $L_{min} = 150 \mu m$ ,  $\gamma = 3$ , generated in 1031 seconds

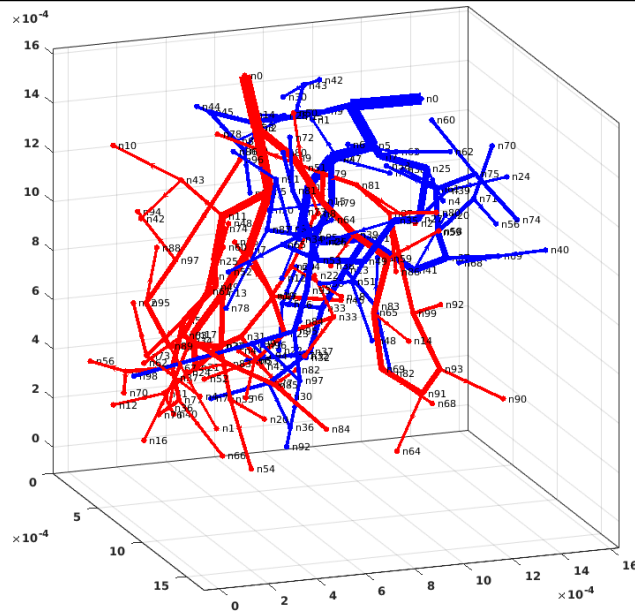
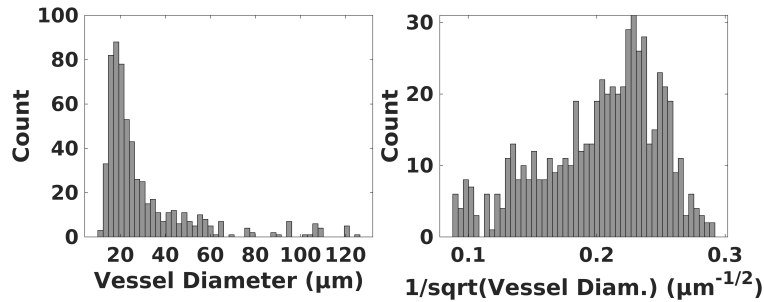


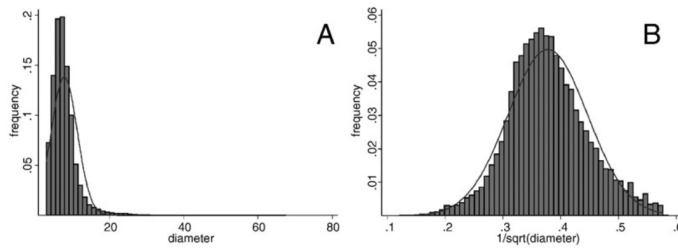
**Figure III.2.8:** Double vascular tree generated with CCO

The tool suffers from a rather long computation time, despite the parallel evaluation of the 5 candidate trees at each new node addition. Matlab is of course not the best language for this kind of tasks, and it could be interesting to re-write this program in a more computational-efficient one now that we have a better understanding on the CCO method.

In the case where two trees are generated, implementing the closing method from [Hartung et al. 2021](#) would allow to obtain a closed, balanced network.



a. Distributions in a graph generated with 300 terminal nodes



b. Distributions found in the literature

**Figure III.2.9:** Comparison of diameters distribution between our CCO implementation and literature observations. (a) shows two different representations of the diameter distribution ( $D$  and  $1/\sqrt{D}$ ) in a graph generated with our CCO implementation. (b) shows the same representations of distribution observed in the human brain, from [Lauwers et al. 2008](#).

### III.3 Conclusion and future perspectives

This chapter presented our work towards using realistic 3D vascular networks as a basis for MRI simulations. The first section presented the MRvF results obtained with synthetic 2D, synthetic 3D and image-segmented 3D networks. The improvement on the quantification of vascular properties brought by the realistic 3D networks seems to be well worth the computation time, which encourages us to pursue further developing tools to obtain such networks. The results presented here were partially presented in international conferences and should be the object of a peer-reviewed publication. While segmenting databases of fine-scale imaging from the literature is a solution, it is likely that the shared data will not cover all the pathological cases one would want to study with MRvF. In addition, segmenting closed networks seems impracticable. It would require extremely good brain preparation, imaging, segmentation and reconstruction, which are no simple tasks.

A convenient solution giving access to closed networks with complete user control on all the parameters is to generate numerical networks using physical and physiological constraints, as we did in the second section of this chapter. The tool presented here is already functional, but is still under development, as a proof of concept at the very least. It indeed suffers from long computation times, which should be solved by a new implementation. The potential of CCO is nevertheless extremely interesting. By implementing a closing method to make generated arterial and venous trees, such as done in [Hartung et al. 2021](#), one obtains a fully

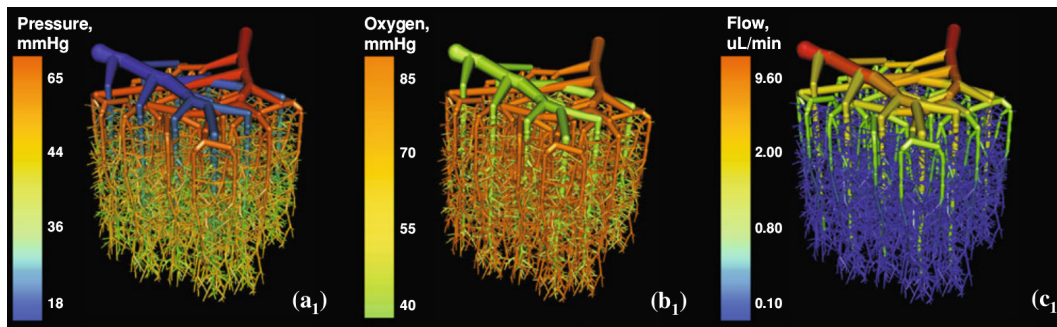


**Figure III.3.1:** Parameters variation along the branches, from [Linninger et al. 2013](#)

closed network. It should then be possible to perform simulations of blood flow,  $pO_2$ , and  $SO_2$  distributions and to compare the results to MRF acquisitions ([Lorthois et al. 2011a](#); [Lorthois et al. 2011b](#); [Linninger et al. 2013](#); [Stéphanou et al. 2017](#); [Peyrounette et al. 2018](#)). In that case, realistic simulations could also be used within the MRF ASL technique ([Su et al. 2017](#)) or to follow the bolus of exogenous contrast agents. Such physiological simulations are already under study, as demonstrated in figure [III.3.1](#). Using such results in our MRvF simulation tool would give us both geometrical and physiological realism. We expect this to improve our results further, being better able to represent healthy as well as pathological vascular networks.

We only generated rather small networks in the present work, but the CCO can be applied to large volumes, such as a whole mouse brain hemisphere, as done by [Hartung et al. 2021](#) and shown in fig. [III.3.2](#). The authors used the CCO method to build the different scales of the

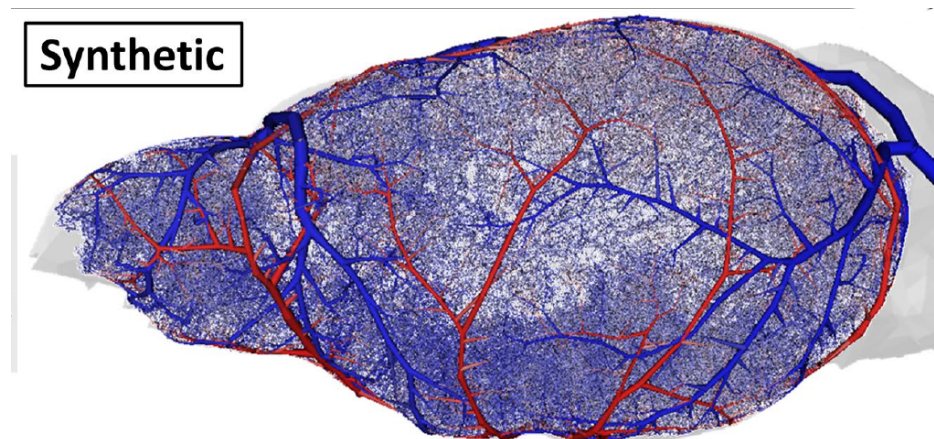


**Figure III.3.2:** Mouse hemisphere built with CCO built from large vessels observed with  $\mu$ CT, from [Hartung et al. 2021](#)

vascular network of a whole mouse hemisphere using large-scale vessel imaging performed with  $\mu$ CT as an initial graph. Such a large volume could be chopped in MRI-size voxels to use in our simulation tool, along with the time-varying vector of parameters associated.

To explore the possibility of imaging whole animal brains at a fine scale, both for whole-network segmentation or to obtain a basis for CCO generation, we performed phase-contrast imaging on a mouse brain at the European Synchrotron Radiation Facility (ESRF) in Grenoble



(fig. III.3.3a) with the help of Dr. Ludovic Broche. The depth of the technique will not be discussed here, but it allows high-resolution ( $<1\mu\text{m}$ ) imaging of soft tissues with very good contrast. Two healthy mice brains were used, as shown in fig. III.3.3b. Fig. III.3.3c give more details on the experiment conducted.

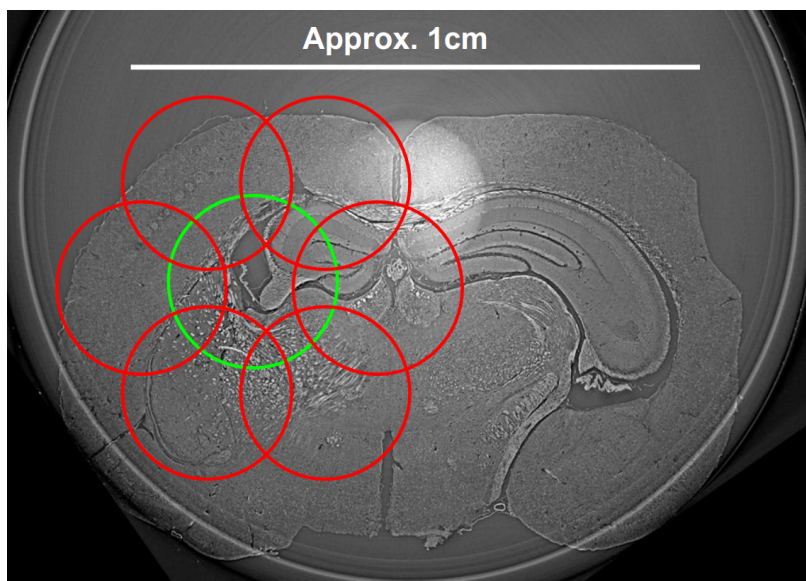
The data was not processed yet, but we hope to be able to stitch the fine-scale volumes together and perform segmentation and reconstruction of the vascular network. The coarser-scale images would be used to obtain an angiography of the large vessels. If this experiment on healthy brains meets expectations, a second experiment could be tried with tumoral brains. The tumoral tissues are indeed hard to image at such a fine scale with usual techniques that imply mechanical brain slicing, due to their fragility.



a. The ESRF, photo from esrf.fr



b. Mice brains to be imaged



c. A slice of a mouse brain imaged at  $3\mu\text{m}$  iso., with a graphical representation of the volumes scanned at  $0.65\mu\text{m}$  iso.

**Figure III.3.3:** Phase-contrast imaging at the ESRF. The brains were prepared by Nora Collomb from the GIN. After PBS perfusion of the vascular network to rinse the blood, the brains were bathed in solutions of ethanol of increasing concentration, up to 80%. Only one brain could be imaged, with an isotropic resolution of 3 microns first, before acquiring several overlapping volumes with an isotropic resolution of 0.65 microns.



## CHAPTER IV

---

# DESIGNING EFFICIENT SEQUENCES FOR MRvF

---

In the previous chapter, we showed that it is possible to improve the performance of MRvF using advanced numerical simulations to generate dictionaries. Another obvious way to obtain better estimates (or to reduce the acquisition times) is to work on the acquisition part. In the first implementation of MRvF, a multi-gradient-echo sequence (GESFIDSE) was chosen because it was known from previous quantitative BOLD experiments for its sensitivity to microvascular properties. However, the used fingerprint (ratio post- / pre-CA) has not been properly quantified, especially for  $\text{SO}_2$  measurements. Furthermore, the MRF concept allows in theory the use of any type of acquisition sequence, provided that it is sensitive to the parameters of interest and that there is bijectivity between the parameters and signals spaces, even in the presence of noise. This opens new possibilities for using unconventional acquisitions. In the following chapter, we introduce two simple tools that we used to assess MRvF sequence sensitivity to blood oxygenation. We first used these methods to assess the potential of GESFIDSE and other multi-echo sequences for  $\text{SO}_2$  measurements and show that a simple reorganization of the echo times can already improve the estimates. Second, using literature search and numerical simulations, we identified new types of acquisition patterns based on bSSFP sequences acquired in the transient and in the steady-state regimes with specific RF phase cycling schemes. These optimizations led to potential MRvF sequences that should provide  $\text{SO}_2$  estimates without the need for contrast agent injection.



---

**CONTENTS**


---

<b>IV.1</b>	<b>Methods to evaluate the encoding capacity of a sequence</b>	<b>119</b>
IV.1.1	Point-wise standard deviation of the dictionary . . . . .	119
IV.1.2	Monte-Carlo method . . . . .	121
<b>IV.2</b>	<b>Studies on multi gradient echo sequences</b>	<b>122</b>
IV.2.1	In-silico fingerprint evaluation . . . . .	122
IV.2.2	Evaluation on retrospective pre-clinical data . . . . .	126
IV.2.3	Limitation of GESFIDSE based sequences . . . . .	127
<b>IV.3</b>	<b>Studies on balanced SSFP-based sequences</b>	<b>127</b>
IV.3.1	Review on bSSFP BOLD sensitivity . . . . .	127
IV.3.1.1	Steady-state regime . . . . .	128
IV.3.1.2	Transient-state regime . . . . .	134
IV.3.1.3	Potential for MRvF . . . . .	135
IV.3.2	In-silico fingerprint design . . . . .	137
IV.3.2.1	Test of $T_2^*$ -sensitive MRF fingerprints . . . . .	137
IV.3.2.2	Optimization of potential bSSFP MRF sequences . . . . .	138
IV.3.3	Preliminary in vivo results . . . . .	143

---

## IV.1 Methods to evaluate the encoding capacity of a sequence

Choosing the right fingerprint is essential for MRF, and reproducible fingerprint evaluation tools are needed to quantify their encoding capacity, that is, their capacity to estimate the parameters of interest. The terms “sequence”, “pattern”, “fingerprint” and “acquisitions” are often used as synonyms, which can be misleading. In the following:

- “Sequence” will be used to talk about the actual MR sequence, consisting of RF pulses, TE and TR timing, gradients etc.
- A “fingerprint” is created using one or several sequences. It can merely be the signal coming from the sequence, as classically done in [Ma et al. 2013](#) and most of the MRF studies, or a combination of signals, as done in [Christen et al. 2014b](#) and [Lemasson et al. 2016](#).
- “Signals” are the result of acquisitions or simulations of a fingerprint. In ambiguous case, their origin (acquired or simulated) will be precised.

### IV.1.1 Point-wise standard deviation of the dictionary

A first rather intuitive idea to assess the encoding capacity of a fingerprint is to measure how much the shapes of the simulated signals in a dictionary vary when the simulation properties change. These variations can be plotted by fixing all properties but one, as illustrated in fig. [IV.1.1](#). Here, the fingerprint used is that from [Ma et al. 2013](#), and the effects of  $T_1$  and  $T_2$  are plotted separately. One can notice the large signal shape variation on the first 200 pulses when  $T_1$  varies. This is not the case for  $T_2$  variations and illustrates the effect of the initial inversion pulse. Building on this concept, one can compute the point-wise standard deviation

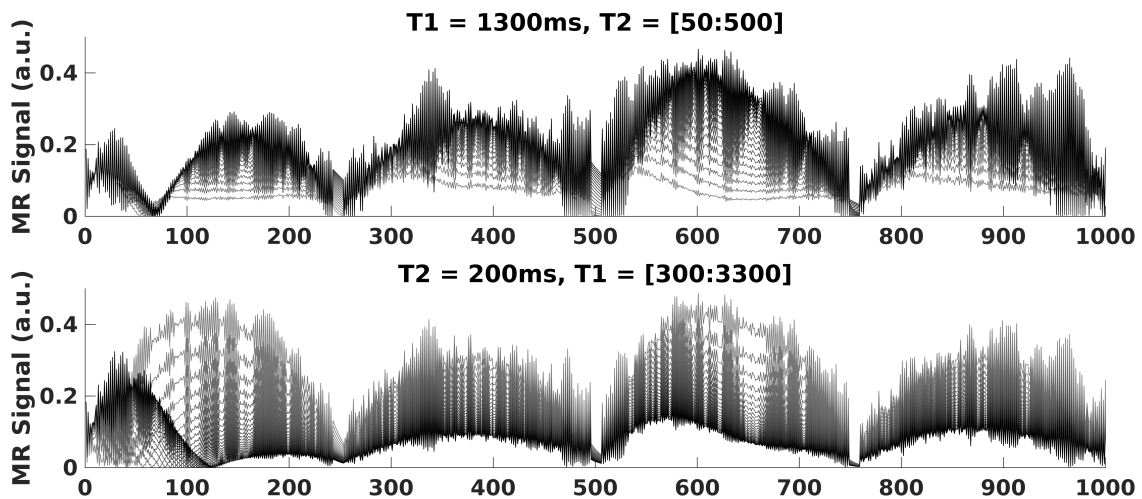
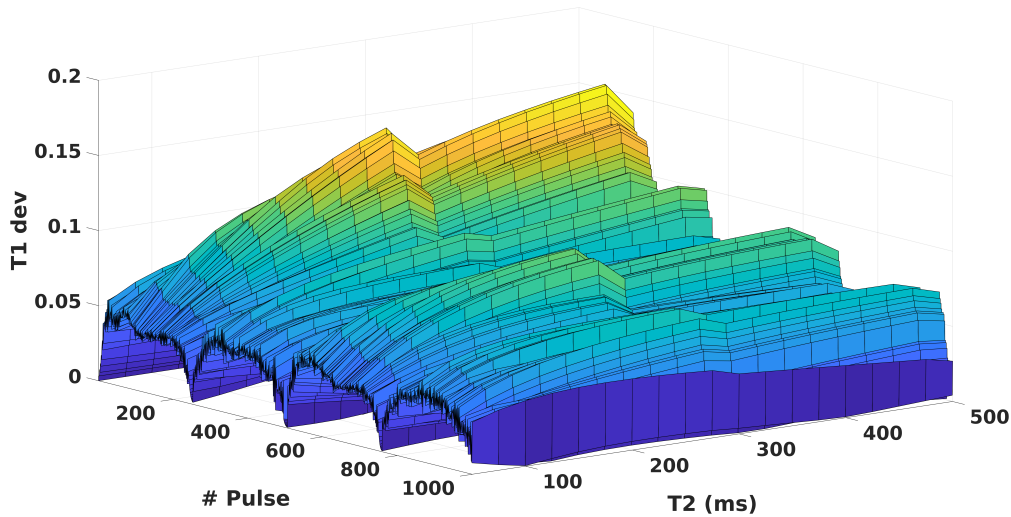


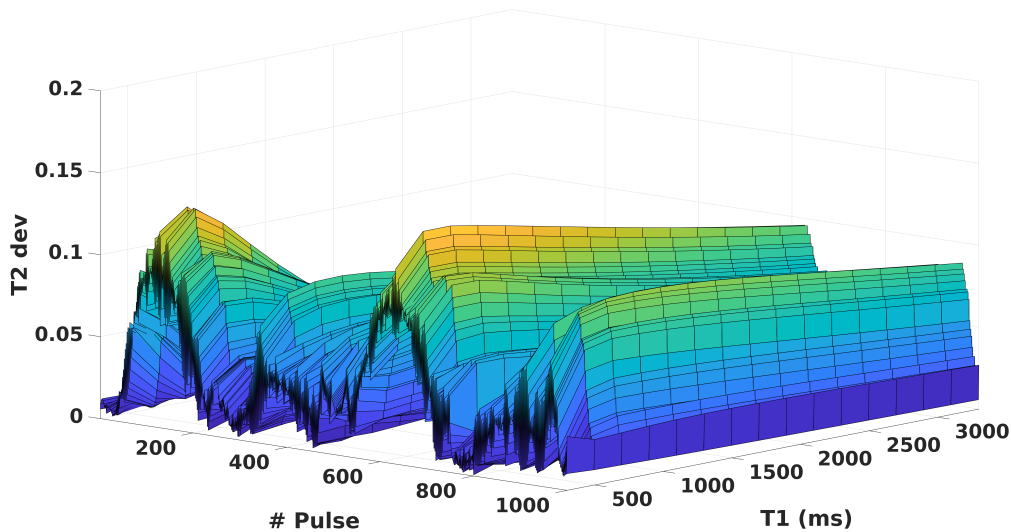
**Figure IV.1.1:** Signal shape variations when fixing all but one properties in a dictionary simulated using the fingerprint from [Ma et al. 2013](#). Simulations performed with our Bloch tool.

of the signals when all but one properties are fixed. This yields an estimate of the signals

separation when the considered properties changes. It is also related to the possibility to match the correct simulated and acquired signals during MRF reconstruction. Repeating this step while varying the different values of the fixed properties, one can map the sensitivity of a fingerprint in the whole parameter space, as shown in fig. IV.1.2. This method provides a



a. Sensitivity on  $T_1$  estimates assessed with the standard deviation of dictionary signals for different  $T_2$  values



b. Sensitivity on  $T_2$  estimates assessed with standard deviations of dictionary signals for different  $T_1$  values

**Figure IV.1.2:** Standard deviation evaluation on the fingerprint from [Ma et al. 2013](#). Only  $T_1$  and  $T_2$  values are considered over the ranges [300, 3300]ms and [50, 500]ms, respectively. Simulations performed with our Bloch tool.

graphical representation that allows the selection of only the parts of the fingerprint sensitive to the parameters of interest. It is a good indicator of a fingerprint's sensitivity across its whole parameter space. However, it does not produce an objective metric of the fingerprint's encoding capacity.

### IV.1.2 Monte-Carlo method

A more quantitative approach for fingerprinting evaluation has been described in [Sommer et al. 2017](#). It relies on several repetitions of an evaluation process using simulated signals contaminated with random noise, and hence is referred to here as a ‘‘Monte-Carlo’’ method. The steps to follow are:

- Generate a dictionary for a fingerprint
- Extract a signal  $S$  and its parameter vector  $\mathbf{P}$ :  $S = f(\mathbf{P})$
- Add noise to  $S$  to obtain  $S_n$
- Search in the dictionary for the closest match  $\hat{S}$  to  $S_n$ ,  $\hat{S} = f(\hat{\mathbf{P}})$
- Compute  $\epsilon = \|\mathbf{P} - \hat{\mathbf{P}}\|$  the error on the reconstruction due to noise

If the fingerprint were optimal, there should be  $S_n == \hat{S}$  and  $\epsilon = 0$  in all cases. This is of course not the case when performing in vivo acquisitions with a realistic noise level. Repeating these steps a large number of times with random noise for several signals in the dictionary allows for computing an objective error on the estimates for a certain noise type. It has been shown that 2000 repetitions on 50 signals across the parameter space lead to reasonable estimates. Several fingerprints have been evaluated in the paper and the results were tested on healthy volunteers. Fig. [IV.1.3](#) shows the difference in image quality between fingerprints that present different Monte Carlo evaluation scores. There

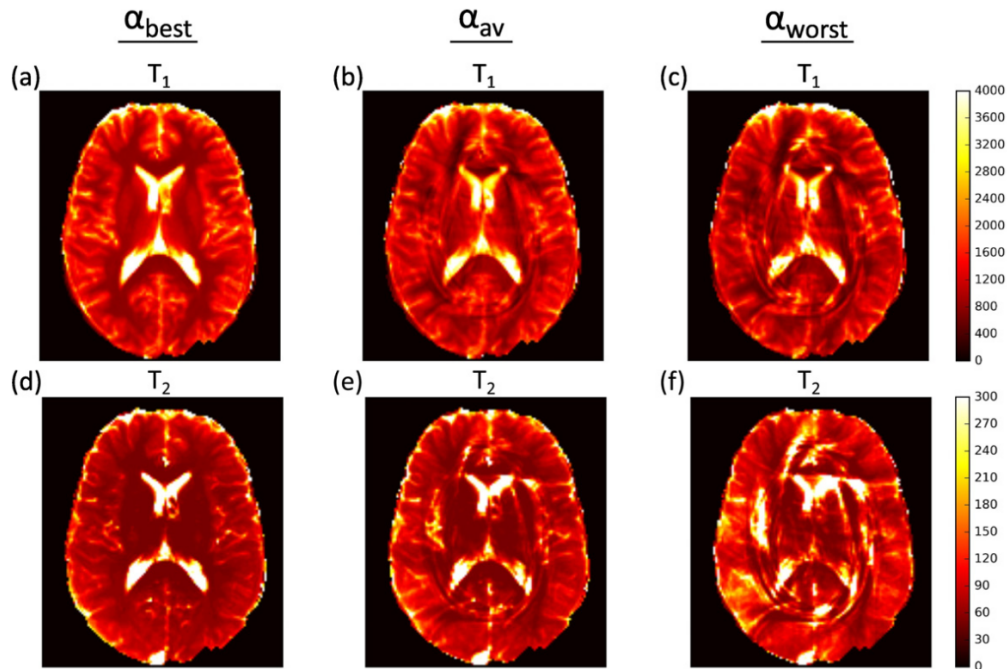


**Figure IV.1.3:** Maps shown in [Sommer et al. 2017](#), presenting 3 maps obtained on one healthy volunteer with RF trains (noted  $\alpha$ ) evaluated with the Monte-Carlo method. The fingerprints rank from the best to worst from left to right. Scales are in ms.

is a clear agreement between the prediction of the method and the quality of the maps. For example, the best-predicted fingerprint shows remarkable resistance to undersampling artifacts compared to the worst-predicted one.

The noise considered during fingerprint evaluation should be selected according to the type of acquisition scheme. When performing a fully sampled acquisition, one can consider a thermal noise and estimate the SNR from the acquisitions. In case an undersampled sampling scheme is used, the authors showed that it is sufficient to add a noise corresponding to aliasing. The thermal noise can be modeled as a gaussian distribution with a null mean and standard deviation  $\sigma = \text{mean}(\text{dictionary}/\text{SNR})$ . The aliasing noise should be locally proportional to the signal intensity  $s$ . The noise is thus sampled point-wise from a normal distribution with null mean and standard deviation  $\sqrt{s^2/\text{SNR}}$ .

It is important to note that this method is only able to compare dictionaries that contain the same number of elements. The approach is sensitive to dictionary size because a very coarse dictionary, where the parameter values are distant one from another, is more likely to have more separated signals. This reduces the chance of a mismatch and increases the likeliness of a perfect match on all repetitions; yet, in case of a mismatch, the error would be higher. Comparing dictionaries with a different number of signals is thus unreliable.

## IV.2 Studies on multi gradient echo sequences

As described in chapter I, the most used MR technique for mapping blood oxygenation is the BOLD effect, which relies on multi gradient echo sequences. This is also the case for the first implementation of the MRvF approach which used the GESFIDSE sequence, that consists of multiple gradient echo readings separated by a 180-degree RF pulse. The fingerprint used was the ratio of signals acquired post- and pre- injection of CA. The choice of this particular fingerprint was based on physics intuition and previous attempts to measure microvascular properties using the qBOLD approach. However, this fingerprint has not been properly quantified and the sensitivity to blood volume, radius, and oxygenation is not clear. In particular, it has been noted in previous MRvF studies that the  $\text{SO}_2$  values seemed too high in healthy tissues. In this section, we used the evaluation tools presented above to test the GESFIDSE sequence and see if better fingerprints based on multi-echo acquisitions can be found. Because the lab had already built-up a database of pre-clinical scans containing GESFIDSE acquisitions (acquired pre- and post-injection of CA in different pathological models), we conducted a retrospective study to validate our predictions.

### IV.2.1 In-silico fingerprint evaluation

The standard deviation method was used to evaluate three fingerprints from the GESFIDSE sequence:

- pre-CA fingerprint
- post-CA fingerprint
- ratio fingerprint: post-CA / pre-CA

to the different vascular parameters. The results are presented in fig. IV.2.1. The left column (a,d,g) shows the sensitivity of the pre-CA fingerprint. It can be noted that it is sensitive to  $\text{SO}_2$  mostly before the 180 pulse (Echotime=60ms). This can be linked with the BOLD effect



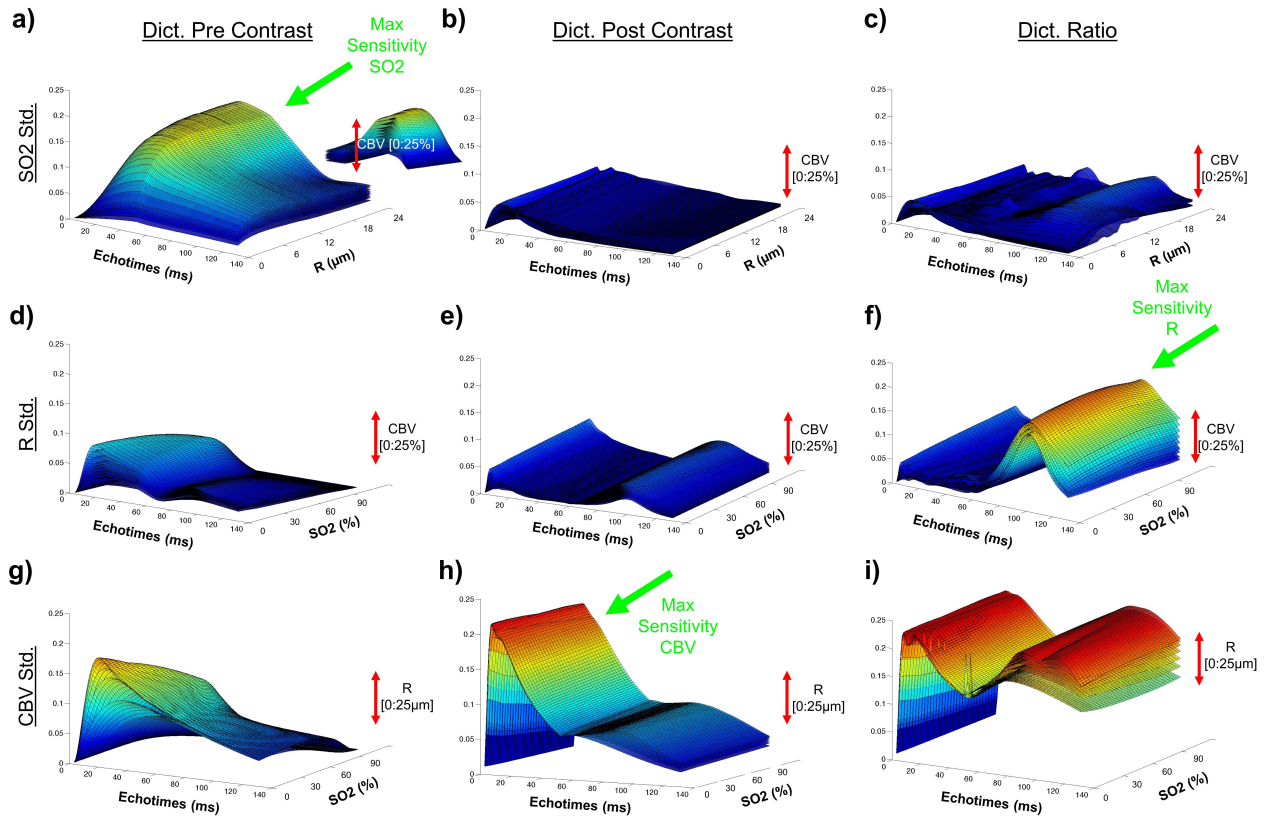


**Figure IV.2.1:** Standard-deviation evaluation of fingerprints from the GESFIDSE sequence to vascular parameters. CBV here stands for Cerebral Blood Volume, which is the BVf. Simulations performed with MRVox

which predicts a high signal change due to a change in blood oxygenation when  $TE \approx 30$ ms (at 4.7T). This sensitivity is lost when the contrast agent is used (b,c). The pre-CA exhibits a good sensitivity to BVf, and to some extent, to R. The post-CA fingerprint (central column) mostly provides sensitivity to BVf. Finally, the right column, represents the sensitivity of the ratio fingerprint, with relatively large variations with R and BVf, but not  $SO_2$ .

Based on these observations, it seems that the original ratio fingerprint (used in the first MRvF papers) was not optimal, especially for  $SO_2$  estimates. However, the results suggest that just reorganizing the pre- and post-CA from the same sequence could be beneficial, especially if the first echoes of the pre-CA fingerprint are included. One obvious option is the concatenation of the pre- and post-CA, shown in fig. IV.2.2. The different fingerprints are shown with a variable  $SO_2$  (BVf and R fixed). It can be seen that the signals are more spread in the concatenation fingerprint than in the original one. The ratio fingerprint has yet the advantage of avoiding the need to simulate for different  $T_2$  values. Indeed, for BVf values inferior to 20%, the CA injection does not significantly change the  $T_2$  of the whole voxel. The ratio operation had the effect of eliminating the  $\exp(-t/T_2)$  component from both signals. The same thing is also true for large  $B_0$  inhomogeneities effects which are canceled when using the ratio of the signals. To use the concatenation fingerprint in practice, it thus becomes necessary to include at least different  $T_2$  values in the dictionary to correctly identify the change in  $T_2^*$  decay associated with the CA injection.

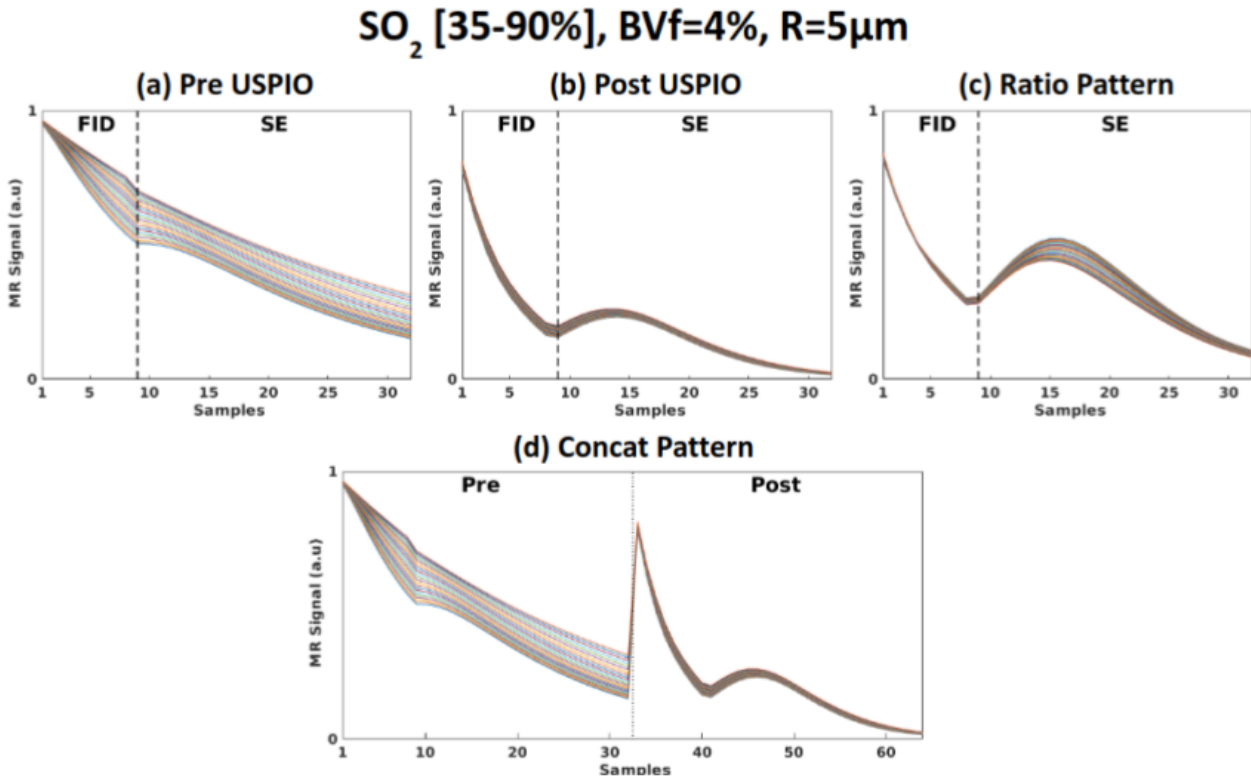


**Figure IV.2.2:** Concatenation and ratio fingerprints considered for the GESFIDSE sequence. Signals are shown with all parameters but SO<sub>2</sub> fixed. Simulations performed with MRVox.

This can be done directly by setting several  $T_2$  values in the simulation parameters, but in the case of a GESFIDSE sequence, it is sufficient to simulate the signals with an infinite value for  $T_2$  and to later multiply the signals by  $\exp(-t/T_2)$  for different  $T_2$  values. Doing so allows using as many  $T_2$  as wanted without changing the number of signals to simulate.

To test the encoding capacity of such a reorganisation, two sequences were tested:

- MGEFIDSE: one spin echo at TE=60ms, regular sampling with gradient echoes, 32 echoes
- MGEFIDSE double echo: double 180°, TE = 60 and 100ms, with the same gradient echo sampling time as a GESFIDSE, 43 echoes

for three fingerprints each:

- pre-CA alone (32 or 43 echoes)
- Ratio post- / pre-CA (32 or 43 echoes)
- Concatenation [pre-CA, post-CA] (64 or 86 echoes)

meaning that 6 Monte-Carlo evaluations were performed. The dictionaries to evaluate were made with MRVox considering 5 parameters: BVf, R, SO<sub>2</sub>,  $T_2$  and ADC. Fig. IV.2.3 shows the results of these evaluations. The bars represent the mean and standard deviation of the



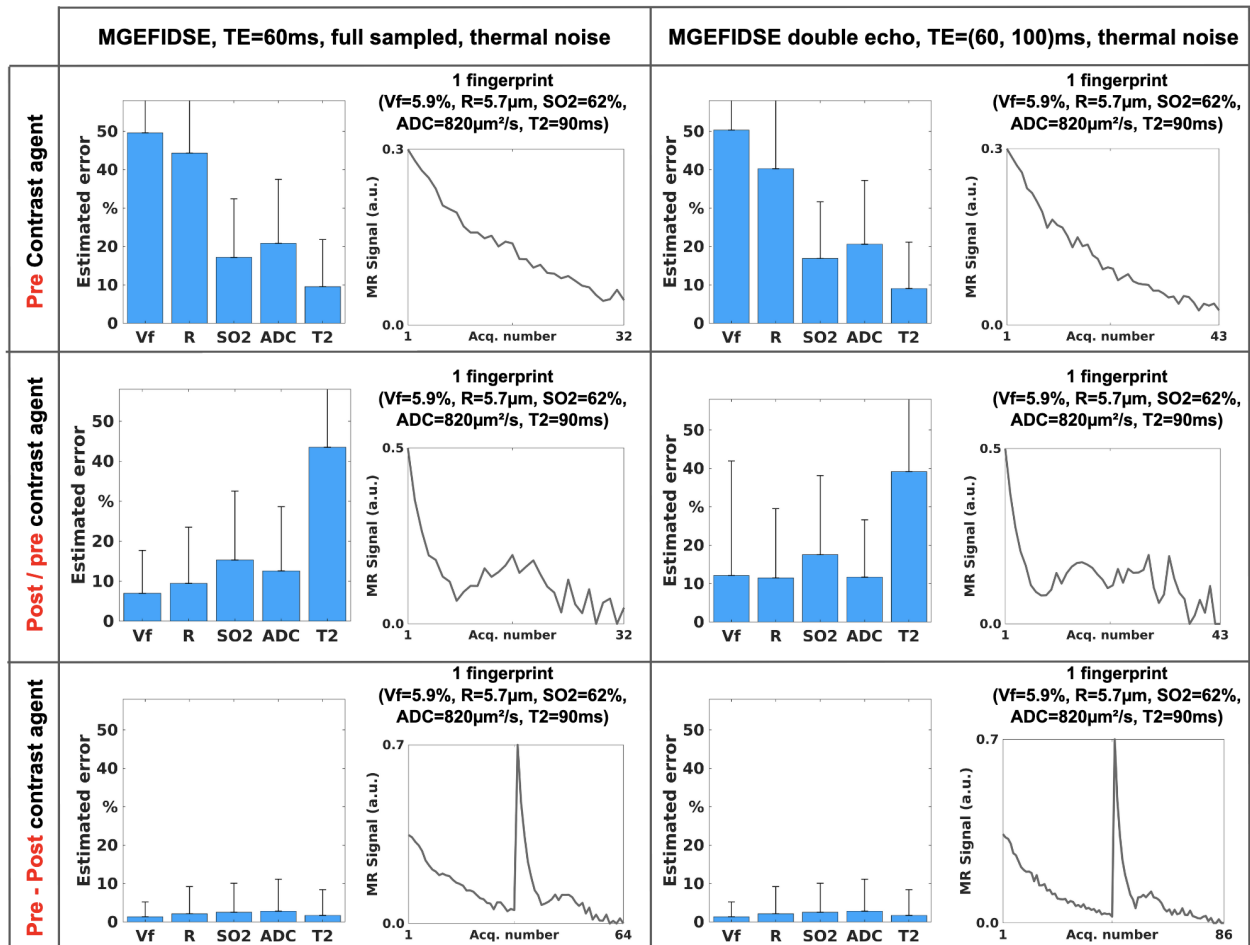


**Figure IV.2.3:** Results from the Monte-Carlo evaluation of three fingerprints from multi gradient echo sequences. Pre- and post-CA signals are noised before the pattern is made to account for error propagation in the ratio and concatenation (“Pre - Post”) fingerprints. Thermal noise with  $\text{SNR} = 20$  was used. The bars represent the mean and standard deviation of the noise-induced error on the estimation of each parameter across the 2000 repetitions on 50 signals. Vf corresponds to BVf. Simulations performed with MRVox.

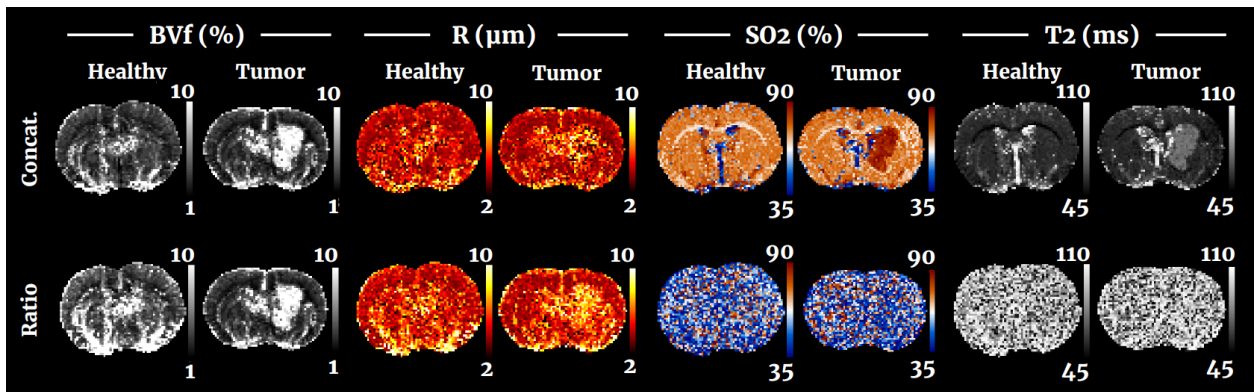
noise-induced error on the estimation of each parameter across the 2000 repetitions on 50 signals. For the ratio and concatenation, noises were added to the pre- and post-CA signals before computing the pattern in order to account for error propagation. The thermal noise was set to  $\text{SNR} = 20$  to match observations made on previous acquisitions.

For both sequences, it can be seen in fig. IV.2.3 that the ratio and the pre-CA fingerprints should not produce accurate estimates of  $\text{SO}_2$ , in line with our previous findings (fig. IV.2.1). An increase in BVf and R sensitivity can however be observed for the ratio fingerprint, as well as the expected decrease in  $T_2$  sensitivity. In opposite, the concatenation fingerprint shows a substantial increase in sensitivity for all the parameters.

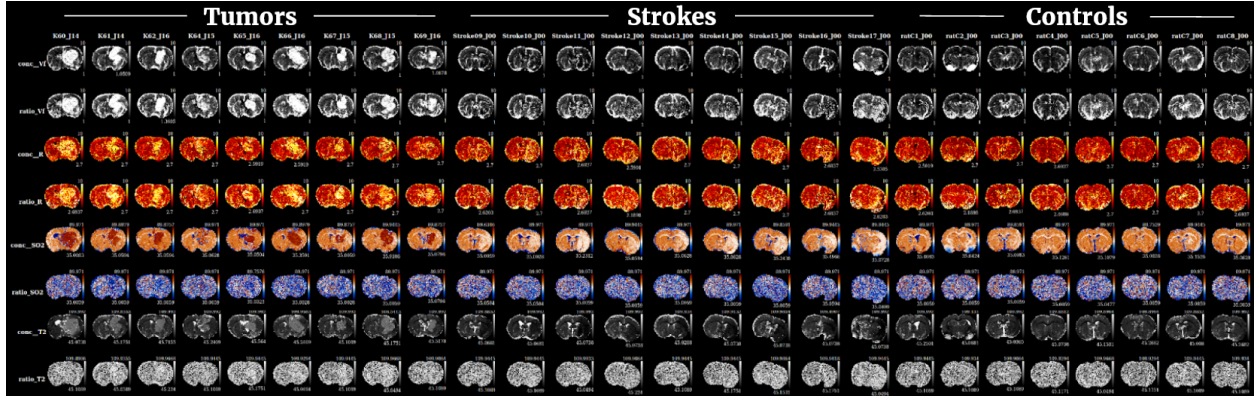
The addition of a second spin echo in the double-echo GESFIDSE sequence did not seem to improve the results.

## IV.2.2 Evaluation on retrospective pre-clinical data

The previous results suggested that the concatenation of the GESFIDSE pre- and post-CA fingerprint should significantly improve the vascular parameters estimates ( $SO_2$  in particular) compared to the ratio fingerprint. Thus, we tested this hypothesis on the animal data used in section III.1, using the 3D realistic dictionary presented in that same section. The ADC dimension was not simulated here to keep the focus on the vascular parameters. Parametric maps obtained in three animal groups with the ratio and concatenation fingerprints are presented in fig. IV.2.4, with a focus on one tumor-bearing and one healthy animal. An overview of the obtained maps on three groups of animals (tumor-bearing, stroke-bearing, healthy) is also shown to illustrate the reproducibility of the experiment. The improvement



a. Focus on two animals



b. Results on groups of animals

**Figure IV.2.4:** Maps produced with MRvF on animals with the ratio and concatenation fingerprint. The dictionary used is the one presented in section III.1, simulated from realistic vascular networks with MRVox. a. focuses on two representative animals, b. shows maps obtained on animals bearing 9L tumors or strokes and from the control group

in the  $SO_2$  estimates brought by the concatenation is clear. The  $SO_2$  maps obtained with the ratio are very noisy and hardly show any anatomical contrast. Note that they are different from what was found in Christen et al. 2014b, possibly due to the many changes made in the simulation code since then, and the addition of a  $T_2$  dimension in the dictionary. Note also the smaller differences in BVf and R maps, that could be expected from the Monte-Carlo evaluations. Finally, it can also be seen that  $T_2$  maps can be produced with the concatenation

fingerprint but not with the ratio one.

### IV.2.3 Limitation of GESFIDSE based sequences

According to our results, it seems possible to improve the MRvF estimates simply by reorganizing the echoes of the GESFIDSE sequence acquired pre- and post-CA injection. In particular, the  $\text{SO}_2$  maps seem greatly improved after using the concatenation of the acquisitions which opens new opportunities for retrospective analysis of data as well as further preclinical studies on lesions. Our tools have however not shown further improvements in the maps when more spin echoes, gradient echoes, or other types of hybrid concatenation of the GESFIDSE acquisitions are used (not shown). As suggested by our Monte-Carlo results on the pre-CA fingerprint, it also seems that GESFIDSE-based MRvF sequences require contrast agent injection. This may be troublesome in a clinical context and reduces the scope of MRvF. In addition, we note that the GESFIDSE sequence was initially used for MRvF because it had shown good results with standard  $T_2$  and  $T_2^*$  exponential fitting in qBOLD experiments. In theory, MRF can work with way more complex temporal evolution and should not be limited to standard multi gradient echo sequences. It is thus possible that a sequence tailored specifically for MRvF measurement could be used to obtain a fingerprint yielding better results. The next section presents the work done towards the identification of such a sequence.

## IV.3 Studies on balanced SSFP-based sequences

MRF offers virtually infinite possibilities of sequence design to try and achieve sensitivity to parameters of interest. Yet, finding the right sequence starting from a purely random one is practically intractable. As a starting point, we propose to use the balanced SSFP sequences, which are known to be sensitive to the BOLD effect, as detailed below.

### IV.3.1 Review on bSSFP BOLD sensitivity

Balanced SSFP sequences are known to be sensitive to magnetic field inhomogeneities and off-resonance effects. Usually, these effects are considered artifacts due to corresponding banding effects in anatomical scans. Yet, in a few lines of studies, bSSFP sequences have also been considered for BOLD fMRI experiments. Although the potential of these approaches is considerable, practical considerations such as shim quality have greatly limited their use. It should however be interesting to reconsider these sequences in the MRF context where multiple parameters can change over time and different effects can be included as new dimensions in the dictionaries. The following section explores the relationship between bSSFP and  $B_0$  inhomogeneities, taking examples from the literature and from simulations that we run on simple cases. The extensive validation of our simulation tools (II) makes us confident that they are robust enough for this search. We studied the potential of the standard steady-state regime but also less investigated behaviors in the transient parts of the signal evolution.

### IV.3.1.1 Steady-state regime

The most commonly used part of bSSFP sequences is the steady-state that establishes after several excitation pulses.

The sensitivity of the steady-state signal to  $B_0$  inhomogeneities can be studied with the simulation tools presented in chapter II. In fig. IV.3.1a, we show the simulated steady-state level reached after 100 pulses of a balanced sequence for  $FA = 60^\circ$ ,  $TR = 1$  second and different TEs. For this experiment, we considered several homogeneous voxels subjected to different gradients of  $B_0$  that create linear dephasings across the voxel. Simulations were performed with the Bloch tool. It can be seen that the signal evolution changes with the

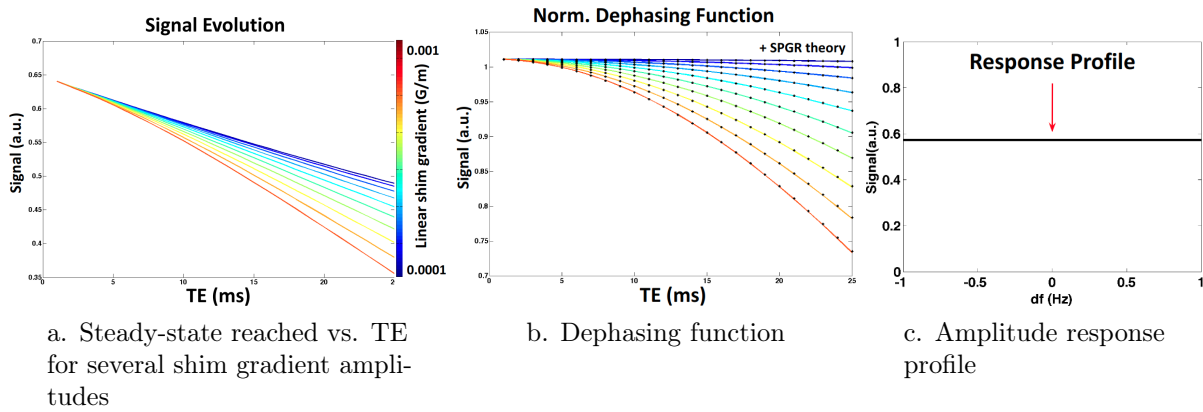


**Figure IV.3.1:** Steady-state simulations for  $TR = 1s$ ,  $FA = 60^\circ$  and  $df = 0Hz$ . The red arrow indicates the  $df$  used on the response profile. The color code indicates the gradient strength used for each curve, given in Gauss/meter. Simulations were performed with the Bloch equations.

amplitude of the linear shim gradient. Spins are in phase at short TEs and the dephasing is more pronounced for longer TE and higher gradient amplitude ( $d\varphi(TE) = \gamma \cdot (B_0 + G) \cdot TE$ ), reducing the steady-state level. The level of signal reached at each TE and shim amplitude can be normalized relatively to that obtained with the same TE but without shim gradient. This yields to the dephasing functions shown in fig. IV.3.1b, which can be directly compared to the theoretical dephasing functions obtained with spoiled SSFP sequence. In this particular case, the bSSFP and spoiled GRE functions are identical. This can be explained by the long TR used here that acts as a spoiling mechanism: no transverse magnetization remains just before each new pulse. The spread of the dephasing functions at higher TE indicates a good sensitivity of this sequence to intra-voxel dephasing, which is interesting for MRvF experiments.

For one TE value and without adding  $B_0$  inhomogeneities, but setting a global off-resonance frequency offset ( $df$ , in Hertz apart from the Larmor frequency) in the voxel, one can draw the response profile of the bSSFP steady-state signal. Fig. IV.3.1c shows the response profile for  $TR = 1s$ . The red arrow indicates the  $df$  used to obtain the two left panels (0 Hz in this case). This particular flat profile points to the lack of sensitivity of the sequence to  $df$ , which is expected from a spoiled sequence.

Reducing the TR of a bSSFP sequence changes the signal behavior. Fig. IV.3.2 reproduces the

precedent simulations for  $FA = 60^\circ$  and  $TR = 26\text{ms}$ . Two  $df$  are considered: the on-resonance

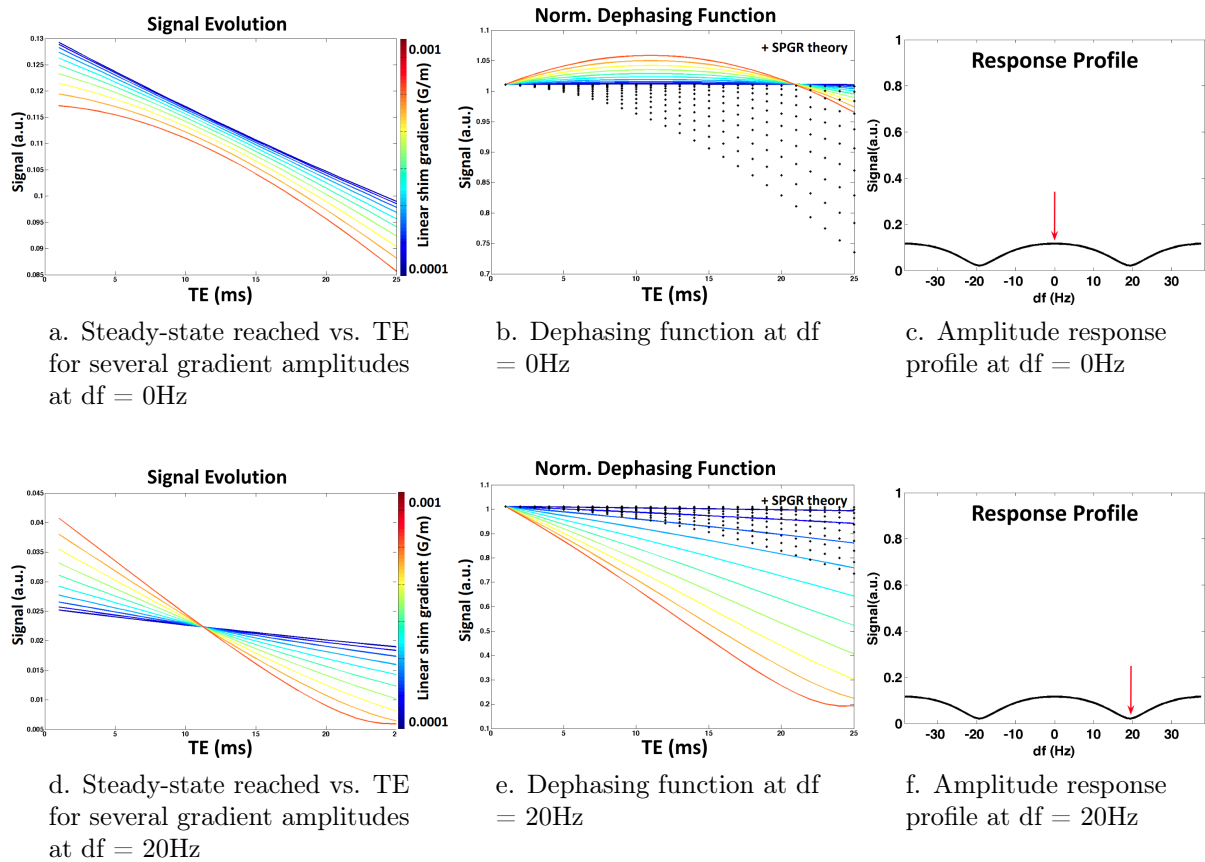


**Figure IV.3.2:** Steady-state simulations for  $TR = 26\text{ms}$ ,  $FA = 60^\circ$  and  $df = 0$  (upper row) or  $20\text{Hz}$  (lower row). The red arrow indicates the  $df$  used on the response profile. The color code indicates the gradient strength used for each curve, given in Gauss/meter. Simulations were performed with the Bloch equations.

case where  $df = 0\text{Hz}$  and an off-resonance situation at  $df = 20\text{Hz}$ . One can notice the variations of the response profile for short  $TR$ . The difference in behavior in the evolution of the steady-state level with increasing  $TE$  is clear. The case where  $df = 0\text{Hz}$  presents a higher signal level (fig. IV.3.2c) but is slightly sensitive to intra-voxel dephasing. On the contrary, the case  $df = 20\text{Hz}$  has a lower signal level but the dephasing functions are dramatically more spread apart. In this case, the dephasing effects are even more pronounced than the ones obtained with SPGR sequences such as the GESFIDSE sequence. It is worth noting that in the conditions of the experiment, the steady-state reached is the same for all signals at  $TE \approx 11\text{ms}$  and corresponds to a spin echo-like behavior.

Fig. IV.3.3 illustrates the situation for  $TR = 26\text{ms}$  but  $FA = 10^\circ$ . The variations of the steady-state levels are different from the previous cases even if the dephasing functions are close to that from fig. IV.3.2b. The response profile has a completely different shape.

These simulations show the influence of  $B_0$  inhomogeneities on steady-state balanced sequences. It suggests that in some particular cases, this effect can be larger than with SPGR sequences.



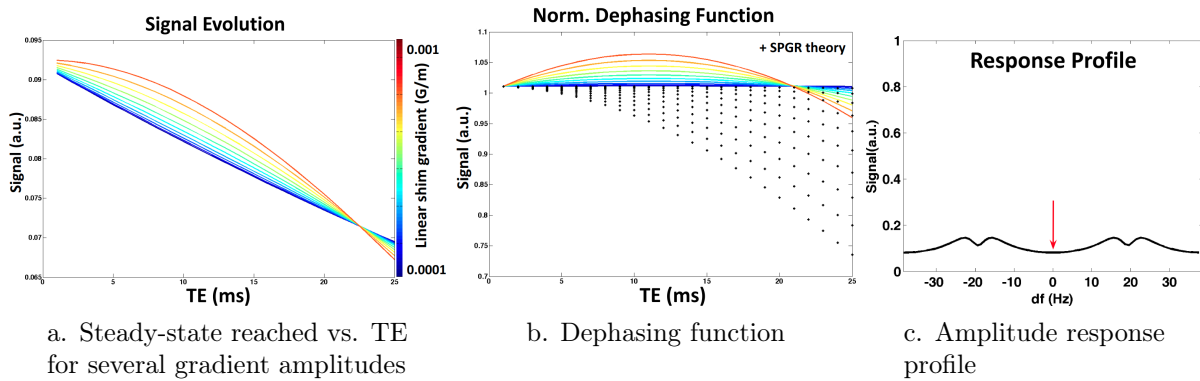


**Figure IV.3.3:** Steady-state simulations for  $TR = 26\text{ms}$ ,  $FA = 10^\circ$  and  $df = 0\text{Hz}$ . The red arrow indicates the  $df$  used on the response profile. The color code indicates the gradient strength used for each curve, given in Gauss/meter. Simulations were performed with the Bloch equations.

The behavior is however hard to predict and depends on several acquisition parameters.

Based on the same type of simulations and intuitions, several teams have proposed to use bSSFP sequences in the steady-state regime for BOLD fMRI experiments. Two lines of work have been proposed based on 2 different signal response profiles. They are illustrated in Fig. IV.3.4: (a) the profile is called “passband” with a flat amplitude response profile around  $df=0$  Hz and (b) a profile called “transition-band” with a sharp phase response profile around  $df=0\text{Hz}$ .

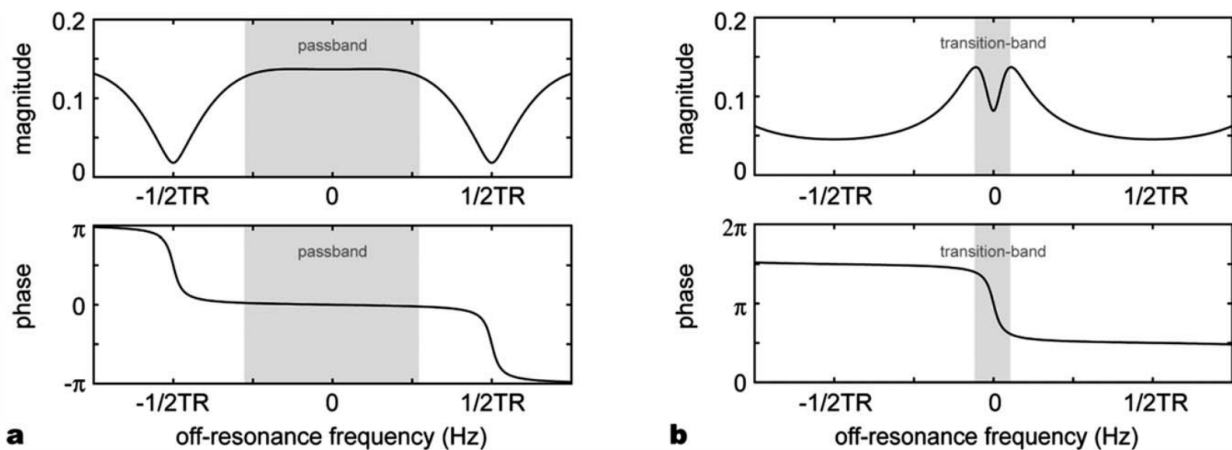
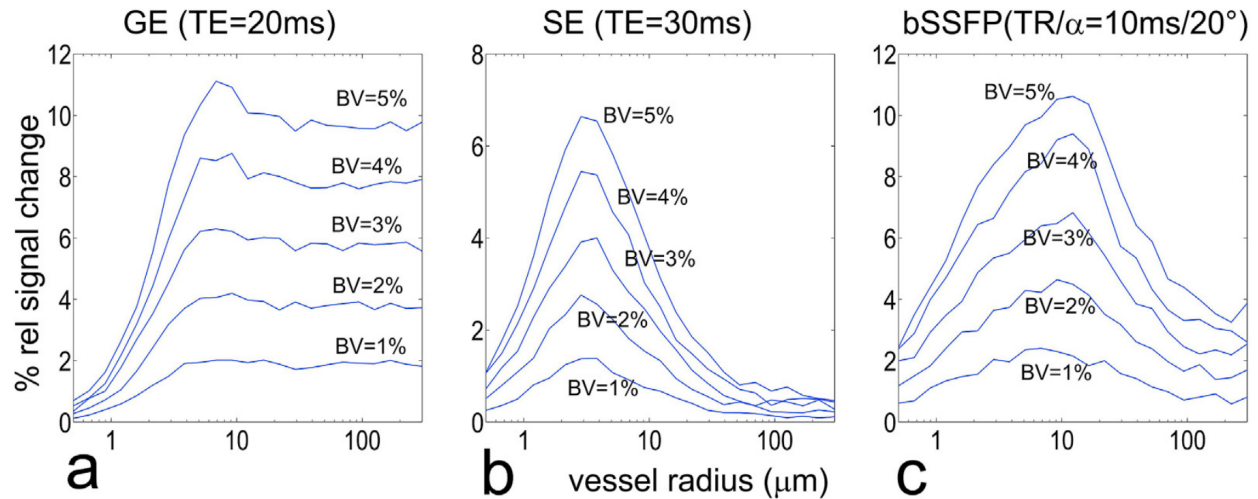


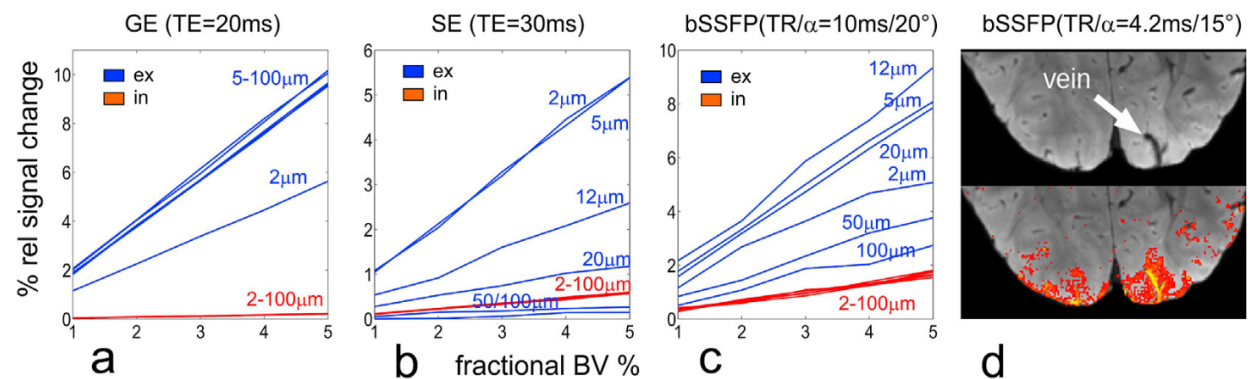
**Figure IV.3.4:** Illustrations of two different response profiles used for bSSFP BOLD experiments, from Kim et al. 2012. a. corresponds to a  $25^\circ$  FA train with phase-cycling ( $\pi$  increments). b. corresponds to a  $5^\circ$  FA train without phase-cycling. Unknown simulation method.

For the passband regime, Báez-Yáñez et al. 2017 reproduced the simulations made by Boxerman et al. 1995 (and also used in our thesis to validate MRVox results, see section II.1.3.2) to show the sensitivity of the bSSFP sequence to the BOLD effect as well as the

influence of the vessel size and blood volume fraction inside a voxel. One can see in fig. IV.3.5a that passband bSSFP presents the same amount of signal variations as a standard spoiled GRE sequence but with a spin echo-like behavior. Fig. IV.3.5b shows that a passband bSSFP is able to discriminate vessel sizes, based on signal changes on neuronal activation measured on a volunteer.



a. Relative signal change associated with an  $\text{SO}_2$  variation corresponding to neuronal activation for different BVf, simulated for different sequences.



b. Relation between extra- and intravascular (“ex” and “in”, resp.) signal contributions with BVf for Gradient Echo, Spin Echo, and bSSFP, and an example of measured activation detected with a bSSFP (visual checkerboard stimulation)

**Figure IV.3.5:** Illustration of bSSFP potential for fMRI, from Bález-Yáñez et al. 2017. Curves are simulated from voxels with randomly oriented cylinders. Magnetic field perturbations are computed in the Fourier space, similar to what is done in MRVox. Diffusion is modeled with random walks of  $10^5$  protons. Steady-state obtained after 500 to 2,500 dummy pulses.

BOLD SSFP sequences have shown very promising results for fMRI experiments (fig. IV.3.5b), but they are not used in practice because the different specific regimes and response profiles are difficult to reach and maintain. In particular, any local  $df$  variations due to imperfect shim will tend to alter the BOLD sensitivity. A recent work inspired by MRF-like acquisitions has



however proposed to circumvent this limitation by combining multiple bSSFP acquisitions with proper RF phase cycling patterns. Doing so, [Guo et al. 2020](#) showed that the response profiles can be shifted (fig. [IV.3.6](#), upper row) and that at least one of them can correspond to a good BOLD sensitivity for the actual experimental conditions. The results of this “Oscillating Steady-State Imaging” (or OSSI-bSSFP) acquisition pattern suggest that the approach should be more efficient than standard spoiled GRE sequences for BOLD fMRI experiments (see fig. [IV.3.6d](#)). In our context, this type of acquisition pattern seems clearly promising as it is directly related to blood oxygenation effects.

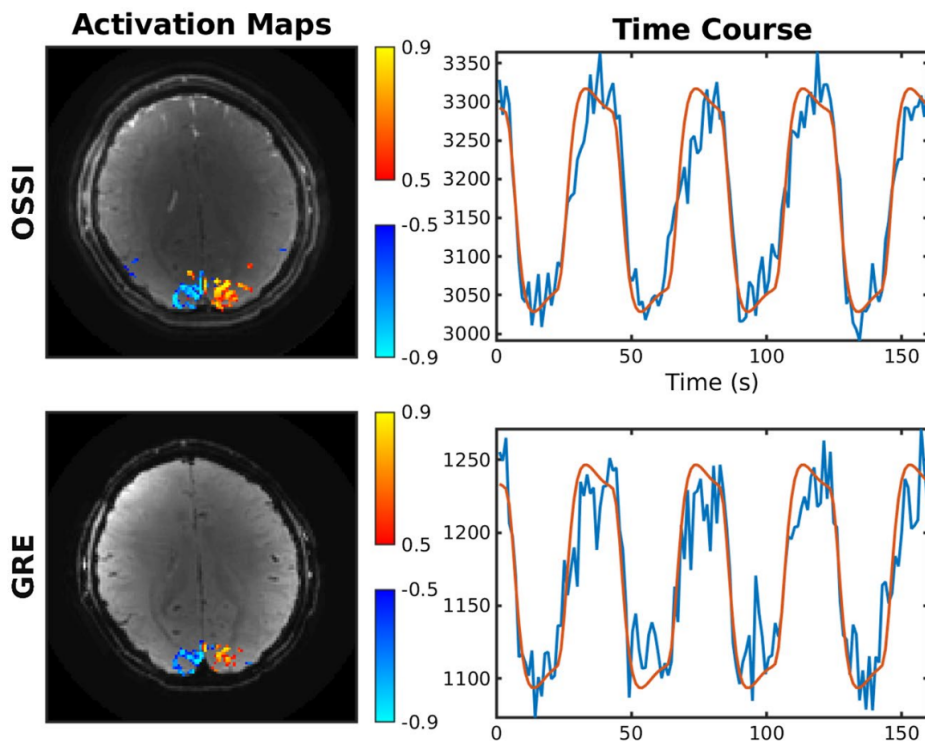
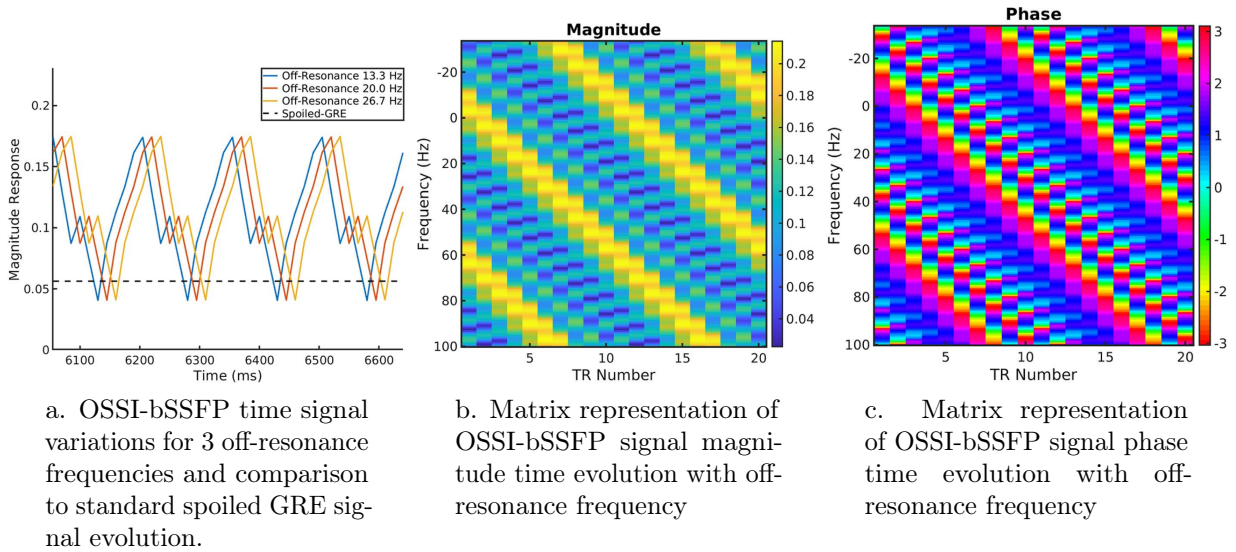


**Figure IV.3.6:** Influence of off-resonance frequencies on the time evolution of OSSI-bSSFP sequences, and fMRI experiment results. a. b. and c. are simulations performed with a Bloch equation simulator. Homogeneous voxels are simulated at different  $\Delta f$  and summed with ponderation to obtain a change in  $T_2^*$  corresponding to an activation. Establishment of a steady-state was ensured by applying the sequence for  $5 \times T_1$ . Figures from [Guo et al. 2020](#).

### IV.3.1.2 Transient-state regime

A less explored part of the bSSFP sequence is its transient-state, from the first pulse to the establishment of the steady-state. Because of its complex evolution, this part of the signal is usually not acquired and replaced by dummy scans before acquiring steady-state images. A few studies (e.g. [Deiming et al. 1994](#) and [Hargreaves et al. 2001](#)) have worked towards manipulating the magnetization in the transient-state to reduce the number of dummy scans needed to reach the steady-state. Fig. [IV.3.7](#) from [Hargreaves et al. 2001](#) shows simulated results from these studies. The upper signal in each panel corresponds to a standard bSSFP

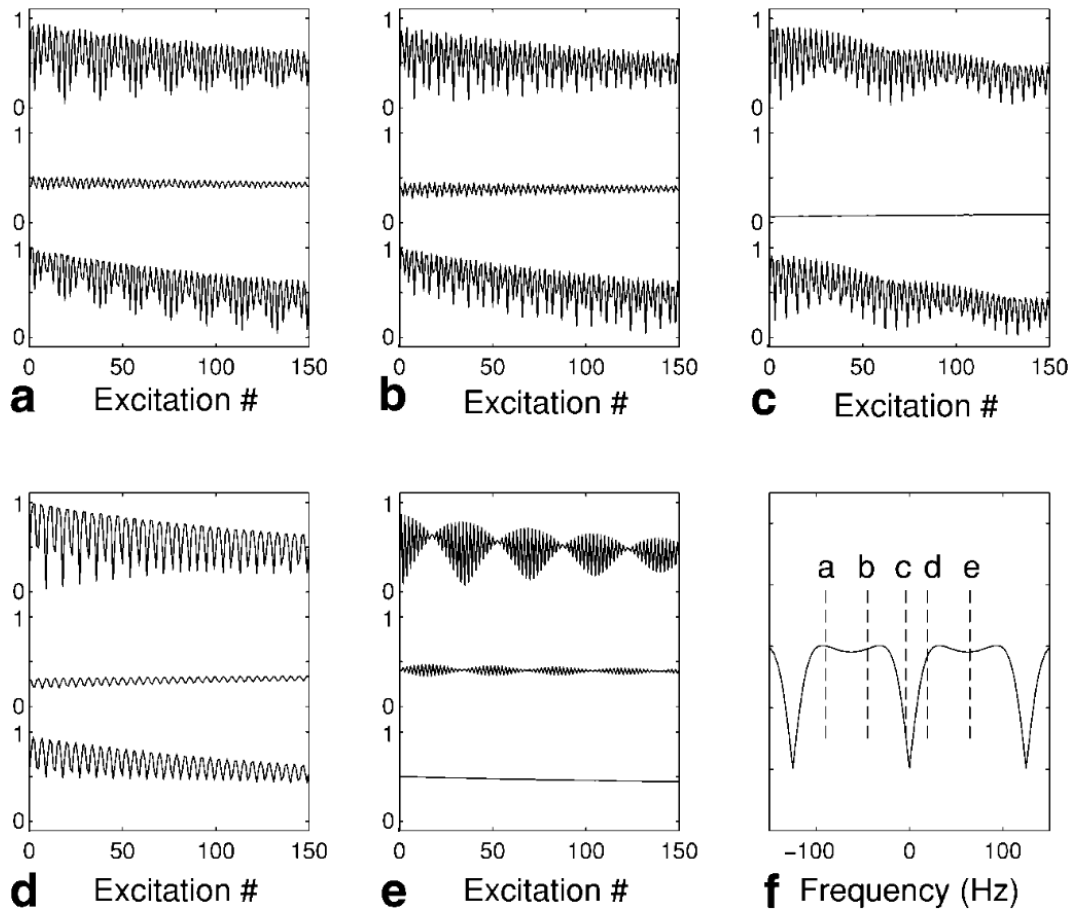


**Figure IV.3.7:** Simulation (unspecified method) study on the transient-state of classical or prepared bSSFP sequences at different off-resonance frequencies, from [Hargreaves et al. 2001](#). The upper signal in each panel corresponds to a standard bSSFP sequence, the lower signals are obtained with preparation schemes to reduce the oscillations in the transient-state. Each panel simulates the same three sequences at a different  $\Delta f$ , as shown in the lower-right image (f).

sequence, the lower signals are obtained with preparation schemes to reduce the oscillations in the transient-state. Each panel is simulated at a certain  $\Delta f$ , as shown in the lower-right image. Beyond the results obtained by the authors, this figure highlights the large signal variations that can be achieved in the transient-state of a bSSFP and their dependencies on field inhomogeneities. This property is particularly interesting for MRvF as the precision of the technique depends on the ability to differentiate the signal shapes.

More recently, [Assländer et al. 2019](#) studied the sensitivities of the transient-state of bSSFP sequences to intra-voxel dephasing. Fig. IV.3.8 shows the behavior of different isochromats for different sequences. On the right side (panel c), it can be seen that isochromats experiencing

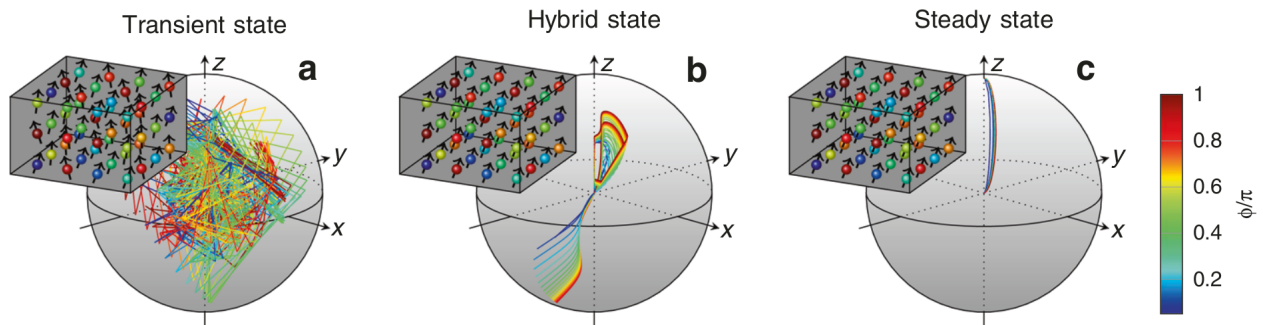


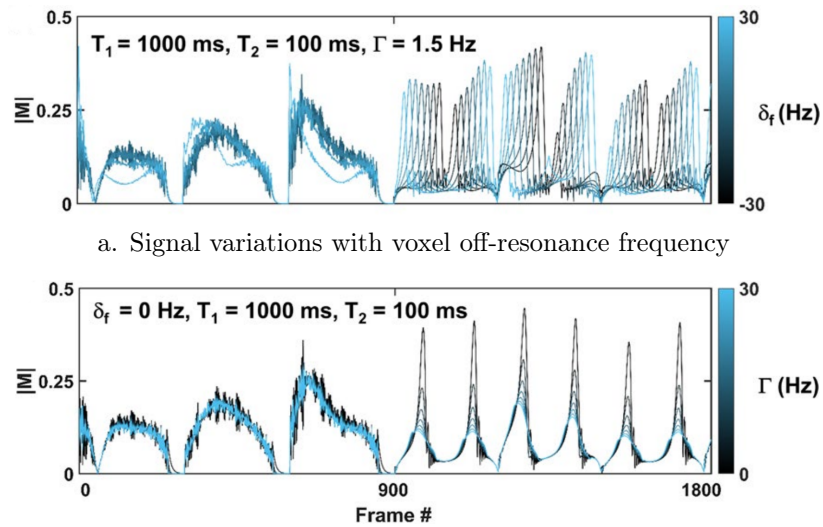
**Figure IV.3.8:** Simulation (Bloch equations) study on the transient, hybrid and steady-state signal of bSSFP sequences. Magnetization trajectories are plotted in 3D for multiple isochromats, from [Assländer et al. 2019](#).

different field inhomogeneities during the steady-state of balanced GRE sequences follow approximately all the same trajectory, constraining the potential sensitivity of the sequence to BOLD effects. However, the transient-state case obtained with the application of random pulses (panel a), allows the isochromats to have unique 3D trajectories. The resulting signal from all these individual isochromats should thus be very sensitive to intra-voxel dephasing. Other regimes such as the hybrid state (achieved under certain conditions of flip-angle increment from pulse to pulse, panel b) are also presented in the paper, suggesting other ways to work with bSSFP sequences.

### IV.3.1.3 Potential for MRvF

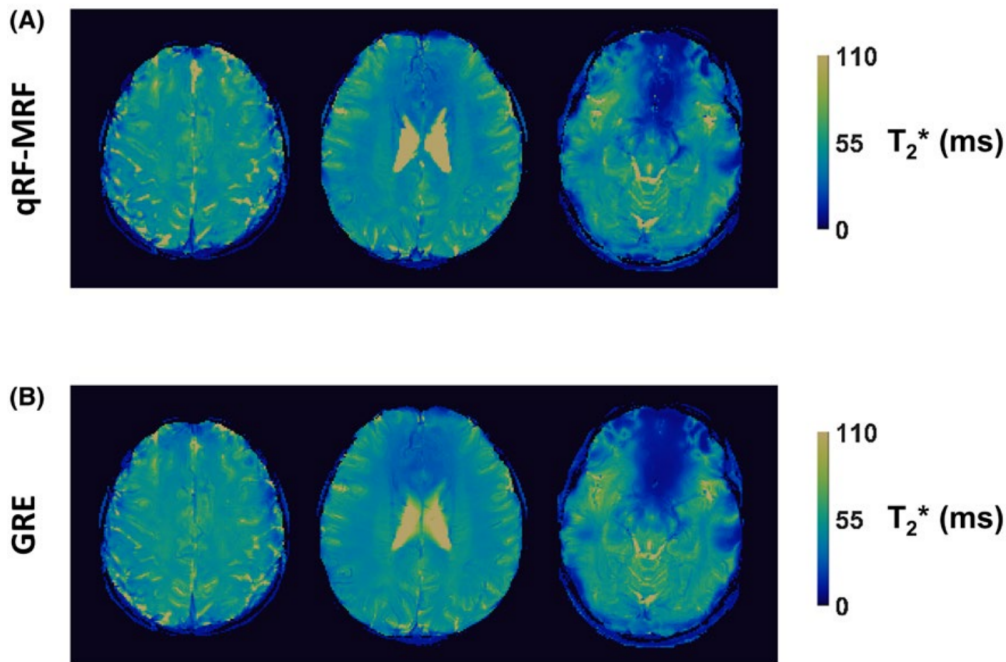
The brief review above shows that bSSFP sequences can be sensitive to off-resonance frequencies and to intra-voxel dephasing, both in their transient and steady-state. It also shows that it is possible to obtain a large number of distinct signal shapes from a single bSSFP sequence by playing with the TR, TE, FA, and RF phase cycling. Although these behaviors are usually not used in standard MR acquisition schemes, they should however be highly informative in the MRvF context. Our aim being to perform acquisitions without CA injection, we only consider the direct result from a sequence as a fingerprint.

We note that two recent papers [Wang et al. 2019](#) and [Boyacioglu et al. 2021](#) have proposed to use bSSFP MRF sequences to acquire  $T_2^*$  maps. Instead of using multiple gradient echo sequences, they rely on bSSFP and phase-cycling, as presented above. Fig. IV.3.9 shows that the fingerprint from Wang et al. is sensitive to both whole-voxel off-resonance frequency (fig. IV.3.9a) and to variations of a gamma distribution of  $df$  inside the voxel, yielding intra-voxel dephasing (fig. IV.3.9b). The maps obtained in [Wang et al. 2019](#) with their proposed bSSFP MRF are compared to maps obtained with a classical gradient echo sequence fitting in fig. IV.3.9c. These results are very promising for our MRvF experiments as accessing intra-voxel  $df$  distributions is what we are looking for to measure blood oxygenation. The following section presents the work done during our thesis to find potential MRvF fingerprints based on bSSFP sequences.



a. Signal variations with voxel off-resonance frequency

b. Signal variations with intra-voxel distribution of off-resonance frequencies



c.  $T_2^*$  maps obtained from MRF with the fingerprint presented above, compared against maps obtained with a classical gradient echo sequence fitting

**Figure IV.3.9:** MRF bSSFP  $T_2^*$  sequence from Wang et al. 2019. The 900 first pulses of the sequence are similar to Ma et al. 2013. The following pulses have constant FA, TE and TR, and a phase cycling is applied. a. and b. show simulated signal variations with global and intra-voxel off-resonance. Homogeneous voxels with different  $\delta_f$  are simulated and summed with a Lorentzian ponderation of width  $\Gamma$  to correspond to a range of  $T_2^*$ . c.  $T_2^*$  maps obtained with the proposed sequence are compared to classical GRE acquisitions. Figures from Wang et al. 2019.

## IV.3.2 In-silico fingerprint design

### IV.3.2.1 Test of $T_2^*$ -sensitive MRF fingerprints

Building on the concepts presented above, we compared the GESFIDSE pre-CA fingerprint against fingerprints from bSSFP-based sequences found in the literature and known for their sensitivities to  $B_0$  inhomogeneities:

- The “qRF-MRF” fingerprint proposed in [Wang et al. 2019](#) is made sensitive to  $T_1$  and  $T_2$  using the 900 first pulses presented in [Ma et al. 2013](#) and then made sensitive to  $T_2^*$ -using quadratic phase cycling.
- The OSSI-inspired fingerprint starts with a repetition of 40 pulses with a constant FA and TR to create a transient-state before starting the phase cycling scheme described in [Guo et al. 2020](#).
- The “random” bSSFP uses random variations of FA and TR to create a transient-state without using RF phase cycling as suggested in [Assländer et al. 2019](#).

Note that the first two fingerprints rely on phase cycling to achieve a robust signal level as well as sensitivity to  $\Delta B_0$ .

Dictionaries of 10,000 signals were generated with MRVox2D for the 4 fingerprints and evaluated with the Monte-Carlo method. The parameters considered were:  $BVf = [1:10]\%$ ,  $R = [1:10]\mu\text{m}$ ,  $SO_2 = [0.35:0.9]$ ,  $T_2 = [45:110]\text{ms}$  and  $ADC = [600:1200]\mu\text{m}^2/\text{s}$ , distributed on a scrambled Sobol set. All fingerprints but the qRF-MRF were treated with thermal noise as they were designed for cartesian sampling. The qRF method was treated with aliasing noise as it was already shown to be robust against such artifacts. [Fig. IV.3.10](#) presents the results obtained, as well as an example of noised signal for each fingerprint.

The GESFIDSE pre-CA fingerprint provided poor results without contrast agent as expected. The qRF-MRF provided comparable estimates for the parameters considered. However, it can be seen that both the OSSI-inspired and random fingerprints performed better, in particular for  $SO_2$  estimates. In this case, it seems that  $SO_2$  maps could be acquired without contrast agent injection and still provide similar precision as the GESFIDSE concatenation fingerprint. The following section presents the work done to optimize the TR and FA trains of the OSSI-inspired and random sequences.



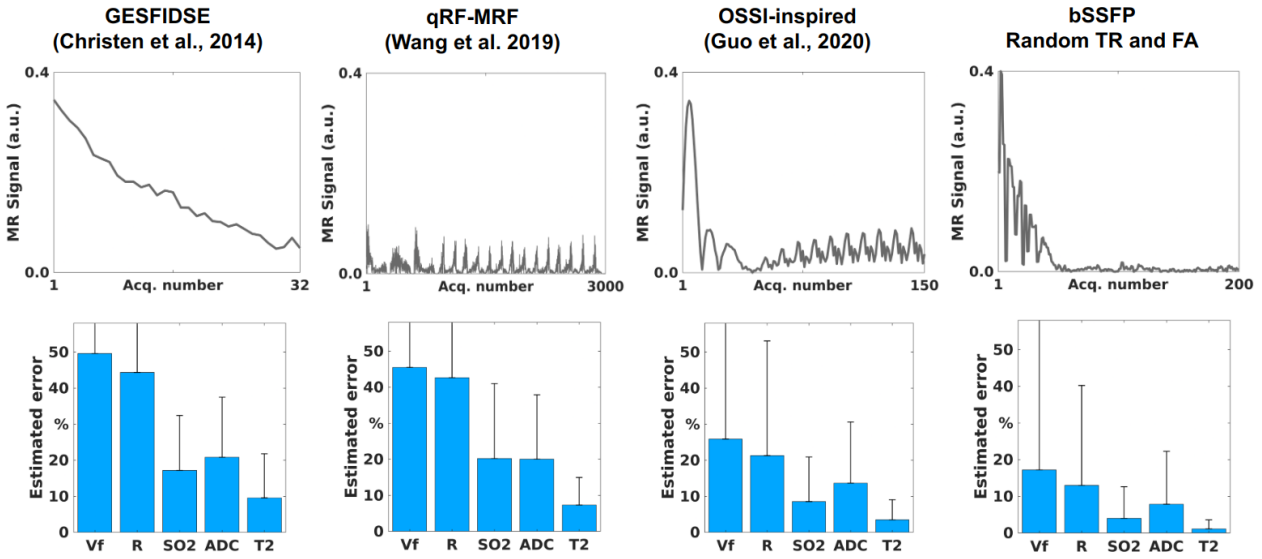


**Figure IV.3.10:** Monte-Carlo evaluation of the GESFIDSE pre-CA and 3 bSSFP fingerprints known to exhibit  $T_2^*$  sensitivity. All fingerprints were treated with thermal noise, except the qRF-MRF which was treated with aliasing noise. The bars represent the mean and standard deviation of the noise-induced error on the estimation of each parameter across the 2000 repetitions on 50 signals. Vf corresponds to BVf. Simulations performed with MRVox.

### IV.3.2.2 Optimization of potential bSSFP MRF sequences

From above, two types of sequences were selected based on the evaluation of one FA and TR train for each. Yet it is likely that better combinations of FA and TR are possible. A brute-force approach was considered, varying FA and TR trains for each of the two sequence type, and evaluating the encoding capacity for MRvF of each resulting fingerprint with the Monte-Carlo method presented above. We considered the two sequence types from above and added one for comparison:

- The transient-state and OSSI phase cycling (see above)
- The random TR and FA train without phase cycling (presented above as well)
- The standard bSSFP with constant TR and FA and no phase cycling

Fig. IV.3.11 presents one fingerprint for each sequence type and the signal variations associated with  $SO_2$  changes. For each sequence type, between 11 and 15 combinations of FA and TR trains were tested:

- For the OSSI-inspired sequence, the phase cycling was kept the same in all tested cases. Classical variations of the RF phase, such as  $90^\circ$  increments, were tried on the first 40 pulses where no cycling was initially applied
- For the “random” sequence, it is the maximum of the allowed range of variation that was varied. Similar classical phase cycling was tried on occasions
- For the bSSFP, the constant FA and TR were varied from one trial to another. In cases, the classical phase cycling was also tried



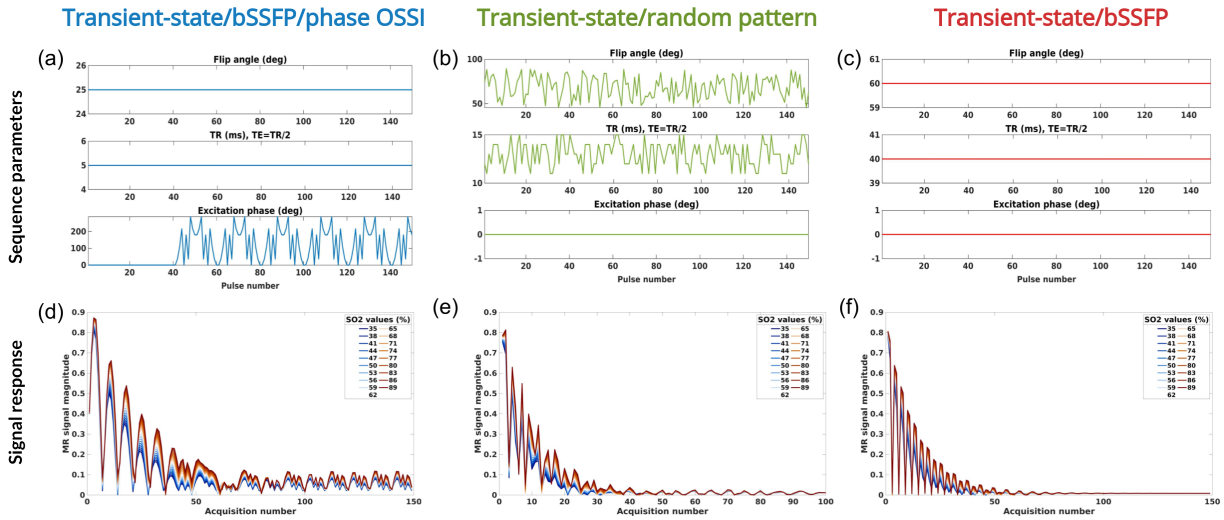


**Figure IV.3.11:** Fingerprints from the three sequence types considered for manual optimization for  $\text{SO}_2$  estimation. The FA, TR, and RF phase are presented on the top row.  $\text{TE} = \text{TR}/2$  in all cases. The bottom row presents the signal variations for all parameters fixed but the  $\text{SO}_2$ . Simulations performed with MRVox

For each different fingerprint of each sequence type, dictionaries with 13,680 signals were generated with MRVox.  $\text{BV}_f$ , R,  $\text{SO}_2$ , and  $T_2$  were considered in the simulations. The ADC was not varied here to reduce the computational cost. Monte-Carlo evaluation with thermal noise was applied to each fingerprint. Fig. IV.3.12 shows the result of this evaluation for each fingerprint from each sequence type, only for the  $\text{SO}_2$ .

Several fingerprint candidates presenting relatively low errors on the  $\text{SO}_2$  estimates can be selected from fig. IV.3.12. Two in particular retained our attention:

- OSSI-inspired with  $\text{FA} = 60^\circ$  and  $\text{TR} = 10\text{ms}$
- Random trains with  $\text{FA} = [0, 90]^\circ$  and  $\text{TR} = [11, 15]\text{ms}$

They were chosen for their good performance on  $T_2$  estimates but also on the other metrics (not shown here).

For both these fingerprints, we further concatenated the TR and FA trains 4 times with a 1-second pause to counterbalance the low signal level reached in the steady-state. Fig. IV.3.13a shows the final fingerprint for the OSSI-inspired candidate. Standard deviation analysis was performed on these fingerprints for several  $\text{SO}_2$ , R and  $\text{BV}_f$  values, as shown in fig. IV.3.13b and IV.3.13c. A Monte-Carlo evaluation was also run on these new fingerprints, and showed improvements in the  $\text{SO}_2$  estimation, as shown in fig. IV.3.13d.

Furthermore, we assessed the robustness of the two candidates to acquisition artefacts using two dictionaries of 95,760 signals that were generated with either a  $B_0$  (frequency offset) or  $B_1$  (pulse amplitude) dimension in addition to those considered before. Variations of

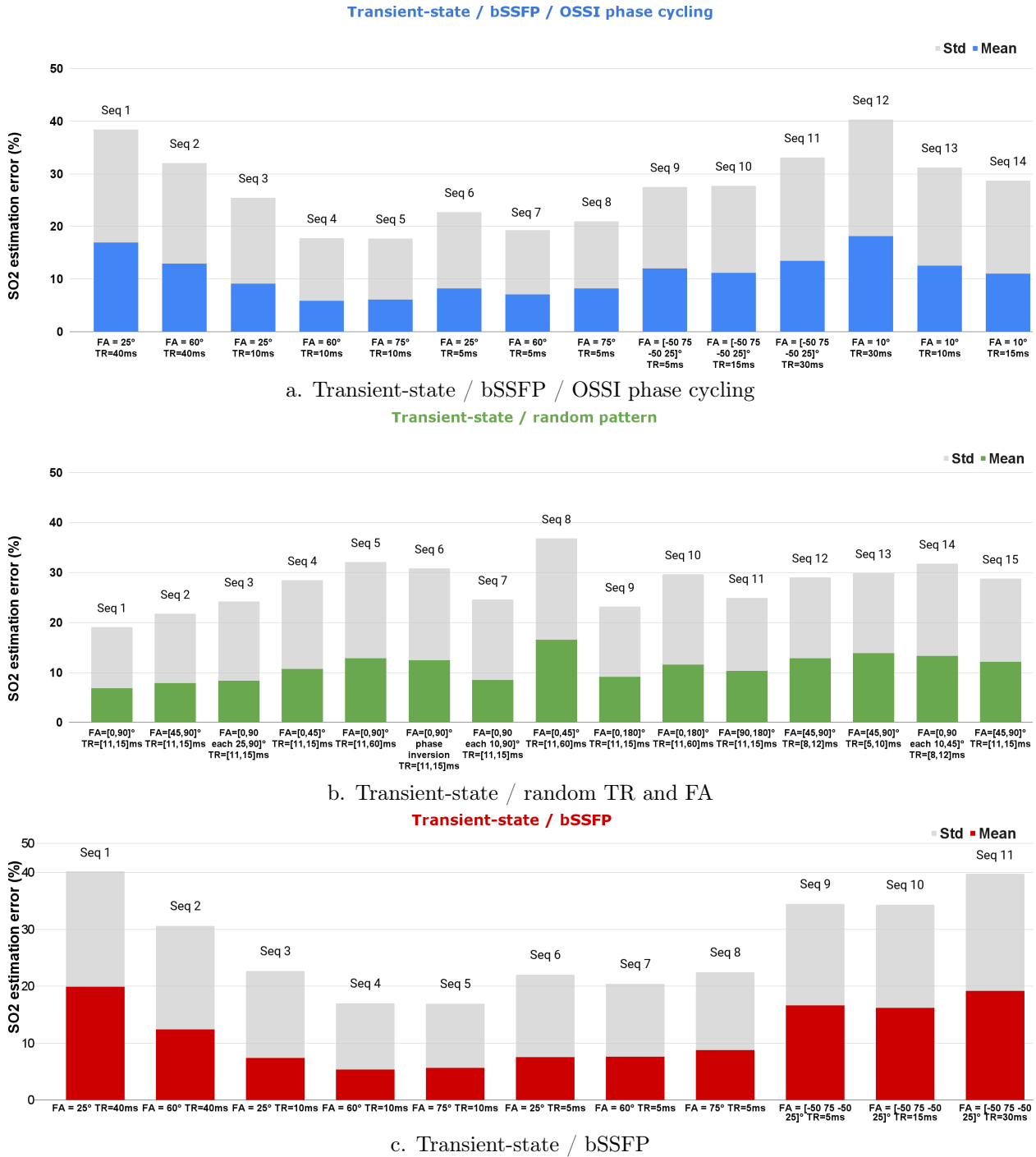


**Figure IV.3.12:** Monte-Carlo evaluation of the SO<sub>2</sub> encoding capacity of three types of sequences. The bars represent the mean and standard deviation of the noise-induced error on the SO<sub>2</sub> estimation across the 2000 repetitions on 50 signals. Simulations performed with MRVox.

B<sub>0</sub> and B<sub>1</sub> can indeed induce variations in the signal that can overlap with those from the parameters of interest. Fig. IV.3.14 shows the results of a Monte-Carlo evaluation on these two dictionaries for the OSSI-inspired candidate, as well as the signal variations brought by

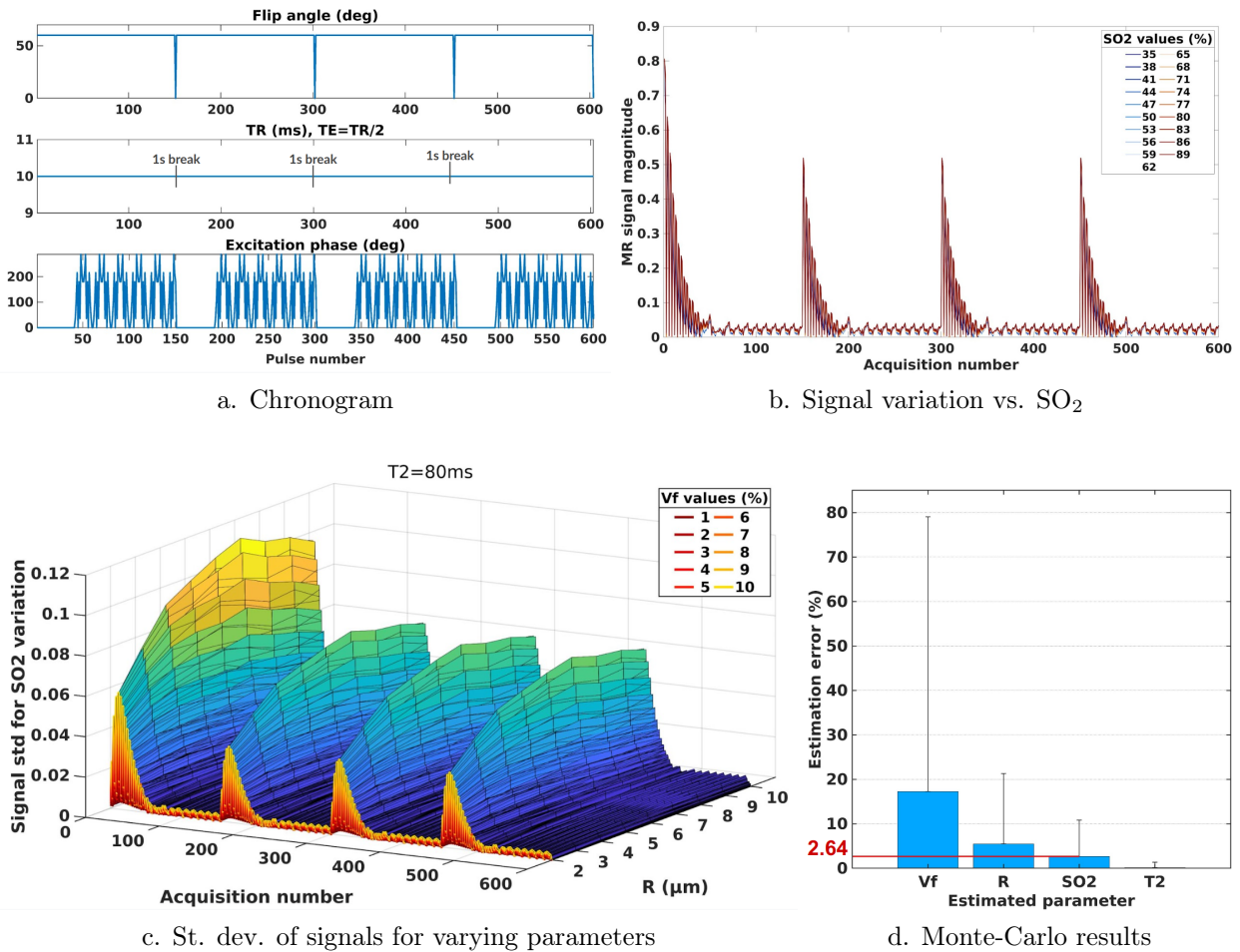


**Figure IV.3.13:** Steps taken to further improve the candidates identified by the manual research of optimal parameters. The fingerprint shown here is the best candidate from the OSSI-inspired sequence type. The bars represent the mean and standard deviation of the noise-induced error on the estimation of each parameter across the 2000 repetitions on 50 signals. Simulations performed with MRVox.

the new dimensions. The  $B_0$  artifacts bring a temporal shift of the oscillating pattern, and large variations in the transient state regime. The  $B_1$  artifacts are associated with a simple amplitude offset. Interestingly, the dictionary containing the  $B_1$  dimension produces better estimates than the other. For the  $\text{SO}_2$  estimates, both dictionaries make an average error well below 10%. This fingerprint is thus expected to provide good estimates, at least for the  $\text{SO}_2$ , without any contrast agent.

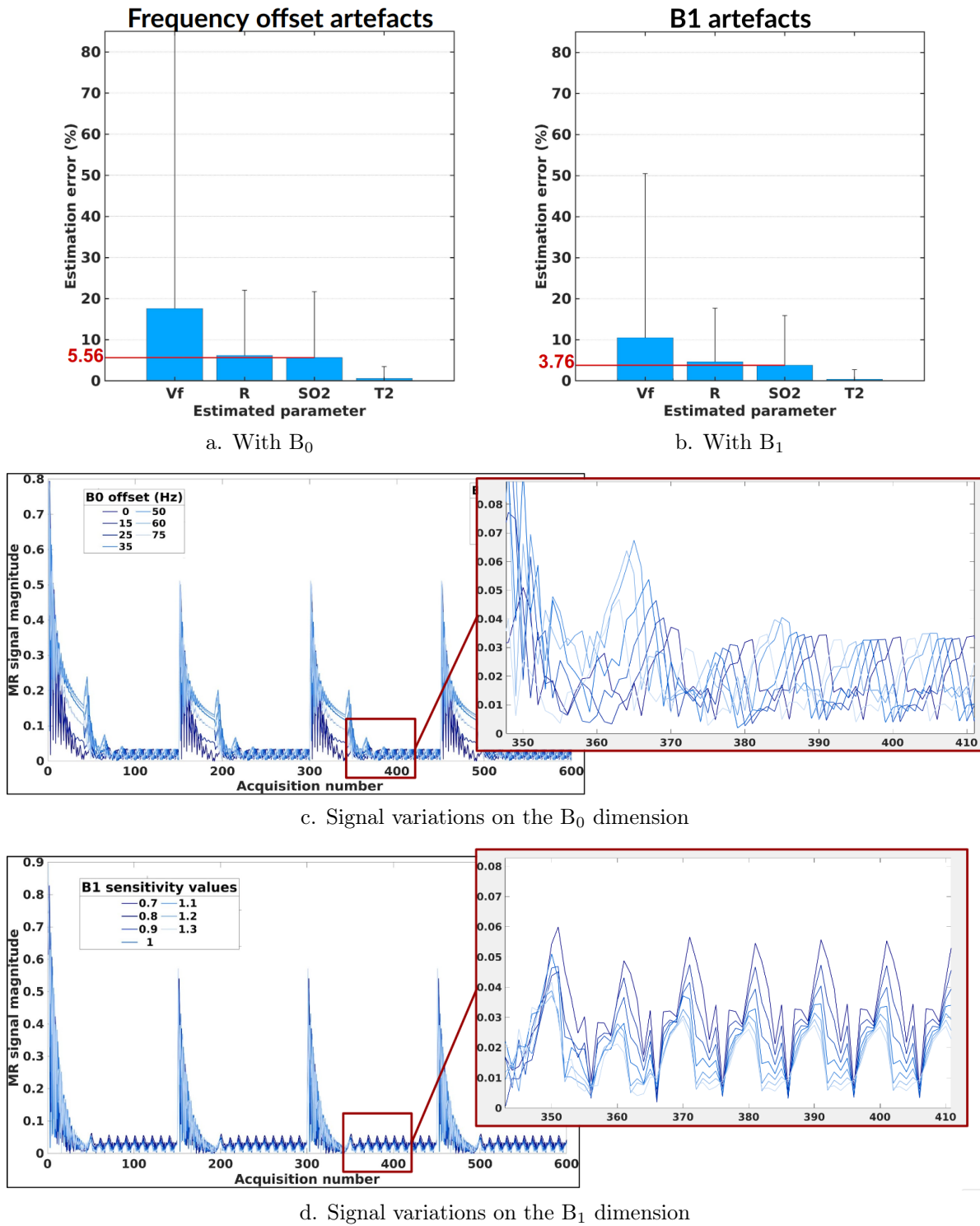


**Figure IV.3.14:** Evaluation of the OSSI-inspired candidate fingerprint against two imaging artifacts. The Monte-Carlo results for the vascular parameters and  $T_2$  are shown on the top row. The two lower panels show how the signal varies with either  $B_0$  and  $B_1$  changes. The bars represent the mean and standard deviation of the noise-induced error on the estimation of each parameter across the 2000 repetitions on 50 signals. Simulations performed with MRVox.

### IV.3.3 Preliminary in vivo results

The OSSI-inspired fingerprint presented above was used to make acquisitions on a live healthy mouse at 4.7T. The animal was anesthetized with 5% isoflurane for induction and 1% for maintenance inside the magnet. A relatively high resolution scan was desired, leading to very small voxels in a mouse brain. For a  $80 \times 80$  acquisition matrix in a  $20 \times 20\text{mm}^2$  FOV, a 2mm slice thickness and 4 averages were used to achieve a high SNR. 14 interleaves were used, with an acquisition bandwidth of 277kHz. The total scan time was 25:15 minutes. Corresponding to that acquisition, a first small dictionary was generated with 6 parameters:

- $\text{SO}_2$ : 5 values in range [35, 85] %
- BVf: 13 values in range [2, 10] %
- R: 4 values in range [2, 10]  $\mu\text{m}$
- $T_1$ : 4 values in range [1100, 1500] ms
- $T_2$ : 4 values in range [65, 95] ms
- $B_0$ : 5 values in range [0, 50] Hz

corresponding to 6400 signals.

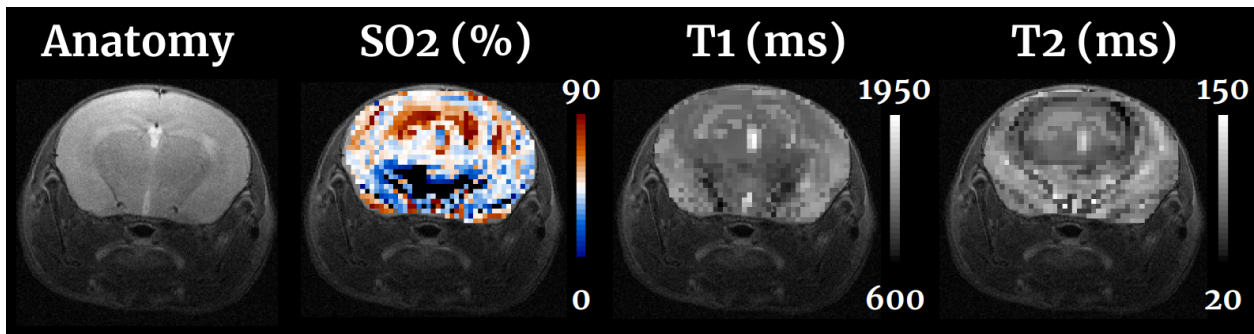
$T_1$  was included as it was found to have an important influence on the oscillations amplitude (not shown here). The learning algorithm from [Boux et al. 2021](#) (see section II.4) was used to estimate parametric maps from the acquired data. Figure IV.3.15 presents some of the parametric maps obtained and the corresponding value distributions.

These results are far from perfect, but are still encouraging, especially considering the small number of generated signals across a 6-parameters space. Obvious artifacts are visible on the  $\text{SO}_2$  map, but the values obtained still mostly fall in the physiological range despite the learning step. The obtained values are lower than what can be expected from a healthy animal. However, the animal stayed a rather long time in the magnet for adjustments, and it was noted that its breathing frequency was relatively low, even under 1% breathed isoflurane, which could induce a diminution of the  $\text{SO}_2$ .

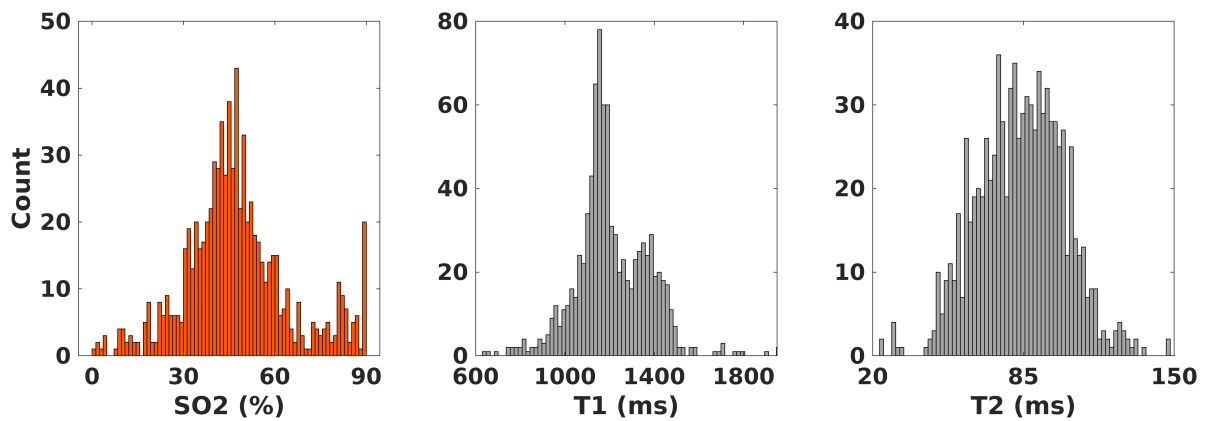
The  $T_2$  maps obtained presents artifacts similar to those of the  $\text{SO}_2$  map, which tends to indicate shimming problems. Care was given to draw a shim volume thicker than the acquired slice and containing only brain tissue. However, the relatively large slice thickness used made the acquisition more sensitive to  $B_0$  inhomogeneities, which seems to have artifacted our data. Extending the  $B_0$  range in the dictionary and adding more values could help reduce these artifacts. The presented  $T_1$  map is very encouraging and underlines the sensitivity of the fingerprint to this parameter. Note the remarkable extension of the limited simulated range by the learning algorithm.

The pixels estimated with a negative  $\text{SO}_2$  were rejected from the  $\text{SO}_2$  map and appear as black. It is expected that this effect is linked with the absence of a  $B_1$  dimension in the dictionary.  $B_1$  was indeed observed to induce signal variations that can overlap with those from  $\text{SO}_2$  variation. It was however not simulated here due to lack of available time. Bigger dictionaries are to be produced soon with a more adapted parameter space sampling, and are expected to further improve these results.

It is also likely that the hyper parameters of our reconstruction tool can be tuned to produce better estimates. Experiments towards an optimal tuning are to be carried out.



a. Reconstructed maps



b. Histograms of obtained values

**Figure IV.3.15:** First results of in vivo MRvF without contrast agent on a live mouse at 4.7T, using the OSSI-inspired fingerprint presented above. The maps are produced with the learning tool from [Boux et al. 2021](#). Mean measured values for the presented parameters are:  $SO_2 = 47.5 \pm 17.3 \%$ ,  $T_1 = 1208 \pm 163\text{ms}$ ,  $T_2 = 84 \pm 19 \text{ms}$ . Black voxels in the  $SO_2$  maps correspond to  $SO_2 < 0$  estimates from the learning tool.

The obtained  $SO_2$  map is still encouraging, and seems to confirm that  $SO_2$  mapping without any contrast agent is possible. The fingerprint optimization will be continued, driven by both physical intuition and automatic tools to improve its sensitivity and robustness against acquisition noise.

## GENERAL CONCLUSION

---

This work is the latest addition to methodological developments that have been ongoing in the team for over two decades, aiming at imaging the brain vascular network and quantifying microvascular properties of clinical value. We proposed here to improve the accuracy and clinical applicability of MRvF, a vascular exploration method that relies on the MRF framework, focusing on oxygenation measurements. This recently introduced MRI paradigm has opened new exciting opportunities for MR quantification but requires a combination of numerical simulations, specific acquisition methodology, and parametric map reconstruction algorithms.

First, we detailed the developments done on the simulation and acquisition parts. Building on existing tools, either shared by the community or developed in the team, we proposed simulation frameworks for both MRF and MRvF dictionary conception. In particular, we renewed MRVox, the simulation tool used to simulate the MR response of inhomogeneous voxels. The simulations' consistency has been improved and parallel computation solutions have been implemented to make dictionary generation easier. A 3D version of the code has also been implemented to further improve the agreement between simulations and in vivo acquisitions. These tools are now shared with the MR community. Further developments will include closed vascular networks, flow simulations, and performance improvement. Efforts have been made to improve the versatility of the pre-clinical MRF acquisition modules previously developed in the team. These modules were evaluated with MR sequences proposed in the literature. We achieved a working point that allows for acquisitions on small animals and sequence evaluations. The modules have been shared with collaborators in Copenhagen university but limitations still remain. The number of pulses that can be used in a sequence is limited. In addition, we observed unexpected signal changes depending on the slice offset in the scanner. We will work on solving these issues with the help of Bruker technical staff. A collaboration with Philips Research was initiated and their MRF module has been installed on our scanner. First acquisitions on phantoms and humans demonstrated the flexibility of the module and encouraging results were obtained on relaxometry experiments using sequences from the literature.

Eventually, reconstruction tools and associated visualization solutions were specifically developed for MRF purposes. They have been integrated into a pipeline processor developed and maintained by the team, which was released as an open-source tool for the community.

Secondly, we demonstrated how MRvF's sensitivity could be increased by refining the MR simulations. We segmented vascular networks from whole-brain, 3D microscopies publicly available, and used them as a simulation basis in the 3D version of MRVox. To account for the limited number of voxels that were processed in a tractable time, the simulated dictionary was learned by a bayesian-based algorithm tool developed in the team. On retrospective data from healthy and pathological rats, our proposed MRvF dictionary performed better than the previous 2D and 3D approaches, producing oxygenation maps with contrast and absolute values in better agreement with the literature. In addition, only our approach correlated



with intracranial  $pO_2$  measurements in lesions. Limitations of the proposed method have also been identified. In particular, no microscopy databases in pathological tissue are currently available. Including such abnormal networks in our simulations is expected to provide better estimates in lesions. We have started to implement dedicated solutions such as constructive algorithms to generate *in silico* realistic vascular networks to be able to produce a large variety of realistic synthetic voxels.

Finally, we searched for a better MRvF acquisition sequence that would be both more sensitive to blood oxygenation and contrast agent free. Tools proposed in the literature to evaluate the sensitivity of a given sequence to parameters of interest have been implemented. These tools have been validated on retrospective animal data, using different combinations of acquisitions performed before and after contrast-agent injection. We eventually presented a combination that performed better than the initial approach.

To find a sequence that is sensitive to oxygenation but does not require contrast agent injection, we started by searching the MR literature. We looked for unconventional sequences used for functional imaging as well as sequences that were underused due to large sensitivities to magnetic field inhomogeneities. From these intuitions, several sequence types were evaluated and a sequence showing promising *in silico* results was found. *In vivo* trials on animals have started and preliminary results are presented. In parallel, state-of-the-art automatic sequence optimization algorithms are evaluated to help finding new sequences that will be more accurate and robust to imaging artifacts.

In conclusion, the developments from this Ph.D. project have led to the creation of an MRF pipeline able to acquire and process preclinical and clinical data. The results obtained for brain oxygenation measurements can already be used to improve  $SO_2$  estimates and a number of collaborations have been started to further test the technique in different conditions. Potential improvements could be further obtained following our new developments on realistic simulations and the next *in vivo* tests of bSSFP sequence candidates for contrast agent free oxygenation mapping. Given our encouraging results, our tools could be further used as basis for the development of single MRF sequences that could replace whole MR exams. This would allow for shorter exams, better suiting emergency imaging. In this case, automatic optimization procedures could be used to integrate both structural and functional information into the MRF fingerprints in a reasonable time. MRF also presents the exciting possibility to rapidly share a whole MR sequence through a single text-file, avoiding possible months of MR sequence development and software adaptation. Collaboration between research teams and multi-center trials should thus be facilitated and lead to faster distribution on clinical scanners and benefits for patient care.

## BIBLIOGRAPHY

---

- Albers, G. W. et al., **Thrombectomy for Stroke at 6 to 16 Hours with Selection by Perfusion Imaging**, *New England Journal of Medicine* **378**, 708 (2018).
- Assländer, J., **A Perspective on MR Fingerprinting**, *Journal of Magnetic Resonance Imaging* **n/a** (2020).
- Assländer, J., M. A. Cloos, F. Knoll, D. K. Sodickson, J. Hennig and R. Lattanzi, **Low rank alternating direction method of multipliers reconstruction for MR fingerprinting**, *Magnetic Resonance in Medicine* **79**, 83 (2018).
- Assländer, J., D. S. Novikov, R. Lattanzi, D. K. Sodickson and M. A. Cloos, **Hybrid-state free precession in nuclear magnetic resonance**, *Communications Physics* **2**, 1 (2019).
- Baele, P. and P. Van der Linden, *Le transport de l'Oxygène par le sang* (2002), URL: <https://www.virtanes.be/oxy.PDF>.
- Báez-Yáñez, M. G., P. Ehses, C. Mirkes, P. S. Tsai, D. Kleinfeld and K. Scheffler, **The impact of vessel size, orientation and intravascular contribution on the neurovascular fingerprint of BOLD bSSFP fMRI**, *NeuroImage* **163**, 13 (2017).
- Bandettini, P. A. and E. C. Wong, **Effects of biophysical and physiologic parameters on brain activation-induced  $R2^*$  and  $R2$  changes: Simulations using a deterministic diffusion model**, *International Journal of Imaging Systems and Technology* **6**, 133 (1995).
- Barker, G. J., A. Simmons, S. R. Arridge and P. S. Tofts, **A simple method for investigating the effects of non-uniformity of radiofrequency transmission and radiofrequency reception in MRI**. *The British Journal of Radiology* **71**, 59 (1998).
- Barnholtz-Sloan, J. S., Q. T. Ostrom and D. Cote, **Epidemiology of Brain Tumors**, *Neurologic Clinics* **36**, 395 (2018).
- Barud, M., W. Dabrowski, D. Siwicka-Gieroba, C. Robba, M. Bielacz and R. Badenes, **Usefulness of Cerebral Oximetry in TBI by NIRS**, *Journal of Clinical Medicine* **10**, 2938 (2021).
- Bernstein, M. A., K. F. King and X. J. Zhou, *Handbook of MRI Pulse Sequences* (Elsevier).
- Bloch, F., **Nuclear Induction**, *Physical Review* **70**, 460 (1946).
- Bluemke, E., E. Stride and D. P. Bulte, **A General Model to Calculate the Spin-Lattice Relaxation Rate (  $R_1$  ) of Blood, Accounting for Hematocrit, Oxygen Saturation, Oxygen Partial Pressure, and Magnetic Field Strength Under Hyperoxic Conditions**, *Journal of Magnetic Resonance Imaging* **55**, 1428 (2022).
- Bolar, D. S., B. R. Rosen, A. G. Sorensen and E. Adalsteinsson, **QUantitative Imaging of eXtraction of oxygen and Tissue consumption (QUIXOTIC) using venular-targeted velocity-selective spin labeling**, *Magnetic Resonance in Medicine* **66**, 1550 (2011).
- Boux, F., F. Forbes, J. Arbel, B. Lemasson and E. L. Barbier, **Bayesian Inverse Regression for Vascular Magnetic Resonance Fingerprinting**, *IEEE Transactions on Medical Imaging* **40**, 1827 (2021).

- Boxerman, J. L., L. M. Hamberg, B. R. Rosen and R. M. Weisskoff, **Mr contrast due to intravascular magnetic susceptibility perturbations**, *Magnetic Resonance in Medicine* **34**, 555 (1995).
- Boyacioglu, R., C. Wang, D. Ma, D. F. McGivney, X. Yu and M. A. Griswold, **3D magnetic resonance fingerprinting with quadratic RF phase**, *Magnetic Resonance in Medicine* **85**, 2084 (2021).
- Broisat, A., B. Lemasson, M. Ahmadi, N. Collomb, S. Bacot, A. Soubies, D. Fagret, C. Rémy, C. Ghezzi and E. L. Barbier, **Mapping of brain tissue hematocrit in glioma and acute stroke using a dual autoradiography approach**, *Scientific Reports* **8**, 9878 (2018).
- Brossard, C., O. Montigon, F. Boux, A. Delphin, T. Christen, E. L. Barbier and B. Lemasson, **MP3: Medical Software for Processing Multi-Parametric Images Pipelines**, *Frontiers in Neuroinformatics* **14** (2020).
- Brown, J. M. and W. R. Wilson, **Exploiting tumour hypoxia in cancer treatment**, *Nature Reviews. Cancer* **4**, 437 (2004).
- Cao, W., Y. V. Chang, E. K. Englund, H. K. Song, S. Barhoum, Z. B. Rodgers, M. C. Langham and F. W. Wehrli, **High-speed whole-brain oximetry by golden-angle radial MRI**, *Magnetic Resonance in Medicine* **79**, 217 (2018).
- Caraguel, F., A.-C. Lesart, F. Estève, B. van der Sanden and A. Stéphanou, **Towards the Design of a Patient-Specific Virtual Tumour**, *Computational and Mathematical Methods in Medicine* **2016**, e7851789 (2016).
- Cencini, M., L. Matteo, J. D. Kaggie, R. F. Schulte, M. Tosetti and G. Buonincontri, “Musculoskeletal MR Fingerprinting with dictionary-based fat and water separation”, *Proceedings of International Society of Magnetic Resonance in Medicine*, (2018).
- Chiarelli, P. A., D. P. Bulte, R. Wise, D. Gallichan and P. Jezard, **A calibration method for quantitative BOLD fMRI based on hyperoxia**, *NeuroImage* **37**, 808 (2007).
- Cho, J., Y. Kee, P. Spincemille, T. D. Nguyen, J. Zhang, A. Gupta, S. Zhang and Y. Wang, **Cerebral metabolic rate of oxygen (CMRO<sub>2</sub>) mapping by combining quantitative susceptibility mapping (QSM) and quantitative blood oxygenation level-dependent imaging (qBOLD)**, *Magnetic Resonance in Medicine* **80**, 1595 (2018).
- Cho, J., J. Lee, H. An, M. S. Goyal, Y. Su and Y. Wang, **Cerebral oxygen extraction fraction (OEF): Comparison of challenge-free gradient echo QSM+qBOLD (QQ) with 15O PET in healthy adults**, *Journal of Cerebral Blood Flow & Metabolism* **41**, 1658 (2021).
- Christen, T., D. S. Bolar and G. Zaharchuk, **Imaging Brain Oxygenation with MRI Using Blood Oxygenation Approaches: Methods, Validation, and Clinical Applications**, *American Journal of Neuroradiology* **34**, 1113 (2013).
- Christen, T., P. Bouzat, N. Pannetier, N. Coquery, A. Moisan, B. Lemasson, S. Thomas, E. Grillon, O. Detante, C. Rémy, J.-F. Payen and E. L. Barbier, **Tissue Oxygen Saturation Mapping with Magnetic Resonance Imaging**, *Journal of Cerebral Blood Flow & Metabolism* **34**, 1550 (2014).
- Christen, T., B. Lemasson, N. Pannetier, R. Farion, C. Remy, G. Zaharchuk and E. L. Barbier, **Is T2\* Enough to Assess Oxygenation? Quantitative Blood Oxygen Level-Dependent Analysis in Brain Tumor**, *Radiology* **262**, 495 (2012).

- Christen, T., B. Lemasson, N. Pannetier, R. Farion, C. Segebarth, C. Rémy and E. L. Barbier, **Evaluation of a quantitative blood oxygenation level-dependent (qBOLD) approach to map local blood oxygen saturation**, *NMR in Biomedicine* **24**, 393 (2011).
- Christen, T., N. A. Pannetier, W. W. Ni, D. Qiu, M. E. Moseley, N. Schuff and G. Zaharchuk, **MR vascular fingerprinting: A new approach to compute cerebral blood volume, mean vessel radius, and oxygenation maps in the human brain**, *NeuroImage* **89**, 262 (2014).
- Cohen, O., S. Huang, M. T. McMahon, M. S. Rosen and C. T. Farrar, **Rapid and quantitative chemical exchange saturation transfer (CEST) imaging with magnetic resonance fingerprinting (MRF)**, *Magnetic Resonance in Medicine* **80**, 2449 (2018).
- Coudert, T., A. Delphin, J. M. Warnking, B. Lemasson, E. L. Barbier and T. Christen, “Searching for an MR Fingerprinting sequence to measure brain oxygenation without contrast agent”, *ISMRM 31st Annual Meeting & Exhibition, May 2022, London, United Kingdom*, (2022).
- Deiming, M. and O. Heid, “Magnetization Prepared True FISP Imaging”, *Proc 2nd Annual Meeting SMR*, (1994).
- Deleforge, A., F. Forbes and R. Horaud, **High-dimensional regression with gaussian mixtures and partially-latent response variables**, *Statistics and Computing* **25**, 893 (2015).
- Delphin, A., *vascularTree - Constrained Constructive Optimization (CCO)*, URL: <https://github.com/adelphin/vascularTree-CCO>, (2022).
- Delphin, A., F. Boux, C. Brossard, J. Warnking, B. Lemasson, E. Barbier and T. Christen, “Using 3D realistic blood vessel structures machine learning for MR vascular Fingerprinting”, *ISMRM 31st Annual Meeting & Exhibition, May 2022, London, United Kingdom*, (2022).
- Delphin, A., F. Boux, C. Brossard, J. Warnking, B. Lemasson, E. L. Barbier and T. Christen, “Optimizing signal patterns for MR vascular fingerprinting”, *ISMRM & SMRT Virtual Conference & Exhibition*, (2020).
- Delphin, A., F. Boux, C. Brossard, J. M. Warnking, B. Lemasson, E. L. Barbier and T. Christen, **Realistic microvascular geometries for MR vascular Fingerprinting**, In preparation (2022).
- Delphin, A., F. Boux, C. Brossard, J. M. Warnking, B. Lemasson, E. L. Barbier and T. Christen, “Optimisation des motifs de signaux pour l’IRM Fingerprinting vasculaire”, *5e Congrès scientifique de la Société Française de Résonance Magnétique en Biologie et Médecine*, (2021).
- Delphin, A., F. Boux, C. Brossard, J. M. Warnking, B. Lemasson, E. L. Barbier and T. Christen, “Towards optimizing MR vascular fingerprinting”, *ISMRM & SMRT Virtual Conference & Exhibition*, (2021).
- Di Giovanna, A. P., A. Tibo, L. Silvestri, M. C. Müllenbroich, I. Costantini, A. L. Allegra Mascaro, L. Sacconi, P. Frasconi and F. S. Pavone, **Whole-Brain Vasculature Reconstruction at the Single Capillary Level**, *Scientific Reports* **8**, 12573 (2018).
- Dickson, J. D., T. W. J. Ash, G. B. Williams, A. L. Sukstanskii, R. E. Ansorge and D. A. Yablonskiy, **Quantitative phenomenological model of the BOLD contrast mechanism**, *Journal of Magnetic Resonance* **212**, 17 (2011).

- Drew, P. J., **Vascular and neural basis of the BOLD signal**, *Current Opinion in Neurobiology* **58**, 61 (2019).
- Englund, E. K., M. A. Fernández-Seara, A. E. Rodríguez-Soto, H. Lee, Z. B. Rodgers, M. Vidorreta, J. A. Detre and F. W. Wehrli, **Calibrated fMRI for dynamic mapping of CMRO<sub>2</sub> responses using MR-based measurements of whole-brain venous oxygen saturation**, *Journal of Cerebral Blood Flow & Metabolism* **40**, 1501 (2020).
- Fan, A. P., H. An, F. Moradi, J. Rosenberg, Y. Ishii, T. Nariai, H. Okazawa and G. Zaharchuk, **Quantification of brain oxygen extraction and metabolism with [15O]-gas PET: A technical review in the era of PET/MRI**, *NeuroImage* **220**, 117136 (2020).
- Fan, H., L. Bunker, A. Z. Durfee, X. J. Zhou, A. E. Hillis and H. Lu, “Simultaneous perfusion, diffusion, T2\*, and T1 mapping with MR Fingerprinting (MRF-PDT)”, *Proceedings of International Society of Magnetic Resonance in Medicine*, (2022).
- Farmanfarma, K. K., M. Mohammadian, Z. Shahabinia, S. Hassanipour and H. Salehiniya, **Brain cancer in the world: an epidemiological review** 6 (2019).
- Feigin, V. L. et al., **Global, regional, and national burden of stroke and its risk factors, 1990–2019: a systematic analysis for the Global Burden of Disease Study 2019**, *The Lancet Neurology* **20**, 795 (2021).
- Flassbeck, S., S. Schmidt, P. Bachert, M. E. Ladd and S. Schmitter, **Flow MR fingerprinting**, *Magnetic Resonance in Medicine* **81**, 2536 (2019).
- Flood, A. B., P. E. Schaner, P. Vaupel, B. B. Williams, B. Gallez, E. Y. Chen, A. Ali, T. Liu, V. H. Lawson, W. Schreiber and H. M. Swartz, **Clinical and Statistical Considerations when Assessing Oxygen Levels in Tumors: Illustrative Results from Clinical EPR Oximetry Studies**. in P.-D. Ryu, J. C. LaManna, D. K. Harrison and S.-S. Lee (ed. by), *Oxygen Transport to Tissue XLI*, vol. 1232 (Springer International Publishing).
- Fung, Y. C., **The Veins**. in Y. C. Fung (ed. by), *Biomechanics: Circulation* (Springer).
- Genois, É., L. Gagnon and M. Desjardins, **Modeling of vascular space occupancy and BOLD functional MRI from first principles using real microvascular angiograms**, *Magnetic Resonance in Medicine* **85**, 456 (2021).
- Gertsenshteyn, I., M. Giurcanu, P. Vaupel and H. Halpern, **Biological validation of electron paramagnetic resonance (EPR) image oxygen thresholds in tissue**, *The Journal of Physiology* **599**, 1759 (2021).
- Gómez, P. A., M. Molina-Romero, G. Buonincontri, M. I. Menzel and B. H. Menze, **Designing contrasts for rapid, simultaneous parameter quantification and flow visualization with quantitative transient-state imaging**, *Scientific Reports* **9**, 8468 (2019).
- Gould, J., **Breaking down the epidemiology of brain cancer**, *Nature* **561**, S40 (2018).
- Graham, K. and E. Unger, **Overcoming tumor hypoxia as a barrier to radiotherapy, chemotherapy and immunotherapy in cancer treatment**, *International Journal of Nanomedicine* **13**, 6049 (2018).
- Gray, L. H., A. D. Conger, M. Ebert, S. Hornsey and O. C. A. Scott, **The Concentration of Oxygen Dissolved in Tissues at the Time of Irradiation as a Factor in Radiotherapy**, *The British Journal of Radiology* **26**, 638 (1953).
- Greve, J. M., **The BOLD effect**, *Methods in Molecular Biology* (Clifton, N.J.) **771**, 153 (2011).

- Guenther, C., T. Amthor, M. Doneva and S. Kozerke, [A unifying view on extended phase graphs and Bloch simulations for quantitative MRI](#), *Scientific Reports* **11**, 21289 (2021).
- Guo, J. and E. C. Wong, [Venous oxygenation mapping using velocity-selective excitation and arterial nulling](#), *Magnetic Resonance in Medicine* **68**, 1458 (2012).
- Guo, S. and D. C. Noll, [Oscillating steady-state imaging \(OSSI\): A novel method for functional MRI](#), *Magnetic Resonance in Medicine* **84**, 698 (2020).
- Haacke, E. M., R. W. Brown, M. R. Thompson and R. Venkatesan, [Magnetic resonance imaging: physical principles and sequence design](#) (1999).
- Hales, P. W., F. J. Kirkham and C. A. Clark, [A general model to calculate the spin-lattice \(T1\) relaxation time of blood, accounting for haematocrit, oxygen saturation and magnetic field strength](#), *Journal of Cerebral Blood Flow & Metabolism* **36**, 370 (2016).
- Hamarneh, G. and P. Jassi, [VascuSynth: Simulating vascular trees for generating volumetric image data with ground-truth segmentation and tree analysis](#), *Computerized Medical Imaging and Graphics* **34**, 605 (2010).
- Hargreaves, B., [Matlab/C Bloch Equation Simulator](#), URL: <http://mrsrl.stanford.edu/~brian/blochsim/>, (2005).
- Hargreaves, B., [Matlab EPG implementation](#), URL: <https://web.stanford.edu/~bah/software/epg/>, (2015).
- Hargreaves, B. A., S. S. Vasanaawala, J. M. Pauly and D. G. Nishimura, [Characterization and reduction of the transient response in steady-state MR imaging](#), *Magnetic Resonance in Medicine* **46**, 149 (2001).
- Hartung, G., S. Badr, S. Mihelic, A. Dunn, X. Cheng, S. Kura, D. A. Boas, D. Kleinfeld, A. Alaraj and A. A. Linninger, [Mathematical synthesis of the cortical circulation for the whole mouse brain—part II: Microcirculatory closure](#), *Microcirculation* **28** (2021).
- Hashem, M., Q. Zhang, Y. Wu, T. W. Johnson and J. F. Dunn, [Using a multimodal near-infrared spectroscopy and MRI to quantify gray matter metabolic rate for oxygen: A hypothermia validation study](#), *NeuroImage* **206**, 116315 (2020).
- He, X. and D. A. Yablonskiy, [Quantitative BOLD: Mapping of human cerebral deoxygenated blood volume and oxygen extraction fraction: Default state](#), *Magnetic Resonance in Medicine* **57**, 115 (2007).
- Hennig, J., [Multiecho imaging sequences with low refocusing flip angles](#), *Journal of Magnetic Resonance* (1969) **78**, 397 (1988).
- Hennig, J., [Echoes—how to generate, recognize, use or avoid them in MR-imaging sequences. Part I: Fundamental and not so fundamental properties of spin echoes](#), *Concepts in Magnetic Resonance* **3**, 125 (1991).
- Hoge, R. D., [Calibrated fMRI](#), *NeuroImage* **62**, 930 (2012).
- Horitsugi, G., T. Watabe, Y. Kanai, H. Ikeda, H. Kato, S. Naka, M. Ishibashi, K. Matsunaga, K. Isohashi, E. Shimosegawa and J. Hatazawa, [Oxygen-15 labeled CO<sub>2</sub>, O<sub>2</sub>, and CO PET in small animals: evaluation using a 3D-mode microPET scanner and impact of reconstruction algorithms](#), *EJNMMI Research* **7**, 91 (2017).
- Hosford, P. S., J. A. Wells, I. N. Christie, M. F. Lythgoe, J. Millar and A. V. Gourine, [Electrochemical carbon fiber-based technique for simultaneous recordings of brain](#)



- tissue PO<sub>2</sub>, pH, and extracellular field potentials, *Biosensors and Bioelectronics: X* **3**, 100034 (2019).
- Janasik, D. and T. Krawczyk, **19F MRI Probes for Multimodal Imaging\*\***, *Chemistry – A European Journal* **28**, e202102556 (2022).
- Jiang, D., S. Deng, C. G. Franklin, M. O’Boyle, W. Zhang, B. L. Heyl, L. Pan, P. A. Jerabek, P. T. Fox and H. Lu, **Validation of T<sub>2</sub>-based oxygen extraction fraction measurement with 15O positron emission tomography**, *Magnetic Resonance in Medicine* **85**, 290 (2021).
- Jiang, D. and H. Lu, **Cerebral oxygen extraction fraction MRI: Techniques and applications**, *Magnetic Resonance in Medicine* **88**, 575 (2022).
- Jiang, Y., D. Ma, R. Jerecic, J. Duerk, N. Seiberlich, V. Gulani and M. A. Griswold, **MR fingerprinting using the quick echo splitting NMR imaging technique**, *Magnetic Resonance in Medicine* **77**, 979 (2017).
- Jiang, Y., D. Ma, N. Seiberlich, V. Gulani and M. A. Griswold, **MR fingerprinting using fast imaging with steady state precession (FISP) with spiral readout**, *Magnetic Resonance in Medicine* **74**, 1621 (2015).
- Jordan, S. P., S. Hu, I. Rozada, D. F. McGivney, R. Boyacioglu, D. C. Jacob, S. Huang, M. Beverland, H. G. Katzgraber, M. Troyer, M. A. Griswold and D. Ma, **Automated Design of Pulse Sequences for Magnetic Resonance Fingerprinting using Physics-Inspired Optimization**, *Proceedings of the National Academy of Sciences* **118**, e2020516118 (2021).
- Kain, M., M. Bodin, S. Loury, Y. Chi, J. Louis, M. Simon, J. Lamy, C. Barillot and M. Dojat, **Small Animal Shanoir (SAS) A Cloud-Based Solution for Managing Preclinical MR Brain Imaging Studies**, *Frontiers in Neuroinformatics* **14** (2020).
- Karch, R., F. Neumann, M. Neumann and W. Schreiner, **A three-dimensional model for arterial tree representation, generated by constrained constructive optimization**, *Computers in Biology and Medicine* **29**, 19 (1999).
- Kim, T. S., J. Lee, J. H. Lee, G. H. Glover and J. M. Pauly, **Analysis of the BOLD characteristics in pass-band bSSFP fMRI**, *International Journal of Imaging Systems and Technology* **22**, 23 (2012).
- Kirkman, M. A. and M. Smith, **Brain Oxygenation Monitoring**, *Anesthesiology Clinics* **34**, 537 (2016).
- Kirst, C., S. Skriabine, A. Vieites-Prado, T. Topilko, P. Bertin, G. Gerschenfeld, F. Verny, P. Topilko, N. Michalski, M. Tessier-Lavigne and N. Renier, **Mapping the Fine-Scale Organization and Plasticity of the Brain Vasculature**, *Cell* **180**, 780 (2020).
- Klassen, M. and R. S. Menon, **NMR Simulation Analysis of Statistical Effects on Quantifying Cerebrovascular Parameters**, *Biophysical Journal* **92**, 1014 (2007).
- Kobayashi, Y. and Y. Terada, **Diffusion-weighting Caused by Spoiler Gradients in the Fast Imaging with Steady-state Precession Sequence May Lead to Inaccurate T<sub>2</sub> Measurements in MR Fingerprinting**, *Magnetic Resonance in Medical Sciences* **18**, 96 (2019).
- Kovacsova, Z., G. Bale, G. Bale, G. Bale, S. Mitra, F. Lange and I. Tachtsidis, **Absolute quantification of cerebral tissue oxygen saturation with multidistance broadband NIRS in newborn brain**, *Biomedical Optics Express* **12**, 907 (2021).



- Kulpanovich, A. and A. Tal, [The application of magnetic resonance fingerprinting to single voxel proton spectroscopy](#), *NMR in Biomedicine* **31**, e4001 (2018).
- Lauwers, F., F. Cassot, V. Lauwers-Cances, P. Puwanarajah and H. Duvernoy, [Morphometry of the human cerebral cortex microcirculation: General characteristics and space-related profiles](#), *NeuroImage* **39**, 936 (2008).
- Lee, H. and F. W. Wehrli, [Whole-brain 3D mapping of oxygen metabolism using constrained quantitative BOLD](#), *NeuroImage* **250**, 118952 (2022).
- Lemasson, B., N. Pannetier, N. Coquery, L. S. B. Boisserand, N. Collomb, N. Schuff, M. Moseley, G. Zaharchuk, E. L. Barbier and T. Christen, [MR Vascular Fingerprinting in Stroke and Brain Tumors Models](#), *Scientific Reports* **6**, 37071 (2016).
- Lemasson, B., S. Valable, R. Farion, A. Krainik, C. Rémy and E. L. Barbier, [In vivo imaging of vessel diameter, size, and density: A comparative study between MRI and histology](#), *Magnetic Resonance in Medicine* **69**, 18 (2013).
- Li, W., F. Xu, D. Zhu, P. C. M. van Zijl and Q. Qin, [T2-oximetry-based cerebral venous oxygenation mapping using Fourier-transform-based velocity-selective pulse trains](#), *Magnetic Resonance in Medicine* **88**, 1292 (2022).
- Linninger, A., I. G. Gould, T. Marinnan, C.-Y. Hsu, M. Chojecki and A. Alaraj, [Cerebral Microcirculation and Oxygen Tension in the Human Secondary Cortex](#), *Annals of Biomedical Engineering* **41**, 2264 (2013).
- Linninger, A., G. Hartung, S. Badr and R. Morley, [Mathematical synthesis of the cortical circulation for the whole mouse brain-part I. theory and image integration](#), *Computers in Biology and Medicine* **110**, 265 (2019).
- Liu, H., O. van der Heide, C. A. T. v. d. Berg and A. Sbrizzi, [Fast and Accurate Modeling of Transient-State Gradient-Spoiled Sequences by Recurrent Neural Networks](#), *NMR in Biomedicine* **34** (2021).
- Lorthois, S., F. Cassot and F. Lauwers, [Simulation study of brain blood flow regulation by intra-cortical arterioles in an anatomically accurate large human vascular network: Part I: methodology and baseline flow](#), *NeuroImage* **54**, 1031 (2011).
- Lorthois, S., F. Cassot and F. Lauwers, [Simulation study of brain blood flow regulation by intra-cortical arterioles in an anatomically accurate large human vascular network. Part II: Flow variations induced by global or localized modifications of arteriolar diameters](#), *NeuroImage* **54**, 2840 (2011).
- Lorthois, S. and F. Cassot, [Fractal analysis of vascular networks: Insights from morphogenesis](#), *Journal of Theoretical Biology* **262**, 614 (2010).
- Lorthois, S., F. Lauwers and F. Cassot, [Tortuosity and other vessel attributes for arterioles and venules of the human cerebral cortex](#), *Microvascular Research* **91**, 99 (2014).
- Lu, H. and Y. Ge, [Quantitative evaluation of oxygenation in venous vessels using T2-Relaxation-Under-Spin-Tagging MRI](#), *Magnetic Resonance in Medicine* **60**, 357 (2008).
- Lu, H., F. Xu, K. Grgac, P. Liu, Q. Qin and P. van Zijl, [Calibration and validation of TRUST MRI for the estimation of cerebral blood oxygenation](#), *Magnetic Resonance in Medicine* **67**, 42 (2012).
- Ma, D., V. Gulani, N. Seiberlich, K. Liu, J. L. Sunshine, J. L. Duerk and M. A. Griswold, [Magnetic resonance fingerprinting](#), *Nature* **495**, 187 (2013).

- Ma, J. and F. W. Wehrli, **Method for Image-Based Measurement of the Reversible and Irreversible Contribution to the Transverse-Relaxation Rate**, *Journal of Magnetic Resonance, Series B* **111**, 61 (1996).
- Manohar, S. and D. Razansky, **Photoacoustics: a historical review**, *Advances in Optics and Photonics* **8**, 586 (2016).
- Marques, J. P. and R. Bowtell, **Application of a Fourier-based method for rapid calculation of field inhomogeneity due to spatial variation of magnetic susceptibility**, *Concepts in Magnetic Resonance Part B: Magnetic Resonance Engineering* **25B**, 65 (2005).
- Marty, B., A. L. Lopez Kolkovsky, E. C. Araujo and H. Reyngoudt, **Quantitative Skeletal Muscle Imaging Using 3D MR Fingerprinting With Water and Fat Separation**, *Journal of Magnetic Resonance Imaging* **53**, 1529 (2021).
- McFaline-Figueroa, J. R. and E. Q. Lee, **Brain Tumors**, *The American Journal of Medicine* **131**, 874 (2018).
- McGivney, D. F., R. Boyacıoğlu, Y. Jiang, M. E. Poorman, N. Seiberlich, V. Gulani, K. E. Keenan, M. A. Griswold and D. Ma, **Magnetic resonance fingerprinting review part 2: Technique and directions**, *Journal of Magnetic Resonance Imaging* **51**, 993 (2020).
- Montigon, *GitHub - populse/mri\_conv*, URL: [https://github.com/populse/mri\\_conv](https://github.com/populse/mri_conv), (2020).
- Murphy-boesch, J., G. J. So and T. L. James, **Precision mapping of the B1 field using the rotating-frame experiment**, *Journal of Magnetic Resonance (1969)* **73**, 293 (1987).
- Pannetier, N., C. S. Debacker, F. Mauconduit, T. Christen and E. L. Barbier, **A Simulation Tool for Dynamic Contrast Enhanced MRI**, *PLoS ONE* **8**, e57636 (2013).
- Perlman, O., K. Herz, M. Zaiss, O. Cohen, M. S. Rosen and C. T. Farrar, **CEST MR-Fingerprinting: Practical considerations and insights for acquisition schedule design and improved reconstruction**, *Magnetic Resonance in Medicine* **83**, 462 (2020).
- Perlman, O., H. Ito, K. Herz, N. Shono, H. Nakashima, M. Zaiss, E. A. Chiocca, O. Cohen, M. S. Rosen and C. T. Farrar, **Quantitative imaging of apoptosis following oncolytic virotherapy by magnetic resonance fingerprinting aided by deep learning**, *Nature Biomedical Engineering* **6**, 648 (2022).
- Peyrounette, M., Y. Davit, M. Quintard and S. Lorthois, **Multiscale modelling of blood flow in cerebral microcirculation: Details at capillary scale control accuracy at the level of the cortex**, *PLOS ONE* **13**, e0189474 (2018).
- Poorman, M. E., M. N. Martin, D. Ma, D. F. McGivney, V. Gulani, M. A. Griswold and K. E. Keenan, **Magnetic resonance fingerprinting Part 1: Potential uses, current challenges, and recommendations**, *Journal of Magnetic Resonance Imaging* **51**, 675 (2020).
- Portnoy, Sharon, Schrauben, Eric, Chau, Vann and Macgowan, Christopher, “Flow-Encoded Magnetic Resonance Fingerprinting: Simultaneous Measurement of Flow, T1, & T2 with Whole Brain Coverage”, *Proceedings of the 27th Annual Meeting of ISMRM*, (2019).

- Pouliot, P., L. Gagnon, T. Lam, P. K. Avti, C. Bowen, M. Desjardins, A. K. Kakkar, E. Thorin, S. Sakadzic, D. A. Boas and F. Lesage, **Magnetic resonance fingerprinting based on realistic vasculature in mice**, *NeuroImage* **149**, 436 (2017).
- Rochefort, L. de, T. Liu, B. Kressler, J. Liu, P. Spincemaille, V. Lebon, J. Wu and Y. Wang, **Quantitative susceptibility map reconstruction from MR phase data using bayesian regularization: Validation and application to brain imaging**, *Magnetic Resonance in Medicine* **63**, 194 (2010).
- Roldán, M. and P. A. Kyriacou, **Near-Infrared Spectroscopy (NIRS) in Traumatic Brain Injury (TBI)**, *Sensors* **21**, 1586 (2021).
- Rolfe, D. F. and G. C. Brown, **Cellular energy utilization and molecular origin of standard metabolic rate in mammals**, *Physiological Reviews* **77**, 731 (1997).
- Salomir, R., B. D. de Senneville and C. T. Moonen, **A fast calculation method for magnetic field inhomogeneity due to an arbitrary distribution of bulk susceptibility**, *Concepts in Magnetic Resonance* **19B**, 26 (2003).
- Scheffler, K., **A pictorial description of steady-states in rapid magnetic resonance imaging**, *Concepts in Magnetic Resonance* **11**, 291 (1999).
- Schuman, S., S. S. Iyer, M. Yurt, X. Cao, C. Liao, Z. Zhong, G. Wang, G. Zaharchuk, S. Vasanaawala and K. Setsompop, "Toward a 1-minute high-resolution brain exam - MR Fingerprinting with fast reconstruction and ML-synthesized contrasts", *Proceedings of International Society of Magnetic Resonance in Medicine*, (2022).
- Semenza, G. L., **Hypoxia and cancer**, *Cancer Metastasis Reviews* **26**, 223 (2007).
- Sobesky, J., O. Z. Weber, F.-G. Lehnhardt, V. Hesselmann, M. Neveling, A. Jacobs and W.-D. Heiss, **Does the Mismatch Match the Penumbra?**, *Stroke* **36**, 980 (2005).
- Sommer, K., T. Amthor, M. Doneva, P. Koken, J. Meineke and P. Börner, **Towards predicting the encoding capability of MR fingerprinting sequences**, *Magnetic Resonance Imaging* **41**, 7 (2017).
- Sørensen, B. S. and M. R. Horsman, **Tumor Hypoxia: Impact on Radiation Therapy and Molecular Pathways**, *Frontiers in Oncology* **10** (2020).
- Spence, A. M., M. Muzi, K. R. Swanson, F. O'Sullivan, J. K. Rockhill, J. G. Rajendran, T. C. H. Adamsen, J. M. Link, P. E. Swanson, K. J. Yagle, R. C. Rostomily, D. L. Silbergeld and K. A. Krohn, **Regional hypoxia in glioblastoma multiforme quantified with [18F]fluoromisonidazole positron emission tomography before radiotherapy: correlation with time to progression and survival**, *Clinical Cancer Research: An Official Journal of the American Association for Cancer Research* **14**, 2623 (2008).
- Steinberg, I., D. M. Huland, O. Vermesh, H. E. Frostig, W. S. Tummers and S. S. Gambhir, **Photoacoustic clinical imaging**, *Photoacoustics* **14**, 77 (2019).
- Stéphanou, A., S. R. McDougall, A. R. A. Anderson and M. A. J. Chaplain, **Mathematical modelling of the influence of blood rheological properties upon adaptative tumour-induced angiogenesis**, *Mathematical and Computer Modelling* **44**, 96 (2006).
- Stéphanou, A., A.-C. Lesart, J. Deverchère, A. Juhem, A. Popov and F. Estève, **How tumour-induced vascular changes alter angiogenesis: insights from a computational model**, *Journal of theoretical biology* **419**, 211 (2017).

- Strilciuc, S., D. A. Grad, C. Radu, D. Chira, A. Stan, M. Ungureanu, A. Gheorghe and F.-D. Muresanu, **The economic burden of stroke: a systematic review of cost of illness studies**, *Journal of Medicine and Life* **14**, 606 (2021).
- Su, P., D. Mao, P. Liu, Y. Li, M. C. Pinho, B. G. Welch and H. Lu, **Multiparametric estimation of brain hemodynamics with MR fingerprinting ASL**, *Magnetic Resonance in Medicine* **78**, 1812 (2017).
- Swartz, H. M., H. Hou, N. Khan, L. A. Jarvis, E. Y. Chen, B. B. Williams and P. Kuppusamy, **Advances in Probes and Methods for Clinical EPR Oximetry**, *Advances in experimental medicine and biology* **812**, 73 (2014).
- Swartz, H. M., B. B. Williams, H. Hou, N. Khan, L. A. Jarvis, E. Y. Chen, P. E. Schaner, A. Ali, B. Gallez, P. Kuppusamy and A. B. Flood, **Direct and Repeated Clinical Measurements of pO<sub>2</sub> for Enhancing Cancer Therapy and Other Applications**, *Advances in experimental medicine and biology* **923**, 95 (2016).
- Swartz, H. M., B. B. Williams, B. I. Zaki, A. C. Hartford, L. A. Jarvis, E. Y. Chen, R. J. Comi, M. S. Ernstoff, H. Hou, N. Khan, S. G. Swartz, A. B. Flood and P. Kuppusamy, **Clinical EPR: Unique Opportunities and Some Challenges**, *Academic Radiology* **21**, 197 (2014).
- Tatum, J. L. et al., **Hypoxia: importance in tumor biology, noninvasive measurement by imaging, and value of its measurement in the management of cancer therapy**, *International Journal of Radiation Biology* **82**, 699 (2006).
- Tippareddy, C., W. Zhao, J. L. Sunshine, M. Griswold, D. Ma and C. Badve, **Magnetic resonance fingerprinting: an overview**, *European Journal of Nuclear Medicine and Molecular Imaging* **48**, 4189 (2021).
- Todorov, M. I., J. C. Paetzold, O. Schoppe, G. Tetteh, S. Shit, V. Efremov, K. Todorov-Völgyi, M. Düring, M. Dichgans, M. Piraud, B. Menze and A. Ertürk, **Machine learning analysis of whole mouse brain vasculature**, *Nature Methods* **17**, 442 (2020).
- Vaupel, P. and A. Mayer, **Hypoxia in cancer: significance and impact on clinical outcome**, *Cancer and Metastasis Reviews* **26**, 225 (2007).
- Vaupel, P. and A. Mayer, **Hypoxia in Tumors: Pathogenesis-Related Classification, Characterization of Hypoxia Subtypes, and Associated Biological and Clinical Implications**. in H. M. Swartz, D. K. Harrison and D. F. Bruley (ed. by), *Oxygen Transport to Tissue XXXVI*, vol. 812 (Springer New York).
- Vonarbourg, A., A. Sapin, L. Lemaire, F. Franconi, P. Menei, P. Jallet and J. Le Jeune, **Characterization and detection of experimental rat gliomas using magnetic resonance imaging**, *Magnetic Resonance Materials in Physics, Biology and Medicine* **17**, 133 (2004).
- Wang, C. Y., Y. Liu, S. Huang, M. A. Griswold, N. Seiberlich and X. Yu, **31P magnetic resonance fingerprinting for rapid quantification of creatine kinase reaction rate in vivo**, *NMR in Biomedicine* **30**, e3786 (2017).
- Wang, C. Y., S. Coppo, B. B. Mehta, N. Seiberlich, X. Yu and M. A. Griswold, **Magnetic resonance fingerprinting with quadratic RF phase for measurement of T<sub>2</sub>\* simultaneously with df, T<sub>1</sub>, and T<sub>2</sub>**, *Magnetic Resonance in Medicine* **81**, 1849 (2019).
- Wang, D., J. Ostenson and D. S. Smith, **snapMRF: GPU-accelerated magnetic resonance fingerprinting dictionary generation and matching using extended phase graphs**, *Magnetic Resonance Imaging* **66**, 248 (2020).

- Wang, Z., C. Mascarenhas and X. Jia, [Positron Emission Tomography After Ischemic Brain Injury: Current Challenges and Future Developments](#), *Translational Stroke Research* **11**, 628 (2020).
- Warach, S. J. et al., [Acute Stroke Imaging Research Roadmap III Imaging Selection and Outcomes in Acute Stroke Reperfusion Clinical Trials](#), *Stroke* **47**, 1389 (2016).
- Weigel, M., [Extended phase graphs: Dephasing, RF pulses, and echoes - pure and simple](#), *Journal of Magnetic Resonance Imaging* **41**, 266 (2015).
- Wright, G. A., B. S. Hu and A. Macovski, [Estimating oxygen saturation of blood in vivo with MR imaging at 1.5 T](#), *Journal of Magnetic Resonance Imaging* **1**, 275 (1991).
- Yablonskiy, D. A. and E. M. Haacke, [Theory of NMR signal behavior in magnetically inhomogeneous tissues: The static dephasing regime](#), *Magnetic Resonance in Medicine* **32**, 749 (1994).
- Yang, M., Y. Jiang, D. Ma, B. B. Mehta and M. A. Griswold, [Game of Learning Bloch Equation Simulations for MR Fingerprinting](#), arXiv:2004.02270 [physics] (2020).
- Yarnykh, V. L., [Actual flip-angle imaging in the pulsed steady state: A method for rapid three-dimensional mapping of the transmitted radiofrequency field](#), *Magnetic Resonance in Medicine* **57**, 192 (2007).
- Yoshihara, T., Y. Hirakawa, M. Hosaka, M. Nangaku and S. Tobita, [Oxygen imaging of living cells and tissues using luminescent molecular probes](#), *Journal of Photochemistry and Photobiology C: Photochemistry Reviews* **30**, 71 (2017).
- Zhang, J., T. Liu, A. Gupta, P. Spincemille, T. D. Nguyen and Y. Wang, [Quantitative mapping of cerebral metabolic rate of oxygen \(CMRO<sub>2</sub>\) using quantitative susceptibility mapping \(QSM\)](#), *Magnetic Resonance in Medicine* **74**, 945 (2015).
- Zhao, B., K. Setsompop, E. Adalsteinsson, B. Gagoski, H. Ye, D. Ma, Y. Jiang, P. Ellen Grant, M. A. Griswold and L. L. Wald, [Improved magnetic resonance fingerprinting reconstruction with low-rank and subspace modeling](#), *Magnetic Resonance in Medicine* **79**, 933 (2018).
- Zhu, X.-H., J. M. Chen, T.-W. Tu, W. Chen and S.-K. Song, [Simultaneous and noninvasive imaging of cerebral oxygen metabolic rate, blood flow and oxygen extraction fraction in stroke mice](#), *NeuroImage* **64**, 437 (2013).
- Zhu, X.-H. and W. Chen, [In vivo 17 O MRS imaging – Quantitative assessment of regional oxygen consumption and perfusion rates in living brain](#), *Analytical Biochemistry* **529**, 171 (2017).
- Zhu, X., Q. Huang, A. DiSpirito, T. Vu, Q. Rong, X. Peng, H. Sheng, X. Shen, Q. Zhou, L. Jiang, U. Hoffmann and J. Yao, [Real-time whole-brain imaging of hemodynamics and oxygenation at micro-vessel resolution with ultrafast wide-field photoacoustic microscopy](#), *Light: Science & Applications* **11**, 138 (2022).
- Zur, Y., M. L. Wood and L. J. Neuringer, [Spoiling of transverse magnetization in steady-state sequences](#), *Magnetic Resonance in Medicine* **21**, 251 (1991).

## LIST OF FIGURES

---

I.1.1	Hemoglobin dissociation curve in human physiological conditions . . . . .	8
I.2.1	Illustration of tumoral angiogenesis . . . . .	10
I.2.2	Comparison of MRI perfusion/diffusion mismatch and PET-measured OEF maps, from Sobesky et al. 2005 . . . . .	11
I.3.1	EPR imaging principle from Gertsenshteyn et al. . . . .	13
I.3.2	MRI anatomical scan and PET-measured OEF maps on a healthy volunteer, adapted from Cho et al. 2021 . . . . .	15
I.3.3	Illustration of NIRS working principle from Roldán et al. . . . .	16
I.3.4	PAI imaging of an entire mouse cortex under a cycle of normoxia-hypoxia-normoxia challenges, from Zhu et al. 2022 . . . . .	16
I.3.5	$T_2$ variations with $SO_2$ for different hematocrit predicted by the model from Lu et al. 2012 . . . . .	17
I.3.6	Anatomical, venous $T_2$ and associated oxygenation maps in 6 volunteers, from Li et al. 2022 . . . . .	18
I.3.7	$T_1$ variations with $SO_2$ for different hematocrit predicted by the model from Bluemke et al. 2022 . . . . .	19
I.3.8	Comparison of $CMRO_2$ maps from QSM and qBOLD ( $R_2^*$ -based) from Zhang et al. 2015 . . . . .	20
I.3.9	Magnetic field perturbation around a blood vessel . . . . .	21
I.3.10	$SO_2$ measurements during a gas challenge, from Christen et al.2014a . . . . .	23
I.3.11	Parametric maps from QSM, qBOLD, and the proposed QSM+qBOLD from Cho et al. 2018 . . . . .	25
I.4.1	MR Fingerprinting basic principles . . . . .	26
I.4.2	MR vascular Fingerprinting basic principles . . . . .	29
I.4.3	Parametric maps obtained on a healthy subject with MRvF at 3T, from Christen et al. 2014 . . . . .	30
I.4.4	Parametric maps obtained with MRvF and steady-state analysis at 4.7T, from Lemasson et al. 2016 . . . . .	31
II.1.1	Dephasing helix of a number of isochromats after applying a gradient along the z-axis . . . . .	39
II.1.2	EPG representation of dephasing states of the magnetization in a voxel . . . . .	40
II.1.3	Graphical depiction of the effect of an RF pulse on the magnetization . . . . .	41
II.1.4	Visual representation of the evolution of dephasing states with EPG . . . . .	42
II.1.5	Magnetic field perturbation around a blood vessel . . . . .	43
II.1.6	Representation of the magnetic field and magnetization inside a voxel in MRVox . . . . .	44
II.1.7	Sequence, signal, and isochromats in real-time, from MRVox . . . . .	45
II.1.8	Assessing the possible geometries with a fixed FOV . . . . .	46
II.1.9	3D vascular geometries generated by MRVox3D . . . . .	48
II.1.10	Graphical outputs from MRVox3D . . . . .	49
II.1.11	Example of geometry imported in MRVox3D . . . . .	50



II.1.12	Chronogram of a bSSFP sequence . . . . .	51
II.1.13	Comparison of the 3 simulation methods for a bSSFP sequence . . . . .	52
II.1.14	Maximum relative error between the different simulation methods for bSSFP acquisitions . . . . .	53
II.1.15	Chronograms of FID- and Echo-type gradient spoiling strategies. . . . .	53
II.1.16	Comparison of the 3 simulation methods for different types of gradient spoiling . . . . .	54
II.1.17	Maximum relative error between the different simulation methods for FID acquisitions . . . . .	54
II.1.18	RF spoiled signal vs. quadratic phase increment . . . . .	55
II.1.19	Relative error between methods for 100, 512, and 1024 isochromats considered in Bloch simulation . . . . .	56
II.1.20	$\Delta R2$ and $\Delta R2^*$ changes observed with R variation for a given $\Delta\chi$ . Comparison of MRVox2D and models . . . . .	57
II.1.21	$\Delta R2$ and $\Delta R2^*$ changes observed with R variation for a given $\Delta\chi$ . Comparison of MRVox3D and models . . . . .	58
II.2.1	Overview of the Bruker MRF Modules . . . . .	60
II.2.2	Example of interleaved spirals . . . . .	61
II.2.3	Chronograms of acquisitions without and with spoiling . . . . .	62
II.2.4	Relative $B_1$ maps produced with different methods . . . . .	64
II.2.5	Examples of agreement between FID-type acquisitions and simulations . . . . .	65
II.2.6	Examples of agreement between Echo-type acquisitions and simulations . . . . .	66
II.2.7	Effects of inversion time change and spoiling . . . . .	67
II.2.8	Second echoes of two balanced SSFP acquisitions . . . . .	68
II.2.9	Acquisition with a complex phase pattern . . . . .	69
II.2.10	Sequence from Gómez et al. on a stabilized mouse brain . . . . .	70
II.2.11	Sequence from Jiang et al. 2015 on a live rat . . . . .	71
II.2.12	Demonstration of the difference in signal shape vs offset to magnet center . . . . .	74
II.3.1	CSV sequence description file for Philips scanners . . . . .	75
II.3.2	Parametric maps acquired on a beetroot with the MRF-brain sequence . . . . .	77
II.3.3	Comparison of image quality for a cartesian and spiral acquisition . . . . .	78
II.3.4	Echoes from bSSFP acquisitions with and without RF phase cycling . . . . .	79
II.3.5	Acquisition on a healthy volunteer with the Gómez et al. 2019 sequence . . . . .	80
II.3.6	Parametric maps from 2 different sequences on a healthy volunteer . . . . .	81
II.4.1	Tool for reconstruction exploration . . . . .	82
II.4.2	Graphical interface of the MP3 software . . . . .	84
II.4.3	MP3-based screening tool . . . . .	86
II.4.4	Example of use of the MP3 screening tool . . . . .	86
III.1.1	Overview of the use of realistic voxels for MRvF . . . . .	92
III.1.2	Example of voxels used in the dictionaries . . . . .	94
III.1.3	Coverage of the geometrical parameter space in the three dictionaries . . . . .	94
III.1.4	Maps obtained with the DBM and DBL reconstruction methods . . . . .	96
III.1.5	Maps obtained with the different dictionaries using the DBL method . . . . .	97
III.1.6	Boxplot representation of parameters values obtained with DBL . . . . .	98
III.1.7	Table of p-values for crossed 2-sample t-test on DBL $SO_2$ results . . . . .	98
III.1.8	Boxplot representation of parameters values obtained with DBM . . . . .	99



III.1.9	pO <sub>2</sub> measurements from the intracranial optic-fiber probe . . . . .	100
III.1.10	SO <sub>2</sub> maps obtained with the DBL method on C6 tumor-bearing rats . . . . .	101
III.1.11	SO <sub>2</sub> maps obtained with the DBL method on stroke bearing rats . . . . .	102
III.2.1	Basic working principle of CCO . . . . .	105
III.2.2	Examples of trees obtained using VascuSynth. . . . .	106
III.2.3	Graphical illustration of tree optimization . . . . .	109
III.2.4	Demonstration of the rotation from the bifurcation plane to $z = 0$ . . . . .	110
III.2.5	Optimization of the bifurcation position . . . . .	111
III.2.6	Example of a small graph . . . . .	111
III.2.7	Example of a small graph . . . . .	112
III.2.8	Double vascular tree generated with CCO . . . . .	112
III.2.9	Comparison of diameters distribution between our CCO implementation and literature observations. . . . .	113
III.3.1	Parameters variation along the branches, from <a href="#">Linninger et al. 2013</a> . . . . .	114
III.3.2	Mouse hemisphere built with CCO built from large vessels observed with $\mu$ CT, from <a href="#">Hartung et al. 2021</a> . . . . .	114
III.3.3	Synchrotron phase-contrast imaging . . . . .	115
IV.1.1	Signal shape variations when fixing all but one properties in a dictionary . . . . .	119
IV.1.2	Standard deviation evaluation on the fingerprint from <a href="#">Ma et al. 2013</a> . . . . .	120
IV.1.3	Results from three MRF experiments with fingerprints evaluated with the method from <a href="#">Sommer et al.</a> . . . . .	121
IV.2.1	Standard-deviation evaluation of fingerprints from the GESFIDSE sequence to vascular parameters . . . . .	123
IV.2.2	Concatenation and ratio fingerprints considered for the GESFIDSE sequence . . . . .	124
IV.2.3	Results from the Monte-Carlo evaluation of three fingerprints from multi gradient echo sequences . . . . .	125
IV.2.4	Maps produced with MRvF on healthy and pathological animals using the ratio and concatenation fingerprints . . . . .	126
IV.3.1	Steady-state reached for bSSFP simulations for TR = 1s, FA = 60° and df=0Hz . . . . .	128
IV.3.2	Steady-state reached with bSSFP simulations for TR = 26ms, FA = 60° and df=20Hz . . . . .	129
IV.3.3	Steady-state reached with bSSFP simulations for TR = 26ms, FA = 10° and df=0Hz . . . . .	130
IV.3.4	Illustrations of two different response profiles used for bSSFP BOLD experiments . . . . .	130
IV.3.5	Illustration of bSSFP potential for fMRI, from <a href="#">Báez-Yáñez et al.</a> . . . . .	131
IV.3.6	Influence of off-resonance frequencies on the time evolution of OSSI-bSSFP sequences and fMRI experiment results . . . . .	133
IV.3.7	Simulation study on the transient-state of classical or prepared bSSFP sequences . . . . .	134
IV.3.8	Simulation study on the transient, hybrid, and steady-state signal of bSSFP sequences. Magnetization trajectories are plotted in 3D for multiple isochromats . . . . .	135
IV.3.9	MRF bSSFP T <sub>2</sub> * sequence from <a href="#">Wang et al.</a> . . . . .	136
IV.3.10	Monte-Carlo evaluation of the GESFIDSE pre-CA and bSSFP fingerprints known to exhibit T <sub>2</sub> * sensitivity . . . . .	138
IV.3.11	Fingerprints from the three sequence types considered for manual optimization for SO <sub>2</sub> estimation . . . . .	139

IV.3.12 Monte-Carlo evaluation of the SO <sub>2</sub> encoding capacity of fingerprints from three sequence types . . . . .	140
IV.3.13 Steps taken to further improve the candidates identified by the manual research of optimal parameters. . . . .	141
IV.3.14 Evaluation of the OSSI-inspired candidate fingerprint against two imaging artifacts . . . . .	142
IV.3.15 First results of in vivo MRvF without contrast agent on a live mouse at 4.7T	144

## PUBLISHED WORK

---

### Articles

- A. Delphin, F. Boux, C. Brossard, J. M. Warnking, B. Lemasson, E. L. Barbier and T. Christen, **Realistic microvascular geometries for MR vascular Fingerprinting**, In preparation (2022)
- C. Brossard, O. Montigon, F. Boux, A. Delphin, T. Christen, E. L. Barbier and B. Lemasson, **MP3: Medical Software for Processing Multi-Parametric Images Pipelines**, *Frontiers in Neuroinformatics* **14** (2020)

### Conference abstracts

- A. Delphin, F. Boux, C. Brossard, J. Warnking, B. Lemasson, E. Barbier and T. Christen, “Using 3D realistic blood vessel structures machine learning for MR vascular Fingerprinting”, *ISMRM 31st Annual Meeting & Exhibition, May 2022, London, United Kingdom*, (2022) - **Poster presentation**
- T. Coudert, A. Delphin, J. M. Warnking, B. Lemasson, E. L. Barbier and T. Christen, “Searching for an MR Fingerprinting sequence to measure brain oxygenation without contrast agent”, *ISMRM 31st Annual Meeting & Exhibition, May 2022, London, United Kingdom*, (2022) - **Poster presentation**
- A. Delphin, F. Boux, C. Brossard, J. M. Warnking, B. Lemasson, E. L. Barbier and T. Christen, “Towards optimizing MR vascular fingerprinting”, *ISMRM & SMRT Virtual Conference & Exhibition*, (2021) - **Oral presentation**
- A. Delphin, F. Boux, C. Brossard, J. M. Warnking, B. Lemasson, E. L. Barbier and T. Christen, “Optimisation des motifs de signaux pour l’IRM Fingerprinting vasculaire”, *5e Congrès scientifique de la Société Française de Résonance Magnétique en Biologie et Médecine*, (2021) - **Power pitch**
- A. Delphin, F. Boux, C. Brossard, J. Warnking, B. Lemasson, E. L. Barbier and T. Christen, “Optimizing signal patterns for MR vascular fingerprinting”, *ISMRM & SMRT Virtual Conference & Exhibition*, (2020) - **Poster presentation**

### Awards

- Best perfusion abstract 2021 - ISMRM Perfusion Study Group  
Winning video: <https://youtu.be/DshJOF09wKs>

### Others

- Ph.D. Defense: <https://youtu.be/grXcxjxt6OQ>



# RÉSUMÉ FRANÇAIS - FRENCH SUMMARY

---

## Introduction

Le rôle de l'oxygène dans la vie est central. Il y a deux milliards d'années, la "grande oxygénation" a vu l'augmentation de la concentration en oxygène dans les océans et l'atmosphère. Cette période est souvent considérée comme le début de l'apparition des organismes eucaryotes, dont font partie les formes de vie complexes telles que nous les connaissons, y compris les humains. Les cellules eucaryotes dépendent de réactions basées sur l'oxygène pour produire l'énergie nécessaire à leur fonctionnement. Toutes les cellules, tous les tissus et tous les organes n'ont cependant pas les mêmes exigences. Le cerveau humain consomme beaucoup d'oxygène : il représente 20% de la consommation totale d'oxygène du corps humain pour seulement 2% de sa masse. Or, comme le reste de l'organisme, il est incapable de stocker l'oxygène et est donc en danger lorsque le flux sanguin qui assure son approvisionnement est altéré. De tels événements sont souvent liés à des lésions ou à la mort de cellules, ce qui, pour le cerveau, a des répercussions désastreuses sur les fonctions cognitives.

Plusieurs pathologies cérébrales peuvent être liées à des perturbations de l'oxygénation. L'accident vasculaire cérébral (AVC), qui résulte de perturbations locales de la circulation sanguine, présente une coupure nette de l'approvisionnement en oxygène des cellules cérébrales. Les effets à long terme de l'AVC dépendent directement de la durée pendant laquelle ces tissus sont privés de leur source d'énergie. Dans les tumeurs, la croissance cellulaire non régulée crée des zones sous-perfusées qui sont privées d'apport en oxygène. En réaction, on observe souvent une angiogenèse chaotique dans les lésions, avec la création de nouveaux réseaux de vaisseaux anormaux. Ce processus n'est généralement pas suffisant et entraîne un flux sanguin intermittent et des épisodes hypoxiques transitoires. En conséquence, la pression hypoxique conduit à la sélection de cellules tumorales agressives, et augmente leur radio et chimiorésistance. Heureusement, la prise en charge des accidents vasculaires cérébraux et des tumeurs s'est améliorée au cours des dernières années. La fenêtre thérapeutique pour les AVC aigus est étendue grâce à l'essor des thérapies endovasculaires et des solutions pour prévenir l'hypoxie tumorale et augmenter l'efficacité du traitement sont en cours de développement.

La littérature souligne souvent les avantages potentiels des techniques de cartographie de l'oxygénation cérébrale pour les soins aux patients. On peut prévoir un meilleur triage des patients en urgence, des traitements de soins spécifiques aux patients, des prédictions précises des résultats et une meilleure compréhension des pathologies. Actuellement, les méthodes cliniquement disponibles pour mesurer l'oxygénation comprennent les sondes intracrâniennes et la tomographie par émission de positons (TEP). La première est utilisée depuis des décennies et reste la technique préférée de surveillance de l'oxygénation au chevet du patient, mais elle ne fournit que des mesures locales et est particulièrement invasive. La seconde est utilisée pour fournir des cartes de la concentration d'un marqueur d'hypoxie, mais donne

peu d'informations dans le reste du cerveau. Elle nécessite également l'injection d'un traceur radioactif, ce qui n'est pas toujours possible dans un contexte de soins aigus. La recherche et le développement d'une meilleure cartographie de l'oxygénation est donc un sujet d'intérêt. Plusieurs nouvelles techniques ont été proposées au fil des ans, et reposent sur un certain nombre de principes physiques différents. La résonance paramagnétique électronique et les techniques opto-acoustiques ont donné des résultats prometteurs *in vivo* mais ne sont disponibles que dans quelques laboratoires de recherche. L'IRM est connue pour être sensible à une grande variété de contrastes et de propriétés physiques, dont le paramagnétisme de la désoxyhémoglobine. L'effet "blood oxygenation level dependent" (ou BOLD) a révolutionné le domaine des neurosciences et l'étude des fonctions cérébrales. Dans le contexte des soins aigus, l'IRM souffre pourtant de sa faible vitesse d'acquisition et ne fournit pas de mesures quantitatives.

En 2013, un nouveau paradigme IRM appelé MR Fingerprinting (MRF) a été proposé pour réduire considérablement la durée des examens IRM et fournir plusieurs mesures quantitatives en même temps. Le principe de base de la MRF repose sur la comparaison de l'évolution temporelle complexe des signaux IRM *in vivo* avec des simulations numériques avancées de la même expérience. En 2014, notre équipe a démontré que la technique pouvait être adaptée pour être en mesure de cartographier quantitativement l'oxygénation cérébrale et plusieurs autres paramètres vasculaires d'intérêt ([Christen et al. 2014b](#)). Cependant, cette preuve de concept des approches "MR vascular Fingerprinting (MRvF)" présentait certaines limites. L'injection d'un agent de contraste était nécessaire, et la sensibilité de la méthode n'était pas idéale.

Ce projet de doctorat s'est déroulé à l'Institut des Neurosciences de Grenoble dans l'équipe "Neuroimagerie fonctionnelle et perfusion cérébrale". Il fait partie d'un projet plus large qui vise à résoudre les limites actuelles de la MRvF et à inclure des mesures d'oxygénation dans un protocole unique d'imagerie de l'AVC aigu par MRF. Le laboratoire s'appuie sur sa plateforme IRM préclinique et clinique IRMaGe et sur l'expertise combinée de neurologues et de chercheurs en IRM. Le but de cette thèse était de développer un pipeline MRF flexible englobant les simulations numériques, les acquisitions précliniques et cliniques et la reconstruction d'images, afin de permettre une conception efficace des protocoles MRF. Il a ensuite été utilisé pour améliorer les mesures MRvF. La thèse a été financée par le projet TRACE de l'Université Grenoble Alpes qui porte sur l'oxygénation du cerveau et les soins aigus pour les lésions cérébrales traumatiques.

La présente thèse est organisée en 4 chapitres résumés ci-dessous.

## Résumé du chapitre I :

### Cartographie de l'oxygénation du cerveau : définitions, intérêt et techniques

Ce premier chapitre présente brièvement les bases du transport de l'oxygène dans l'organisme

et les différentes quantités qui ont été définies pour exprimer la présence et la consommation d'O<sub>2</sub> dans les tissus. Nous discutons de la nécessité de cartographier l'oxygénation du cerveau pour la recherche médicale et les soins aux patients. Les méthodes existantes pour la quantification de l'oxygène in vivo et la cartographie de l'oxygénation du cerveau sont présentées, avec un accent particulier sur les techniques basées sur l'IRM et les bases théoriques de la sensibilité de l'IRM à l'oxygénation des tissus. Enfin, une présentation approfondie de la MRF est proposée, y compris sa version dérivée pour la cartographie de l'oxygénation cérébrale.

## Définition de l'oxygénation cérébrale

Malgré son rôle essentiel dans le corps humain, l'oxygène ne peut être stocké pour une utilisation ultérieure. Son approvisionnement à l'ensemble du corps est assuré par une ventilation constante de l'air dans les poumons et par la circulation sanguine. Au niveau des poumons l'O<sub>2</sub> traverse les parois des capillaires et se dissout dans le sang. Une partie des molécules d'O<sub>2</sub> reste simplement dans cet état, augmentant la pO<sub>2</sub> du sang. Mais la plupart est capturée par l'hémoglobine (Hb), une protéine contenue dans les érythrocytes (globules rouges). Chaque molécule d'hémoglobine peut se lier à un maximum de 4 molécules d'O<sub>2</sub> et est généralement liée à 4 ou à aucune. Ces deux états sont appelés désoxyhémoglobine (dHb) et oxyhémoglobine, (HbO<sub>2</sub>). La saturation du sang en oxygène SO<sub>2</sub> est définie comme suit :

$$SO_2 = \frac{HbO_2}{HbO_2 + dHb}$$

Dans des conditions normales, le gradient de pO<sub>2</sub> dans les alvéoles est généralement assez fort pour maintenir la pO<sub>2</sub> du sang suffisamment élevée et atteindre SO<sub>2</sub> ≈ 1. Le sang est alors pompé par le cœur et distribué dans tout le corps. La pO<sub>2</sub> dans les cellules saines est faible en raison de la consommation constante d'O<sub>2</sub> et des membranes biologiques qui empêchent la diffusion d'O<sub>2</sub>. Il existe donc toujours un fort gradient de pO<sub>2</sub> entre le sang et les tissus sains. L'O<sub>2</sub> dissous diffuse le long du gradient vers les tissus, diminuant la pO<sub>2</sub> dans le sang. Cela provoque la dissociation de l'oxygène de l'hémoglobine, diminuant ainsi la SO<sub>2</sub> dans le sang veineux. Ce sang veineux est continuellement pompé vers les poumons pour restaurer sa SO<sub>2</sub>, assurant ainsi une oxygénation correcte de l'ensemble du corps.

On définit également le ratio métabolique cérébral d'O<sub>2</sub>:

$$CMRO_2 = 4 \times CBF \times [Hb] \times (SaO_2 - SvO_2)$$

Où CBF est le flux sanguin cérébral, et SaO<sub>2</sub> et SvO<sub>2</sub> sont les SO<sub>2</sub> artérielle et veineuse. La fraction d'extraction d'oxygène est aussi communément utilisée:

$$OEF = \frac{SaO_2 - SvO_2}{SaO_2}$$

## Intérêt de la cartographie de l'oxygénation cérébrale

La consommation cérébrale d'oxygène varie dans le temps et dans l'espace. Cette particularité permet d'identifier les régions cérébrales impliquées dans des tâches cognitives spécifiques,



comme on le fait en IRM fonctionnel. Cette technique ne requiert pas particulièrement de mesure quantitative.

Il est cependant établi qu'un certain nombre de pathologies altèrent l'oxygénation cérébrale, ce qui est directement lié à une perte fonctionnelle et à un taux de mortalité élevé. Les exemples des glioblastomes et des AVC sont donnés pour mettre en évidence le besoin, établi dans la littérature, de meilleures méthodes de cartographie de l'oxygénation cérébrale.

Idéalement, une telle méthode doit être le moins invasive possible, avoir une résolution spatiale et temporelle adaptée à son application (triage des patients en urgence, mesures fréquentes répétées pour le suivi d'évolution...), et être disponible pour les besoins cliniques.

## Méthodes de mesures existantes

Cette section décrit les méthodes de mesure de l'oxygénation cérébrale utilisées en clinique ou encore au stade de recherche. Ces méthodes sont évaluées selon les critères définis ci-dessus.

De nombreuses mesures n'utilisant pas l'IRM existent pour déterminer l'oxygénation des tissus, comme la quantification de l'effet BOLD (qBOLD) ou la cartographie quantitative de susceptibilité (QSM). On peut retenir qu'elles souffrent généralement d'une invasivité assez élevée et d'une résolution spatiale ou d'une profondeur maximale d'imagerie trop faible. De nombreuses possibilités intéressantes sont toutefois en cours de développement et promettent de résoudre une partie des limitations existantes.

L'IRM est un outil intéressant pour les mesures de l'oxygénation du cerveau en raison de son grand champ de vision et de sa profondeur d'imagerie, de sa haute résolution spatiale et de son caractère non invasif.

Plusieurs méthodes ont été proposées. Elles reposent généralement sur l'acquisition de signaux courts et simples, tels que des décroissances exponentielles, et utilisent l'ajustement d'un modèle multiparamétrique pour quantifier la  $SO_2$ . L'établissement de ces modèles mathématiques n'est généralement possible qu'au prix d'un certain nombre d'approximations sur les propriétés des tissus, et dont la validité dans les cas pathologiques n'est pas garantie. Le processus d'ajustement du modèle est également sujets à des imprécisions numériques.

Plus récemment, l'approche IRM Fingerprint (MRF, voir [Ma et al. 2013](#)) a proposé de considérer le problème à l'envers. Plutôt que d'établir un modèle estimant plusieurs paramètres à partir d'un signal, la MRF simule des signaux provenant de combinaisons de multiples paramètres pour créer un dictionnaire. Les signaux peuvent avoir des évolutions complexes, plus sensibles aux propriétés des tissus que les signaux plus simples requis par les méthodes décrites précédemment. Les propriétés des tissus peuvent être considérées dans toutes les combinaisons possibles, ce qui permet de mieux représenter à la fois les tissus sains et pathologiques.

Les signaux simulés sont ensuite comparés aux signaux acquis, et à chaque voxel *in vivo* sont attribuées les propriétés du voxel simulé ayant donné le signal le plus ressemblant.

Plus précisément, le processus de la MRF requiert:

- Une séquence IRM produisant des signaux dont la forme varie quand les propriétés des

tissus imagés varient. Ces séquences sont généralement bien plus longues que celles employées classiquement, et un sous-échantillonnage spatial devient nécessaire pour éviter des temps d'examen prohibitifs. Il a été montré qu'il est possible de retrouver la forme du signal d'origine malgré le bruit induit par le sous-échantillonnage.

- Un outil de simulation capable de générer les dictionnaires. Cet outil doit être à même de simuler les effets physiques et physiologiques nécessaires liés aux propriétés d'intérêt que l'on souhaite quantifier. Pour des examens IRM classiques, les équations de Bloch sont généralement suffisantes. Dans le cas de l'oxygénation et de la microvascularisation, un outil plus complexe est nécessaire.
- Une méthode capable de reconstruire des cartes paramétriques à partir des acquisitions et d'un dictionnaire. Une simple comparaison des signaux *in vivo* et *in silico* peut suffire, mais de nombreuses équipes ont montré qu'il est préférable d'utiliser des méthodes d'apprentissage machine.

Des preuves de concept de l'efficacité de la MRF ont été montrées dans virtuellement tous les domaines de l'IRM quantitative, y compris pour la mesure de l'oxygénation cérébrale, comme l'a proposé notre équipe en 2014 ([Christen et al. 2014b](#)). La méthode a été baptisée MRvF pour "MR vascular Fingerprinting". Ses limitations ont bien été établies, comme le manque de réalisme des réseaux vasculaires dans les simulations ou le manque de sensibilité de la séquence utilisée.

Le prochain chapitre s'attachera donc à développer des outils pour éliminer ces limitations.

## Résumé du chapitre II : Développement d'outils pour la MRvF

Comme détaillé dans le chapitre précédent, la MRF consiste en plusieurs étapes. Chacune d'entre elles nécessite un développement et une validation minutieux. Ce chapitre présente le travail effectué sur les outils de simulation IRM, les acquisitions aux niveaux préclinique et clinique, et les solutions de reconstruction pour obtenir un pipeline MRF flexible mais robuste. Les développements ont été motivés par la nécessité de surmonter les limites de l'actuelle MRvF exposées dans le chapitre précédent. Nous avons travaillé à partir de codes précédents développés dans le laboratoire, d'outils fournis par la communauté ou par des collaborations, et en utilisant la littérature récente. Les validations des outils ont été effectuées dans des conditions liées au contexte de la MRvF.

### Outils de simulation

#### Outils de simulation pour la MRF classique

Cette section reprend les équations du mouvement de l'aimantation dans un champ magnétiques établies par Bloch en 1946. Deux grands types d'implémentations de ces équations sont utilisés à des fins de simulations.

Une implémentation directe des équations sous forme matricielle est possible. La précision et le temps de calcul sont alors dépendants d'un hyperparamètre, ce qui peut avoir des

conséquences sur la génération de dictionnaires d'un grand nombre de signaux.

Une seconde implémentation appelée Extended Phase Graph (EPG), ou Diagramme de Phase Étendu, est possible et généralement préférée car beaucoup plus rapide. Ses grands principes sont détaillés en profondeur dans le manuscrit.

Des implémentations Matlab de ces deux approches sont partagées par la communauté. Elles ont été récupérées et un outils permettant d'appeler l'une ou l'autre avec le même formalisme, propice à la génération de dictionnaires pour la MRF, a été développé et partagé sur GitHub.

## Outils de simulation pour la MRvF

Les simulations présentées ci-dessus considèrent des voxels homogènes. L'objectif de la MRvF est d'explorer la structure vasculaire interne au voxel, ce qui implique de disposer de voxels non homogènes et structurés.

MRVox est un outil Matlab développé dans l'équipe, initialement pour simuler le passage d'un agent de contraste dans un réseau vasculaire ([Pannetier et al. 2013](#)). Sa principale particularité est sa capacité à simuler la réponse IRM d'un voxel hétérogène en 2D, à n'importe quelle séquence IRM. Un modèle à trois compartiments est utilisé pour définir indépendamment les propriétés physiques et physiologiques de l'espace extravasculaire, des vaisseaux sanguins et des cellules. En particulier, chaque compartiment est doté d'une susceptibilité magnétique, qui est directement liée à la saturation en oxygène dans le compartiment sanguin. Une approche de Fourier est utilisée pour calculer les perturbations de champ magnétique qui résultent de ces différentes susceptibilités, ainsi que l'effet de la diffusion de l'eau dans le voxel. Les vaisseaux sanguins sont considérés comme des cylindres parallèles.

Cet outil a été adapté pour la génération de dictionnaires pour la MRvF. La reproductibilité des simulations a été assurée, et une solution de parallélisation locale a été implémentée.

Une version utilisant des voxels en 3D a été développée. Les vaisseaux sanguins y sont représentés par des cylindres droits d'orientation variable, isotrope ou non. Il est également possible d'importer une géométrie vasculaire générée ou segmentée d'après des images de microscopie.

## Validation des outils

Les équations de Bloch, l'EPG et MRVox ont été validés entre eux dans des cas de figure réalisables pour les 3 outils. Les différences de résultats entre les trois outils sont minimes et explicables, ce qui laisse penser que les outils sont valides.

Les versions 2D et 3D de MRVox ont été comparées à des modèles théoriques d'évolution du signal en fonction des paramètres de géométrie vasculaire. MRVox 2D produit des résultats relativement proches des modèles, malgré la simplicité de son réseau vasculaire 2D. MRVox 3D correspond mieux aux modèles, ce qui est expliqué par le fait que sa représentation vasculaire est plus réaliste et plus proche de celle utilisée pour établir les modèles.

## Acquisitions MRF précliniques

Deux modules d'acquisition MRF pour les IRM précliniques Bruker avaient déjà été développés au laboratoire, correspondant à deux cas de figures classiques. Ces outils ont été améliorés pour permettre plus de flexibilité et testés dans plusieurs conditions, sur des fantômes ou in vivo. Les résultats des acquisitions ont été comparés avec des simulations, avec des résultats encourageants.

Les modules possèdent toutefois un certain nombre de limitations techniques qui ne pourront être résolues que par un remaniement complet de leurs structures. Une différence de signal inexplicable a été observée lorsque l'acquisition a lieu au centre du champ magnétique ou à côté.

Les modules ont toutefois été partagés avec la communauté, puisqu'ils permettent, en connaissant leurs limitations, de tester des séquences et des acquisitions jusqu'alors indisponibles sur les IRM Bruker.

## Acquisitions MRF cliniques

Une collaboration a été démarrée avec Philips Research, qui a installé un module MRF sur l'IRM 3T Philips Achieva de la plateforme IRMaGe. Des essais ont été réalisés sur fantômes et volontaires sains, d'abord avec la séquence proposée par Philips, puis avec des séquences tirées de la littérature. Les résultats obtenus sont très encourageants, le module permettant une large flexibilité dans les réglages de l'acquisition. Des essais de MRvF avec ce module devraient être rapidement possibles.

## Reconstruction de cartes paramétriques

La particularité de la MRF de manipuler des volumes 4D (3 dimensions spatiales + le décours temporel) et de reconstruire simultanément plusieurs cartes paramétriques implique d'utiliser des outils de reconstruction et de visualisation dédiés. Un premier outil a été développé sur Matlab dans ce sens, avant d'être remplacé par une implémentation intégrée au logiciel MP3, développé par l'équipe ([Brossard et al. 2020](#)). Il s'agit d'un gestionnaire de pipeline de traitement et de base de données, diffusé à la communauté. L'un de ses avantages est de gérer l'import de données depuis de nombreux formats, dont les formats propriétaires Bruker et Philips.

Un module de traitement de MRvF dédié à l'implémentation présentée en 2014 avait déjà été développé. Il a servi de base au développement d'un module plus flexible et correspondant à un usage de MRF classique. Le module permet la reconstruction par comparaison des signaux, ou via un outil de régression bayésienne développé dans l'équipe ([Boux et al. 2021](#)). Il est possible de télécharger MP3 et les modules de fingerprinting associés sur le GitHub de l'équipe.

Un outil permettant la visualisation d'un grand nombre de cartes paramétriques dans une interface web a également été développé pour MP3.

## Résumé du chapitre III : Améliorer la MRvF par l'usage de réseaux vasculaires réalistes en 3D

Le chapitre précédent a exposé les outils disponibles pour la MRF et la MRvF et les développements que nous proposons. Les efforts ont porté à la fois sur les aspects d'acquisition et de simulation, qui sont les deux principaux leviers pour améliorer la précision des estimations MRF. En particulier, il a été montré qu'il est désormais possible de simuler des dictionnaires basés sur des modèles vasculaires 3D, avec des géométries plus complexes que les simples modèles 2D utilisés jusqu'à présent. Procéder ainsi devrait amener des évolutions du signal plus conformes à la réalité.

D'après la littérature sur la modélisation de l'effet qBOLD, il est relativement facile de représenter un réseau vasculaire 3D sous forme de cylindres droits aux orientations isotropes. Cependant, un tel modèle est loin de la complexité réelle des structures microvasculaires, que ce soit dans un tissu sain ou pathologique. Plusieurs auteurs ont proposé des méthodes pour générer des réseaux vasculaires entièrement connectés, en garantissant le réalisme grâce à des contraintes provenant d'observations physiologiques et de principes de la mécanique des fluides. Plus récemment, des techniques de microscopie de pointe ont été utilisées pour reconstruire les structures vasculaires du cerveau entier sur des souris.

La simulation de volumes 3D s'accompagne bien sûr d'un temps de simulation accru qui rend la génération de grands dictionnaires impossible. Des méthodes de reconstruction de pointe deviendront certainement nécessaires pour reconstruire des cartes paramétriques de haute qualité à partir de dictionnaires plus petits.

Ce chapitre propose une étude *in vivo* sur des données rétrospectives démontrant l'intérêt de segmenter les réseaux vasculaires 3D à partir de microscopies utilisées pour la génération de dictionnaires. Une méthode générative construisant des réseaux vasculaires réalistes à partir de zéro est évaluée dans un second temps.

### Générer des dictionnaires basés voxels 3D segmentés d'après microscopies

Deux bases de données de microscopies haute résolution de cerveaux de souris ont été utilisées (Di Giovanna et al. 2018; Todorov et al. 2020). 28 000 voxels de taille correspondant à celle d'une acquisition IRM ont été générés et le réseau vasculaire qu'ils contiennent segmenté et caractérisé pour connaître la taille des vaisseaux. Chacun de ces voxels a servi de base pour simuler deux dictionnaires : avant et sans agent de contraste, comme proposé originellement pour la MRvF. On attribue au sang une valeur de  $SO_2$  dans chaque voxel. Des dictionnaires aux propriétés correspondantes ont été générés avec des réseaux vasculaires 2D ou 3D synthétique (c'est à dire constitués de cylindres).

Des données acquises au laboratoire au cours des dernières années ont été utilisées. L'étude porte sur des animaux sains ( $N = 8$ ) et porteurs de tumeurs 9L ( $N = 9$ ).

Contrairement à l'approche utilisée en 2014, ce n'est pas le ratio post/pre injection d'agent de contraste qui a été utilisée, mais la concaténation [pre, post].

En utilisant la reconstruction bayésienne développée dans l'équipe, nous avons montré que les résultats obtenus avec le dictionnaire basé sur des voxels réalistes sont en meilleur accord

avec la littérature que ceux obtenus avec les autres dictionnaires.

De plus, seuls les dictionnaires réalistes sont en accord avec les variations de  $\text{SO}_2$  observées entre les tissus sains et tumoraux via des sondes intracrânielles.

Ces résultats seront l'objet d'une publication dans un journal à comité de lecture, dont le manuscrit est en préparation.

### **Synthétisation de réseaux vasculaires : Optimisation Constructive Contrainte (CCO)**

Dans le cadre d'un stage de master 2 co-encadré durant la thèse, un modèle de génération de réseaux vasculaires a été évalué. Il s'agit du modèle "Constructive Constrained Optimization" (CCO), ou Optimisation Constructive Contrainte (Karch et al. 1999). Cette méthode construit itérativement un arbre vasculaire, de son point d'entrée jusqu'à ses multiples points d'arrivée, en respectant des contraintes sur les flux dans les différentes branches qui lui imposent une géométrie réaliste. Les derniers résultats publiés avec cette méthode montrent qu'il est possible de reconstruire avec réalisme l'intégralité du réseau vasculaire d'un hémisphère cérébral de souris en partant d'une simple angiographie des principaux vaisseaux de surface. Le modèle est décrit en détail dans le manuscrit.

Une implémentation Matlab a été initiée, et amène des résultats encourageants quand au réalisme qu'il est possible d'atteindre. Le coût de calcul est cependant élevé, Matlab n'étant pas le langage le plus performant pour ce type de tâches.

## **Résumé du chapitre IV :**

### **Concevoir des séquences MRvF plus efficaces**

Dans le chapitre précédent, nous avons montré qu'il est possible d'améliorer les performances de la MRvF en utilisant des simulations numériques avancées pour générer des dictionnaires. Un autre moyen évident d'obtenir de meilleures estimations (ou de réduire les temps d'acquisition) est de travailler sur la partie acquisition. Dans la première mise en œuvre de la MRvF, une séquence multi-échos de gradient (GESFIDSE) a été choisie parce qu'elle était connue des expériences qBOLD précédentes pour sa sensibilité aux propriétés microvasculaires. Cependant, la sensibilité du pattern utilisé (rapport post / pre agent de contraste) n'a jamais été vraiment évaluée, en particulier pour les mesures de  $\text{SO}_2$ . De plus, le concept MRF permet en théorie l'utilisation de tout type de séquence d'acquisition, à condition qu'elle soit sensible aux paramètres d'intérêt et qu'il y ait bijectivité entre l'espace des paramètres et celui des signaux, même en présence de bruit. Cela ouvre de nouvelles possibilités pour l'utilisation d'acquisitions non conventionnelles. Dans ce chapitre, nous présentons deux outils simples que nous avons utilisés pour évaluer la sensibilité des séquences MRvF à l'oxygénation du sang. Nous avons d'abord utilisé ces méthodes pour évaluer le potentiel de GESFIDSE et d'autres séquences multi-échos pour les mesures de  $\text{SO}_2$  et nous montrons qu'une simple réorganisation des temps d'écho peut déjà améliorer les estimations. Deuxièmement, à l'aide d'une recherche documentaire et de simulations numériques, nous avons identifié de nouveaux types de schémas d'acquisition basés sur des séquences bSSFP acquises en régime transitoire et en régime stable (steady-state), utilisant éventuellement un cyclage de phase d'impulsion.



Ces optimisations ont conduit à des séquences MRvF potentielles qui pourraient estimer de  $\text{SO}_2$  sans nécessiter l'injection d'un agent de contraste.

## Évaluer la sensibilité d'une séquence

Deux outils ont été utilisés.

- Le premier consiste à calculer l'écart type entre tous les signaux d'un dictionnaire, pour chaque point temporel. En fixant toutes les propriétés des tissus sauf une, le vecteur de valeurs obtenu est en quelque sorte un résumé des variations des signaux lorsque cette propriété varie. Cette méthode permet de comprendre quelle partie du signal est porteuse d'information, ou non, pour un paramètre donné.
- Le second est une approche Monte-Carlo proposée dans la littérature ([Sommer et al. 2017](#)) et présente l'avantage de prendre en considération le bruit d'acquisition. Cette méthode permet aussi de quantifier la précision des estimations qui pourraient être obtenues avec le dictionnaire évalué.

En se basant sur la séquence GESFIDSE acquise avec et sans agent de contraste, nous avons montré *in silico* et en utilisant ces outils qu'il est préférable d'utiliser la concaténation [pre, post] injection que d'autres combinaisons, ce qui a été validé sur des données précliniques rétrospectives.

Ce type de séquence reste simple au regard de la complexité autorisée par la MRF, ce qui explique peut-être le besoin d'injecter un agent de contraste. La section suivante présente donc les travaux menés pour identifier d'autres types de séquences qui pourraient être sensibles à l'oxygénation cérébrale sans injection.

## Étude sur les séquences bSSFP

Les séquences de type "balanced Steady-State Free Precession" (bSSFP) ont été étudiées par le passé pour leur sensibilité à l'effet BOLD. Elles correspondent bien mieux aux acquisitions réalisées habituellement en MRF.

Nous proposons une revue de littérature ainsi qu'une étude sur simulations pour résumer les intérêts de la bSSFP pour la mesure de l'oxygénation cérébrale. Au regard de ces travaux, trois types de séquences dérivant de la bSSFP ont été choisis, et environ 15 séquences pour chaque type ont été testées avec la méthode Monte-Carlo, en collaboration avec un autre étudiant de thèse. Cette étude a identifié une séquence prometteuse, qui, *in silico*, permettrait de mesurer l'oxygénation cérébrale sans agent de contraste.

Des premiers tests précliniques *in vivo* encourageants ont été menés. Des plus gros dictionnaires doivent être générés et plus de données acquises pour conclure. Des essais sur des volontaires sains devraient aussi avoir lieu prochainement.

## Conclusion

Ce travail est le dernier ajout aux développements méthodologiques en cours dans l'équipe depuis plus de deux décennies, visant à imager le réseau vasculaire cérébral et à quantifier



les propriétés microvasculaires d'importance clinique. Nous avons proposé d'améliorer la précision et l'application clinique de la MRvF, une méthode de cartographie de l'oxygénation cérébrale qui s'appuie sur la MRF. Ce paradigme d'IRM récemment introduit a ouvert de nouvelles opportunités excitantes pour l'IRM quantitative mais nécessite une combinaison de simulations numériques, une méthodologie d'acquisition spécifique et des algorithmes de reconstruction de cartes paramétriques.

Tout d'abord, nous avons détaillé les développements effectués sur les parties simulation et acquisition. En nous appuyant sur des outils existants, partagés par la communauté ou développés dans l'équipe, nous avons proposé des outils de simulation pour la conception des dictionnaires MRF et MRvF. En particulier, nous avons renouvelé MRVox, l'outil de simulation utilisé pour simuler la réponse IRM de voxels inhomogènes. La cohérence des simulations a été améliorée et des solutions de calcul parallèle ont été implémentées pour faciliter la génération de dictionnaires. Une version 3D du code a également été implémentée pour améliorer encore la concordance entre les simulations et les acquisitions in vivo. Ces outils sont maintenant partagés avec la communauté MR. Les développements futurs porteront sur les réseaux vasculaires fermés, la simulation de flux et l'amélioration des performances. Des efforts ont été faits pour améliorer la polyvalence des modules d'acquisition MRF préclinique précédemment développés dans l'équipe. Ces modules ont été évalués avec des séquences MR proposées dans la littérature. Nous avons atteint un point de fonctionnement qui permet des acquisitions sur de petits animaux et des évaluations de séquences. Les modules ont été partagés avec des collaborateurs de l'université de Copenhague. Des limites subsistent cependant. Le nombre d'impulsions pouvant être utilisées dans une séquence est limité. De plus, nous avons observé des changements inattendus du signal en fonction de la position de la tranche dans le scanner. Nous allons travailler à la résolution de ces problèmes avec l'aide du personnel technique de Bruker.

Une collaboration avec Philips Research a été initiée et leur module MRF a été installé sur notre scanner. Les premières acquisitions sur des fantômes et des humains ont démontré la flexibilité des modules et des résultats encourageants ont été obtenus sur des expériences de relaxométrie utilisant des séquences de la littérature. Finalement, des outils de reconstruction et des solutions de visualisation associées ont été développés spécifiquement pour les besoins de la MRF. Ils ont été intégrés dans un processeur de pipeline développé et maintenu par l'équipe, qui a été publié comme un outil open-source pour la communauté.

Deuxièmement, nous avons démontré comment la sensibilité de la MRvF pouvait être augmentée en affinant les simulations. Nous avons segmenté les réseaux vasculaires à partir de microscopies 3D du cerveau entier accessibles au public, et les avons utilisés comme base de simulation dans la version 3D de MRVox. Pour tenir compte du nombre limité de voxels qui ont été traités en un temps raisonnable, le dictionnaire simulé a été appris par un outil de régression bayésienne développé dans l'équipe. Sur des données rétrospectives provenant de rats sains et pathologiques, le dictionnaire MRvF que nous avons proposé a donné de meilleurs résultats que les approches 2D et 3D précédentes, produisant des cartes d'oxygénation avec des contrastes et des valeurs absolues en meilleur accord avec la littérature. En outre, seule notre approche était en corrélation avec les mesures de  $pO_2$  intracrâniennes dans les lésions. Des limites de la méthode proposée ont également été identifiées. En particulier, aucune base de données de microscopie dans des tissus pathologiques n'a été partagée à ce jour.

L'inclusion de tels tissus dans nos simulations devrait permettre d'obtenir de meilleures estimations dans les lésions. Nous avons commencé à mettre en œuvre des solutions dédiées telles que des algorithmes constructifs pour générer *in silico* des réseaux vasculaires réalistes.

Enfin, nous avons cherché une meilleure séquence d'acquisition MRvF qui serait à la fois plus sensible à l'oxygénation du sang et sans agent de contraste. Des outils proposés dans la littérature pour évaluer la sensibilité d'une séquence donnée aux paramètres d'intérêt ont été mis en œuvre. Ces outils ont été validés sur des données rétrospectives chez l'animal, en utilisant différentes combinaisons d'acquisitions réalisées avant et après injection de produit de contraste. Nous avons finalement présenté une combinaison dont les performances étaient supérieures à celles de l'approche initiale.

Pour trouver une séquence sensible à l'oxygénation mais ne nécessitant pas d'injection de produit de contraste, nous avons commencé par rechercher dans la littérature IRM. Nous avons recherché des séquences non conventionnelles utilisées pour l'imagerie fonctionnelle ainsi que des séquences sous-utilisées en raison de leur grande sensibilité aux inhomogénéités du champ magnétique. À partir de ces intuitions, plusieurs types de séquences ont été évalués et une séquence présentant des résultats *in silico* prometteurs a été trouvée. Des essais *in vivo* sur des animaux ont commencé et les résultats préliminaires sont présentés. En parallèle, des algorithmes d'optimisation de séquence automatique de pointe sont évalués pour aider à trouver de nouvelles séquences qui seront plus précises et plus robustes aux artefacts d'imagerie.

En conclusion, les développements de ce projet de doctorat ont conduit à la création d'un pipeline MRF capable d'acquérir et de traiter des données précliniques et cliniques. Les résultats obtenus pour les mesures d'oxygénation cérébrale peuvent déjà être utilisés pour améliorer les estimations de la  $SO_2$  et un certain nombre de collaborations ont été entamées pour tester davantage la technique dans différentes conditions. Des améliorations potentielles pourraient être obtenues suite à nos nouveaux développements sur des simulations réalistes et aux prochains tests *in vivo* des séquences bSSFP candidates pour la cartographie de l'oxygénation sans agent de contraste. Compte tenu de nos résultats encourageants, nos outils pourraient être utilisés comme base pour le développement de séquences MRF uniques qui pourraient remplacer des examens IRM complets. Cela permettrait de réaliser des examens plus courts, mieux adaptés à l'imagerie d'urgence. Dans ce cas, des procédures d'optimisation automatique pourraient être utilisées pour intégrer les informations structurelles et fonctionnelles dans les signaux MRF en un temps raisonnable. La MRF offre également la possibilité de partager rapidement une séquence IRM complète par le biais d'un seul fichier texte, évitant ainsi des mois de développement de la séquence et d'adaptation logicielles. La collaboration entre les équipes de recherche et les essais multicentriques devrait ainsi être facilités et conduire à une diffusion plus rapide sur les scanners cliniques et à des avantages pour les soins aux patients.



---

## Abstract

---

Blood oxygenation saturation ( $SO_2$ ) is a microvascular property of clinical relevance. Pathologies such as cancer or stroke may induce a hyper- or hypo-oxygenation of the cerebral tissues. Interestingly, Magnetic Resonance Imaging (MRI) is sensitive to the oxygenation level in the blood, a phenomenon known as the blood-oxygen level dependent (BOLD) effect.

Our team has recently proposed to use the MR vascular Fingerprinting (MRvF) approach to map brain oxygenation. This technique relies on the MR Fingerprinting (MRF) framework, which uses a dictionary approach to analyze the data. The proposed implementation yields encouraging results on animal models and humans but suffers from a lack of sensitivity. In addition, it requires contrast agent injections which severely limit its application in a clinical context. The aim of this PhD work was to develop flexible MRvF tools that would address both the current method's lack of sensibility and poor translationality.

First, technical developments were led on all stages of the MRvF pipeline. We worked on the expansion of an original MRF acquisition tool designed for pre-clinical scanners and collaborated with Philips research team on a clinical MRF acquisition pipeline. We implemented classical MR simulations using Bloch equations to generate structured dictionaries and participated in the development of a more complex tool to perform simulations on realistic 3D microvascular networks. Finally, reconstruction methods using either classical direct matching or a Bayesian learning algorithm were implemented in a home-made, open-source database processing software. Using these new tools, we focused on improving the accuracy of the MRvF method by refining the realism of the simulations. A retrospective study on data obtained at 4.7T on 40 animals, in healthy and pathological conditions (stroke + tumors), using a new dictionary built from 28,000 3D voxels containing vascular networks segmented from microscopy databases, showed substantial improvements of the  $SO_2$  measurements compared to the first MRvF implementation.

A second point of focus was to find a fast MRF sequence able to produce  $SO_2$  estimates without requiring contrast agent injection. Based on literature search, we tested 40 unconventional MRI sequences that presented transient and steady states sensitive to the BOLD effect. A Monte-Carlo method was used to evaluate the encoding capacity of the sequences. Our in silico study identified acquisition patterns which seemed to provide contrast agent-free  $SO_2$  estimates with better accuracy and robustness to scanner artifacts than the initial MRvF implementation.

The tools developed for our project will serve as a basis to design unique MRF protocols that could replace MR acute stroke exams and improve patient care.

**Keywords:** MRI, Fingerprinting, Brain, Oxygenation, Vascularization, Simulations

---

## Résumé

---

La saturation en oxygène du sang ( $SO_2$ ) est une propriété microvasculaire d'importance clinique. Des pathologies telles que le cancer ou les accidents vasculaires cérébraux peuvent induire une hyper- ou une hypo-oxygénation des tissus cérébraux. Il est intéressant de noter que l'imagerie par résonance magnétique (IRM) est sensible au niveau d'oxygénation du sang, un phénomène connu sous le nom d'effet BOLD (blood-oxygen level dependent).

Notre équipe a récemment proposé d'utiliser l'approche MR vascular Fingerprinting (MRvF) pour cartographier l'oxygénation du cerveau. Cette technique s'appuie sur l'IRM Fingerprint (MRF), qui utilise une approche par dictionnaire pour analyser les données. L'implémentation proposée donne des résultats encourageants sur des modèles animaux et des humains mais souffre d'un manque de sensibilité. De plus, elle nécessite des injections de produit de contraste qui limitent fortement son application dans un contexte clinique. L'objectif de ce travail de thèse était de développer des outils MRvF flexibles permettant de remédier au manque de sensibilité et au faible caractère translationnel de la méthode actuelle.

Tout d'abord, des développements techniques ont été menés sur toutes les étapes du pipeline MRvF. Nous avons travaillé à l'amélioration d'un outil d'acquisition MRF original conçu pour les scanners précliniques et collaboré avec l'équipe de Philips Research sur un pipeline d'acquisition MRF clinique. Nous avons mis en œuvre des simulations IRM classiques utilisant des équations de Bloch pour générer des dictionnaires structurés et avons participé au développement d'un outil plus complexe pour effectuer des simulations sur des réseaux microvasculaires 3D réalistes. Enfin, des méthodes de reconstruction utilisant soit le matching direct classique, soit un algorithme d'apprentissage bayésien, ont été mises en œuvre dans un logiciel de traitement de base de données développé au laboratoire et open-source.

Grâce à ces nouveaux outils, nous nous sommes attachés à améliorer la précision de la méthode MRvF en affinant le réalisme des simulations. Une étude rétrospective sur des données obtenues à 4,7T sur 40 animaux, dans des conditions saines et pathologiques (AVC + tumeurs), en utilisant un nouveau dictionnaire construit à partir de 28 000 voxels 3D contenant des réseaux vasculaires segmentés à partir de bases de données de microscopie, a montré des améliorations substantielles des mesures de  $SO_2$  par rapport à la première implémentation MRvF.

Un deuxième point de travail était de trouver une séquence MRF rapide capable de produire des estimations de  $SO_2$  sans nécessiter d'injection de produit de contraste. Sur la base d'une recherche bibliographique, nous avons testé 40 séquences IRM non conventionnelles présentant des états transitoires et stables sensibles à l'effet BOLD. Une méthode de Monte-Carlo a été utilisée pour évaluer la capacité d'encodage des séquences. Notre étude in silico a identifié des modèles d'acquisition qui semblaient fournir des estimations de  $SO_2$  sans agent de contraste avec une meilleure précision et une meilleure robustesse aux artefacts du scanner que l'implémentation MRvF initiale.

Les outils développés dans le cadre de notre projet serviront de base à la conception de protocoles MRF uniques qui pourraient remplacer les examens d'AVC aigus par IRM et améliorer les soins aux patients.

**Mots-clés :** IRM, Fingerprinting, Cerveau, Oxygénation, Vasculature, Simulations

---